Stability Analysis of Converter Control Strategies for Power Electronics-Dominated Power Systems

Dissertation

zur Erlangung des akademischen Grades
Doktor der Ingenieurwissenschaften
(Dr.-Ing.)
Technische Fakultät
der Christian-Albrechts-Universität zu Kiel
vorgelegt von

M. Sc. *Roberto Rosso*

Kiel
2020

1. Gutachter: Prof. Marco Liserre, Ph.D.
2. Gutachter: Prof. Dr.-Ing. Andreas Lindemann
3. Gutachter: Prof. Dr.-Ing. Christian Rehtanz
Datum der mündlichen Prüfung: 25.08.2021

To my wife Danila and
to our lovely children Elide and Aurelio

Aknowledgment

I would first like to thank WRD GmbH for financially supporting my work on this thesis and for giving me the opportunity to pursue my industrial PhD.

I am also grateful to my doctoral supervisor and mentor, Prof. Marco Liserre, for the opportunity to work in his research group at the Chair of Power Electronics. His wise words went beyond technical talk relating to our work and I will always treasure his precious advice for my future career and private life. I would also like to thank Dr. Soenke Engelken, who was my supervisor at the company. He always supported me during my research, even before I started my PhD, and it is also thanks to him if this industrial PhD was possible.

I am thankful to Prof. Andreas Lindemann and Prof. Christian Rehtanz for reviewing my PhD thesis, and also to the other members of the examination committee, Prof. Axel Müller-Groeling and Prof. Thomas Meurer. It was a great pleasure and an honor for me to discuss my work with them.

A special thanks must also go to my colleagues Jair Cassoli and Dr. Angelo Mendonca for their support and advice during this time. I am also indebted to the colleagues at the chair of Power Electronics, especially Dr. Sante Pugliese, who shared many important moments with me during my time in Kiel.

My heartfelt gratitude must also go to my family, especially to my wife Danila, without whom I would have never achieved this goal. Thank you for always being by my side, encouraging me and for convincing me not to give up, especially during the toughest moments of this journey. Thank you for making it possible to realize my dream.

Finally, I would like to apologize to my daughter Elide, who was born just a few months after I began my PhD. I wish that I could have been there with you when you took your first steps and at other important moments in your early life. I hope you will know one day how much of a boost it was for me to come home and get a hug from you.

Aurich, September 2021

Roberto Rosso

Deutsch Kurzfassung der Arbeit

Das elektrische Stromnetz, dessen Struktur durch Jahrzehnte von Studien konsolidiert wurde, befindet sich in einem Veränderungsprozess. Die steigende Eindringung von umrichterbasierter Energieerzeugung, die mit der zunehmenden Durchdringung von erneuerbaren Energien zugeordnet ist, begrenzt die Menge der Energie, die durch konventionelle Kraftwerke, bzw. durch Synchronmaschinen ins Netz eingespeist wird. Das hat zufolge, dass Themen wie Ersatz von Momentanreserve aus der Schwungmasse von konventionellen Kraftwerken, aber auch weitere potentiell nötige Systemdienstleistungen wie unverzögerte Bereitstellung von Fehlerströmen zu berücksichtigen sind. Das hat zu Diskussionen zwischen Netzbetreibern weltweit geführt, wie das elektrische Energiesystem mit gleichbleibender Effizienz und Zuverlässigkeit in der erwarteten Konfiguration weiter betrieben werden kann.

In diesem Szenario, wurde das Konzept von "grid-forming (GFM) converters" (auf Deutsch: netzbildende bzw. spannungsprägende Umrichter) als mögliche Lösung für die Erhöhung der Durchdringung von umrichterbasierter Energieerzeugung eingeführt. Ursprünglich für den Einsatz in Inselnetze oder Microgrids gedacht, muss das Konzept für Anwendungen in Verbundnetze angepasst werden. Aktuell ist aber eine eindeutige Definition des Verhaltens eines GFM Umrichters nicht vorhanden, sodass das Thema gerade von mehreren Gremien weltweit adressiert wird. Wegen der ursprünglichen Überlegungen bezüglich Reduktion von Schwungmasse und Systemträgheit, ist das Konzept eines netzbildenden Umrichters oft mit der Idee einer synthetischen Schwungmasse identifiziert worden. Allerdings, entspricht das zusätzliche Eigenschaften gegenüber der reinen Emulation einer virtuellen Trägheit, die aber eindeutig definiert werden müssten, um anschauliche Hinweise für die Entwicklung von Umrichter-Regelverfahren an Hersteller signalisieren zu können.

In dieser Dissertation wird das Thema von netzbildenden Umrichtern aus der Regelperspektive betrachtet, und werden dabei sowohl die potentielle Vorteile, als auch relevanten Problematiken einer solchen Technologie identifiziert. Die Eigenschaften eines netzbildenden Umrichters sind mithilfe einer umfangreichen Literaturrecherche zuerst identifiziert, dann wird eine generalisierte Regelstruktur für solche Umrichter abgeleitet. Besonderes Augenmerk wird auf das Synchronisierungsverfahren von netzgekoppelten Umrichtern gelegt, dass nach Stand der Technik von Umrichter-Regelverfahren durch Einsetzung einer getrennten Synchronisierungseinheit stattfindet, aber bei netzbildenden Umrichtern oft durch die Emulation der Leistungssynchronisierungsverfahren einer realen Synchronmaschine erfolgt. Eine umfassende klein-Signal Stabilitätsanalyse wird deshalb durchgeführt, um sowohl die Konsequenzen des identifizierten Verhaltens auf die Umrichter-Stabilität, als auch die Effekte der Interaktionen zwischen Umrichtern in der nahen Umgebung bestimmen zu können. Potentielle Herausforderungen gebunden mit der netzbildenden Umrichtertechnologie werden schließlich identifiziert und mögliche Lösungen werden vorgeschlagen, deren Auswirkung durch hardware-in-the-loop (HIL) Simulationen, als auch durch experimentelle Ergebnisse in einer Laborumgebung mithilfe von power-HIL (PHIL) Prüfstände validiert werden.

English Summary

The electric power system, whose well-established structure consolidated over decades of studies is composed of large centralized generating units, transmission systems, and distributed loads, is currently experiencing a significant transformation, posing new challenges for its safe operation in the near future. The increasing amount of grid-connected power electronics-based converters associated with renewable energy sources, is reducing the amount of energy produced by means of conventional generating units, generally represented by large synchronous machines (SMs) directly connected to the grid. As a consequence, declining system inertia, as well as reduced fault currents affecting short-circuit level and retained voltage under fault conditions, are expected. This has caused concerns among system operators (SOs) worldwide about the stability of the future power system, triggering discussions in different countries about the need for new converter control strategies, which would allow safe system operation under the expected grid configuration.

In this scenario, the concept of ”grid-forming (GFM) converters” has been recently proposed as a possible solution allowing high-penetration of power electronics-based generation. Initially introduced in the context of microgrids, the concept of GFM converters needs to be reviewed for applications in wide interconnected systems. Indeed, at the present time, a well-established formulation is still missing in the literature, and several committees worldwide are currently working on a definition for identifying the characteristics of such converters. Due to the initial concern of SOs related to declining system inertia, the concept of GFM converters has been often associated with the idea of virtual inertia, and namely the emulation of a synthetic inertial response by means of a power electronics-based converter. Yet, this is only one aspect related to the increase of power electronics-based generation, and the concept of a GFM converter includes other features, which, however, need to be properly specified in order to provide clear guidelines for manufacturers aiming to the development of suitable converter control strategies.

This thesis addresses the topic of GFM converters from a control perspective, and aims to characterize potential features, as well as the relevant issues related to this technology. First, the characteristics of a GFM converter are identified according to an extensive literature overview, so that by reviewing international practice on this technology, a general formulation for a GFM converter control structure is identified. Particular emphasis is given to the synchronization principle adopted by the converter which, contrary to state-of-the-art grid-connected converters adopting a dedicated unit for grid synchronization purposes, is generally achieved in a GFM converter by reproducing the power-synchronization mechanism of a SM. An extensive small-signal stability analysis is performed in order to identify the implications of the identified converter behaviour on converter stability, as well as the effects due to the interactions between converters operating nearby. Finally, potential issues related to the implementation of a GFM converter are highlighted, and possible solutions are proposed, whose effectiveness is validated by means of hardware-in-the-loop (HIL) simulations, as well as experimental tests in a laboratory environment, by adopting power-HIL (PHIL) test benches.

Contents

German summary . . . . F
English summary . . . . G
Used symbols and abbreviations IV
1 Introduction 1
1.1 Motivation for new converter control strategies 1
1.1.1 Discussions at European level about the development of GFM converters 2
1.2 Research proposal 4
1.3 Structure of the thesis 5
1.4 Assignment of publications to the chapters of this thesis 7
2 Operating principles of grid-connected converters 8
2.1 Notation adopted in this thesis 8
2.2 Converters classification according to their control strategy 10
2.2.1 Classification for microgrids 11
2.2.2 Need for more general definitions 15
2.2.3 Conceptual differences between GFL and GFM converters 16
2.2.4 VSMs and GFM converters 19
2.3 Synchronization techniques for grid-connected converters 21
2.3.1 The SRF-PLL 21
2.3.2 The Power-synchronization principle 24
2.4 General structure of GFM converters 27
2.4.1 Outer loop - synchronization loop 28
2.4.2 Outer loop - voltage profile management 35
2.4.3 Inner loop - Generation of the modulation signal 36
2.4.4 Virtual Oscillator Control (VOC) 43
2.5 Summary of the chapter 47
3 Approaches for stability analysis 49
3.1 Concept of stability 49
3.1.1 Stability of a dynamic system 49
3.1.2 Power system stability 50
3.1.3 Stability in microgrids 51
3.1.4 Linear and non-linear systems 53
3.2 Impedance-based analysis 57
3.2.1 Monte-Carlo analysis 59
3.3 Eigenvalue analysis 61
3.3.1 Eigenvalues and eigenvectors 61
3.3.2 Modal analysis 63
3.3.3 The component connection method (CCM) 66
3.4 Robust stability analysis 67
3.4.1 Singular values 68
3.4.2 Matrix norms 70

3.4.3 Small-gain theorem and μ-analysis 71
4 Analysis of the interactions among converters 77
4.1 Impedance-based analysis of the interactions among PLLs 77
4.1.1 Modeling of GFL converters for studying synchronization issues . . 78
4.1.2 Norm calculation for stability margin assessment 80
4.1.3 Monte-Carlo analysis 85
4.1.4 Effects of the inner current control loop 87
4.2 Eigenvalue-based stability analysis of GFM converters 90
4.2.1 Small-signal model of LCL filter-based synchronverter 90
4.2.2 Parameter tuning and eigenvalue analysis 96
4.2.3 Parallel operation of GFM converters 103
4.2.4 Modal analysis 108
4.3 Robust stability analysis of the interactions among GFL and GFM converters 112
4.3.1 Robust stability of GFM converters 112
4.3.2 Model for studying interactions between GFL and GFM converters 120
4.3.3 Interactions between GFL and GFM converters - μ-analysis 125
4.4 Summary of the chapter 130
5 Fault ride-Through (FRT) of GFM converters 132
5.1 Challenges for GFM converters 132
5.1.1 Rotor angle stability 133
5.1.2 Short-circuit currents 138
5.1.3 Literature overview on FRT techniques for GFM converters 140
5.1.4 Actual status draft grid codes for GB 142
5.2 Proposed solutions for overcoming the highlighted issues 144
5.2.1 Estimation of angle instability condition 144
5.2.2 Limitation of short-circuit currents 147
5.3 HIL simulation results 155
5.3.1 Action of the inner control loop 157
5.3.2 Action of the outer control loop 162
5.4 Summary of the chapter 164
6 Experimental validation 166
6.1 Setups descriptions 166
6.1.1 Setup 1 166
6.1.2 Setup 2 168
6.2 Interactions among converters 169
6.2.1 GFM converters 169
6.2.2 GFL converters 176
6.2.3 Interactions between GFL and GFM converters 177
6.3 FRT of GFM converters 179
6.3.1 Symmetrical faults 179
6.3.2 Asymmetrical faults 182
6.3.3 Bolted three-phase faults 183
6.4 Summary of the chapter 187

7 Summary, conclusions, and future research 189
7.1 Summary and conclusions 189
7.2 Research contribution 191
7.3 Future research 192
8 References 195
9 Attachment 215
9.1 Interconnection matrices two GFM in parallel 215
9.2 Publications related to this thesis 215
9.2.1 Journal publications 215
9.2.2 Conference publications 216
9.2.3 Patent applications 217

Used symbols and abbreviations

General symbols

General symbols

Δ	Small deviation
$\mathcal{F}_l(\cdot\,,\cdot)$	Lower linear fractional transformation
s	Laplace operator
$\lvert\cdot\rvert$	Absolute value
$\lVert\cdot\rVert$	Norm of a matrix
$\lVert\cdot\rVert_\infty$	Infinity norm

Superscripts

$*$	Inner setpoints generated in the control
H	Complex conjugate transpose of a matrix
T	Transpose of a matrix

Subscripts

d	d-component
DC	DC-link related
LL	Line-to-line
PCC	PCC-related
PLL	PLL-related
q	q-component
ref	Reference value
set	Setpoint
0	Quantity at the operating point

Special symbols

a	Scale parameter of the Weibull distribution
$\mathbf{A}$	System matrix
$\mathbf{A}_c$	System matrix of the control subsystem
$\mathbf{A}_{filt}$	System matrix of the filter subsystem
$\mathbf{A}_g$	System matrix of the grid subsystem
$\mathbf{A}_j$	Jacobian matrix
$\mathbf{A}_{LCL}$	System matrix of the LCL filter subsystem
$\mathbf{A}_{PQ}$	System matrix of the *P, Q, and V calc.* subsystem

$\mathbf{A}_\pi$	System matrix of the plant subsystem
$\mathbf{A}_{sub}$	System matrix of one subsystem
α	Fortescue operator
α_v	Parameter of the VOC
b	Shape parameter of the Weibull distribution
$\mathbf{B}$	System input matrix
$\mathbf{B}_c$	System input matrix of the control subsystem
$\mathbf{B}_{filt}$	System input matrix of the filter subsystem
$\mathbf{B}_g$	System input matrix of the grid subsystem
$\mathbf{B}_j$	System input matrix of the linearized system
$\mathbf{B}_{LCL}$	System input matrix of the LCL filter subsystem
$\mathbf{B}_{PQ}$	System input matrix of the *P, Q, and V calc.* subsystem
$\mathbf{B}_\pi$	System input matrix of the plant subsystem
$\mathbf{B}_{sub}$	System input matrix of one subsystem
BW	Bandwidth of a controller
β_v	Parameter of the VOC
C	Generalized controller
$\mathbf{C}$	System output matrix
$\mathbf{C}_c$	System output matrix of the control subsystem
C_f	LCL capacitor filter
$\mathbf{C}_{filt}$	System output matrix of the filter subsystem
$\mathbf{C}_g$	System output matrix of the grid subsystem
$\mathbf{C}_j$	System output matrix of the linearized system
$\mathbf{C}_{LCL}$	System output matrix of the LCL filter subsystem
$\mathbf{C}_{PQ}$	System output matrix of the *P, Q, and V calc.* subsystem
$\mathbf{C}_\pi$	System output matrix of the plant subsystem
C_s	Shunt capacitor
$\mathbf{C}_{sub}$	System output matrix of one subsystem
$\mathbf{D}$	System feedforward matrix
$\mathbf{D}_c$	System feedforward matrix of the control subsystem
D_{cd}	$d-$component of the duty-ratio at the operating point
D_{cq}	$q-$component of the duty-ratio at the operating point
D_f	Damping factor of the swing equation
$\mathbf{D}_{filt}$	System feedforward matrix of the filter subsystem
D_{fx}	Damping correction term of the modified synchronverter structure
$\mathbf{D}_g$	System feedforward matrix of the grid subsystem
$\mathbf{D}_j$	System feedforward matrix of the linearized system
$\mathbf{D}_{LCL}$	System feedforward matrix of the LCL filter subsystem
D_p	P droop coefficient
$\mathbf{D}_{PQ}$	System feedforward matrix of the *P, Q, and V calc.* subsystem
$\mathbf{D}_\pi$	System feedforward matrix of the plant subsystem
D_q	Q droop coefficient
$\mathbf{D}_{sub}$	System feedforward matrix of one subsystem

δ	Power angle
δ_{cr}	Critical power angle
δ_m	Maximal power angle of the equal-area criterion
δ_M	Angle displacement corresponding to the maximum power transfer
$\dot{\delta}_{MAX}$	Maximum speed of the machine during the transient
$\ddot{\delta}^+_{MAX}$	Maximum acceleration of the machine during the transient
$\ddot{\delta}^-_{MAX}$	Maximum deceleration of the machine during the transient
δ_x	Diagonal element of the structured uncertainty matrix
δ_0	Initial power angle
E	Amplitude of the voltage at the converter terminals
e^*	Three-phase virtual back-emf voltages
e'	Reference voltage for PWM
E_f	Amplitude of the back-emf voltage of a SM
E_p	Amplitude of the virtual back-emf
ε_v	Parameter of the VOC
f_c	Cut-off frequency of the PLL open loop transfer function
F_{CL}	Closed-loop PLL transfer function simplified model
f_g	Rated grid frequency
$\mathbf{F}_{int}$	System matrix of the interconnected system
F_{OL}	Open-loop PLL transfer function simplified model
f_s	Switching frequency
$f_w(x)$	Probability density function of Weibull distribution
$\hat{f}_w(x)$	Estimated density function by means of a Kernel density estimator
ϕ_I^+	Phase positive sequence currents
ϕ_I^-	Phase negative sequence currents
$\Phi(n)$	State transition matrix Kalman filter
G	Generalized plant
$\mathbf{G}_{cc}$	Transfer function of PI current control
$\mathbf{G}_{dec}$	Transfer function of decoupling term of the current control
$\mathbf{G}_{del}$	Transfer function of the delay introduced by the PWM
G_E	PI gain of the EDPC synchronization loop
$\mathbf{G}_{id}$	Transfer function of the effects of the duty ratio on output currents
$\mathbf{G}_{int}$	System input matrix of the interconnected system
G_p	Perturbed plant
$\mathbf{G}^d_{PLL}$	Transfer function of the effects of PLL on duty cycle
$\mathbf{G}^i_{PLL}$	Transfer function of the effects of PLL on measured currents
h	Bandwidth of the kernel estimator
$\mathcal{H}$	Hardy space
$\mathbf{H}_{int}$	System output matrix of the interconnected system
H_{PLL}	PLL transfer function of the linearized model
$\mathbf{H}(n)$	Measurement matrix Kalman filter
$\mathcal{H}_\infty$	Subspace of $\mathcal{H}$
i'	Current setpoint of an ideal current source

i^*	Setpoint currents calculated by means of a virtual admittance
i^{**}	Setpoint currents for the inner control loop
i_c	Output current of the control subsystem
i_{con}	Output current of the P2C subsystem
i_{conv}	Current source of the Norton equivalent converter model
i_d	d-component measured currents propagated in the GFL control
i_d^*	d-component current setpoint
i_f	Converter filter currents fed back to the control
i_g	Grid current
i_{grid}	Input currents for the grid model in RTDS
i_{Lg}	Grid current of the grid subsystem
i_{Lf1}	Converter-side current of the LCL filter
i_{Lf2}	Grid-side current of the LCL filter
i_{Lv}	Inductor current of the virtual oscillator model
I_m	Estimated maximum instantaneous amplitude of the converter currents
I_m^+	Amplitude positive sequence currents
I_m^-	Amplitude negative sequence currents
I_{max}	Maximum amplitude of the converter currents
i_{PCC}	Currents measured at the PCC
i_q	q-component measured currents propagated in the GFL control
i_q^*	q-component current setpoint
i_v	Virtual currents for pre-synchronization
J	Moment of inertia
$\mathbf{J}_{int}$	System feedforward matrix of the interconnected system
J_{opt}	Optimal virtual moment of inertia from design procedure
K	Parameter of the synchronverter Q-loop
$K(\cdot)$	Kernel smoothing function
$\mathbf{K}(n)$	Kalman gain
k_{dist}	Distance factor
k_i	Integral gain of the PI controller of a SRF-PLL
K_i	Integral gain of the PSC synchronization loop
k_{ii}	Integral gain of a PI-based current control
k_{i_corr}	Integral gain correction term current limitation
k_{i_dp}	Integral gain power estimation loop
k_{iv}	Scaling factor of voltage of the VOC
k_{lim}	limitation gain reference currents
K_{lim}	Critical value of synchronverter parameter K for stability
K_{opt}	Parameter K of the synchronverter Q-loop form design procedure
k_p	Proportional gain of the PI controller of a SRF-PLL
k_{pi}	Proportional gain a PI-based current control
k_{p_dp}	Proportional gain power estimation loop
k_{p_corr}	Proportional gain correction term current limitation
k_{SOGI}	Gain of the SOGI structure

k_{vv}	Scaling factor of voltage of the VOC
$\mathbf{L}$	Return ratio
L_{add}	Additional inductor of the laboratory setup
L_c	Inductance of the additional impedance subsystem
L_f	Inductive component of the filter impedance
L_{f1}	Converter-side filter inductance of LCL filter
L_{f2}	Grid-side filter inductance of LCL filter
L_g	Grid inductance
L_{gb}	Base grid inductance
L_T	Transformer inductance
L_v	Inductive component of the virtual impedance
L_{v_n}	Nominal inductive component of the virtual impedance
L_{v_f}	Inductive component of the virtual impedance during fault
$\mathbf{L}_{xx}$	Interconnection matrix
$\lambda_i(\cdot)$	i-th eigenvalue of a square matrix or of a loop transfer function
m	Scaling factor of the filter impedance multiplication technique
$M_f i_f$	Virtual rotor flux
μ	Structured singular value
N_{con}	Number of converters
ω	Frequency of the inner voltage of a GFM converter
$\widehat{\omega}$	Grid voltage frequency estimated by a generic synchronization unit
ω_{cf}	Cut-off frequency low-pass filter
ω_g	Grid frequency in rad/sec
ω_m	Mechanical rotational speed of a SM
ω_n	Nominal rotational speed / grid frequency
ω_{nt}	Natural frequency of a second-order transfer function
$\omega_{pre-fault}$	Pre-fault value of the grid frequency
ω_{PLL}	Frequency estimated by the PLL
ω_{ref}	Reference grid frequency for the GSU control loop
ω_{set}	Setpoint frequency of an USV-type GFM converter
P	Measured Active power
$\mathbf{P}$	Participation matrix
$\mathbf{P}(n)$	Covariance matrix estimation error of the Kalman filter
$\widehat{P}$	Estimated active power
P_a	Accelerating power
P_{aMAX}^{+}	Maximum positive accelerating power
P_{aMAX}^{-}	Maximum negative accelerating power
P_{app}	Approximated transfer function representing the P loop
P_f	Filtered measured active power
P_i	Mechanical power input
$\mathbf{p}_i$	i-th column of the participation matrix
P_M	Maximum transmissible power
$PT1_P$	First-order approximation of the transfer function $\Delta P/\Delta\theta$

$PT1_Q$	First-order approximation of the transfer function $\Delta Q/\Delta E_p$
$PT1_V$	First-order approximation of the transfer function $\Delta V/\Delta E_p$
P_{rated}	Converter rated active power
P_{ref}	Active power reference value
P_{set}	Active power setpoint
P_u	Active power exchanged between two SMs or a SM and an infinite bus
$\mathit{\Pi}$	Plant
$\boldsymbol{\Pi}$	Uncertain model set
$\boldsymbol{\Phi}_i$	Right eigenvector
$\boldsymbol{\Psi}_i$	Left eigenvector
q_L	90° lagging phase shift
Q	Measured reactive power
Q_f	Filtered measured reactive power
Q_{ref}	Reactive power reference value
Q_{set}	Reactive power setpoint
Q_0	Measurement covariance factor Kalman filter
R_c	Resistance of the additional impedance subsystem
R_{cf}	Damping resistance of the capacitor filter
R_d	Virtual damping resistance of the EDPC synchronization loop
R_f	Resistive component of the filter impedance
R_{f1}	Converter-side resistance of LCL filter
R_{f2}	Grid-side resistance of LCL filter
R_g	Grid resistance
R_{gb}	Base grid resistance
$\mathcal{RH}$	Real rational subspace of $\mathcal{H}$
R_s	Shunt resistance
R_{sum}	Sum of the resistances R_{cf}, R_{f2}, and R_g
R_T	Transformer resistance
R_v	Resistive component of the virtual impedance
R_{v_n}	Nominal resistive component of the virtual impedance
R_{v_f}	Resistive component of the virtual impedance during fault
R_0	Noise covariance factor Kalman filter
$\rho(\cdot)$	Spectral radius of a matrix
S_n	Converter nominal power
S_{PC}	Synchronizing power coefficient
$S_{PC\ index}$	Synchronizing power coefficient index
S_{sc}	Short-circuit power
S_{sp}	Steady-state value of the transfer function $\Delta P/\Delta\theta$
S_{sq}	Steady-state value of the transfer function $\Delta Q/\Delta E_p$
S_{sv}	Steady-state value of the transfer function $\Delta V/\Delta E_p$
σ_v	Inverse of the resistance of the virtual oscillator model
$\overline{\sigma}$	Largest singular value
$\underline{\sigma}$	Smallest singular value

T_{del}	Delay introduced by the PWM
T_e	Electrical torque
T_m	Mechanical torque
T_p	Inverse natural frequency of the approximated P loop transfer function
t_r	Rise-time of a first-order system
t_s	PLL settling-time
T_s	Control sample time
τ	Decay time of an oscillatory mode
τ_{refp}	Dominant pole of the approximated transfer function of the P loop
τ_{refq}	Dominant pole of the approximated transfer function of the Q loop
τ_{refv}	Dominant pole of the approximated transfer function of the $Q-V$ loop
θ	Angle of the inner voltage of a GFM converter
θ_c	Angle of the converter voltage at the output terminals
$\widehat{\theta}$	Grid voltage angle estimated by a generic synchronization unit
θ_g	Grid voltage angle
θ_{PLL}	Grid voltage angle estimated by the PLL
θ_r	Rotor angle of a SM
θ_{set}	Setpoint angle of an USV-type GFM converter
$\mathbf{u}$	Vector of inputs
$\mathbf{u}_c$	Vector of inputs control subsystem
$\mathbf{u}_{CC}$	Vector of inputs of the *PI current control* subsystem
$\mathbf{u}_{del}$	Vector of inputs of the *Delay* subsystem
$\mathbf{u}_{filter}$	Vector of inputs of the *Filter* subsystem
$\mathbf{u}_g$	Vector of inputs of the *Grid* subsystem
$\mathbf{u}_{LCL}$	Vector of inputs of the *LCL filter* subsystem
$\mathbf{u}_\pi$	Vector of inputs plant subsystem
$\mathbf{u}_{plant}$	Vector of inputs of the plant
$\mathbf{u}_{P2C}$	Vector of inputs of the *PLL on currents* subsystem
$\mathbf{u}_{P2V}$	Vector of inputs of the *PLL on voltages* subsystem
$\mathbf{u}_{sys}$	Vector of inputs of the interconnected system
$\mathbf{u}_{sub}$	Vector including all the inputs of the subsystems
$\mathbf{u}_{Zc}$	Vector of inputs of the *Additional impedance* Z_c subsystem
V	Measured PCC voltage amplitude
v'	Voltage setpoint of an ideal voltage source
$\mathbf{v}(n)$	Measurement vector Kalman filter
v_{cf}	Voltage across the capacitor filter
v_{cs}	Voltage across the shunt capacitor
v_{Cv}	capacitor voltage of the virtual oscillator model
ΔV_{corr}	Correction term of the current limitation control
v_d	d-component measured voltages propagated in the GFL control
V_{DC}	DC-link voltage
v_g	Grid voltage
V_g	Grid voltage amplitude

$\widetilde{v}_{grid}$	Voltage of the simulated grid entry point in RTDS
V_{LL}	Line-to-line voltage
V_m	Amplitude of the single-phase PCC voltage
v_{PCC}	Voltages measured at the PCC
v_q	q-component measured voltages propagated in the GFL control
V_{ref}	Reference grid voltage for the GSU control loop
v_s	Voltage of the shunt capacitor
$\mathbf{w}(n)$	Model vector Kalman filter
$W\delta_x$	Frequency-dependent uncertainty function
X/R	X over R ratio
X_{ratio}	X over R ratio factor for virtual admittance calculation
$\mathbf{x}$	Vector of states
$\mathbf{x}(n)$	State-vector Kalman filter
$\widehat{\mathbf{x}}(n)$	State estimate Kalman filter
$\mathbf{x}_c$	State-space vector of the control subsystem
$\mathbf{x}_{plant}$	Vector of states of the plant
X_S	Synchronous reactance of a SM
$\mathbf{x}_{sys}$	Vector of states of the interconnected system
ξ	Parameter of the VOC
$\mathbf{y}$	Vector of outputs
$\mathbf{y}_c$	Vector of outputs control subsystem
$\mathbf{y}_{CC}$	Vector of outputs of the *PI current control* subsystem
$\mathbf{y}_{del}$	Vector of outputs of the *Delay* subsystem
$\mathbf{y}_{filter}$	Vector of outputs of the *Filter* subsystem
$\mathbf{y}_g$	Vector of outputs of the *Grid* subsystem
Y_{geq}	Equivalent grid admittance at the converter terminals
$\mathbf{y}_{LCL}$	Vector of outputs of the *LCL filter* subsystem
$\mathbf{Y}_{ol}$	Transfer function of the open loop output admittance
Y_{out}	Equivalent output admittance of the converter
$\mathbf{y}_{\pi}$	Vector of outputs plant subsystem
$\mathbf{y}_{plant}$	Vector of outputs of the plant
$\mathbf{y}_{P2C}$	Vector of outputs of the *PLL on currents* subsystem
$\mathbf{y}_{P2V}$	Vector of outputs of the *PLL on voltages* subsystem
$\mathbf{y}_{sys}$	Vector of outputs of the interconnected system
$\mathbf{y}_{sub}$	Vector including all the outputs of the subsystems
Y_v	Virtual admittance
$\mathbf{y}_{Zc}$	Vector of outputs of the *Additional impedance* Z_c subsystem
Z_{cn}	Impedance between the n-th converter and the grid equivalent model
Z_g	Impedance of the equivalent grid model
Z_{geq}	Equivalent grid impedance at the converter terminals
Z_{Ln}	Line impedance between the n-th converter and the connection bus
$\mathbf{Z}_{oCC}$	Equivalent converter output impedance considering the current control loop
Z_v	Virtual impedance

ζ	Damping ratio of the oscillatory mode
ζ_p	Damping ratio of the approximated P-loop transfer function
ζ_{PLL}	Damping ratio of the linearized PLL closed-loop transfer function
ζ_q	Damping ratio of the approximated Q-loop transfer function
ζ_v	Damping ratio of the approximated $Q-V$ loop transfer function

Abbreviations

AVC	Alternating Voltage Controller
BESS	Battery Energy Storage Systems
CDF	Cumulative Distribution Function
CFCT	Critical Fault Clearing Time
DERs	Distributed Energy Resources
DFT	Discrete Fourier Transform
DPC	Direct Power Control
EDPC	Enhanced Direct Power Control
EG	Expert Group
EKF	Extended Kalman Filter
FFCI	Fast Fault Current Injection
FLL	Frequency-locked-loop
FRT	Fault Ride-Through
GFL	Grid-following
GFM	Grid-forming
GSU	Grid-supporting
GNC	Generalized Nyquist Criterion
HCC	Hysteresis Current Control
HIL	Hardware-in-the-loop
HVDC	High-voltage direct current
IGD	Implementation Guidance Document
ITM	Ideal Transformer Method
LFDD	Load Frequency Demand Disconnection
LF	Loop Filter
LFT	Linear Fractional Transformation
LHP	Left-Half Plane
LPF	Low-pass filter
LTI	Linear Time Invariant
LVRT	Low-Voltage Ride-Through
MIMO	Multiple-input multiple-output
PCC	Point of Common Coupling
PD	Phase Detector
pdf	probability density function

PHIL	Power-Hardware-in-the-loop
PLC	Power Loop Controller
PLL	Phase-locked loop
PSC	Power Synchronization Control
PV	Photovoltaic
PWM	Pulse Width Modulation
QSG	Quadrature-Signal Generator
RDFT	Recursive Discrete Fourier Transform
RES	Renewable energy sources
SCR	Short-Circuit Ratio
SG	Synchronous Generator
SISO	Single-input single-output
SM	Synchronous Machine
SO	System Operator
SOGI	Second-Order Generalized Integrator
SPC	Synchronous Power Control
SRF	Synchronous Reference Frame
SSV	Structured Singular Value
ST	Smart Transformer
STATCOM	Static Synchronous Compensator
UPS	Uninterruptible Power Supply
VCO	Voltage Controlled Oscillator
VOC	Virtual Oscillator Control
VSC	Voltage Source Converter
VSM	Virtual Synchronous Machine
WT	Wind Turbine

1 Introduction

In this section, the background and the motivation behind the work presented in this thesis, are clarified. An introduction is first provided, discussing the necessity for investigating new converter control strategies enabling high-penetration of power electronics- based generation in the power system of the future, as well as the status of the discussions involving System Operators (SOs) and manufacturers currently ongoing at European level. Finally, the outline of the thesis is reported, along with an overview of the publications related to the different sections.

1.1 Motivation for new converter control strategies

The electric power system is currently experiencing a significant transformation. Its well-established configuration characterized by large centralized generating units, transmission systems, and distributed consumption is moving toward a distributed generation paradigm, where renewable energy sources (RES), such as wind or solar power plants, are going to play a significant role. This trend is highlighted in Fig. 1.1 [1], showing the expected highest instantaneous percentage of RES penetration in relation to power demand by 2025, occurring in any hour of the year for each European country, and which can potentially reach a level up to 100% in several cases. Beside introducing a certain degree of randomness [1] to the availability of energy in every moment, these energy sources are generally coupled to the grid by means of power electronics-based converters. However, not only the generation side, but also loads, as well as transmission systems (e. g. High-Voltage-Direct-Current (HVDC)), are currently evolving toward power electronics-based interfaces, introducing new challenges for the secure operation of the future power system. Therefore, SOs worldwide have expressed

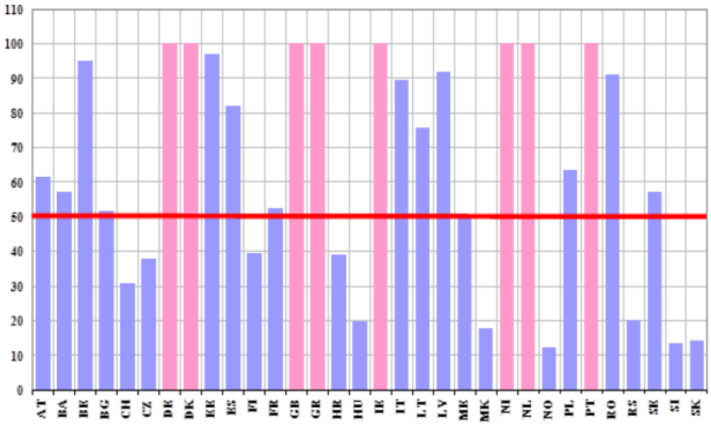

Figure 1.1: Highest hourly penetration levels forecast of RES in Europe by 2025 in relation to demand (from ENTSO-E Ten-Year Network Development Plan 2016) [1], [2].

---

[1] This issue is being tackled by sophisticated renewable forecasting, and many SOs have developed advanced operating systems that can cope even with contingencies like a solar eclipse leading to rapid variation in PV output.

their concerns about the stability of the power system in the expected configuration, and discussions have been triggered in different countries about the necessity for introducing new requirements in their grid codes. In this scenario, the concept of *grid-forming* (GFM) converters has gained particular attention in the last decade, and is currently considered a possible solution for enabling stable operation of a power electronics-dominated power system, ensuring at the same time a safe transition from the current configuration to the expected one.

Compared to state-of-the-art control strategies for grid-connected converters, which are usually characterized in the literature as *grid-following* (GFL) units, GFM converters present a conceptually different behaviour. In fact, while GFL converters mainly behave as controlled current sources, the operating principle of a GFM makes the converter behaving as a voltage source behind impedance. To this extent, recent studies have demonstrated that by increasing penetration of converter-based generation to very high levels while keeping a GFL behaviour might be detrimental for system stability [3]. One of the reasons for that outcome is the reduction of system inertia, which in a classical power system is provided by the rotating masses of large generating units directly coupled to the grid. Nevertheless, this represents only one of the aspects related to the increase of power electronics-based generation, and beside reduction of total system inertia, inadequate supply of fault current infeed, causing a decrease of the grid Short-Circuit-Ratio (SCR), as well as possible instability phenomena caused by the interactions between grid-connected converters operating in close electrical vicinity to each other, need to be taken into account. Preliminary studies have shown that GFM converters have the potential of overcoming these drawbacks [3], and discussions about the details of the electrical characteristics of such converters have moved from the academic sphere to industrial fora, involving SOs, Wind-Turbine (WT), as well Photovoltaic (PV), Battery Energy Storage Systems (BESS), and HVDC converter manufacturers.

1.1.1 Discussions at European level about the development of GFM converters

In the following, an overview on the discussions currently ongoing at European level involving SOs and manufacturers, and concerning the development of grid code requirements for GFM converters, is reported [4]. This summarizes the status of the activities related to the technical group established by the European Network of Transmission System Operator for Electricity (ENTSO-E), the working group convened by the National Grid Electricity System Operator (NGESO) in Great Britain, concluding with an overview of the discussions currently going on at German level.

Discussions at ENTSO-E level

In 2017, ENTSO-E established a technical group on *"High-Penetration of Power Electronic Interfaced Power Sources (included Sources Storages & HVDC)*" (HPoPEIPS), whose members represent the solar, wind, and HVDC industries, as well as power system analysis tool providers, academia, and SOs. The activities of the workgroup have been divided into two separated phases. During the first one, an Implementation Guidance Document (IGD) on Fast Fault Current Injection (FFCI) [5] has been drawn, and preliminary studies highlighting reduction of system strength measured by the indicator of total system inertia have been performed, according to the different expected scenarios for 2030 outlined within the ENTSO-E Ten-Year Network Development Plan [2].

The second phase has been recently concluded, and its outcomes have been summarized in a technical report [1]. In the document, seven main aspects related to system needs are outlined, which are expected to be provided in future by power electronics-based grid-connected converters. These are namely [1]: creating system voltage, contributing to fault level, contributing to system inertia, supporting system survival to allow effective operation of Load Frequency Demand Disconnection (LFDD) for rare system splits, prevent adverse control interactions, and acting as a sink to counter harmonics and unbalance in system voltage. However, it is not expected that each operating unit shall provide all the listed characteristics simultaneously, but it is rather under discussion whether the required capabilities can be shared among operating units spread across the system. To this extent, what proportion of converter interfaced equipment should have the aforementioned capabilities, as well as when and in which point of the system those features need to be available, are still topics of discussion.

Discussions in Great Britain

The British NGESO established in 2017 the GC0100 Workgroup on the implementation of the EU Connection Codes, addressing among others FRT requirements for Great Britain [6]. Upon performing system studies, a number of potential challenges associated with increased penetration of power electronics-based generation over 65 % in the British power system have been identified, including voltage collapse, low fault level, reduced synchronizing torque, and power quality issues [6]. As a consequence, an Expert Group (EG) entitled ”Grid supporting fast fault currents and associated control including Virtual Synchronous Machines (VSM) approaches” has been set up in April 2018, whose members have the same background as those of the workgroup established at ENTSO-E level, namely wind, solar, and HVDC manufacturers, power system tool providers, academia, and SOs [7]. The main goal of the EG was to discuss enhanced converter control strategies that would lead to performances of the converter emulating some characteristics of synchronous machines (SMs), with a particular focus on fast fault current injection and provision of system inertia, and to gather views on the feasibility and cost of such development requirement.

The activities of the EG have been dived into two stages, and namely a first one focusing on the examination of technical solutions and their practical feasibility, including revision of international practice on VSM implementations, and convening on a draft grid code. The second stage, instead, mainly concerned with a cost benefit analysis and the comparison of several possible alternatives for allowing a stable system operation in the future, while identifying the most economical way for achieving the goal. The activities of the EG have been concluded at the end of 2019, and then subsequently the EG was moved to a ”working group” at the beginning of 2020. The draft grid codes elaborated within the EG phase are currently being discussed and refined by the working group, so as to propose a final code modification for converter-based generation, supposed to come into force in the near future (potentially as early as 2021). At the present stage, the most realistic scenario sees the development of GFM requirements, which, however, will not become mandatory for all grid-connected converters, but rather a market-based solution is currently the preferred candidate. Hence, only converters able to fulfill the defined requirements can participate to the established market, and will therefore get remunerated for the provision of the requested features.

Discussions in Germany

Preliminary discussions regarding the need for GFM converter control strategies have started in Germany in early 2015. These have been triggered by the concerns of SOs about the occurrence of a possible system split as the one taking place in central Europe on the 4^{th} of November 2006 [8], and which caused a separation of the European synchronous zone into three areas. It has indeed been recognized that the handling of such scenario would become much more challenging in the future, due to expected increase of the power transfer throughout the areas interested by the aforementioned event. Furthermore, in view of the increasing penetration of power electronics-based generation, a low level of system inertia is expected in the future, as well as potential occurrence of unwanted islanding in areas with high-penetration of power electronics-based generation, where converters are not designed for such operating conditions. For those reasons, new requirements for grid-connected converters should allow avoiding a system breakdown in the case that similar events would take place in the future.

Differently from the GFM concept presented in the ENTSO-E technical report, and from the VSM promoted by NGESO, the discussions currently ongoing at German level are mainly focusing on fast reaction of power plants aiding system frequency regulation, and inclusion of renewable energy sources (RES), such as wind, PV plants, and BESS in the grid restoration process after a black-out, aspects that have been issued within the projects *"Netzregelung 2.0"* [9], and *"Netz:Kraft (Netzwiederaufbau unter Berücksichtigung zukünftiger Kraftwerkstrukturen)"* [10], respectively. Nevertheless, discussions about those developments are still ongoing, and compared to Great Britain, these have been carried out in a less formal context.

1.2 Research proposal

Two main targets constitute the backbone of this thesis, and namely: discussing the concept of GFM converters, as well as their impact on a power electronics-dominated power system, and investigating approaches for assessing small-signal stability of converter control strategies for grid-connected converters. These are further described below:

Target I: GFM converters in bulky power systems

This topic represents formally the motivation behind this work, and consists of analyzing the potentials of GFM converters in stabilizing a system with high-penetration of power electronics-based generation. However, differently from previous literature where GFM converters have been mainly investigated in the context of microgrids, the targeted scenario is represented by a wide interconnected system. Particular emphasis is given to the synchronization principle adopted by the converters, which for a GFL is generally represented by the use of a dedicated synchronization unit, whereas this is often achieved by reproducing the power-synchronization principle of a SM in a GFM converter. Hence, according to the phenomena of interest, an extensive small-signal stability analysis of the interactions between grid-connected converters adopting different working principles is among the main goals of this thesis. Nonetheless, potential issues related to the implementation of a GFM control algorithm on a grid-connected converter are discussed, for which solutions are also proposed, providing an overview of the advantages and challenges related to this technology.

Target II: Methods for stability analysis of grid-connected converters

The second research objective of this work is represented by the investigation of suitable methods for assessing small-signal stability of grid-connected converters adopting different working principles, and operating in a system with high-penetration of converter-based generation. Among the possible techniques commonly adopted in the literature, frequency-domain approaches, such as the impedance-based analysis, have been widely accepted within the power electronics community. On the other hand, time-domain approaches, e. g. eigenvalue analysis and modal analysis, are well established techniques within the power system community. In this thesis, the robust stability analysis by means of structured singular values (SSVs) is proposed as an effective means for assessing stability of grid-connected converters under the investigated system conditions. Although widely used within the control engineering community, this approach is rather seldom utilized in the literature for studying stability of grid-connected converters. The three aforementioned techniques are thoroughly discussed and compared in this thesis, and by giving practical examples of their applications, advantages and limitations of each method are highlighted.

1.3 Structure of the thesis

The structure of the thesis is reported in Fig. 1.2, where the chapters assigned to the main targets described above, along with the publications related to each section, are highlighted.

In Chapter 2, the operating principles of grid-connected converters are discussed. The definitions of converters according to their operation, which have been reported in the microgrid literature, are first introduced. Then the need for modifying those definitions is debated, and a more general classification valid also for applications in bulky power systems is formulated. In this context, the concept of virtual synchronous machines (VSMs) is introduced, highlighting that VSMs represent particular implementations of GFM converters. One of the

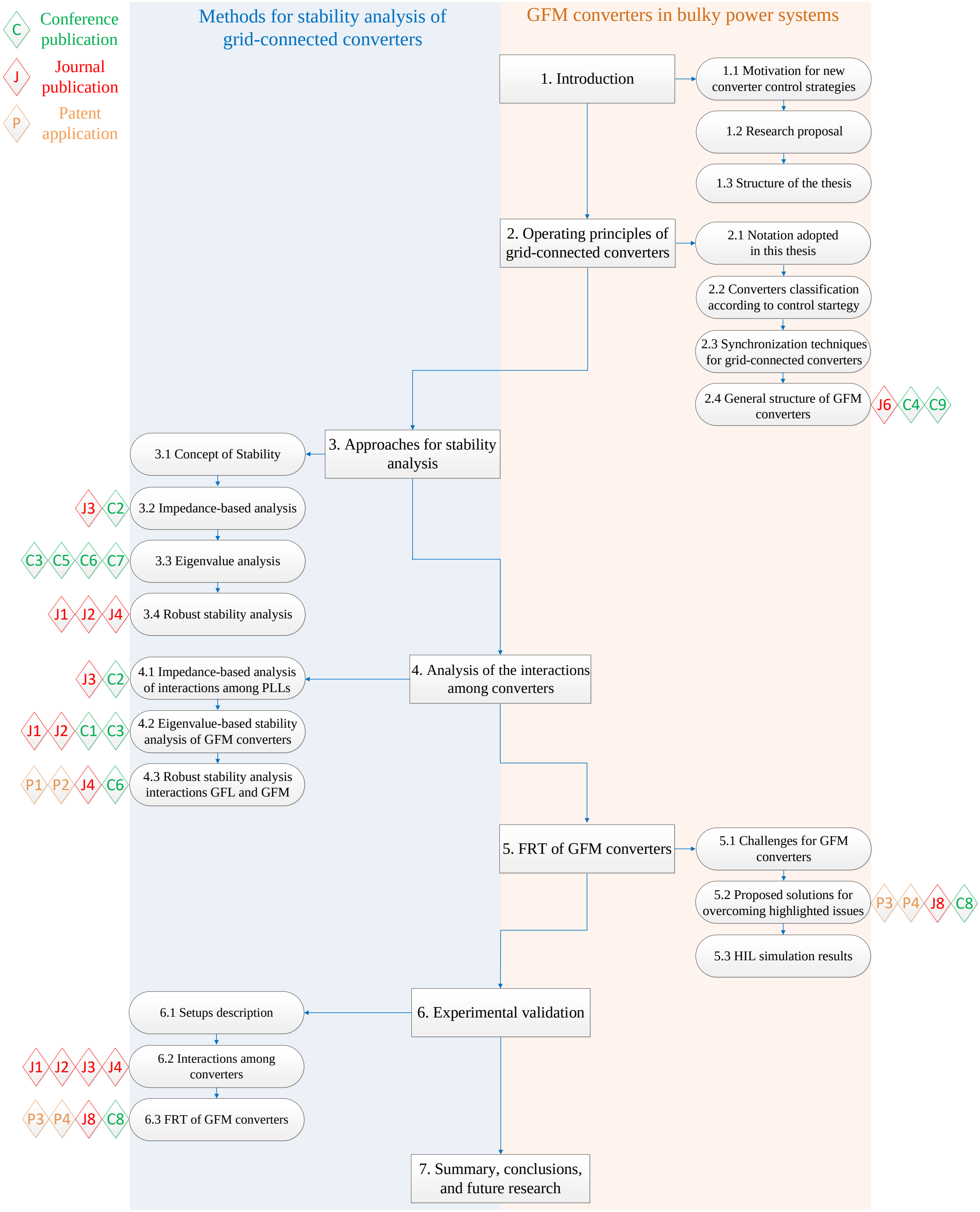

Figure 1.2: Structure of the thesis and related publications.

characteristics identifying VSMs is their synchronization principle, which is thoroughly described and compared to the synchronization principle of a GFL converter, typically achieved by means of phase-locked loops (PLLs) or similar filter structures. Finally, a generalized control structure for GFM converters is reported, along with possible implementations of the main subsystems composing it.

Chapter 3 discusses the approaches for stability analysis investigated in the thesis, pointing out advantages and drawbacks of each method. A brief introduction about linear and nonlinear systems theory introduces this chapter, along with the explanation of the additional challenges characterizing MIMO systems for the assessment of control robustness, thus motivating the robust stability analysis proposed in this work. Practical applications of the methods discussed in Chapter 3, are reported in Chapter 4, for studying the stability of GFL and GFM converters, as well as the interactions between these two types of converters.

Critical aspects related to the implementation of GFM converters are discussed in Chapter 5, where the Fault Ride-Through (FRT) behaviour of this type of converters is addressed. The issues related to this operating condition, and the potential challenges for GFM converters are extensively described, first from the theoretical point of view, then by means of practical examples. Solution for overcoming the highlighted drawbacks are discussed, showing their efficacy by means of simulations results performed by using an hardware-in-the-loop (HIL) test bench. Experimental tests validating the results of the stability analysis performed in Chapter 4, along with the behaviour of the FRT strategy presented in Chapter 5, are presented in Chapter 6, while Section 7 concludes the thesis providing an outlook on possible future research topics.

1.4 Assignment of publications to the chapters of this thesis

The publications related to this thesis are reported in the Appendix (Section 9.2), and are assigned to the different chapters in the following:

- The general structure of a GFM converter proposed in Chapter 2, is based on the works presented in [C4], [C9], and [J6].
- Chapter 3 introduces approaches for stability analysis from the theoretical point of view, similarly as they have been discussed in [C2], [C3], [C5]-[C7], and [J3]. Furthermore, it also introduces the concept of robust stability analysis presented in the works [J1], [J2], and [J4].
- Chapter 4 contains the main results of the journal publications [J1]-[J4], as well as the results of the conference papers [C1], [C2], [C5]-[C7]. Additionally, the patent applications [P1] and [P2] have been motivated by the results presented in the chapter.
- Chapter 5 is mainly based on the publications [C8] and [J8], while the patent applications [P3] and [P4] are relative to the FRT techniques for GFM converters presented in the chapter.
- Chapter 6 shows the experimental results related to the analysis of the interactions between GFL and GFM converters shown in [J1]-[J4], along with the results of the measurement campaign performed in order to test the performances of the FRT strategy presented in [C8] and [J8].

2 Operating principles of grid-connected converters

In this chapter, the operating principles of GFL and GFM converters are described and compared. The converters classification reported in the literature, and elaborated in the context of microgrids is first presented. Then its limitations in serving as a general definition valid also for applications in bulky power systems are pointed out. Hence, the characteristics of GFL and GFM converters independently on the application of interest are discussed, along with the conceptual differences among the two implementations. Among the main characteristics distinguishing the operating principles of grid-connected converters, their synchronization approach is surely one of the most relevant, and the two main strategies adopted by grid-connected converters are discussed and compared. In this context, the concept of virtual synchronous machines (VSMs) is introduced, pointing out that VSMs only represent particular implementations of GFM converters. Finally, a general formulation of the control structure of a GFM converter is proposed, along with a comprehensive overview on the possible implementations of the different subsystems composing it.

2.1 Notation adopted in this thesis

Before discussing the operating principles of grid-connected converters, the notations adopted in the following, are first introduced. Fig. 2.1 shows the general converter structure considered in this thesis, along with the notations used for the signals of interest. The converter is assumed to be a 2-level Voltage Source Converter (VSC) connected the grid by means of an output filter, which, in the most general configuration, is represented by an LCL topology. Nevertheless, according to the applications of interest, this can be reduced to an LC or simply to an L filter. The grid is modeled by means of its Thévenin equivalent representation, hence a voltage source with a series impedance. This can also include the impedance of the converter transformer, which is not explicitly indicated in the figure, but it is commonly adopted in practical applications to provide galvanic isolation. The converter is connected from the DC-side to a primary energy source, whose nature, assuming a constant DC-link voltage, is not relevant for the purposes of the investigation performed in this thesis. Indicating with Point of Common Coupling (PCC) the connection point of the converter to

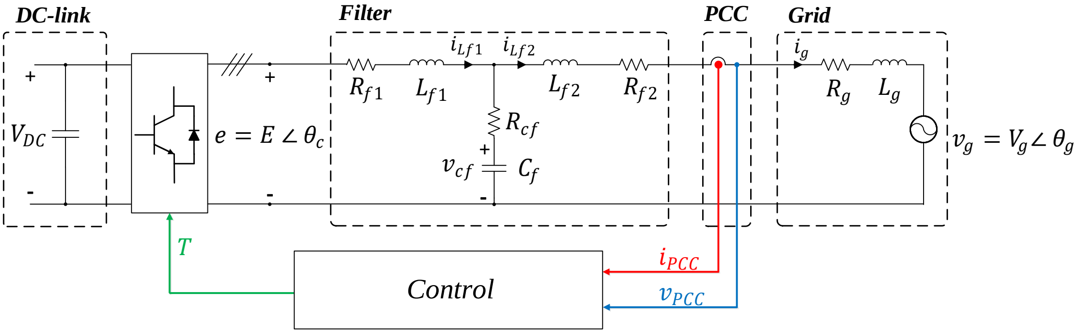

Figure 2.1: Representation adopted for hardware components of a grid-connected converter.

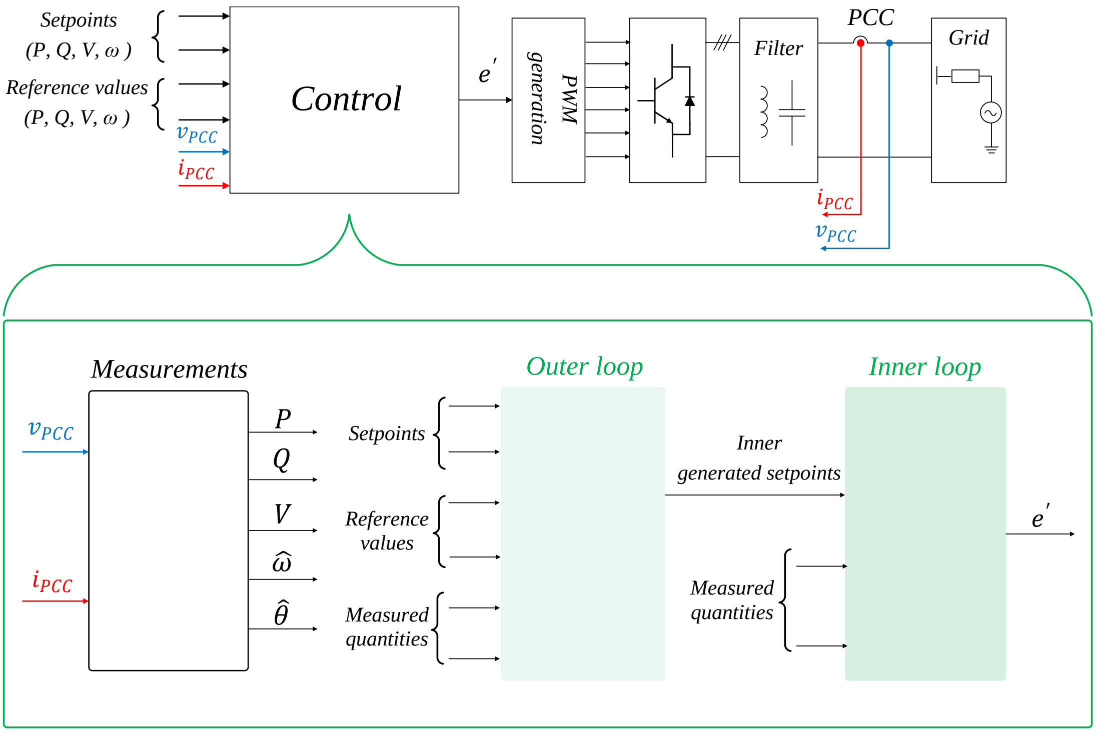

Figure 2.2: Representation adopted for control schemes of grid-connected converters.

the grid, and which is usually represented by the primary side of the isolating transformer, voltages and currents at this point, respectively indicated with the symbols v_{PCC} and i_{PCC} in the figure, are measured and fed back to the control.

Fig. 2.2 shows the notation adopted in this thesis for control schemes of grid-connected converters. Assuming that a Pulse-Width Modulation (PWM) strategy is employed in order to generate the converter pulses, the output of the control is represented by the modulation signal e'. Beside the measured quantities at the PCC, further control inputs are represented by the control *setpoints*, and the *reference values*. To the first category belong input signals identifying a target value for a specific variable to be reached by taking control actions, whereas with reference values are indicated inputs of additional control loops, which can modify the given setpoints according to the operating condition, and which can be generally either activated or deactivated.

In the general control structure shown in Fig. 2.2, three main subsystems are identified. The first one is in charge of the elaboration of the measured quantities, and includes the calculation of the instantaneous active power P and reactive power Q, as well as the amplitude of the voltage at the PCC indicated with V. Additionally, the estimation of the grid frequency $\widehat{\omega}$, as well as of the grid voltage angle $\widehat{\theta}$ are generally performed within this subsystem and forwarded internally in the control. Two cascaded loops are indicated in the figure, which are respectively labeled as *outer loop* and *inner loop*. These include all the control actions taking place in order to generate the modulation signal e' for the PWM according to the externally given target values. Furthermore, according to the considered cascaded structure, the outer loop generates setpoints for the inner control loop by processing the externally given control setpoints and reference values according to the measured instantaneous quantities.

2.2 Converters classification according to their control strategy

At the early stage of development of converter control strategies for grid-connected applications, the main goal was represented by the efficient injection of the energy provided by Distributed Energy Resources (DERs), such as BESSs, WTs, or PV plants, into the power system [11]-[13]. Constituting only a limited percentage of the total produced energy, the research was initially focused on the improvement of the energy conversion process of DERs, minimizing the losses and, in case of PV and wind applications, developing optimized algorithms for achieving Maximum Power Point Tracking (MPPT) [12], [14]. Due to the lack of experience on the real impact of power electronics-based generation in a classical power system, early grid code requirements were mainly focusing on preserving converters hardware integrity, allowing even disconnection from the main utility during faults [15], [16]. Nevertheless, due to the rapid growth of installed units, a revision of the international standards to the new paradigm of the power system became soon necessary, requiring grid-connected converters not only to remain connected during faults, but also to provide ancillary services such as voltage and frequency support by adapting active and reactive power injection [17], [18].

In this scenario, the concept of *microgrids* was introduced at the beginning of the *2000s* [19]. Microgrids were initially thought to represent *controlled cells of a power system* composed by a group of DERs and loads, operating together as single controlled entity, and which can operate both in grid-connected or in isolated/islanded mode [20]. The underlying principle behind microgrids is the establishment of a link in the evolution of a vertically integrated bulk power systems to smart decentralized networks, so as to facilitate the integration of DERs [21]. Hence, in such a system, the proper coordination between operating units represents surely one of the most crucial aspects. As a consequence, a noticeable amount of research on this field has been carried out during the last two decades, among others on specific converter control strategies suitable for these particular applications. In this scenario, the concept of GFM converters has been introduced for the first time, so as to distinguish them from the converters typically adopted in grid-connected applications, and which have been instead classified as GFL units [22]. The term GFM was originally introduced for indicating an operating unit controlled to behave as an ideal voltage source, which could reproduce a reference voltage for the microgrid in case of islanded operation, and eventually compensate for the gap between generation and consumption under such operating conditions. Recently, the concept of GFM converter has been proposed for applications in wider and interconnected transmission networks, requiring therefore a revision of the original definition elaborated in the microgrid context.

The converters classification elaborated for microgrids, and reported in [22], has been widely accepted within the power electronics community for defining the behaviour of converters according to their operation. In the following, these definitions are introduced. Then their limitations in representing a general formulation also valid for applications in bulky power systems are pointed out. Finally, the proposed definitions are reviewed and the characteristics

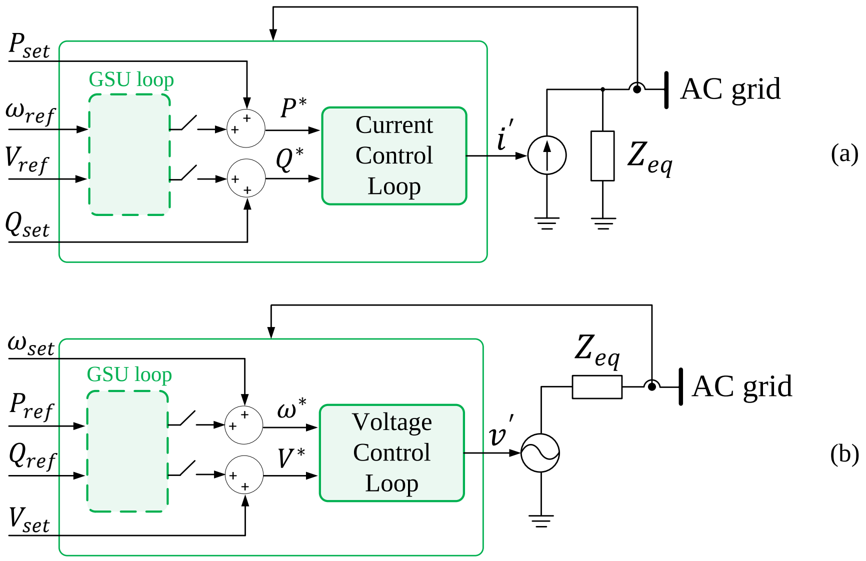

Figure 2.3: Simplified converter representation according to [22]: (a) grid-following (GFL) with possibility of grid-supporting (GSU) capabilities; (b) grid-forming (GFM) with possibility of GSU capabilities.

of GFL and GFM converters complying with the most recent definitions currently discussed within different committees worldwide [1], [3], [7], [23], [24], are outlined.

2.2.1 Classification for microgrids

In the converter classification presented in [22], three main categories of converters are identified. Beside the two aforementioned classes indicated as GFL and GFM, a third type of operating unit labeled as *grid-supporting* (GSU) has been introduced. These definitions are reported below.

Grid-following (or grid-feeding) power converter

The simplified representation of a GFL converter according to [22], is reported in Fig. 2.3 (a), and consists of a controlled current source with a high shunt parallel impedance. Assuming first that the dashed loop, indicated in the figure as GSU loop, is not activated, the current injected by the converter into the grid is controlled by the inner loop(s), so as to regulate active and reactive power to the given setpoints, indicated as P_{set} and Q_{set}, respectively. In order to work properly, a GFL converter needs to be perfectly synchronized with the grid, hence the adjective *following*. To this extent, these type of converters usually adopt a dedicated unit for detecting angle and frequency of the voltage at PCC.

A practical example of the typical control structure of a GFL converter is reported in Fig. 2.4 [25]. Assuming a control in the rotating *dq* reference frame [26], two cascaded PI-based control loops can be identified in the figure. A dedicated unit in charge of the estimation of the grid voltage angle θ, required for transforming quantities from the *abc* to the *dq* frame, and vice-versa, is introduced. The outer loop is in charge of the power regulation, and

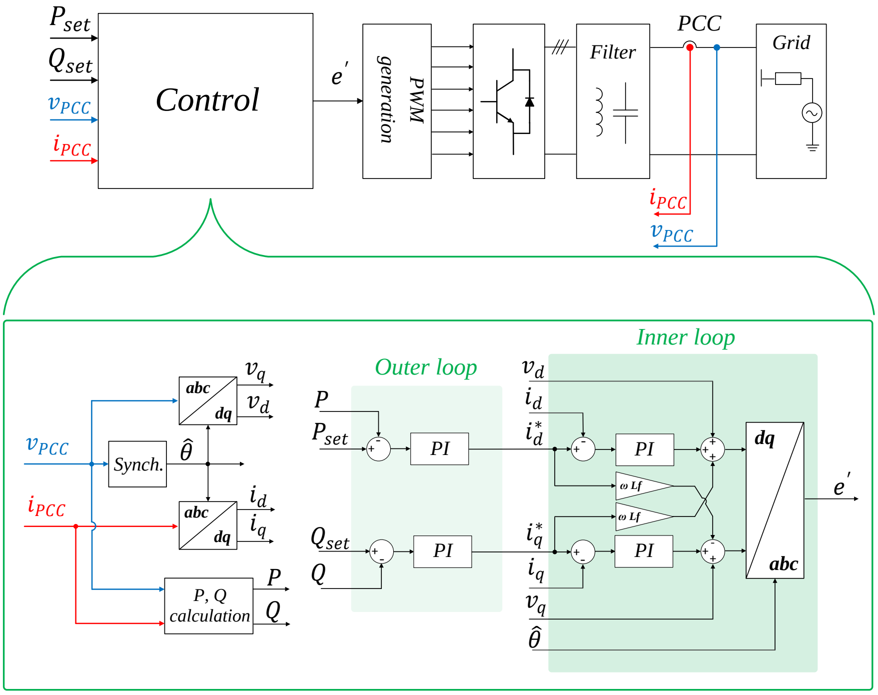

Figure 2.4: Example control structure of a GFL converter [22].

calculates the setpoints currents i_d^* and i_q^*, respectively from the comparison between active and reactive power setpoints P_{set} and Q_{set} to the corresponding measured quantities P and Q. The generated current setpoints are then forwarded to the inner current control loop, also assumed here to be implemented by means of a PI-based current controllers [25].

It is worth to notice that, beside the control in dq-frame considered here, the control in the rotating $\alpha\beta$-frame is also widely adopted in the literature [25]. In that case, proportional resonant (PR) controllers can be employed [27], hence without requiring an estimation of the grid voltage angle θ for transforming quantities between the two reference frames. Nevertheless, the grid frequency needs to be estimated, for which a dedicated unit is, however, necessary.

Grid-forming power converter (UPS-type)

The GFM converter defined in [22], represents an operating unit controlled so as to reproduce the behaviour of an ideal voltage source with given amplitude and frequency. Similar to the case of a GFL examined above, the simplified representation of a GFM converter according to the definition given in [22], is shown in Fig. 2.3 (b), where the GSU loop is not activated. It consists of a controllable voltage source with a low series impedance and, due to this characteristic, an extremely precise synchronization system in order to work in parallel with other GFM units of the same type is necessary [28], since small angle deviations might cause a significant power exchange between them. In a microgrid, such operating units are necessary in order to provide a reference voltage for the other GFL converters operating nearby. A practical example of a GFM converter complying with this definition is represented by an Uninterruptible Power Supply (UPS) system, commonly adopted in order

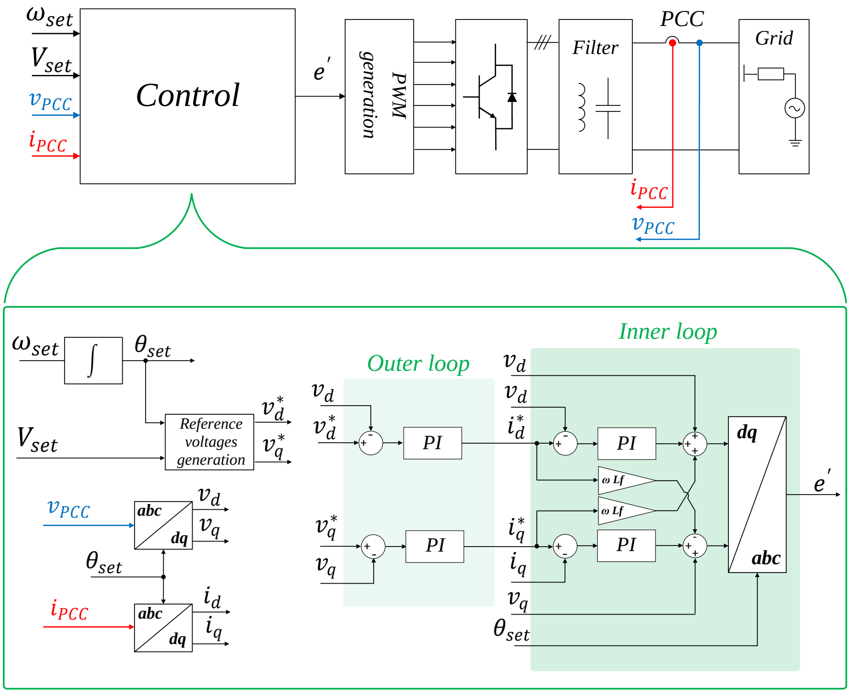

Figure 2.5: Example control structure of a GFM converter (UPS-type) [22].

to ensure continuity of supply for a limited amount of loads in case of disconnection from the grid [28].

The typical control structure of a GFM converter according to the definition provided in [22], is reported in Fig. 2.5. Differently from the example control structure of a GFL converter shown in Fig. 2.4, a synchronization unit is not displayed in this case, due to the fact that amplitude and frequency of the grid voltages do not need to be estimated, but these are rather given as reference signals. Hence, assuming again a control in the rotating reference frame, the voltage setpoints v_d^* and v_q^* are calculated by means of the reference angle θ_{set} internally generated by the control. As for GFL converters, a cascaded structure is usually deployed, which has the advantage of allowing a direct control of the converter currents for hardware protection purposes. The generated voltage setpoints are then processed through an outer voltage loop implemented by means of two PI controllers, calculating the setpoint currents i_d^* and i_q^* for the inner control loop, the latter supposed to be equal to the one adopted in the GFL converter structure shown in Fig. 2.4.

Grid-following-grid-supporting power converter

A GSU converter according to [22], is represented by an operating unit intrinsically behaving either as a GFL or as a GFM converter, but which is additionally equipped with external control loops modifying the converter power setpoints, so as to provide *support* to grid voltage and frequency regulation. The equivalent schemes of the two types of GSU converters indicated in [22], and namely GFL-GSU and GFM-GSU, are reported in Fig. 2.3 (a) and (b), respectively. Compared to the representations of GFL and GFM converters discussed above, the additional external control loops, indicated in the figure as GSU loops, are activated,

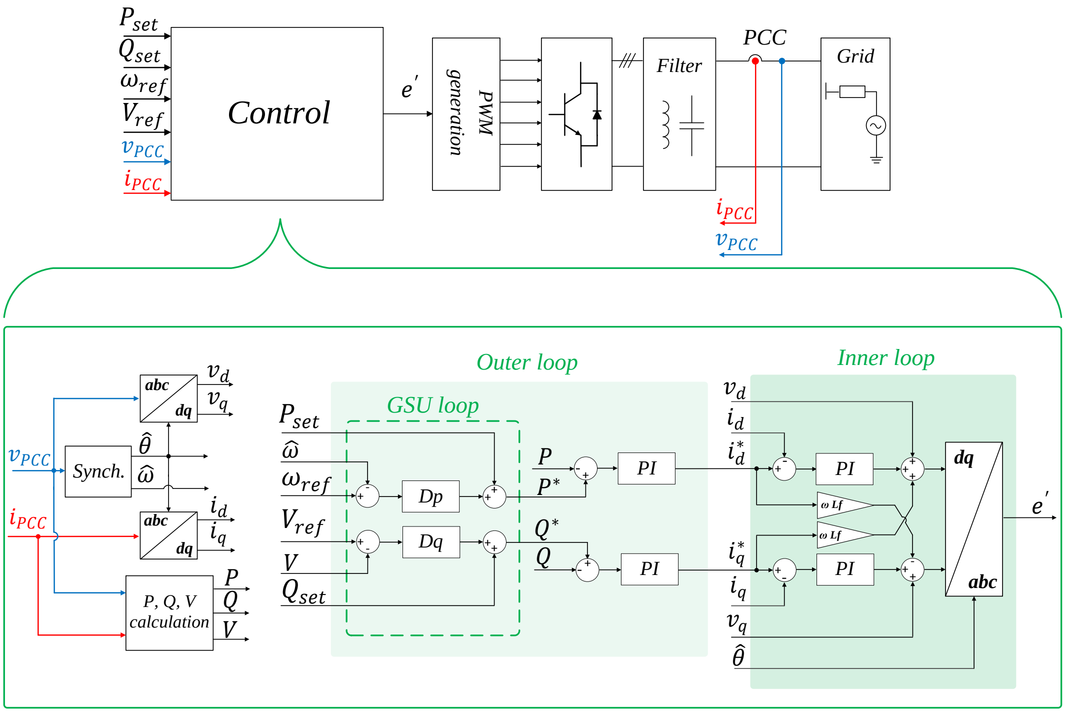

Figure 2.6: Example control structure of a GFL-GSU converter [22].

modifying active and reactive power setpoints according to the given reference values and the actual operating conditions.

A practical example of a GFL-GSU control structure is reported in Fig. 2.6, where the aforementioned external loops are implemented by means of droop controllers. These adjust the original setpoints P_{set} and Q_{set}, and generate the modified active and reactive power setpoints P^* and Q^*, according to the following equations [29], [30]:

$$\begin{cases} P^* = P_{set} + D_p\left(\omega_{ref} - \widehat{\omega}\right) \\ Q^* = Q_{set} + D_q\left(V_{ref} - V\right) \end{cases} \tag{2.1}$$

where D_p and D_q represent active and reactive power droop coefficients, respectively, and the reference inputs ω_{ref} and V_{ref} usually reflect the nominal values of the respective quantities. This control action relating active power to the measured grid frequency and reactive power to voltage amplitude, is similar to the droop control typically implemented in real synchronous generators (SGs) [31]. Moreover, droop controllers are also widely adopted in microgrid applications, since they represent an efficient way for achieving power sharing among operating units without the need for a dedicated communication system [28], [32]. It is, however, worth to notice that the relations indicated in eq. (2.1), are only valid for the case of mainly inductive lines, hence for applications in medium/high-voltage systems, whereas in case of mainly resistive lines (low-voltage applications), the relations between active power and reactive power to frequency and voltages need to be inverted [33].

2.2.2 Need for more general definitions

Even though the converters classification proposed in [22], is well-established within the power electronics community for what concern microgrid applications [21], it requires a revision in order to become generally applicable also for operation in bulky power systems. In this regard, following considerations can be done:

- Converters providing ancillary services as frequency/voltage support by adapting injected active and reactive power are labeled as GSU, and are considered a separated category of converters. Nevertheless, almost the majority of the actual grid codes worldwide require provision of ancillary services, especially for interconnection to medium/high-voltage networks, resulting the original concept of a purely GFL converter according to [22] rather obsolete.
- The definition of a GFM converter is close to the one of a slack-bus, hence resulting not applicable for a converter operating in a wider interconnected network. In fact, a converter behaving as an ideal voltage source with a very low series impedance might be subjected to severe transients (e. g. during grid faults), which may jeopardize the integrity of its hardware components. Furthermore, fluctuations of magnitude and phase of the grid voltage might cause significant excursions of the exchanged active and reactive power between the converter and the grid, which is not always tolerable for a grid-connected converter with limited capacity. Beside the aforementioned example of UPS systems, another example of such GFM units complying with the definition reported in [22], is represented by the Smart Transformer (ST) concept [34], [35]. The ST is a solid-state transformer with embedded control, which do not simply replace a classical transformer, but it can also adapt the amplitude and frequency of the voltage at the low-voltage side of the grid where it is installed, so as to provide ancillary services, hence complying with the concept of a GFM-GSU converter of [22].

At present time, the definitions of GFL and GFM converters are under discussion in several committees worldwide [1], [3], [7], [23], [24]. Instead of formulating binding definitions, in the following, the characteristics outlining the behaviours of GFL and GFM converters for any possible application are listed.

GFL converter

A GFL unit is based on a power converter designed to inject a defined amount of active and reactive power into the grid according to its actual operating condition, presenting the following characteristics:

- Active and reactive power injected by the converter into the grid are regulated controlling active and reactive currents.
- The current setpoints are calculated with respect to the phasor of the fundamental frequency grid voltage, so that the injected currents are controlled in order to have a specific phase displacement with respect to the grid voltage at the PCC. Therefore, a

dedicated synchronization unit is necessary so as to estimate magnitude and phase of the grid voltage at any time.

- The converter might entail additional outer loops modifying active and reactive current setpoints, in order to provide regulation of grid frequency and voltage at the PCC.

GFM converter

A GFM unit is based on a power converter having the following characteristics:

- The converter is explicitly controlled so as to behave as a voltage source behind impedance within the hardware limitations of the device, and within a specified frequency range.
- According to its actual operating conditions, active and reactive power injection are achieved by regulating magnitude and phase of the inner voltage source.
- If the physical limitations of the converter are violated (maximum voltages or currents, energy balance), the converter is temporarily allowed to exhibit a different behaviour so as to prevent itself from hardware damages. This can be eventually achieved by switching to another control strategy during the critical operating condition (e. g. to GFL operating mode), or by modifying the equivalent output impedance.
- Depending on the characteristics of the network, it can either work as a slack-bus for islanded operation, or as a power source, that by means of additional outer loops adapts the injected instantaneous active and reactive power, in order to provide voltage and frequency support.

2.2.3 Conceptual differences between GFL and GFM converters

According to the list of characteristics reported above, the conceptual differences in the behaviour of GFL and GFM converters are outlined in the following. Fig. 2.7 schematically explains the working principles of the two converter types. It is highlighted that a GFL unit regulates the injected power by explicitly controlling active and reactive currents. Therefore, an exact knowledge of the grid voltage characteristics is required, for which a dedicated synchronization unit is usually adopted, so as to properly regulate the phase shift between the injected currents and the grid voltage at the PCC. On the contrary, a GFM converter behaving as a voltage source behind impedance, regulates the injected power by controlling amplitude and phase of its inner voltage source. To this extent, the exact knowledge of the grid voltage angle is not necessarily required, or instead only needed under particular conditions (pre-synchronization to the grid, or during faults).

The potentials of GFM converters in stabilizing a power electronics-dominated power system have been recently investigated in the literature [3]. The main benefits deriving from their implementation can be summarized in the following three aspects:

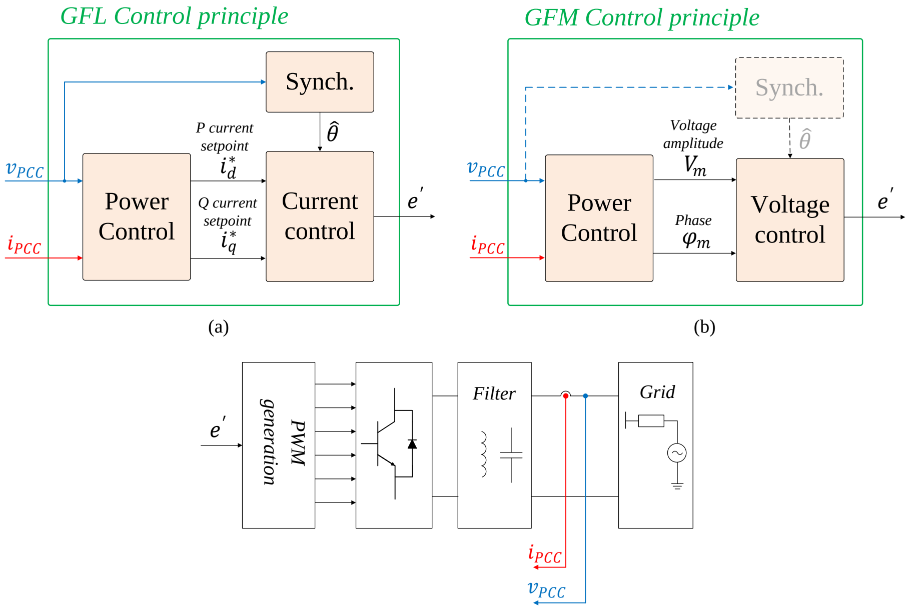

Figure 2.7: Schematic explanation of converters operating principle: (a) GFL, (b) GFM.

1) Damping of system oscillations.
2) Contribution to small-signal stability.
3) Instantaneous reaction to a grid fault.

Regarding the first point, the studies reported in [36] and [37], show that GFM converters operating with a droop control can react almost instantaneously to contingency cases, due to the fact that there is no significant delay between the variation of the converter output power according to a perturbation of the grid frequency. It is indeed shown that, increasing the percentage of converter-based generation in a low-inertia power system, contribution to frequency damping is achieved when the converters reproduce a GFM behaviour, resulting instead in the opposite trend by increasing the amount of GFL units. Nevertheless, it is worth to remark that this frequency damping contribution is not resulting from any inertia emulation characteristic, which is in fact typical of some GFM implementations; yet this is instead due to the fact that, contrary to a GFL converter, a GFM does not require to estimate the grid frequency variation in order to react with a modification of its power setpoint.

For what concern the second point, and namely the stabilizing effects of GFM converters and their contribution to the small-signal stability of a power system with high-penetration of converter-based generation, this represents one of the main contributions of this thesis, and will be thoroughly addressed in Chapter 4. As highlighted in Fig. 2.7 (b), this feature is mainly a consequence of the fact that, contrary to a GFL converter, a GFM unit does not necessarily require a dedicated unit for synchronization purposes during normal operation. In fact, recent studies have demonstrated that the synchronization unit of a grid-connected converter has a significant impact on its stability, especially when operating under weak grid conditions, and in proximity of other converters of the same type.

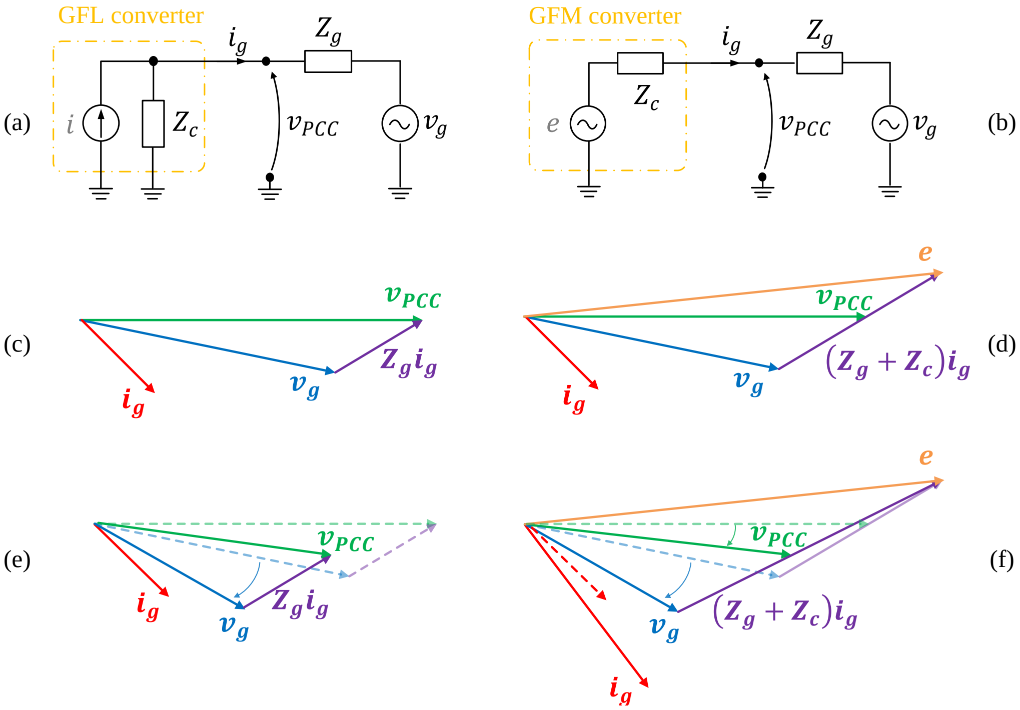

Figure 2.8: Conceptual differences between GFL and GFM converters. Simplified representations: (a) GFL, (b) GFM. Reaction to a grid event - phasor diagram during steady-state operation: (c) GFL, (d) GFM. Phasor diagram according to a perturbation of the grid voltage: (e) GFL, (f) GFM.

The capability of an almost instantaneous reaction to a grid event represents instead one of the leading motivations behind the establishment of the EG convened by the British SO National Grid on VSMs in 2018, and focused on the investigation of new converter control strategies for allowing higher penetration of converter-based generation in the British power system [7]. This aspect can be intuitively understood by means of the example reported in the following. Fig. 2.8 (a) and (b) respectively show the simplified representations of GFL and GFM converters complying with existing literature [22], and with the general definitions reported in Section 2.2.2. Although these two figures might erroneously resemble the definitions of a Norton or a Thévenin equivalent, which are instead theoretically interchangeable, they instead emphasize the fact that GFL converters achieve power injection by controlling the injected currents, while a GFM converter regulates the power by controlling its inner voltage vector. Additionally, the GFM converter under no-load conditions provides a reference voltage for the loads and the other units operating nearby, while the GFL converter necessarily requires a reference angle for proper operation. Even though by adopting different control principles, under steady-state operating conditions both converters regulate the injected active and reactive power according to the given setpoints, and the corresponding vector diagrams are respectively shown in Fig. 2.8 (c) and (d). Nevertheless, at the occurrence of a grid fault, the reactions of the two converters are significantly different.

Because of the inherent current source behaviour of a GFL converter, this reacts to the grid event trying to maintain the current phasor $\mathbf{i}_g$ constant in terms of magnitude and phase, as schematically indicated in the phasor diagram of Fig. 2.8 (e). Indeed, the estimation of the new phase angle of the grid voltage phasor $\mathbf{v}_g$ is first needed for the calculation of the new current setpoints, along with the magnitude of the voltage depression in order to calculate the required amount of reactive power to be injected according to the grid codes. On the contrary, due to the inherent behaviour of a voltage source behind impedance, a GFM converter reacts to the same event by maintaining the inner voltage phasor $\mathbf{e}$ constant in terms of magnitude and phase, hence resulting in an almost instantaneous variation of the current $\mathbf{i}_g$ flowing from the converter into the grid, as schematically shown in Fig. 2.8 (f). Furthermore, properly designing the equivalent impedance of the converter, this current can result in a reactive power injection, therefore contributing to grid voltage support. Even though this prompt converter reaction is beneficial for system stability, and hence highly attractive for SOs, proper countermeasures need to be adopted in order to prevent the converter from hardware damages, an aspect that will be further investigated in Chapter 5.

2.2.4 VSMs and GFM converters

At the early stage of discussions about the need for new converter control strategies in power electronics-dominated power systems, one of the main concerns was related to the reduction of system inertia caused by the substitution of conventional power plants by means of DERs. In this scenario, the concept of VSMs has been introduced for the first time by Hesse and Beck in 2007 [38], the so-called *VISMA* concept. The topic has immediately gained high resonance in the research community, and projects have been funded so as to deeply investigate this concept, e. g. the *VSYNC* Project [39] concluded in 2010. As a consequence, plenty of possible implementations of VSMs have been proposed in the literature during the last decade [30].

The VSM control initially proposed in [38], was based on a full-order electrical and mechanical model of a real SM, including an unnecessary level of details. Nevertheless, according to the original intent of emulating the inertial behaviour of a SM, soon the idea of adopting highly detailed machine models has been abandoned, and reduced-order models mainly focusing on reproducing the swing equation of a SM have gained the upper hand. This is for example the case of the well-known control structure labeled in the literature as *synchronverter* and proposed by Zhong *et al.* in 2011 [40], [41], or the Synchronous Power Control (SPC) introduced by Rodriguez *et al.* [42]-[44].

While a deeper insight on the aforementioned VSM control structures is provided in the following of this chapter, it is here instead worth to notice that, as for the case of GFM converters, a well-established definition for the term VSM is difficult to find in the literature, and the two words *VSM* and *GFM* have been often used interchangeably, creating a certain confusion behind the real meanings of the two notions. In this regard, a contribution has been provided by the British SO NGESO, which, within a collaboration with the University of Strathclyde, has begun in 2015 an investigation of the effects caused by high-penetration of converter-based generation on the stability of the British power system. One of the outcomes of this activity, was identifying a list of requirements that a grid-connected converter should fulfill in order to be classified a VSM [45], [46]. Beside the characteristics already listed in

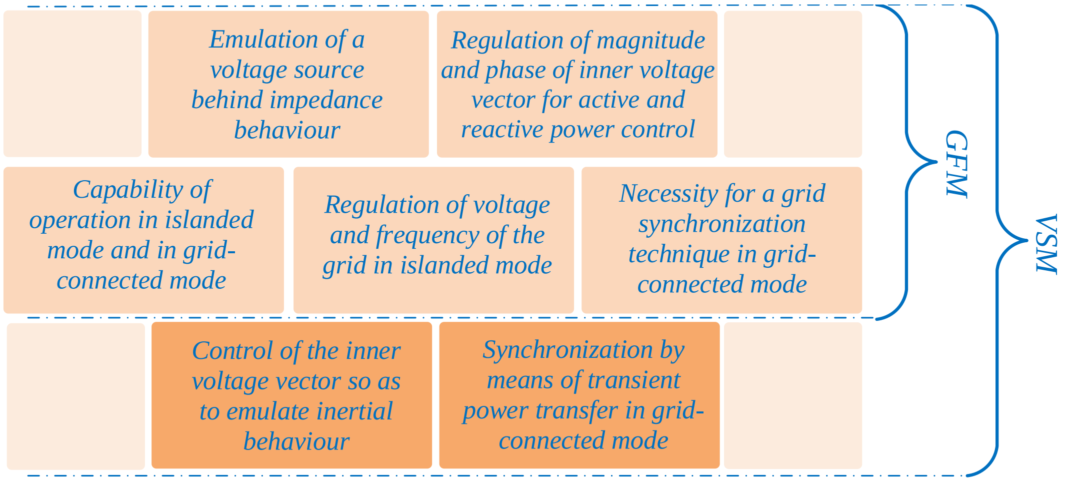

Figure 2.9: Characteristics of VSMs compared to basic features of GFM converters.

the previous section for defining the behaviour of a GFM converter, and which can be also found in the list of requirement initially proposed by NGESO, the following two aspects are additionally mentioned:

1) *The converter has to behave as a voltage source behind a reactance within a specified frequency range. Amplitude and phase angle of the voltage source shall be modified in order to limit the converter currents and reproduce an equivalent inertia constant.*
2) *The converter does not need a dedicated synchronization unit in order to achieve the synchronization to the grid, but rather this is achieved by means of power transfer.*

Thus, it can be concluded that *a VSM only represents a particular implementation of a GFM converter*, and the main characteristics distinguishing a VSM from a GFM converter are mainly concerning the following two aspects: the *inertial behaviour* and the *power-synchronization mechanism*. This is further emphasized in the scheme shown in Fig. 2.9, which summarizes the considerations reported above.

Regarding the first point, it has been previously mentioned that the original idea behind the introduction of the VSM concept was mainly related to the emulation of the inertial behaviour of SMs, which, due to the kinetic energy stored in their large rotating masses, can counteract system frequency fluctuations, thus contributing to power system stability. Attempts to reproduce this inertial behaviour by means of power electronics-based generating units have been investigated in several work, e. g. in [47]-[49], to name but a few. Nevertheless, the type of inertial response reproduced by such controllers relies on a measurement of the actual grid frequency and, therefore, it is not intrinsically embedded in the converter behaviour. For this reason, this kind of inertial contribution has been defined as *synthetic inertia* [50], [51], and the studies performed in [51], have shown that such controllers might become even detrimental for system stability. Hence, an inertial response contributing to system stability can be only provided by a converter reproducing a similar behaviour as the one of a real SM, where the inertial contribution is intrinsically embedded in its working principle, thus not relying on a measurement-based grid frequency estimation.

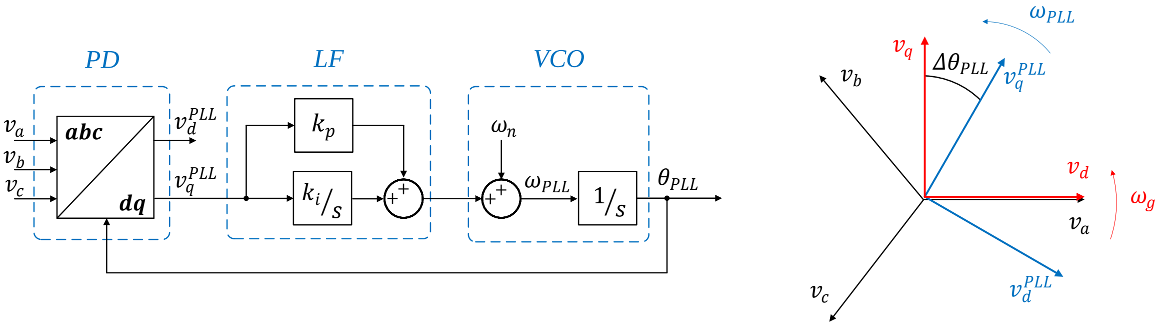

(a) (b)

Figure 2.10: SRF-PLL: (a) scheme; (b) vector diagram explaining the working principle.

The second aspect is related to the synchronization principle adopted by the converter. In fact, contrary to a GFL converter, which requires a dedicated synchronization unit in order to detect the angle of the grid voltage and inject the currents with a proper phase displacement, SMs in a power system can maintain synchronism with each other without the need for any communication means. This phenomena, common to all SMs, and known as *power-synchronization mechanism*, is achieved by means of transient power transfer, and is recognized as the underlying principle holding a power system [52].

2.3 Synchronization techniques for grid-connected converters

Grid synchronization has been considered a crucial research field since the early stages of development of power electronics-based grid-connected converters. To this extent, a dedicated unit has been usually foreseen, and various synchronization techniques have been proposed in the literature. These can be classified into two main categories: *frequency-domain* and *time-domain* approaches [25]. Frequency-domain approaches are based on some discrete implementations of the Fourier analysis, such as Discrete Fourier Transform (DFT) and recursive DFT (RDFT) [53], [54], whereas time-domain approaches are mainly based on adaptive feedback loops, enabling an internal oscillator to track the component of interest of an external signal. The commonly adopted solution is the use of a Phase-Locked Loop (PLL), originally developed for radio-communication purposes [55], and nowadays widely used in grid-connected converters both for single-phase, as well as for three-phase applications. The operating principle of a PLL is briefly discussed in the following.

2.3.1 The SRF-PLL

Among the wide amount of PLL structures presented in the literature, the Synchronous Reference Frame-PLL (SRF-PLL) is probably the most common one. It works in the *dq* rotating frame, and its structure is reported in Fig. 2.10 (a). It is composed of three stages, whose functions are described in the following [25]:

- *Phase Detector* (PD): generates an output signal proportional to the phase difference between the original signal and the estimated one. In a SRF-PLL, this subsystem is implemented by transforming the measured voltages from the *abc* to the *dq*-frame by applying the Park's transformations [56]. While this is straightforward in a three-phase system, a quadrature signal needs to be generated for single-phase applications, so as to transform quantities from the the stationary $\alpha\beta$-frame to the rotating *dq*-frame [25].
- *Loop Filter* (LF): generally represented in a PLL by a low-pass filter for the attenuation of the high-frequency components of the PD, this is implemented in a SRF-PLL by means of a PI controller.
- *Voltage Controlled Oscillator* (VCO): generates an AC output signal corresponding to the estimated grid angle θ_{PLL}, by integrating the estimated grid frequency ω_{PLL}.

The working principle of a SRF-PLL consists of adjusting the estimated angle θ_{PLL} so that the *q*-component of the transformed voltages v_q^{PLL} is nullified. This concept can be understood by looking at the vector diagram shown in Fig. 2.10 (b). The blue arrows in the figure, identify the *dq*-frame corresponding to the angle estimated by the PLL, while the red arrows correspond to the rotating *dq*-frame obtained from the real system grid voltage angle. Indeed, v_q^{PLL} can be considered as a measure of the estimation error, since when the PLL *dq*-frame is perfectly aligned with the real system *dq*-frame, only the *d*-component of the transformed voltages $v_d = v_d^{PLL}$ results different from zero. Hence, the signal v_q^{PLL} is processed through a PI controller, which adjusts the estimated frequency ω_{PLL} until the two reference frames result perfectly aligned with each other.

The tuning of the SRF-PLL has been comprehensively addressed in the literature, both for single phase [57], [58], as well as for three-phase applications [25], [59]-[61]. The SRF-PLL shows excellent tracking capabilities under ideal conditions; yet its performances are strongly deteriorated by unbalances and harmonics disturbances in the grid voltage [59], [60]. The easiest solution for overcoming this inconvenient is to reduce the bandwidth of the PLL [25], [58]. Nevertheless, enhanced control structures have been proposed in order to improve the disturbance rejection capabilities of the PLL under critical conditions, with limited consequences on its dynamic performances [62]-[65].

Linearization of the PLL equations

Linearized models of the SRF-PLL are usually adopted for tuning purposes, as well as for stability assessment. In Fig. 2.11 (a), the linearized PLL model of the structure shown in Fig. 2.10 (a), and commonly adopted for tuning purposes, is shown [25], where k_p and k_i respectively indicate proportional and integral gain of the PI controller. Assuming a normalized input voltage, the open-loop transfer function $F_{OL}(s)$, along with the closed-loop transfer function $F_{CL}(s)$, are given by:

$$F_{OL}(s) = \frac{k_p\, s + k_i}{s^2} \qquad ; \qquad F_{CL}(s) = \frac{k_p\, s + k_i}{s^2 + k_p\, s + k_i} \tag{2.2}$$

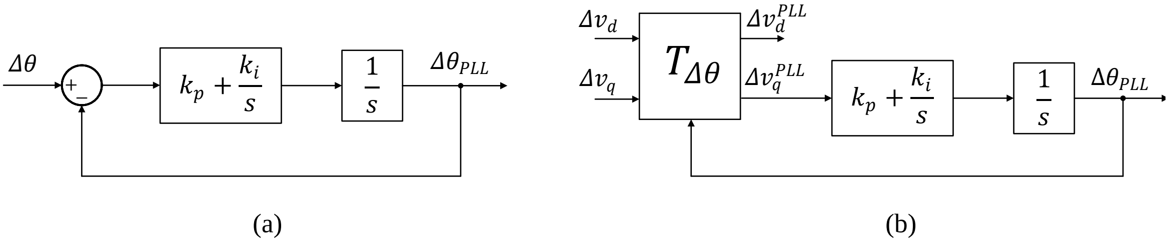

Figure 2.11: Linearized model of the SRF-PLL: (a) model adopted for tuning purposes [25]; (b) model for stability analysis [66].

Expressing the integral gain $k_i = {}^{k_p}/_{T_i}$, the closed-loop transfer function can be written as:

$$F_{CL}(s) = \frac{2\zeta_{PLL}\omega_{nt}\ s + \omega_{nt}^2}{s^2 + 2\zeta_{PLL}\omega_{nt}\ s + \omega_{nt}^2} \tag{2.3}$$

where $\zeta_{PLL} = \sqrt{k_p T_i}/2$ is the damping factor, while $\omega_{nt} = \sqrt{k_p/T_i}$ indicates the natural frequency. Eq. (2.3) represents a standard second-order transfer function, well-known in control theory [67]. Thus, given the desired settling-time t_s, the PLL parameters can be tuned according to the following equations [25]:

$$k_p = 2\zeta_{PLL}\omega_{nt} = \frac{9.2}{t_s} \quad ; \quad T_i = \frac{2\zeta_{PLL}}{\omega_{nt}} = \frac{t_s\zeta_{PLL}}{2.3} \tag{2.4}$$

Regarding the choice of the damping factor ζ_{PLL}, it is usually recommended to set it equal to $1/\sqrt{2}$ [25]. Nevertheless, the studies performed in [61], show that an optimal trade-off of the PLL transient response considering both angle and frequency dynamics can be instead achieved by choosing $\zeta_{PLL} = 1$.

The linearization of the PLL equations in order to study its effects on the stability of a grid-connected converter, has been thoroughly addressed in the literature in recent years [66], [68], [69]. Considering for simplicity a formulation in dq-coordinates, the linearized model of a SRF-PLL suitable for stability analysis is shown in Fig. 2.11 (b) [66]. During steady-state operation, the PLL perfectly tracks the grid voltage angle, and the two coordinate systems shown in Fig. 2.10 (b), namely the red one representing the system dq-frame, and the blue one indicating the PLL dq-frame, are perfectly synchronized with each other. Nevertheless, assuming that a perturbation of the grid voltage occurs, a phase shift $\Delta\theta_{PLL}$ between the two reference frames inevitably occurs and, depending on its control parameters, the PLL requires a certain amount of time before locking the new grid voltage angle. In order to study the effects of this mechanism on the stability of a grid-connected converter, the transfer function relating a perturbation of the grid voltage to the angle detected by the PLL is derived in the following.

According to reference frame theory [56], the transformation matrix $\mathbf{T}_{\Delta\theta}$ relates the quantities in the two dq-frames according to the following expression:

$$\begin{bmatrix} v_d^{PLL} \\ v_q^{PLL} \end{bmatrix} = \mathbf{T}_{\Delta\theta} \begin{bmatrix} v_d \\ v_q \end{bmatrix} = \begin{bmatrix} \cos(\Delta\theta_{PLL}) & \sin(\Delta\theta_{PLL}) \\ -\sin(\Delta\theta_{PLL}) & \cos(\Delta\theta_{PLL}) \end{bmatrix} \begin{bmatrix} v_d \\ v_q \end{bmatrix} \tag{2.5}$$

Therefore, during steady-state operation ($\Delta\theta_{PLL} = 0$), $v_d = v_d^{PLL}$, and $v_q = v_q^{PLL}$. Assuming instead a small perturbation of the grid voltage, and approximating $\cos(\Delta\theta_{PLL}) \approx 1$ and $\sin(\Delta\theta_{PLL}) \approx (\Delta\theta_{PLL})$, eq. (2.5) becomes:

$$\begin{bmatrix} V_d^{PLL} + \Delta v_d^{PLL} \\ V_q^{PLL} + \Delta v_q^{PLL} \end{bmatrix} \approx \begin{bmatrix} 1 & \Delta\theta_{PLL} \\ -\Delta\theta_{PLL} & 1 \end{bmatrix} \begin{bmatrix} V_d + \Delta v_d \\ V_q + \Delta v_q \end{bmatrix} \tag{2.6}$$

Where capital letters are used for indicating quantities at the operating point. Neglecting high-order terms, (2.6) becomes:

$$\begin{cases} \Delta v_d^{PLL} \approx \Delta v_d + V_q \, \Delta\theta_{PLL} \\ \Delta v_q^{PLL} \approx -V_d \, \Delta\theta_{PLL} + \Delta v_q \end{cases} \tag{2.7}$$

Defining the loop filter transfer function $LF(s)$ as:

$$LF(s) = k_p + \frac{k_i}{s} \tag{2.8}$$

and according to the linearized model shown in Fig. 2.11 (b), the following is valid:

$$\Delta\theta_{PLL}(s) = \frac{LF(s) \, \Delta v_q^{PLL}}{s} \tag{2.9}$$

Finally, substituting (2.9) into (2.7) yields:

$$\Delta\theta_{PLL}(s) = \frac{LF(s)}{s + V_d LF(s)} \Delta v_q = H_{PLL}(s) \, \Delta v_q \tag{2.10}$$

2.3.2 The Power-synchronization principle

Due to the fact that the majority of the grid-connected converters is nowadays represented by GFL units, the use of a dedicated synchronization unit, such as a PLL or a similar filter structure, has been considered an essential requirement. Nevertheless, recent studies have shown that, due to their working principle, GFL converters are particularly susceptible to weak grid operating conditions [66], [68]. In order to overcome this inconvenient, Zhang *et al*. have proposed in 2010 the Power Synchronization Control (PSC) for grid-connected Voltage Source Converters (VSCs) [52]. The underlying principle behind the proposed approach, is the power-synchronization mechanism of a real SM already mentioned in Section 2.2.4, and which allows SMs to keep synchronism with each other even under prohibitive

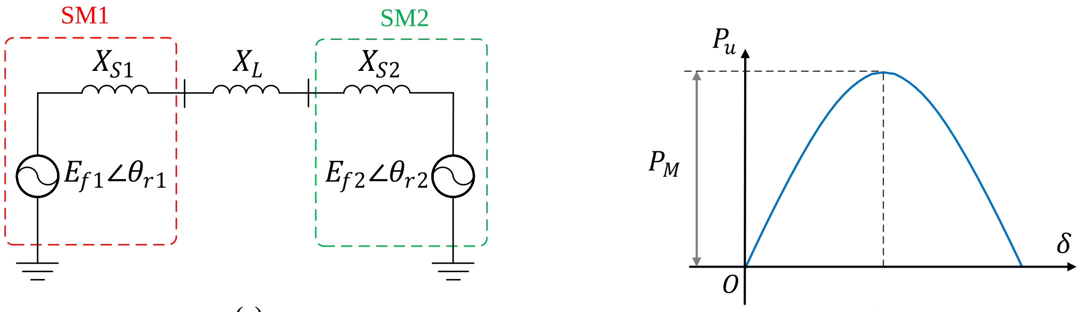

(a) (b)

Figure 2.12: Power exchanged between two SMs: (a) single-line diagram; (b) $P-\delta$ curve.

conditions for converters adopting standard vector control strategies. Without going into the details of the control structure, which will be instead discussed in the next section, the principle behind the power-synchronization mechanism of SMs is succinctly described in the following, according to the example reported in [52]. Let us consider two SMs connected through an inductive transmission line X_L, as schematically depicted in the equivalent single-line diagram of Fig. 2.12 (a). It is assumed that the first machine, indicated in the figure as SM_1, represents a generator, while the second machine (SM_2) is a motor. Indicating with E_{f1} and E_{f2} the back-emf voltages of the two machines, respectively, the expressions of the active and reactive power exchanged between the generator and the motor is given by the following equation [31], [70]:

$$P_u = \frac{E_{f1}E_{f2}}{(X_{S1}+X_L+X_{S2})}\sin(\delta) \tag{2.11}$$

where X_{S1} and X_{S2} represent the synchronous reactances of SM_1 and SM_2, respectively, and $\delta = \theta_{r1} - \theta_{r2}$. According to (2.11), the power exchange P_u between the two machines is a non-linear function of the angular difference δ. This relation is graphically shown in Fig. 2.12 (b), and is usually indicated as *power-angle* (or $P-\delta$) curve in the literature [70]. Under the assumption of a purely inductive impedance between the two voltage sources, the maximum power exchange P_M is obtained for $\delta = 90^\circ$. A further increase of the angle δ over this limit causes a decrease of the exchanged power, a process that is at the basis of the *rotor angle stability* phenomenon of SMs [70], and which will be further discussed in Chapter 5.

Let us assume that the two machines are initially at a steady-state operation, and rotate synchronously without exchanging power with each other. To verify this condition, the angles θ_{r1} and θ_{r2} need to be perfectly in phase, as schematically shown in Fig. 2.13 (a). This situation represents for example the case of a SM (motor or generator) connected to an infinite bus and running at no-load. In this case, the inner back-emf of the machine is perfectly synchronized in terms of magnitude and phase with the voltage phasor of the infinite bus. Indicating with ω_m the mechanical rotational speed, the swing equations for the two machines with the respective conventions of generator (SM_1) and motor (SM_2) are given below:

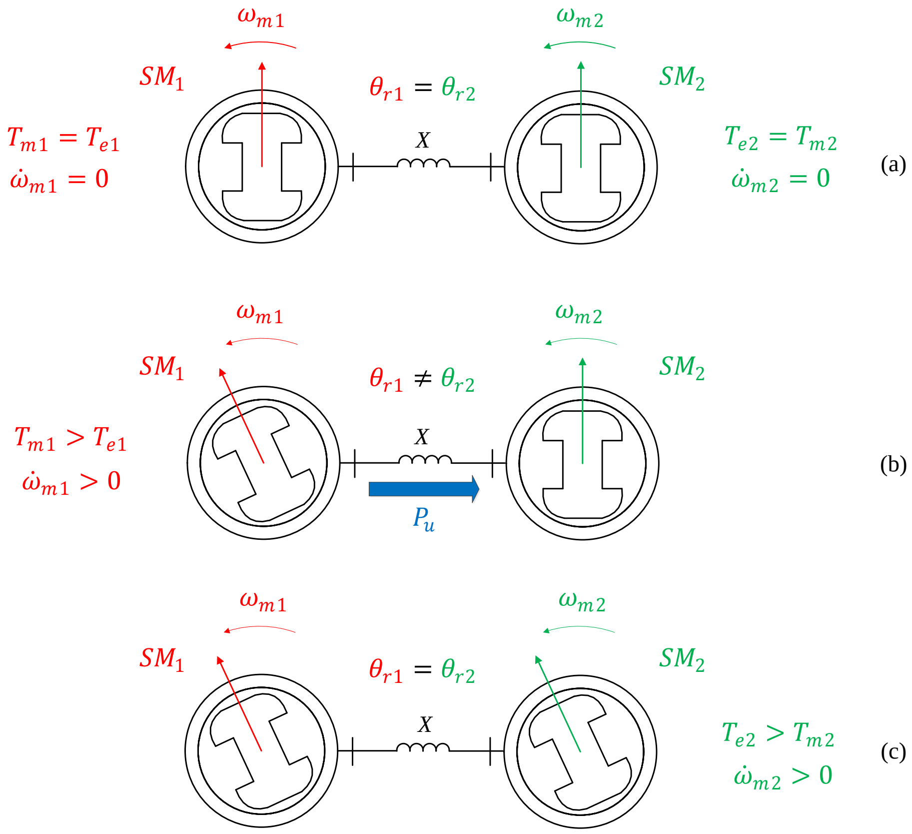

Figure 2.13: Explanation of the power-synchronization principle: (a) initial condition, (b) perturbation of the mechanical torque of SM1, (2) reaction of SM2 to the perturbation.

$$(SM_1):\ \dot{\omega}_{m1} = \frac{T_{m1} - T_{e1}}{J_1} \qquad ; \qquad (SM_2):\ \dot{\omega}_{m2} = \frac{T_{e2} - T_{m2}}{J_2} \tag{2.12}$$

where T_{m1} and T_{e1} indicate respectively the mechanical and the electrical torque of SM_1, T_{m2} and T_{e2} the same quantities for SM_2, and J_1 and J_2 the moment of inertia of the respective machines. Assuming that for a short transient the mechanical torque T_{m1} of SM_1 is suddenly increased and then set back to its initial value, this action causes according to eq. (2.12) an acceleration of the machine ($\dot{\omega}_{m1} > 0$). As a consequence of this perturbation, the mechanical angle between the two machines is increased, as schematically indicated in Fig. 2.13 (b), which translates, according to eq. (2.11), in an increase of the electrical power transferred from the generator to the motor. Assuming that the mechanical load of the motor T_{m2} remains unchanged during this process, the difference between T_{e2} and T_{m2} causes an acceleration of the second machine according to eq. (2.12), until the two rotors synchronize again with each other restoring the power balance, as schematically depicted in Fig. 2.13 (c).

Another simple example which might help better understanding the power-synchronization principle, is given in [31], and is represented by the analogy to two cars joined to each other by means of a rubber band and speeding around a circular track. The two cars represent the two SMs, while the rubber indicates the transmission line. If one car speeds up temporarily,

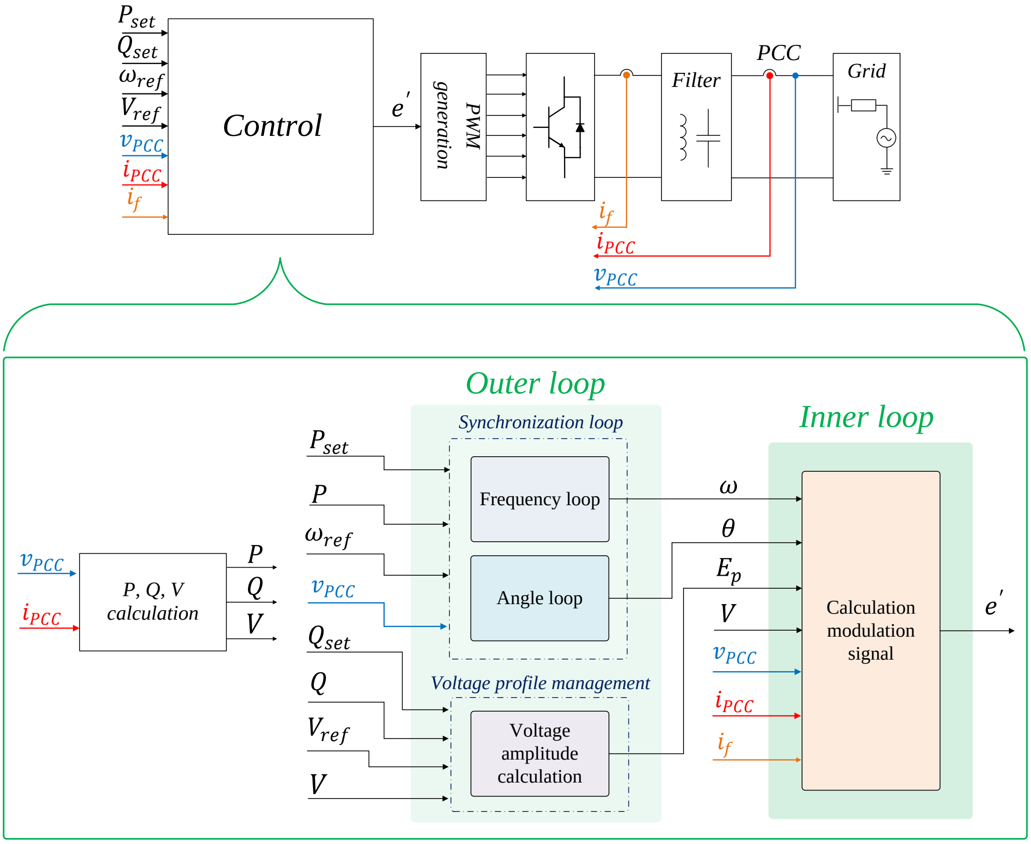

Figure 2.14: Generalized control structure of a GFM converter.

the band connecting the two will stretch, and a force tends to slow down the faster car, while speeding up the slowest one.

The process explained above in a simplified manner, is at the stake of the power-synchronization concept proposed by [52], and is typically reproduced in a VSM. Converters working according to the power-synchronization principle adapt the frequency of an internal oscillator in order to increase or decrease the angle displacement between the inner voltage angle and the grid voltage angle, so as to regulate the power injected by the converter to the given setpoint. Hence, contrary to the classical concept of a GFL converter, a converter working according to the described mechanism, produces an inner reference angle without the need for estimating the grid voltage angle.

2.4 General structure of GFM converters

According to the characteristics of GFM converters identified and discussed in Section 2.2, a general structure is outlined in the following. The main subsystems composing it, along with their inputs and outputs are first identified, then an overview of their possible implementations based on an extensive literature research is reported.

The proposed GFM structure is shown in Fig. 2.14. In the most generic formulation, the measured three-phase converter currents, along with the currents and the voltages at the PCC are among the control inputs of the converter, indicated in the figure with i_f, i_{PCC},

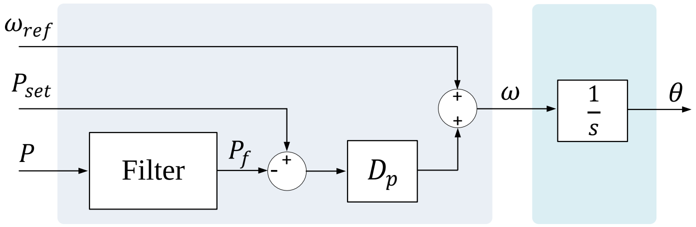

Figure 2.15: Synchronization loop implemented by means of a droop regulator [19], [22], [30], [71], [72].

and v_{PCC}, respectively. Additional control inputs are represented by the active and reactive power setpoints P_{set} and Q_{set} and, considering also grid supporting capabilities, the reference frequency ω_{ref} and the reference voltage V_{ref}. In the converter outer control loop, two separated subsystems are identified, namely the *synchronization loop* and the *voltage profile management*. The outputs of these two subsystems are the angle θ, the frequency ω, and the amplitude E_p of the internal voltage source. An inner control loop is indicated in the figure, which includes all the further control actions taking place in order to produce a proper modulation signal e' for the PWM. In the following, possible implementations of the identified subsystems composing the inner and the outer control loop are examined.

2.4.1 Outer loop - synchronization loop

The synchronization loop indicated in Fig. 2.14, contains two separated subsystems, labeled as *frequency loop* and *angle loop*, respectively in charge of the calculation of the frequency ω and the angle θ. The interconnections between the two subsystems are not explicitly depicted in the figure, since these may vary according to the specific implementation.

Droop regulator

The most simple implementation of the subsystem is represented by the droop regulator depicted in Fig. 2.15 [19], [22], [30], [71], [72]. The mathematical description of the subsystem is given by the following expression:

$$\theta(s) = \frac{1}{s}\left[\omega_{ref} + D_p\left(P_{set} - P_f\right)\right] \tag{2.13}$$

where P_f indicates the filtered measured power P, while the parameter D_p represents the droop coefficient determining the variation of the frequency ω according to the difference between the active power setpoint P_{set} and the filtered measured power P_f. Finally, the output angle θ is simply obtained by integration of the calculated frequency ω.

Though its simple implementation, the droop control structure is very effective, and does not require the use of a dedicated unit in order to estimate grid frequency or angle under normal operating conditions. It has been widely adopted in the context of microgrids [19], as well as for standalone applications [71], but rather seldom for grid-connected converters.

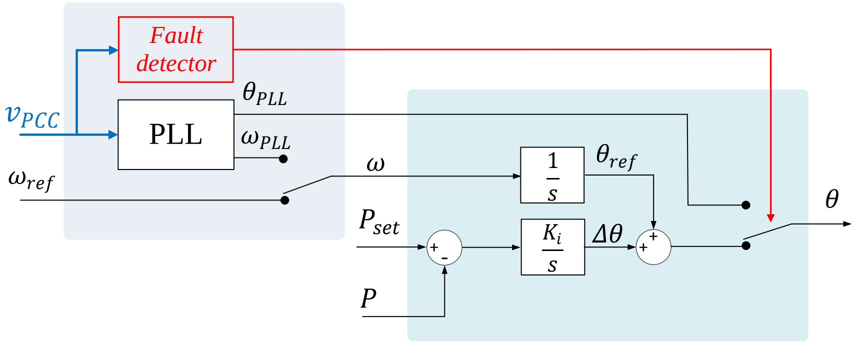

Figure 2.16: Synchronization loop of the Power Synchronization Control (PSC) for grid-connected converters proposed in [52].

Nevertheless, recent studies have proven that the same response of a VSM can be obtained by means of a droop controller where the measured power is properly filtered, proving the equivalence between the two structures [30], [72]. To this extent, the VSM0H control proposed by Roscoe *et al.* in [46], and deeply investigated in [51], is basically represented by a droop controller where the measured power P is processed by means of a boxcar filter, so as to limit the dynamic of the converter response.

Power-synchronization control (PSC)

The second examined implementation of the synchronization loop of a GFM converter is represented by the PSC for grid-connected converters proposed by Zhang *et al.* already introduced in the previous section, and whose structure is reported in Fig. 2.16 [52]. Initially thought for HVDC applications, it has gained the attention of the research community for its capability of operating a grid-connected converter under very weak grid conditions, extremely critical for a standard vector controlled VSC. The mathematical expression of the angle calculated by the PSC subsystem is given below:

$$\theta(s) = \theta_{ref} + \frac{1}{s}\left[K_i(P_{set} - P)\right] \tag{2.14}$$

The angle θ results from the addition of a reference angle θ_{ref} to a quantity obtained by processing the difference between the power setpoint P_{set} and the measured power P by means of an integrator with gain K_i. Similar to the droop control examined above, and according to the power-synchronization principle, the angle of the inner voltage source is increased or decreased so as to modify the phase displacement δ between the inner voltage source and the grid according to the measured power deviation.

However, differently from the droop structure previously examined, where the frequency is modified according to the power difference, in the SPC structure, is the angle θ to be obtained by directly adding a quantity to the reference angle θ_{ref}. The latter is calculated by integrating the reference frequency ω_{ref} and, therefore, an estimation of the actual grid frequency is not explicitly obtained from the power deviation, but it could be eventually

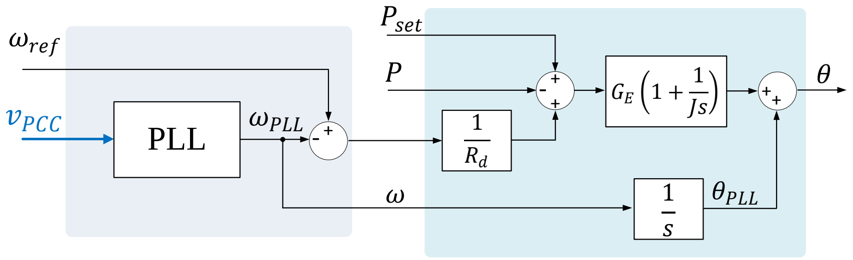

Figure 2.17: EDPC synchronization loop proposed in [73], [74].

provided by a dedicated unit, e. g. a PLL. In this regard, even though the proposed structure can work very well under normal operating conditions, a back-up PLL is foreseen for pre-synchronization purposes, as well as for operation under fault conditions. In this case, a vector current control is activated in the inner loop in order to prevent the converter from the risk of instability and hardware damages, thus requiring a fault detector in order to trigger a fault operating mode and switch the source of the angle θ.

Enhanced direct power control (EDPC)

The structure shown in Fig. 2.17, has been presented in [73], [74], and it has been implemented in the GFM control proposed by the authors so as to study the effects of increased power electronics-based penetration on the stability of the British power system. The introduced GFM control structure has been labeled as Enhanced Direct Power Control (EDPC), and presented as a modification to the DPC concept discussed in [75] and [76].

Conceptually similar to the SPC examined above, and mainly focusing on the contribution of GFM converters on system stability during faults, a PLL is foreseen during both normal operating conditions, as well as during faults in order to provide a reference angle for either the GFM control, or for the vector current control activated at occurrence of the fault. Hence, contrary to the PSC, the PLL is always activated in order to avoid switching the source of the converter reference angle, preventing from possible dangerous transients.

The angle θ calculated according to the structure shown in Fig. 2.17, is given by the following expression:

$$\theta(s) = \theta_{PLL} + G_E\left(1+\frac{1}{Js}\right)\left[P_{set} - P + \frac{1}{R_d}(\omega_{ref} - \omega_{PLL})\right] \tag{2.15}$$

where to the reference angle θ_{PLL} provided by the PLL, the output of a PI controller with gain G_E and time constant J is added, the latter processing the sum of the difference between the power setpoint P_{set} and the measured power P. Furthermore, in [73], a frequency droop control with gain $1/R_d$ acting on the difference between the reference frequency ω_{ref} and the frequency estimated by the PLL (ω_{PLL}) is also included. Beside this frequency droop action, eq. (2.15) mainly differs from eq. (2.14) for the introduction of the PI controller, whose time

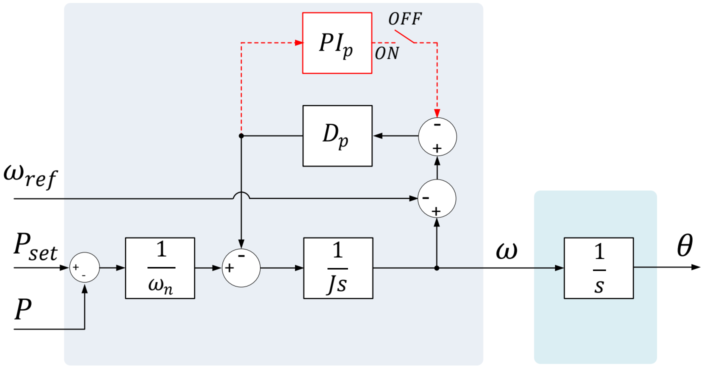

Figure 2.18: Synchronization loop of the synchronverter control [41].

constant J acts as an additional degree of freedom for shaping the response of the converter according to a frequency variation in a similar fashion as in a real SM [73], [74].

Synchronverter

The synchronverter structure proposed by Zhong *et al*. [40], [41], is surely one of the most popular VSM implementations among those presented in the literature. It became very popular during the last decade due to the fact that it does not require a dedicated synchronization unit for pre-synchronization purposes, as well as during normal operation. A sequence of switching actions has been proposed in [41], as a modification to the original concept discussed in [40], emulating the synchronization process of a real SM prior connection to the grid. This in fact needs to be perfectly synchronized in terms of magnitude and phase with the grid voltage phasor before connection, and this process will be better described in Chapter 6 by means of a practical example. Nevertheless, the synchronverter behaviour during faults has not been explicitly addressed in the aforementioned works, and several strategies have been proposed by other authors, which will be examined in detail in Chapter 5.

The synchronization loop of a VSM is generally implemented so as to reproduce the swing equation of a real SM, reported below for simplicity:

$$\dot{\omega}_m = \frac{T_m - T_e - D_f \omega_m}{J} \tag{2.16}$$

where, compared to the simplified expression given in (2.12), the additional frequency-dependent damping factor D_f is introduced. The synchronization loop of the synchronverter is reported in Fig. 2.18. According to the proposed structure, the parameter D_p not only represents the virtual damping factor of the VSM, but it also accounts for the steady-state $P-f$ droop behaviour of the control, as it will be further discussed in the following. The mechanical torque T_m is directly calculated by dividing the power setpoint P_{set} for the nominal grid frequency ω_n. Similarly, the measured electrical torque T_e is also derived from the measured power P at the point of connection by dividing for the same quantity. It is worth to point out that the structure reported in the figure, slightly differs from the original one

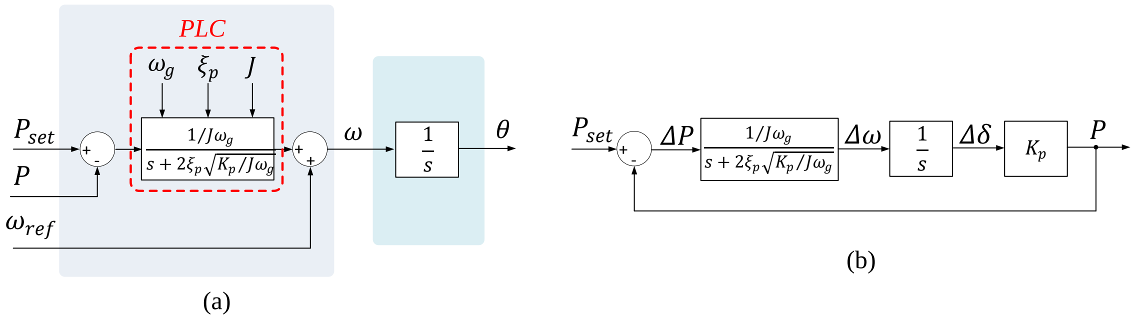

(a)

(b)

Figure 2.19: (a) Synchronization loop of the SPC, (b) simplified closed-loop transfer function of the power [43].

proposed in [40], [41], where instead T_e is calculated, as for a real SM, from the air-gap power equation [77]. As a consequence, in order to obtain the measured power at the PCC, it would be necessary to subtract the virtual stator losses caused by the filter resistance. Nevertheless, the simplification shown in Fig. 2.18, is widely adopted in the literature [78]-[80], and is therefore considered in the following. The dashed branch indicated in the figure, is introduced so as to activate or deactivate the $P-f$ droop control action. Indeed, when the switch is closed, the PI control cancels out the deviation between the reference frequency ω_{ref} and the internal frequency ω. Hence, indicating with $PI_p(s)$ the transfer function of the PI controller, the expression of the calculated angle θ according to the structure of Fig. 2.18, becomes:

$$\theta(s)=\frac{1}{s}\left[\frac{\left(P_{set}-P\right)\frac{1}{J\omega_n}}{s+\frac{D_p}{J\left(1+D_pPI_p(s)\right)}}+\omega_{ref}\frac{\frac{D_p}{J\left(1+D_pPI_p(s)\right)}}{s+\frac{D_p}{J\left(1+D_pPI_p(s)\right)}}\right] \tag{2.17}$$

Synchronous Power Control (SPC)

The second examined synchronization loop implementation of a VSM, is the one of the SPC proposed by Rodrigez *et al.* in [42]-[44], and reported in Fig. 2.19 (a). A first-order transfer function acting on the deviation between the power setpoint P_{set} and the measured power P, and labeled as Power Loop Controller (PLC) is implemented in the frequency loop. Its expression is given below [43]:

$$PLC(s)=\frac{\frac{1}{J\omega_g}}{s+2\zeta_p\sqrt{\frac{K_p}{J\omega_g}}} \tag{2.18}$$

where J indicates the virtual moment of inertia, ω_g is the grid angular frequency, and K_p is a coefficient representing the steady-state value of the transfer function between a variation of the power angle δ and the power injected by the converter into the grid. The reason why the PLC expression is given in the form of eq. (2.18), is essentially to express the closed-loop transfer function of the simplified active power loop shown in Fig. 2.19 (b), by means of a second-order parametric function of the following form [43]:

$$\frac{P}{P_{set}}(s) = \frac{\omega_{nt}^2}{s^2 + 2\zeta_p \omega_{nt}\, s + \omega_{nt}^2} \tag{2.19}$$

where ζ_p represents the damping ratio, and $\omega_{nt} = \sqrt{K_p / J\omega_g}$ is the natural frequency. The expression of the angle θ calculated according to the synchronization loop depicted in Fig. 2.19, is given by:

$$\theta(s) = \frac{1}{s}\left[\left(P_{set} - P\right) PLC(s) + \omega_{ref}\right] \tag{2.20}$$

Modifications of the examined VSM impementations

Even though the synchronization loops of the two examined VSM implementations might look different at first glance, similarities among the two structures can be easily identified. Hence, by differentiating eq. (2.17) with respect to the power difference $P_{diff} = P_{set} - P$, yields for the synchronverter:

$$\frac{\partial\theta}{\partial P_{diff}}(s) = \frac{1}{s}\left[\frac{\frac{1}{J\omega_n}}{s + \frac{D_p}{J}}\right] \tag{2.21}$$

A similar calculation applied to eq. (2.20), gives the following result for the SPC:

$$\frac{\partial\theta}{\partial P_{diff}}(s) = \frac{1}{s}\left[\frac{\frac{1}{J\omega_g}}{s + 2\zeta_p\sqrt{\frac{K_p}{J\omega_g}}}\right] \tag{2.22}$$

As a consequence, the two expressions become equivalent when the control parameters of the two VSM implementations are chosen as follows:

$$J\omega_n = J\omega_g \quad ; \quad \frac{D_p}{J} = 2\zeta_p\sqrt{\frac{K_p}{J\omega_g}} \tag{2.23}$$

It has been indeed mentioned above, that for the synchronverter control structure the factor D_p not only represents the virtual damping factor of the VSM, but it also corresponds to the steady-state $P-f$ behaviour of the inherent droop control. This represents a limitation of the synchronverter, due to the fact the droop coefficient is usually constrained by specifications, losing, therefore, one degree of freedom in the control tuning procedure. Due to the considerations reported above regarding the equivalence between the two examined VSM implementations, same conclusions can be drawn for the SPC, where a droop steady-state characteristic is, hence, inherently implemented in the control structure.

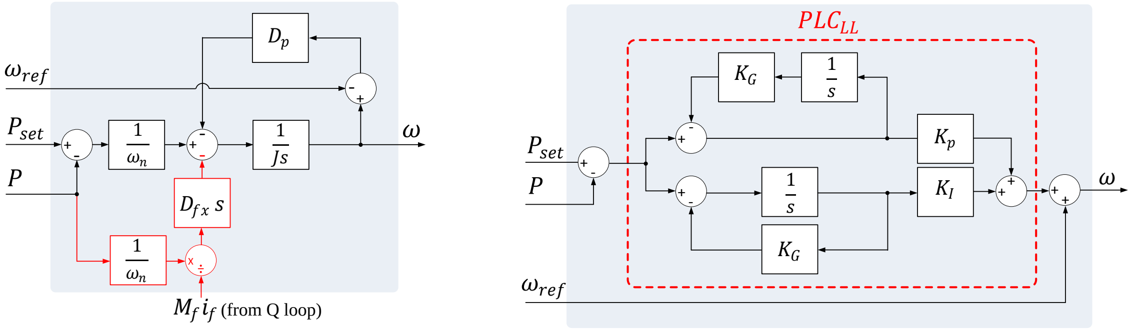

(a) (b)

Figure 2.20: Modification to the frequency loop of VSM implementations for decoupling $P-f$ droop factor from virtual damping factor: (a) synchronverter [80], (b) SPC [81].

In order to overcome this inconvenient, a modification to the synchronverter structure has been proposed in [80], which is schematically shown in Fig. 2.20 (a). A damping correction loop is namely introduced, modifying the expression of the calculated frequency as follows:

$$\omega(s) = \frac{\left(P_{set}-P\right)\frac{1}{J\omega_n} + \omega_{ref}\frac{D_p}{J} - s\frac{D_{fx}}{J}\left(\frac{P}{\omega_n M_f i_f}\right)}{s+\frac{D_p}{J}} \tag{2.24}$$

where $M_f i_f$ represents the virtual rotor flux calculated in the reactive power loop of the synchronverter. The proposed modification introduces the additional parameter D_{fx}, which affects the dynamic response of the control, but whose action is nullified at steady-state.

Similarly, a modification to the frequency loop of the SPC has been proposed in [81], and shown in Fig. 2.20 (b). A lead-lag filter is implemented, whose effects are similar to those of the solution discussed above for the synchronverter. The expression of the PLC is modified according to the following equation:

$$PLC_{LL}(s) = \frac{K_P\, s + K_I}{s+K_G} \tag{2.25}$$

where the parameters K_P, K_I, and K_G can be independently chosen so as to respectively set the damping, the inertia, and the droop characteristic of the control. As a consequence, the simplified closed loop transfer function (2.19) becomes [81]:

$$\frac{P}{P_{set}}(s) = \frac{(2\zeta_p\omega_n - K_G)s + \omega_n^2}{s^2 + 2\zeta_p\omega_n\, s + \omega_n^2} \tag{2.26}$$

hence providing an additional degree of freedom without increasing the order of the power regulating transfer function.

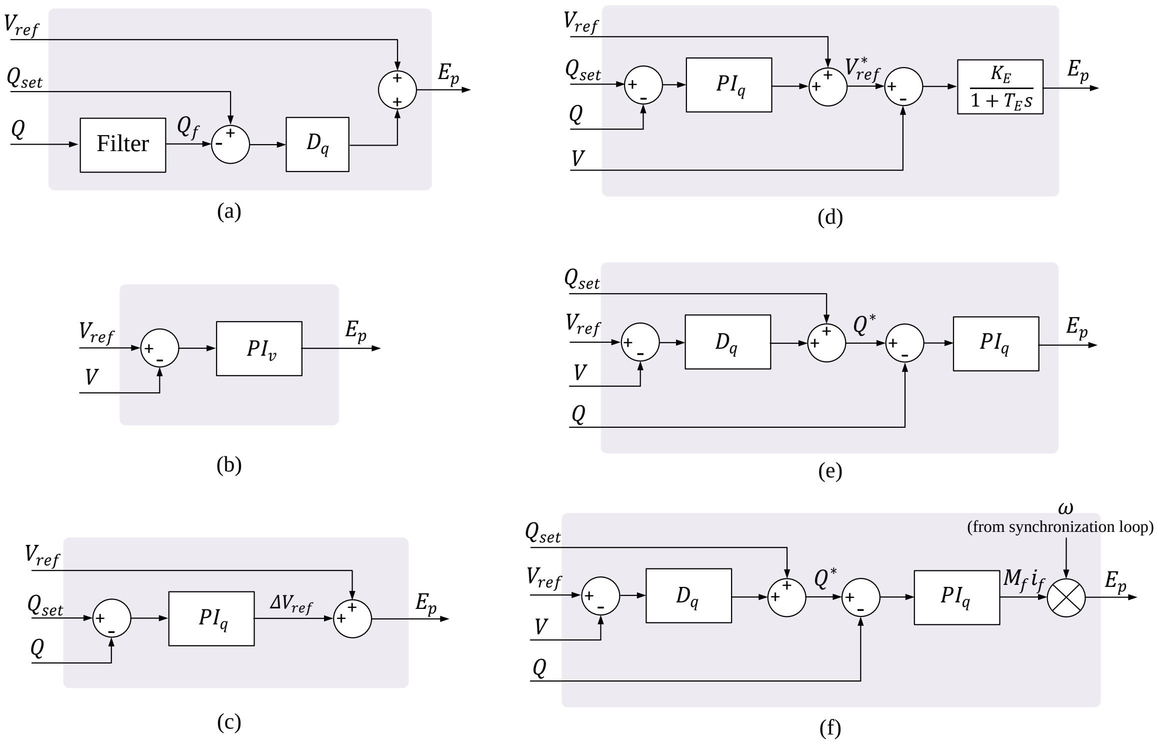

Figure 2.21: Different implementations of the voltage profile management loop: (a) droop control [19], [22], [30], [46], [71]; (b) PI-based voltage control for SPC [82]; (c) PI-based reactive power control for SPC [43], [44]; (d) cascaded structure with PI control in the first stage and droop in the second stage [52]; (e)-(f) cascaded structure with droop in the first stage and PI control in the second stage [40], [41], [73], [74].

2.4.2 Outer loop - voltage profile management

Several implementations of the synchronization loop of a GFM converter have been reported in the previous sections, showing a relatively wide variety of possible choices. Regarding the subsystem in charge of the voltage regulation, the commonly adopted solutions can be summarized in three main categories: droop control, PI-based control, and cascaded controls involving droop and PI regulators. The considered schemes are shown in Fig. 2.21, and discussed in the following.

The first examined implementation is the droop control reported in Fig. 2.21 (a), which is usually adopted in combination with droop controllers in the synchronization loop [19], [22], [30], [46], [71]. In analogy to the droop structure shown in Fig. 2.15, the filtering of the measured reactive power is explicitly introduced in the figure, as also indicated in [30]. The difference between the reactive power setpoint Q_{set} and the filtered measured power Q_f is processed through a proportional gain D_q. Subsequently, this quantity is added to the reference voltage V_{ref}, in order to calculate the amplitude of the inner voltage E_p of the GFM converter. The equation describing this implementation is:

$$E_p = V_{ref} + D_q\big(Q_{set} - Q_f\big) \tag{2.27}$$

The two schemes reported in Fig. 2.21 (b) and (c), represent PI-based solutions, which have been proposed for the implementation of the voltage profile management subsystem of the SPC. In the first case, a PI controller with transfer function PI_v regulates the measured voltage V at the PCC to the reference value V_{ref}, and has been presented in [82], for the implementation of a VSM-based Static Synchronous Compensator (STATCOM). In the second case, a PI controller with transfer function PI_q is implemented in order to regulate the reactive power Q to the setpoint Q_{set}, where, additionally, a feedforward of the reference voltage V_{ref} is included [43], [44]. The equations describing the two structures are reported below:

$$\begin{cases} E_p(s) = PI_v(s)\big(V_{ref} - V\big) & (Fig.\ 2.21(b)) \\ E_p(s) = PI_q(s)\big(Q_{set} - Q\big) + V_{ref} & (Fig.\ 2.21(c)) \end{cases} \tag{2.28}$$

The schemes shown in Fig. 2.21 (d) and (e), represent two cascaded structures involving droop and PI controllers. The first implementation is the one adopted in the PSC [52], and consists of a PI controller in the outer stage, processing the reactive power difference, and an Alternating Voltage Controller (AVC) with a droop characteristic in the inner stage. The second implementation is instead widely adopted in the GFM literature [40], [41], [73], [74], and consists of a droop controller in the first stage reacting to the voltage deviation, followed by a PI control in the second stage, the latter regulating the reactive power of the converter to the modified reactive power setpoint Q^*. The expressions describing the two formulations are reported below:

$$\begin{cases} E_p(s) = \big[PI_q(s)\big(Q_{set} - Q\big) + V_{ref} - V\big]\frac{K_E}{1+T_E s} & (Fig.\ 2.21(d)) \\ E_p(s) = \big[D_q\big(V_{ref} - V\big) + Q_{set} - Q\big]PI_q(s) & (Fig.\ 2.21(e)) \end{cases} \tag{2.29}$$

In the specific case of the synchronverter, the structure is conceptually similar to the one of Fig. 2.21 (e), but the output of the PI controller represents a virtual mutual flux, indicated with $M_f i_f$, so that E_p is calculated according to the following equation [40], [41]:

$$E_p(s) = \big\{\big[D_q\big(V_{ref} - V\big) + Q_{set} - Q\big]PI_q(s)\big\}\omega \qquad (Fig.\ 2.21(f)) \tag{2.30}$$

where ω is the frequency calculated in the synchronization loop.

2.4.3 Inner loop - Generation of the modulation signal

After having examined the most relevant solutions among those proposed in the literature, for the two subsystems composing the outer loop of the generalized GFM structure, possible

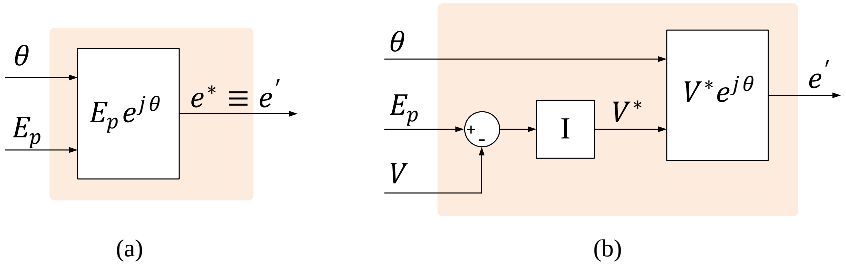

(a) (b)

Figure 2.22: Simplest implementations of the inner loop: (a) direct voltage synthesis [40], [41], [83], (b) voltage magnitude control [20].

implementations of the inner control loop are discussed in the following. In the description provided at the beginning of this section, the role of this subsystem has been identified as all the further actions taking place in order to reproduce the modulation signals for the PWM from the information provided by the outer control loop related to the angle θ, the frequency ω, and the amplitude E_p of the inner voltage signal. To this extent, a wide amount of solutions can be found in the microgrids literature, and which mainly focus on reproducing the reference voltage setpoint calculated in the outer loop at the converter terminals. This is mainly due to the fact that, as already mentioned in Section 2.2.1, the original concept of a GFM converter was rather close to the one of a perfect voltage source with a low series impedance. On the other hand, the virtual impedance concept has emerged as a possibility for properly shaping the equivalent output impedance of the converter, without the need for modifying the design of the converter hardware components, and which turns out to be particularly useful for applications in wide interconnected systems. Solutions complying whit these two approaches are examined in the following.

Inner loop - Direct PCC voltage control

Various voltage control schemes have been proposed in the literature, for the regulation of the voltage at the converter terminal. The easiest implementation is the direct voltage synthesis proposed in [83] for HVDC applications, and schematically shown in Fig. 2.22 (a). The reference signal $\mathbf{e}'$ is generated by the internal voltage oscillator as:

$$\mathbf{e}' \equiv \mathbf{e}^* = \begin{bmatrix} e_a^* \\ e_b^* \\ e_c^* \end{bmatrix} = \begin{bmatrix} E_p \sin(\theta) \\ E_p \sin(\theta - \frac{2}{3}\pi) \\ E_p \sin(\theta + \frac{2}{3}\pi) \end{bmatrix} \tag{2.31}$$

The calculated voltages are then directly adopted as modulation signals for the PWM. No specific voltage feedback is foreseen, and the capacity of disturbance rejection of this structure is limited. A similar implementation has been proposed for the synchronverter in [40], [41]. Nevertheless, it is worth to notice that the idea behind the implementation proposed in the synchronverter structure, is that the calculated reference voltage $\mathbf{e}'$ does not represent the voltage setpoint at the converter terminals, but rather the virtual back-emf voltage of the

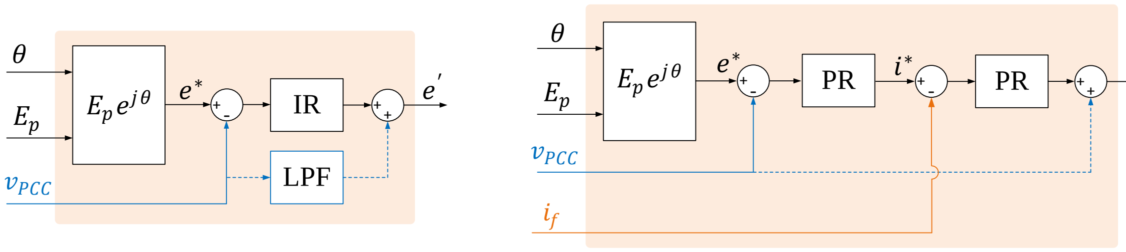

(a)

(b)

Figure 2.23: Vector voltage control: (a) single-loop voltage control [86], [87], (d) double-loop voltage control [87], [88], [89].

VSM. Thus, in the original synchronverter concept, the converter filter serves as the synchronous reactance of the VSM, being the regulation of the voltage vector at the converter terminals not explicitly foreseen.

The second examined implementation of the inner loop is shown in Fig. 2.22 (b). This has been proposed in [20], in the context of converter controls for microgrid applications, and represents a further improvement compared to the first examined structure. A feedback of the measured converter voltage amplitude at the connection point is introduced, so that by means of an integral controller the voltage V is regulated to the reference voltage amplitude E_p.

In order to achieve a better regulation of the converter voltages, the vector voltage control can surely provide superior performances compared to the two previously examined implementations. This can be realized either by means of a single-loop or a multiple-loop structure, as shown in Fig. 2.23 (a) and (b), respectively. Assuming a control in $\alpha\beta$ coordinates, an integral-resonant (IR) controller is shown in the scheme of Fig. 2.22 (c). Indeed, studies have shown that using a resonant controller (or equivalently an I controller in dq-frame) can bring a 90° phase lag at the crossover frequency, enhancing the stability of the control loop [84], [85]. Nevertheless, in order to further enhance the tracking capabilities of the control, which result instead limited in the low frequency range by only adopting a resonant controller (in $\alpha\beta$-frame), an integral factor is also included, so as to increase the gain in the low-frequency range [86], [87]. In order to further widen the stability region of the controller, a feedforward loop with a low-pass filter (LPF) is introduced, indicated in the figure by the dashed branch [85].

One of the main limitations of the previously described structures, is that a direct control of the converter currents is not possible, which might lead to converter tripping during severe transients and/or grid faults. In order to overcome this limitation, a dual-loop structure can be employed, as schematically shown in Fig. 2.23 (b). Compared to the single-loop structure, an inner current control loop of the filter current i_f is introduced. Beside protecting the converter from the risk of overcurrents, a proper tuning of the inner current control allows achieving active damping of the LC filter [88], [89]. Nevertheless, the equivalent output impedance of the converter might exhibit a negative real part in the high-frequency range, triggering possible control instability phenomena. In order to overcome this issue, a feedforward of

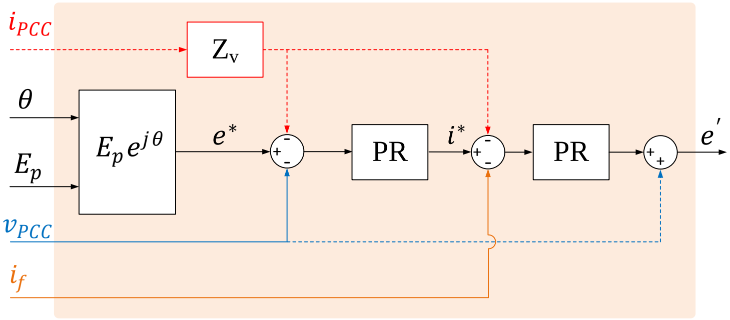

Figure 2.24: Multiple-loop voltage vector control with virtual impedance implementation [90]-[94].

the measured voltage v_{PCC} has been proposed in the literature, whose effects have been investigated in [87].

Inner loop - Virtual impedance implementation

In spite of controlling the voltage at the PCC, in order to exactly reproduce the output reference voltage calculated in the outer loop, methods have been proposed so as to shape the output impedance of the converter according to the operating condition. These techniques have been labeled as *virtual impedance* implementations, and have been initially investigated in microgrid applications, while recently also extended to grid-connected converters. Among the possible features of virtual impedance implementations, mitigation of harmonics, sub-harmonics, and unbalances [90], [91], power flow control [92], and current limitations during faults [93], are surely the most interesting performances allowed by this control loop that have gained the attention of the research community in the last decade [94]. Additionally, passivity-based controllers for enhancing stability of grid-connected converters have been recently proposed in the literature, as an efficient way for ensuring converter stability in a power electronics-based power system [95], [96]. Finally, the virtual impedance concept becomes particularly useful in the context of VSMs, since for the emulation of a real SM behaviour, the output impedance of the converter should reproduce determined characteristics, as it will be further discussed in the following.

Fig. 2.24 shows the typical implementation of a virtual impedance scheme [94]. Compared to the structure shown in Fig. 2.23 (b), feedforward terms are added to the outer and/or the inner loop of the multiple-loop vector control structure. In analogy to the scheme reported in Fig. 2.23 (b), it is assumed that PR controllers are adopted in the cascaded loops, which might be substituted by PI regulators if a control in dq coordinates is instead implemented. In most of the cases, the implemented virtual impedance Z_v is of the form:

$$Z_v(s) = R_v + sL_v \tag{2.32}$$

where R_v and L_v indicate the resistive and inductive components, respectively.

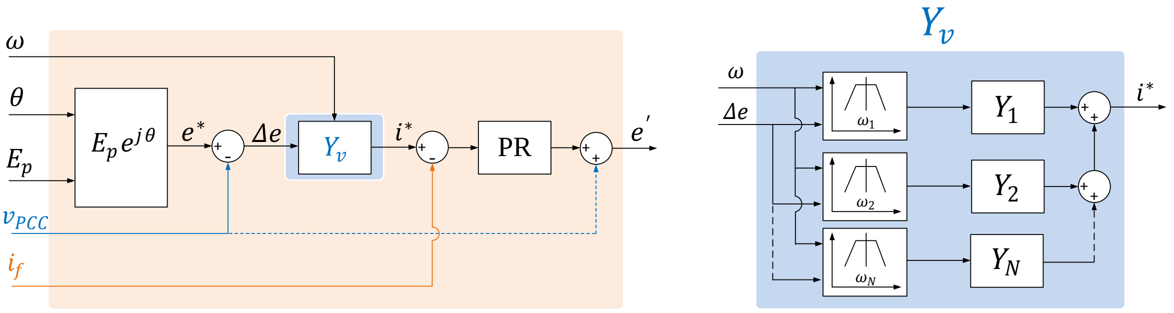

(a)

(b)

Figure 2.25: Virtual admittance implementation: (a) inner loop control scheme [43], (b) virtual admittance implementation [97].

One of the main drawbacks of this implementation is that the derivative of the measured current i_{PCC} needs to be performed, resulting this solution particularly sensitive to measurement noise and harmonic distortion. In order to overcome this inconvenient, the *virtual admittance* concept has been proposed in [43], and [97], as part of the SPC implementation. The inner loop control scheme corresponding to a virtual admittance implementation is reported in Fig. 2.25 (a). The virtual admittance is designed so as to reproduce a first-order LPF behaviour, and allows calculating current setpoints i^* from the difference between the virtual back-emf voltage e^* calculated in the outer control loop, and the measured voltages v_{PCC} at the point of connection, according to the following equation:

$$i^*(s) = \Delta e \, Y_v(s) = \frac{e^* - v_{PCC}}{R_v + sL_v} \tag{2.33}$$

where R_v and L_v have the same meaning as in (2.32). One of the main advantages of virtual impedance/admittance implementations in VSMs is related to the capability of arbitrarily choosing the equivalent output impedance of the converter, so as to reproduce a similar behaviour as the one of a real SM. Indeed, this turns out to be particularly useful when the grid impedance at the connection point of the converter is mainly resistive, so that the parameters of the emulated virtual impedance/admittance can be chosen in order to guarantee that the equivalent output impedance of the converter shows an inductive behaviour, hence contributing to the decoupling between active and reactive power control loops [98].

Another possible feature of the virtual admittance implementation has been presented in [97], and concerns the possibility of actively damping selected harmonics of the grid voltage. The working principle is schematically shown in Fig. 2.25 (b), where band-pass filters tuned at different frequencies $\omega_1,...,\omega_N$ are implemented. These allow choosing independently the virtual admittance value to apply at specific frequencies, by decomposing the signal Δe in its harmonic components, hence allowing active damping at the frequencies of interest.

A relevant aspect for the emulation of a SM by means of a conventional converter is the size of its output filter. Indeed, typical values for the inductance of a converter filter are in the range of 0.1 *pu* [25], whereas common values of the synchronous reactances of real SMs are

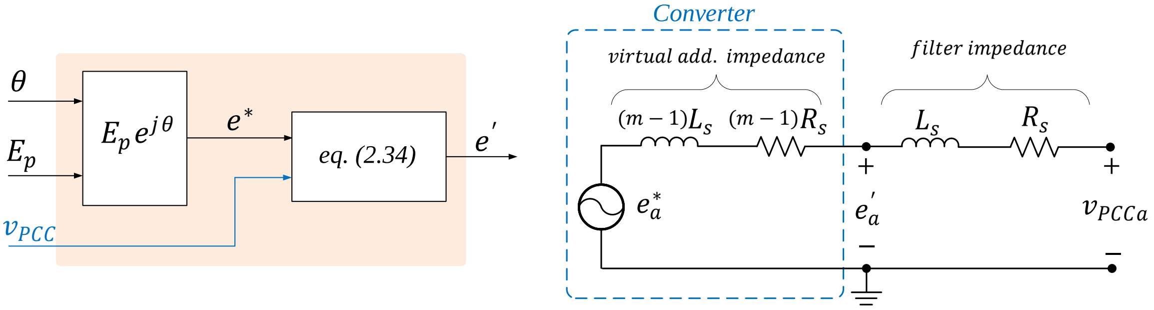

(a) (b)

Figure 2.26: Virtual impedance implementation proposed in [99]: (a) inner loop control scheme, (b) equivalent single-phase converter scheme.

in the range of 1.5 *pu* [31]. The relevance of this aspect will become more clear in Chapter 4, where the effects of the grid and converter filter impedance on the stability of GFM converters are investigated. In order to compensate for this mismatch, a simple and intuitive method for virtually increasing the value of the converter output filter impedance has been proposed in [99]. Presented as an improvement of the synchronverter structure, the modified inner loop control scheme according to [99] is reported in Fig. 2.26. Differently from the concept adopted in the original synchronverter scheme [40], [41], where, according to Fig. 2.22 (a), the reference voltage calculated in the outer loop is directly used as a modulation signal for the converter PWM, in the proposed implementation, the modulation signal for each phase is calculated according to the following equation:

$$e'_x = \frac{(m-1)v_{PCCx} + e^*_x}{m} \tag{2.34}$$

where $x = \{a, b, c\}$, and $m \geq 1$ is a proportional scaling factor for adjusting the equivalent output impedance to the desired value. The principle behind this calculation can be understood by looking at the equivalent single-phase scheme depicted in Fig. 2.26 (b), where it can be observed that in case of $m = 1$, eq. (2.34) reduces to eq. (2.31) of the classical synchronverter scheme. The proposed solution only requires measurements of the converter voltages at the PCC, hence without involving any measurement of converter currents. The main drawback of this implementation consists on the fact that only multiples of the real filter impedance can be reproduced, so that inductive and resistive components of the emulated filter impedance cannot be freely chosen.

The last virtual impedance implementation examined in this overview, is based on the control proposed in [100], and consists on the application of the model reference $\mathcal{H}_\infty$ design approach in order to shape the output impedance of the converter and achieve active damping of the converter LCL filter [101]. The proposed approach allows designing an inner control loop specifying the desired grid current dynamic of the converter, i. e. the one of an L filter, while the $\mathcal{H}_\infty$ theory is adopted so as to synthetize a (sub)-optimal inner controller [102], [103]. In Fig.2.27 (a) the block diagram of the inner loop is shown, while in

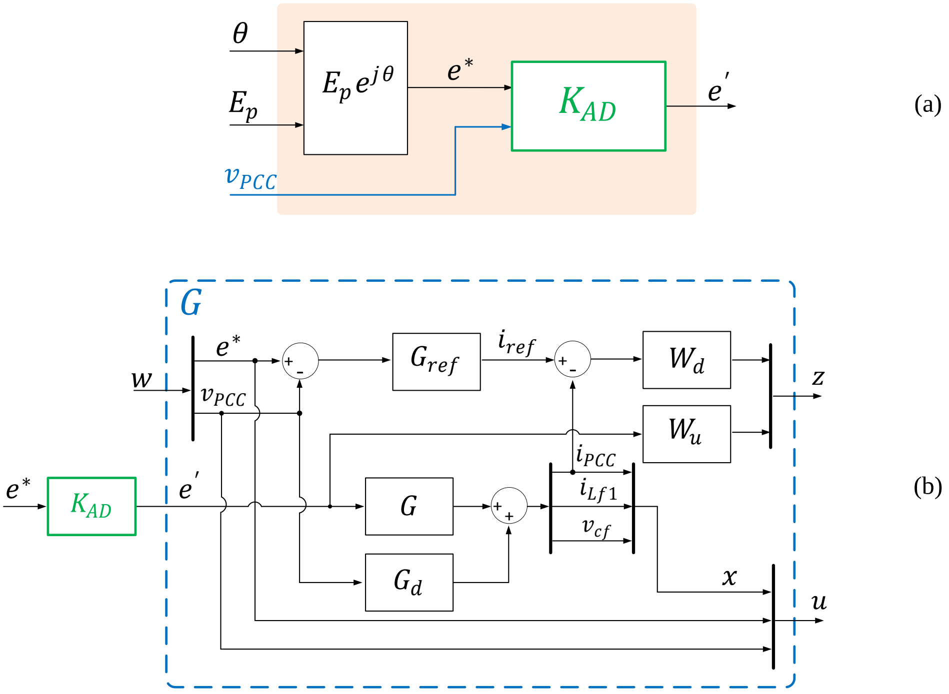

Figure 2.27: Virtual impedance implementation proposed in [100]-[102]: (a) inner loop control scheme, (b) construction of the generalized plant G for control synthesis.

Fig. 2.27 (b), the construction of the generalized plant G used for synthesizing the control is depicted.

The $\mathcal{H}_\infty$ algorithm aims on minimizing a cost function that includes both the controller and the plant dynamics, along with some plant modifiers named cost weights, indicated with W_d and W_u in Fig. 2.27 (b). Assuming that the converter is equipped with an output LCL filter, the controller K_{AD} properly calculates the modulation signal e' of the converter, so as to reshape the open-loop dynamic of the filter, described by the transfer functions $G(s)$, and $G_d(s)$, so as to reproduce the behaviour of a given reference function $G_{ref}(s)$, e. g. the one of an L filter with given characteristics. In the specific case, the transfer function $G(s)$, and $G_d(s)$ are defined according to the superposition principle as:

$$i_{PCC}(s) = G(s)e' + G_d(s)v_{PCC} \tag{2.35}$$

$W_d(s)$ and $W_u(s)$ represent instead frequency dependent weighting functions, which need to be properly designed so as to minimize the shaping error (difference between reference current against nominal current), or the actuation voltage e', respectively. However, the weighting functions require to be designed so as to result complementary with each other in the spanned frequency range, such that a proper compromise needs to be met.

Considerations about the examined virtual impedance implementations

All the examined implementations discussed in this overview, aim on modifying the equivalent output impedance shown by the converter, altering it from the one resulting by con-

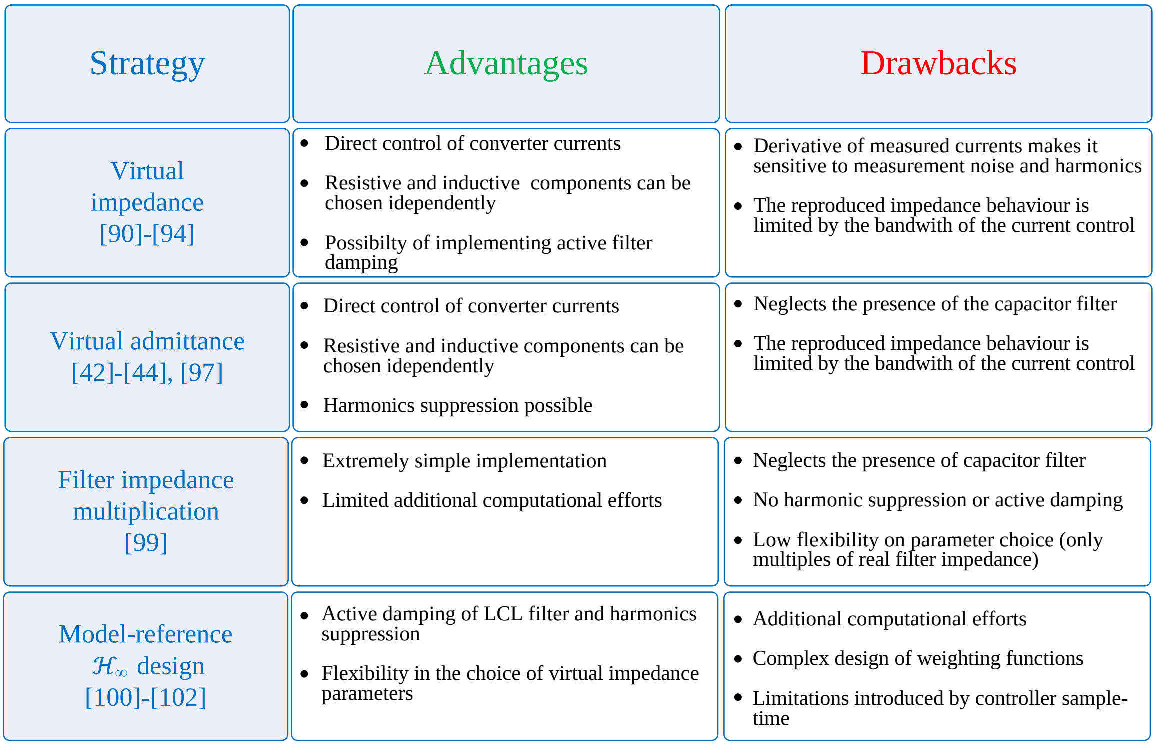

Strategy	Advantages	Drawbacks
Virtual impedance [90]-[94]	- Direct control of converter currents - Resistive and inductive components can be chosen idependently - Possibilty of implementing active filter damping	- Derivative of measured currents makes it sensitive to measurement noise and harmonics - The reproduced impedance behaviour is limited by the bandwith of the current control
Virtual admittance [42]-[44], [97]	- Direct control of converter currents - Resistive and inductive components can be chosen idependently - Harmonics suppression possible	- Neglects the presence of the capacitor filter - The reproduced impedance behaviour is limited by the bandwith of the current control
Filter impedance multiplication [99]	- Extremely simple implementation - Limited additional computational efforts	- Neglects the presence of capacitor filter - No harmonic suppression or active damping - Low flexibility on parameter choice (only multiples of real filter impedance)
Model-reference $\mathcal{H}_\infty$ design [100]-[102]	- Active damping of LCL filter and harmonics suppression - Flexibility in the choice of virtual impedance parameters	- Additional computational efforts - Complex design of weighting functions - Limitations introduced by controller sample-time

Figure 2.28: Comparison characteristics of the examined virtual impedance implementations.

sidering only the converter filter hardware components. Nevertheless, each of the examined solutions differ from the others for different aspects, e. g. implementation complexity and reproduced accuracy. To this extent, the advantages and drawbacks of the examined virtual impedance implementations are summarized in the table reported in Fig. 2.28, so that according to the application of interest, the most suitable approach can be chosen.

The simplest solution is the filter impedance multiplication presented in [99]. Though extremely simple to implement, its main limitation is represented by the fact that the elements of the reproduced impedance cannot be freely chosen. On the contrary, the model reference implementation presented in [100]-[102] is probably the most accurate approach, which theoretically allows exactly designing the frequency behaviour of the reproduced impedance. This, however, noticeably increases control complexity, and a proper choice of the weighting function is not straightforward, especially due to the limitations introduced by the control sampling time.

2.4.4 Virtual Oscillator Control (VOC)

Among the GFM implementations proposed in the literature, the concept of Virtual Oscillator Controls (VOCs) has gained wider interest within the research community in the last years. Based on a different working priciple compared to the other synchronization strategies already examined in this section, this is discussed separately hereafter. However, analogies

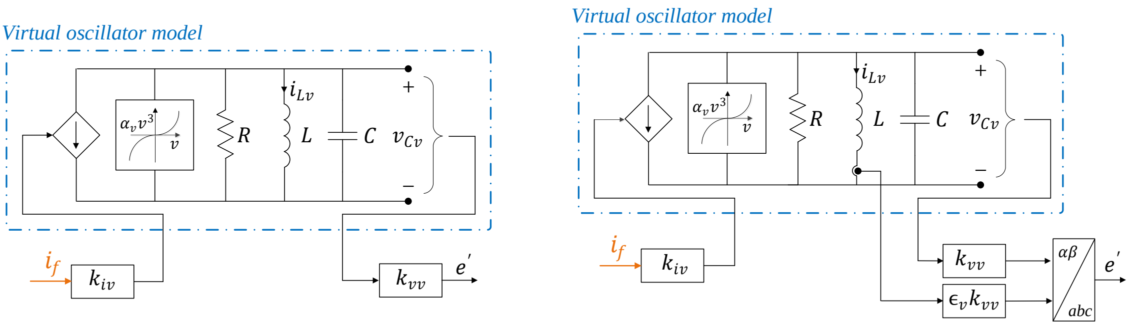

(a) (b)

Figure 2.29: (a) VOC based on a Van der Pol oscillator for a single-phase converter [104], [105], (b) VOC based on a Van der Pol oscillator for a three-phase converter [106].

to the structures previously examined are highlighted in the following, so that its implementation can still be subordinated to the generalized structure presented in Fig. 2.14.

A VOC is a nonlinear controller, which makes the converter reproducing the dynamic of a weakly nonlinear limit-cycle oscillator. One of the most appealing properties of this approach, is that it allows converters to synchronize with each other starting from an arbitrary initial conditions, without the need for any communication means. In the context of microgrids, an implementation for a single-phase converter has been presented in [104], and [105]. Its structure is shown in Fig. 2.29 (a), and is succinctly described in the following.

The employed oscillator model is the so-called *Van der Pol oscillator*, whose equations for the inductor current i_{Lv} and the capacitor voltage v_{Cv} are reported below [104]:

$$\begin{cases} L\frac{di_{Lv}}{dt} = v_{Cv} \\ C\frac{dv_{Cv}}{dt} = \sigma_v v_{Cv} - \alpha_v v_{Cv}^3 - i_{Lv} - k_{iv} i_f \end{cases} \tag{2.36}$$

where the value of the resistance shown in the figure is $R = -{}^{1}/_{\sigma_v}$, while k_{vv} and k_{iv} represent scaling factors for voltage and current, respectively. The modulation signal e' is directly calculated from the output capacitor voltage v_{Cv} properly scaled by a factor k_{vv}. Thus, adopting the notation of Fig. 2.14, the following can be written [106]:

$$e' = k_{vv} v_{Cv}(t) = E_p \cos(\theta) = E_p \cos(\omega_{ref} t + \Delta\theta) \tag{2.37}$$

Defining the following quantities:

$$\varepsilon_v := \sqrt{\frac{L}{C}}; \quad \beta_v := \frac{3\alpha_v}{k_{vv}^2 \sigma_v}; \quad g(y) := y - \frac{\beta_v}{3} y^3; \quad \omega_{ref} := \frac{1}{\sqrt{LC}}; \tag{2.38}$$

the oscillator dynamic is described by the equations reported below:

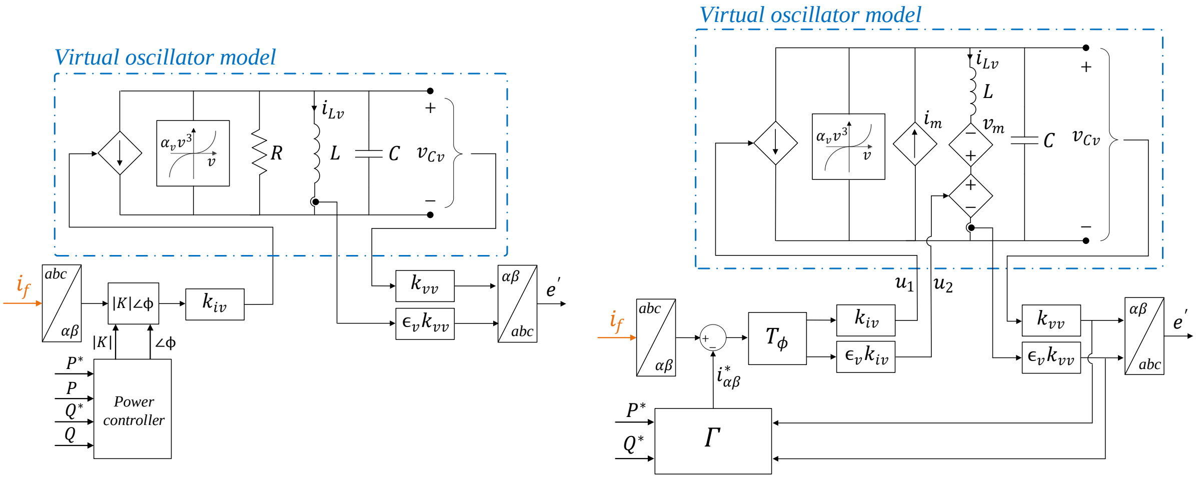

(a) (b)

Figure 2.30: (a) VOC based on a Van der Pol oscillator with regulation of active and reactive power [109], (b) VOC based on an Andronov-Hopf oscillator with regulation of active and reactive power [110].

$$\begin{cases} \dot{E}_p = \omega_{ref}\varepsilon_v\Big(\sigma_v\, g\big(E_p cos(\omega_{ref}t+\Delta\theta)\big)-k_{vv}k_{iv}i_f\Big)cos(\omega_{ref}t+\Delta\theta) \\ \dot{\Delta\theta} = -\frac{\omega_{ref}\varepsilon_v}{E_p}\Big(\sigma_v\, g\big(E_p cos(\omega_{ref}t+\Delta\theta)\big)-k_{vv}k_{iv}i_f\Big)sin(\omega_{ref}t+\Delta\theta) \end{cases} \tag{2.39}$$

Though it can be demonstrated that by properly choosing control parameters of a VOC, the latter can behave as a classical droop controller [105], one of the expected advantages of a VOC lies on the fact that its working principle is based on instantaneous time-domain signals, rather than phasorial electrical quantities. Thus, superior performances of VOCs compared to classical droop controllers have been claimed. To this extent, the work presented in [106] compares the behaviour of a droop controller and of a VOC for the case of a three-phase converter in a micorgrid application. The considered control scheme is reported in Fig. 2.29 (b), which is basically identical to the scheme reported in Fig. 2.29 (a), with the only difference that the two signals $k_{vv}v_{Cv}$, along with $\varepsilon_v k_{vv} i_{Lv}$ are employed as the $\alpha\beta$ components of the modulation signal e'. The results presented in [106], show a better dynamic behaviour of the VOC compared to a droop control when the frequency regulation range is higher than a defined threshold, however resulting in the opposite trend in case of a small frequency regulation range.

It is worth to notice that the VOC scheme proposed in [104]-[106], does not allow regulation of active and reactive power, being therefore not suitable for grid-connected applications. Thus, modifications to the original VOC based on the Van der Pol oscillator have been presented in [107] and [108], where a dispatchable VOC (dVOC) has been proposed, as well as in [109], where the control of active and reactive power is achieved by means of the control scheme shown in Fig. 2.30 (a). In the latter, a multiplication of the measured converter currents i_f by the complex factor $K = |K|\angle\phi$ allows modifying the magnitude and the phase of the input current of the virtual oscillator. The quantities $|K|$ and ϕ are calculated by means of a power control loop, thus enabling regulation of the converter output power to the given setpoint.

Finally, Fig. 2.30 (b) shows the control scheme proposed in [110], which is based on the *Andronov-Hopf oscillator* described by the following equations [110]:

$$\begin{cases} L\frac{di_{Lv}}{dt} = v_{Cv} + v_m - \varepsilon_v u_2 \\ C\frac{dv_{Cv}}{dt} = -i_{Lv} + i_m - u_1 \end{cases} \tag{2.40}$$

where v_m and i_m are:

$$\begin{cases} v_m = \frac{\xi}{\omega_{ref}}\left(2\left(\frac{V_{ref}}{k_{vv}}\right)^2 - \|x\|^2\right)\varepsilon_v i_{Lv} \\ i_m = \frac{\xi}{\varepsilon_v \omega_{ref}}\left(2\left(\frac{V_{ref}}{k_{vv}}\right)^2 - \|x\|^2\right) v_{Cv} \end{cases} \tag{2.41}$$

In (2.41), V_{ref} is indicated in terms of its RMS value, ξ is a constant affecting the convergence speed to steady-state, and $\|x\|$ represents the euclidean norm of the state vector $x = [v_{Cv} \ \varepsilon_v i_{Lv}]^T$. The dynamic of the output voltage vector $v_{\alpha\beta} = k_{vv}[v_{Cv} \ \varepsilon_v i_{Lv}]$ is given by:

$$\begin{bmatrix} \dot{v}_\alpha \\ \dot{v}_\beta \end{bmatrix} = \begin{bmatrix} \frac{\xi}{k_{vv}^2}(2V_{ref}^2 - \|v_{\alpha\beta}\|) & -\omega_{ref} \\ \omega_{ref} & \frac{\xi}{k_{vv}^2}(2V_{ref}^2 - \|v_{\alpha\beta}\|) \end{bmatrix} \begin{bmatrix} v_\alpha \\ v_\beta \end{bmatrix} - \frac{k_{vv}k_{iv}}{C}\begin{bmatrix} \mathbf{T}_\phi \end{bmatrix} \begin{bmatrix} i_\alpha - i_\alpha^* \\ i_\beta - i_\beta^* \end{bmatrix} \tag{2.42}$$

where:

$$\begin{bmatrix} \mathbf{T}_\phi \end{bmatrix} = \begin{bmatrix} cos(\phi) & -sin(\phi) \\ sin(\phi) & cos(\phi) \end{bmatrix} \tag{2.43}$$

and, similarly as in [109], ϕ represents a parameter producing a phase shift of the input signals in order to affect active and reactive power injection. The current setpoints i_α^* and i_β^* are instead calculated as follows:

$$\begin{bmatrix} i_\alpha^* \\ i_\beta^* \end{bmatrix} = \begin{bmatrix} \mathbf{\Gamma} \end{bmatrix} \begin{bmatrix} P^* \\ Q^* \end{bmatrix} = \frac{2}{3\|v_{\alpha\beta}\|^2} \begin{bmatrix} v_\alpha & v_\beta \\ v_\beta & -v_\alpha \end{bmatrix} \begin{bmatrix} P^* \\ Q^* \end{bmatrix} \tag{2.44}$$

According to this implementation, and considering the notation adopted in (2.39), the dynamical model for E_p and the phase angle $\Delta\theta$ results:

$$\begin{cases} \dot{E}_p = \frac{\xi}{k_{vv}^2} E_p\left(2V_{ref}^2 - E_p^2\right) - \frac{k_{vv}k_{iv}}{3C}\frac{2}{E_p}\left[sin(\phi)(Q - Q^*) + cos(\phi)(P - P^*)\right] \\ \Delta\dot{\theta} = -\frac{k_{vv}k_{iv}}{3C}\frac{2}{E_p^2}\left[sin(\phi)(P - P^*) + cos(\phi)(Q - Q^*)\right] \end{cases} \tag{2.45}$$

revealing that the choice of the parameter ϕ can affect the relation between P and Q versus ω and E_p.

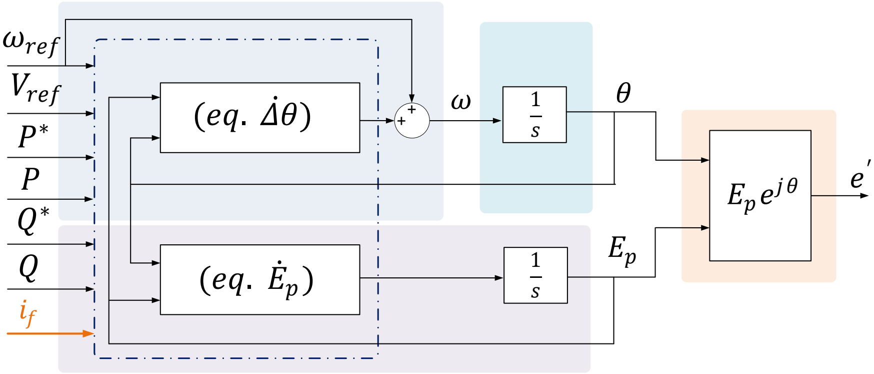

Figure 2.31: General structure of a VOC compliant with the general GFM structure of Fig. 2.14.

Without loss of generality, the control structure of a VOC can be mapped in the general GFM structure presented in Fig. 2.14, according to the scheme reported in Fig. 2.31. In fact, independently on the considered VOC implementation among those previously examined, the equations of the VOC are represented by a set of two non-linear differential equations for E_p and $\Delta\theta$, both for the Van der Pol-type oscillator investigated in [104]-[106] (eq. (2.39)), as well as for the Andronov-Hopf-based structure issued in [110] (eq. (2.45)).

2.5 Summary of the chapter

This chapter has discussed the operating principles of power electronics-based converters, and a classification according to their control strategies has been presented. The definitions provided in the literature, and elaborated in the context of microgrids in order to classify the converters according to their operation, have been first introduced, along with example control schemes showing their typical structures. Since the focus of this thesis is not specifically related to microgrid applications, but rather on wide interconnected power electronics-dominated power systems, the limitations of these definitions in serving as a general classification for converters independently on the examined application, have been highlighted. Hence, the characteristics of converters belonging to the two categories indicated as GFL and GFM have been refined, analyzing their features and their behaviour under different operating conditions.

In this scenario, the concept of VSMs has been introduced, and the main characteristics of these converters have been identified according to the indications provided by the British SO NGESO. It has been pointed out that the terms *VSM* and *GFM converter* have been often used as synonyms in the literature, creating confusion about the real meanings of the two. Hence, by examining in detail the characteristics of these two types of converters, it has been emphasized that VSMs only represent particular implementations of GFM converters. Indeed, in addition to the outlined basic requirements of GFM converters, VSMs can reproduce, to some extents, specific characteristics of real SMs, namely the inertial behaviour and the synchronization principle. In this regard, particular emphasis has been given to the synchronization principle of power electronics-based grid-connected converters, distinguishing between two main approaches: the first one is the use of a dedicated unit typical of a GFL unit, while the second one is the synchronization by means of active power transfer intrinsic in the behaviour of a real SM, and known in the literature as *power-synchronization* principle. Hence, these two approaches have been examined in detail, highlighting the conceptual differences among them.

Finally, according to the identified characteristics of GFM converters, a generalized structure has been presented. This work has been carried out in combination with a comprehensive overview on the most relevant GFM implementations that have been proposed in the literature, by identifying the main subsystems composing the common structure of a GFM converter. Inputs and outputs of each subsystem are then outlined, and possible solutions for the implementation of each of the identified subsystem have been discussed according to the performed literature overview. Similarities among the proposed solutions, along with advantages and drawbacks of the examined structures have been highlighted.

3 Approaches for stability analysis

This chapter introduces the concept of stability of a dynamic system, and provides an overview of the techniques commonly adopted in the literature, for assessing stability of grid-connected converters. These include frequency-domain approaches, such as the impedance-based analysis, and time-domain approaches, e. g. eigenvalue analysis. The features and the drawbacks of each approach are comprehensively exposed, while their application to practical cases of study is presented in the next chapter.

3.1 Concept of stability

There exist various methods for investigating stability of dynamic systems. Driven by different objectives, techniques have been developed and became well-established approaches within different research communities worldwide. With few exceptions, linear system theory is often preferred over non-linear approaches, both in the power system community, as well as in the power electronics one. Indeed, the real power system is generally a very large, hybrid (discrete-continuous), and non-linear system that, although highly complex, still represents a physical system. Thus, its stability analysis can be performed as for any other dynamic system [24].

Motivating the use of linear system theory, adopted in this work for performing stability analysis of grid-connected converters, is among the objectives of this section. In order to outline the main goal of this thesis, concerning the stability analysis of grid-connected converters in power systems with high-penetration of converter-based generation, in the following, the general definition of stability of a dynamic system is first discussed. This is then shaped for the case of a power systems according to the definition provided in [111], and then profiled for the case of a microgrid [21], where some of the physical effects typical of this type of system reflect the scenario targeted in this work.

3.1.1 Stability of a dynamic system

Before discussing the definition of power system stability, the mathematical concept of stability of a dynamic system is first briefly introduced [112]. This is often referred as Lyapunov's stability, from the name of the Russian mathematician and engineer who laid the foundation of the theory which now carries his name.

Definition (Lyapunov's stability). *Let* $\mathbf{B_R}$ *denote the spherical region (or ball) defined by* $\|x\| < R$ *in state-space, and* S_R *the sphere itself, defined by* $\|x\| = R$*. The equilibrium state* $\mathbf{x} = 0$ *is said to be stable if, for any* $R > 0$*, there exists* $r > 0$*, such that if* $\|x(0)\| < r$*, then* $\|x(t)\| < R$*, for all* $t > 0$*. Otherwise, the equilibrium point is unstable.*

This indicates that the origin is defined stable if, given that we want to maintain the state trajectory $x(t)$ within the ball of arbitrarily specified radius $\mathbf{B_R}$, a value $r(R)$ can be found,

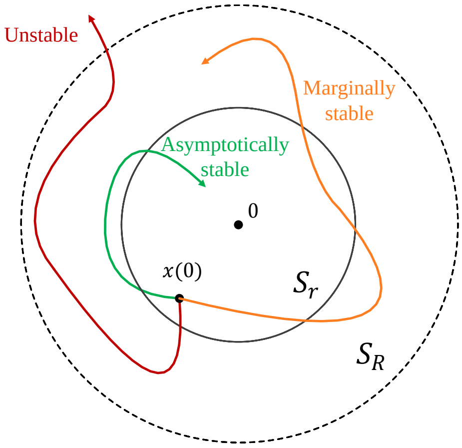

Figure 3.1: Graphical interpretation of Lyapunov 's stability.

such that starting the state from within the ball $\mathbf{B_r}$ at time 0 guarantees that the state will stay within the ball $\mathbf{B_R}$ thereafter. A particular condition of stability is the *asymptotic stability* defined below [112].

Definition (Asymptotic stability). *An equilibrium point 0 is asymptotically stable if it is stable, and if in addition there exists some* $r > 0$ *such that* $\|x(0)\| < r$ *implies that* $x(t) \to 0$ *as* $t \to \infty$.

The asymptotic stability implies that starting close to the equilibrium point, the system trajectories converge to 0 as the time approaches infinity, and the ball $\mathbf{B_r}$ is defined *domain of attraction*. An equilibrium point that is Lyapunov stable but not asymptotically stable is called *marginally stable*. A graphical interpretation of the introduced stability definitions is reported in Fig. 3.1.

3.1.2 Power system stability

Power system stability is conceptually similar to the stability of any dynamic system. However, a clear classification of power system stability has been debated for decades in various committees worldwide [113], [114], and only recently a definition has been formulated within a task force committee [111], which meets nowadays the consensus of the power system community. This is reported below for simplicity.

Definition (Power system stability). *Power system stability is the ability of an electric power system, for a given initial operating condition, to regain a state of operating equilibrium after being subjected to a physical disturbance, with most system variables bounded so that practically the entire system remains intact.*

According to the definition reported above, the system is considered to be stable if, after a perturbation, a new state of operating equilibrium is reached, or if the system returns to the original operating condition. Thus, this formulation is consistent with the definition of asymptotic stability in the sense of Lyapunov previously discussed. Nevertheless, due to the high complexity of the phenomena taking place in a power system, efforts have been made

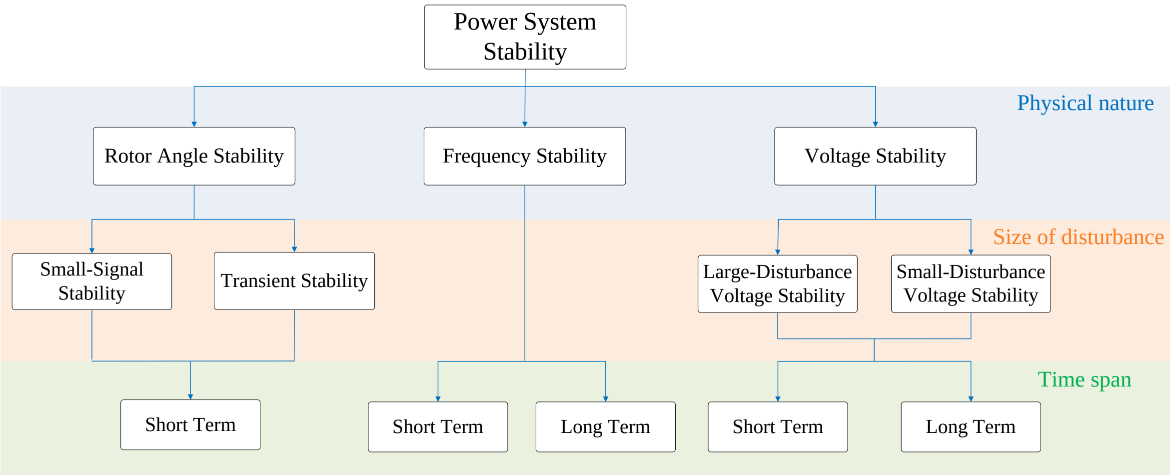

Figure 3.2: Classification of power system stability [111].

in order to classify stability into appropriate categories. These are shown in Fig. 3.2, and succinctly listed below [111]:

- *Rotor angle stability*: represents the ability of SMs of an interconnected power system to remain in synchronism after being subjected to a disturbance.
- *Frequency stability*: is the ability of a power system to maintain steady frequency following a severe system perturbation causing a significant imbalance between generation and load.
- *Voltage stability*: refers to the ability of a power system to maintain steady-state voltage at all buses after being subjected to a disturbance from a given initial operating condition.

Further details can be found in [31] and [111]. However, it is here important to notice, that the stability categories defined above are typical of a classical power system, where the penetration of converter-based generation is rather limited. In fact, increasing the penetration of converter-based operating units, intrinsic differences such as feeder types, high share of RES, converter interfaced components, and low inertia, give rise to the need for revising the definition of stability in such type of systems. A classical example of a system presenting the aforementioned characteristics is represented by a microgrid, whose definition has been already introduced in Section 2.2.1. In the following, the conceptual differences concerning stability in a classical power system and in a microgrid are discussed.

3.1.3 Stability in microgrids

In grid-connected operating conditions, voltage and frequency are mainly imposed by the main grid, limiting the role of microgrids to the provision of ancillary services. Therefore, the problem of stability in a grid-connected microgrid reduces to the stability of individual components such as particular DERs or of a set of loads. Due to the systematic differences between microgrids and conventional power systems, challenges might be of a different type.

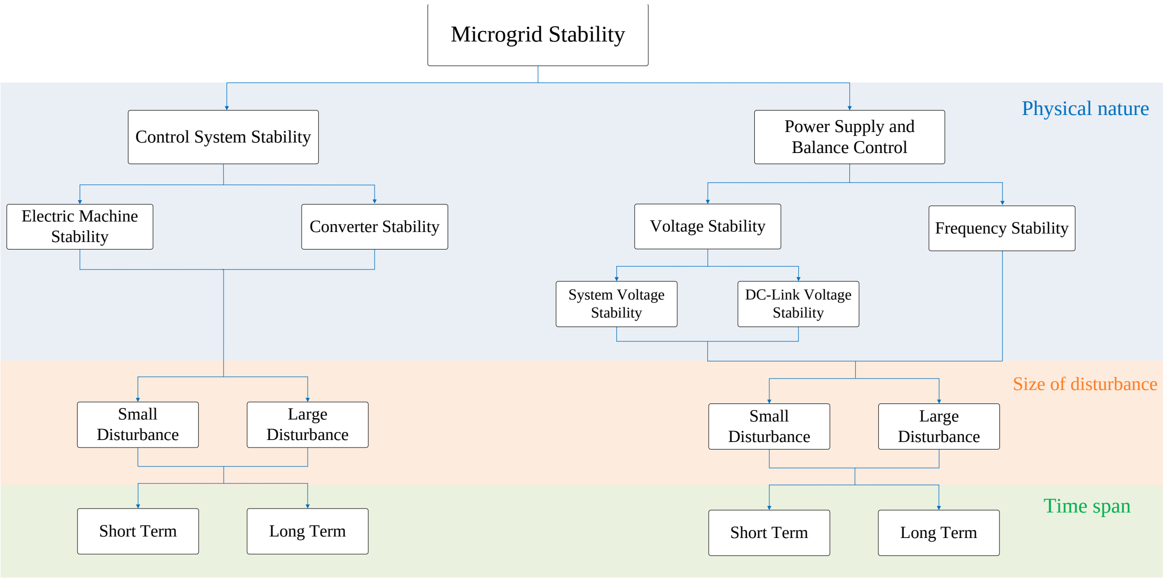

Figure 3.3: Classification of stability in microgrids [21].

For example, frequency stability is more challenging for microgrids due to the low system inertia and high proportion of DERs, compared to the case of a conventional grid, where instead transient and voltage stability are of major concern. Furthermore, due to the low share of generation by means of conventional synchronous plants, inter-area oscillations and angle stability problems are generally not expected in such kind of systems. Another typical aspect of microgrids is the low X/R ration of feeder lines, which contributes to the coupling between voltage and frequency. As a consequence, phenomena like voltage collapse is manifested by fluctuations of all system variables in a microgrid, being therefore difficult classifying phenomena as *voltage instability* or *frequency instability* based solely on measurements of respective variables.

Even though the work presented in this thesis is not necessarily related to microgrids, some of the concepts that have been discussed in the last decades in this context, might become useful for understanding the phenomena of interest for this work. To this extent, the concept of stability in a microgird is first discussed, according to the definition formulated in [21]. This is reported below.

Definition (Stability in microgirds). *Consider a microgrid which is operating in equilibrum, with state variables taking on appropriate steady-state values satisfying operational constraints. Such a microgrid is stable, if after being subjected to a disturbance, all state variables recover to (possibly new) state-space values which satisfy operational constraints, and without the occurrence of involuntary load shedding.*

The definition of stability provided above is consistent with the one of a classical power system [111], and, consequently, with the definition of asymptotic stability in the sense of Lyapunov. However, it can be noted that particular emphasis is given to the phenomena of load shedding, which is common in a classical power system, but it is preferibly avoided in a microgrid. In analogy to the case of a power system, the classification of stability for microgrids reported in [21], is shown in Fig. 3.3. Without going too much into the details, which interested readers can find in the source document, a distinction between phenomena linked with power sharing and balance, and phenomena related to equipment control system is made. To the latter category belongs the so-called *converter stability*. The tuning of converters inner voltage and current control loops are a major concern for the system small-signal stability. In contrast to low-frequency oscillations caused by outer power control loops, interactions between current and voltage control loops may cause high-frequency oscillations in the range of hundred Hz, up to several kHz, a phenomena known as *harmonic instability* [115]. One of the causes of this type of instability is the high-frequency switching of converters triggering the parallel and series resonances of LCL converter filters or of other parasitic components [21]. However, this can be also triggered by the control loops of the converter, or by the interactions between control loops of converters operating nearby [116], [117].

Among the control loops typically responsible for converter instability, the synchronization loop, typically implemented by means of a PLL or similar filter structures, plays certainly an important role [21]. The instability effects caused by PLLs have been thoroughly investigated in recent years by the power electronics community. Indeed, it has been shown in the literature, that PLLs introduce a negative resistive behaviour in the equivalent output impedance of the converter, exciting therefore possible resonances in the system and contributing to system instability [66], [68], [69]. Even though a possible way for mitigating these effects is the reduction of the PLL-bandwidth [118], deteriorating the PLL performances might give rise to other kind of instability issues, e. g. voltage instability [119]. The influence of the synchronization loops on the stability of grid-connected converters represents one of the main objectives of this thesis, and will be thoroughly investigated in the following chapter.

3.1.4 Linear and non-linear systems

Before introducing the different approaches for stability analysis based on linear control theory that will be investigated in this work, the conceptual differences between linear and non-linear systems are briefly discussed in the following.

Linear control theory has been mainly concerned with the study of linear time-invariant (LTI) control systems, of the form:

$$\begin{cases} \dot{\mathbf{x}} = \mathbf{A}\,\mathbf{x} + \mathbf{B}\,\mathbf{u} \\ \mathbf{y} = \mathbf{C}\,\mathbf{x} + \mathbf{D}\,\mathbf{u} \end{cases} \tag{3.1}$$

with $\mathbf{x}$ indicating a *vector of states*, $\mathbf{u}$ the *vector of inputs*, and $\mathbf{y}$ the *vector of outputs*, expressed as follows:

$$\mathbf{x} = \begin{bmatrix} x_1 & x_2 & \cdots & x_n \end{bmatrix}^T \quad ; \quad \mathbf{u} = \begin{bmatrix} u_1 & u_2 & \cdots & u_m \end{bmatrix}^T \quad ; \quad \mathbf{y} = \begin{bmatrix} y_1 & y_2 & \cdots & y_r \end{bmatrix}^T \tag{3.2}$$

$\mathbf{A}$ represents the *system matrix* of dimension $n \times n$, $\mathbf{B}$ is the *system input matrix* of dimension $n \times m$, $\mathbf{C}$ is the *system output matrix* of size $r \times n$, and $\mathbf{D}$ is the *feedforward matrix* of size $r \times m$ [31]. LTI systems present interesting properties, constituting the underlying principles behind linear control theory. These are listed below [112]:

- under the assumption that **A** is nonsingular, a linear system has a *unique equilibrium point*.
- Regardless of initial conditions, the equilibrium point is stable if all the eigenvalues of **A** have *negative real parts*.
- The transient response of a linear system is composed of *natural modes*, and the general solution can be solved analytically.
- It satisfies the *superposition principle*, meaning that if the input u_1 produces an output y_1, and an input u_2 produces an output y_2, then the input $u = (u_1 + u_2)$ produces the output $y = (y_1 + y_2)$ (additivity).
- If the input u produces an output y, then the input au with $a \in \mathbb{R}$ produces the output ay (homogeneity).
- A sinusoidal input leads to a sinusoidal output of the *same frequency*.

The behaviour of a non-linear system is much more complex compared to a linear system. The superposition principle does not hold any longer, and analysis tools involve more advanced mathematics. The dynamic of non-linear systems is characterized by so-called "*essential non-linear phenomena*", examples of which are reported below [120]:

- *Multiple isolated equilibria*: A linear system can have only one isolated equilibrium point, whereas a non-linear system can have more than one isolated equilibrium point.
- *Bifurcations*: by varying system parameters, the stability of the equilibrium point can change, and so can the number of equilibrium points.
- *Finite escape time*: contrary to linear systems where unstable states go to infinity as time approaches infinity, a non-linear system state can go to infinity in finite time.
- *Limit cycles*: Non-linear systems can display oscillations of fixed amplitude and fixed period without external excitation. These are called limit cycles, or self-excited oscillations.
- *Chaos*: For a stable linear system, small differences in initial conditions can only cause small differences in the output. On the contrary, a non-linear system might be extremely sensitive to initial conditions, leading to unpredictability of the system output.
- *Subharmonic, harmonic, or almost-periodic oscillations*: A non-linear system under periodic excitation can oscillate with frequencies which are submultiples or multiples of the input frequency.

Considering the aspects listed above, it can be intuitively understood that the analysis of a non-linear system might become quite arduous. In fact, the classical techniques adopted for linear systems, such as time-domain analysis, as well as frequency-domain analysis, are not anymore applicable for non-linear systems, due to the fact that direct solution of non-linear differential equations is generally impossible, and frequency domain transformations do not apply any longer [112]. An universal approach for studying non-linear systems has not been devised, on the contrary many methods for the analysis of non-linear systems have been proposed. These include: Phase plane analysis, Lyapunov's theory, and describing functions analysis. Nevertheless, the methods based on Lyapunov's theory have been widely employed in non-linear control theory, and are briefly discussed in the following. The first method is also indicated as *indirect method*, or generally as the *linearization method*. This draws conclusions about the local stability of a non-linear system around an operating equilibrium point from the stability properties of its linear approximation, and it is briefly explained in the following. Let us consider the non-linear system:

$$\begin{cases} \dot{\mathbf{x}} = \mathbf{f}(\mathbf{x},\mathbf{u}) \\ \mathbf{y} = \mathbf{g}(\mathbf{x},\mathbf{u}) \end{cases} \tag{3.3}$$

where:

$$\mathbf{f} = \begin{bmatrix} f_1 & f_2 & \cdots & f_n \end{bmatrix}^T \qquad ; \qquad \mathbf{g} = \begin{bmatrix} g_1 & g_2 & \cdots & g_r \end{bmatrix}^T \tag{3.4}$$

are vectors of non-linear functions. The linearized system can be obtained by adding a small perturbation to the state-space vector $\mathbf{x}$ and to the input vector $\mathbf{u}$:

$$\mathbf{x} = \mathbf{x_0} + \Delta\mathbf{x} \qquad ; \qquad \mathbf{u} = \mathbf{u_0} + \Delta\mathbf{u} \tag{3.5}$$

where the prefix Δ indicates a a small deviation. The non-linear functions $\mathbf{f}(\mathbf{x},\mathbf{u})$ and $\mathbf{g}(\mathbf{x},\mathbf{u})$ can be approximated by means of Taylor's series expansions around the operating point $(\mathbf{x_0},\mathbf{u_0})$:

$$\dot{x}_i = \dot{x}_{i0} + \Delta\dot{x}_i = f_i(\mathbf{x_0},\mathbf{u_0}) + \frac{\partial f_i}{\partial x_1}\Delta x_1 + \ldots + \frac{\partial f_i}{\partial x_n}\Delta x_n + \frac{\partial f_i}{\partial u_1}\Delta u_1 + \ldots + \frac{\partial f_i}{\partial u_m}\Delta u_m, \tag{3.6}$$

with $i = 1,2,\ldots,n$. In a similar fashion, the output vector can be expressed as:

$$y_j = y_{j0} + \Delta y_j = g_j(\mathbf{x_0},\mathbf{u_0}) + \frac{\partial g_j}{\partial x_1}\Delta x_1 + \ldots + \frac{\partial g_j}{\partial x_n}\Delta x_n + \frac{\partial g_j}{\partial u_1}\Delta u_1 + \ldots + \frac{\partial g_j}{\partial u_m}\Delta u_m, \tag{3.7}$$

with $j = 1,2,\ldots,m$. The linearized system assumes the following form:

$$\begin{cases} \Delta\dot{\mathbf{x}} = \mathbf{A}_j\,\Delta\mathbf{x} + \mathbf{B}_j\,\Delta\mathbf{u} \\ \Delta\mathbf{y} = \mathbf{C}_j\,\Delta\mathbf{x} + \mathbf{D}_j\,\Delta\mathbf{u} \end{cases}, \tag{3.8}$$

where the matrices $\mathbf{A}_j$, $\mathbf{B}_j$, $\mathbf{C}_j$, and $\mathbf{D}$ have the same meaning of the matrices $\mathbf{A}$, $\mathbf{B}$, $\mathbf{C}$, and $\mathbf{D}$ defined in (3.1), and are obtained by means of the partial derivatives:

$$\mathbf{A}_j = \begin{bmatrix} \frac{\partial f_1}{\partial x_1} & \cdots & \frac{\partial f_1}{\partial x_n} \\ \vdots & \ddots & \vdots \\ \frac{\partial f_n}{\partial x_1} & \cdots & \frac{\partial f_n}{\partial x_n} \end{bmatrix} ; \mathbf{B}_j = \begin{bmatrix} \frac{\partial f_1}{\partial u_1} & \cdots & \frac{\partial f_1}{\partial u_m} \\ \vdots & \ddots & \vdots \\ \frac{\partial f_n}{\partial u_1} & \cdots & \frac{\partial f_n}{\partial u_m} \end{bmatrix} ; \mathbf{C}_j = \begin{bmatrix} \frac{\partial g_1}{\partial x_1} & \cdots & \frac{\partial g_1}{\partial x_n} \\ \vdots & \ddots & \vdots \\ \frac{\partial g_r}{\partial x_1} & \cdots & \frac{\partial g_r}{\partial x_n} \end{bmatrix} ; \mathbf{D}_j = \begin{bmatrix} \frac{\partial g_1}{\partial u_1} & \cdots & \frac{\partial g_1}{\partial u_m} \\ \vdots & \ddots & \vdots \\ \frac{\partial g_r}{\partial u_1} & \cdots & \frac{\partial g_r}{\partial u_m} \end{bmatrix} ; \tag{3.9}$$

The matrix $\mathbf{A}_j$ is the so-called *Jacobian matrix*, and the relationship between the linearized system and the original non-linear system is stated by the following theorem [31], [112].

Theorem 1 (Lyapunov's linearization method)**.**

- *If the linearized system is strictly stable (i.e., if all eigenvalues of* $\mathbf{A}_j$ *are strictly in the left-half complex plane), then the equilibrium point is asymptotically stable (for the actual non-linear system).*
- *If the linearized system is unstable (i.e., if at least one eigenvalue of* $\mathbf{A}_j$ *is strictly on the right-half complex plane), then the equilibrium point is unstable (for the non-linear system).*
- *If the linearized system is marginally stable (i.e., all eigenvalues of* $\mathbf{A}_j$ *are in the left-half complex plane but at least one of them is on the imaginary axis), then one cannot conclude anything from the linear approximation on the stability of the actual non-linear system (the equilibrium point might be stable, asymptotically stable, or unstable for the non-linear system).*

The proof of this important theorem can be found in [120]. Since any real system is actually non-linear, whether in a small range operation it should be regarded as non-linear or linear strongly depends on the magnitude of the non-linearities affecting the system itself. To this extent, the validity of small-signal stability analysis has been often questioned within the power system community, as well as in the power electronics one, debating the reliability of the results obtained by means of linear control approaches. Nevertheless, small-signal stability represents a necessary condition, in the sense that if the linearized system is not stable, neither will be the original non-linear system. It is therefore worth to emphasize that Lyapunov's linearization theorem is nowadays recognized as the theoretical justification of linear control theory [112].

The second method is called the *direct method*, and represents a generalization of the energy concept associated with a mechanical system. This can be intuitively understood by considering that the motion of a mechanical system is stable if its total mechanical energy decreases at all time, and is based on the following theorem.

Theorem 2 (Lyapunov's stability theorem)**.** *Let* $x = 0$ *be an equilibrium point for the autonomous system*

$$\dot{x} = f(x) \tag{3.10}$$

where $f : D \rightarrow \mathbb{R}^n$ *is a locally Lipschitz map from a domain* $D \subset \mathbb{R}^n$ *into* $\mathbb{R}^n$ *containing* $x = 0$. *Let* $V : D \rightarrow \mathbb{R}$ *be a continuously differentiable function, such that*

$$V(0) = 0 \quad \text{and} \quad V(x) > 0 \ \text{in} \ D - \{0\} \tag{3.11}$$

$$\dot{V}(x) \leq 0 \ \text{in} \ D \tag{3.12}$$

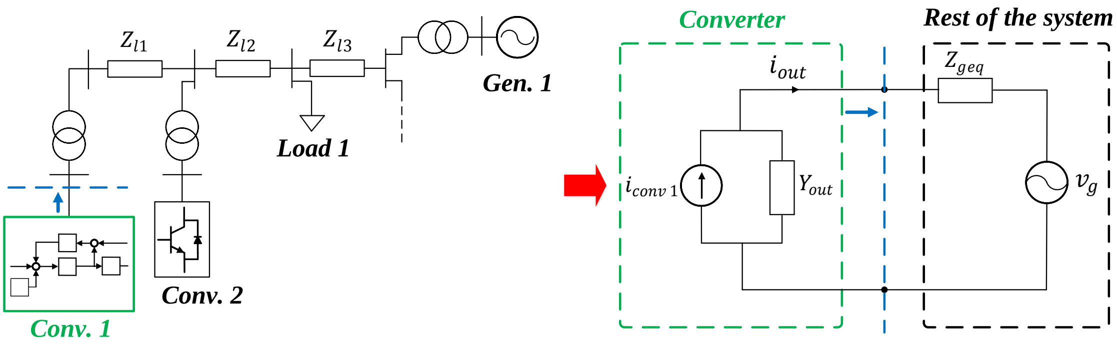

Figure 3.4: Equivalent system representation for impedance-based analysis.

then x = 0 is stable. Moreover, if

$$\dot{V}(x) < 0 \ \ in \ \ D - \{0\} \tag{3.13}$$

then x = 0 is asymptotically stable.

The proof of the theorem is omitted here, but it can be found in [120]. The method is extremely elegant from a mathematical perspective, and can be generally applied to any kind of control systems. However, it lacks from a general way for obtaining the scalar energy-like function (or Lyapunov's function) for the system, which needs to be searched by means of intuition, experience and physical insight [112]. Furthermore, Lyapunov's theorem represents only a sufficient condition for stability, meaning that if the chosen Lyapunov's function candidate does not meet the conditions stated by the theorem, no conclusions can be drawn on system stability, but only that a different candidate function should be tried.

3.2 Impedance-based analysis

Originally introduced for DC-DC converter applications by Middlebrook [121], the frequency-domain approach called impedance-based analysis has been extensively used in recent years within the power electronics community for studying stability of grid connected converters [116], [117], [122]-[124]. It allows assessing locally the stability of a grid-connected converter by applying the Nyquist stability criterion to the ratio between the equivalent output admittance of the converter Y_{out} and the equivalent grid admittance calculated at the converter terminals Y_{geq}. The principle behind the impedance-based stability criterion applied to grid-connected converters is extremely simple and intuitive, and it consists of representing the system in a hybrid form, replacing the converter by means of a Norton equivalent, while the rest of the system by using a Thévenin equivalent representation. This concept is graphically explained in Fig. 3.4, where the equivalent output admittance of the converter not only accounts for the converter hardware components, e. g. the output converter filter, but also models the frequency behaviour of the control [68]. Similarly, the equivalent grid impedance calculated at the converter terminals describes the frequency behaviour of the whole grid, as the sum of the single contributions of the components composing it.

Assuming known the frequency behaviour of the equivalent output admittance Y_{out}, and the one of the equivalent grid impedance Z_{geq}, the expression of the output current of Converter 1, indicated with i_{out} in Fig. 3.4, is given below [122]:

$$i_{out}(s) = H(s)[i_{conv1}(s) - Y_{out}(s)v_g(s)] \tag{3.14}$$

where:

$$H(s) = \frac{1}{1 + Z_{geq}(s)Y_{out}(s)} \tag{3.15}$$

The impedance-based approach is based on the observation that $H(s)$ resembles the closed-loop transfer function of a negative feedback control system, where the forward gain is unity, and the feedback gain is the so-called *return ratio* $L(s) = Z_{geq}(s)Y_{out}(s)$. Stability can be assessed either by calculating the eigenvalues of $H(s)$, or by applying the Nyquist criterion to the return ratio. In order to perform linearization of the system equations, formulations in dq (or equivalently in $\alpha\beta$ coordinates) are commonly adopted [56], while further approaches involving decomposition in positive and negative sequence components have been also proposed in the literature [69]. Nevertheless, recent works have presented an unified formulation for the calculation of the converter output admittance [125], [126] showing the equivalence between the two approaches. Either way, the transfer functions $\mathbf{Y}_{out}(s)$ and $\mathbf{Z}_{geq}(s)$ are represented by 2×2 transfer function matrices, which under particular conditions become symmetric and diagonal, and the system can be analyzed by means of single-input single-output (SISO) transfer functions. However, this is not a general statement, and the occurrence of cross-coupling effects resulting from unsymmetric matrices [68], [127], gives rise to the necessity for a multiple-input multiple-output (MIMO) formulation of the problem, hence involving multivariable analysis. This is for example the case when the effects of the synchronization loop of a grid-connected converter, usually implemented by means of a PLL, are included in the analysis, an aspect that will be further investigated in the next chapter. In case of a MIMO system, the generalization of the Nyquist theorem for SISO systems, the so-called Generalized Nyquist Criterion (GNC) [128]-[130], can be adopted to the return ratio in order to assess converter stability. The theorem is reported below for simplicity.

Theorem 3 (Generalized Nyquist Criterion)**.** *Let P_{ol} denote the number of open-loop unstable poles in $\mathbf{L}(s)$. The closed-loop system with loop transfer function $\mathbf{L}(s)$ and negative feedback is stable if and only if the characteristic loci of the loop transfer function, taken together, encircle the point (-1, j0) P_{ol} times anticlockwise, assuming that there are no hidden unstable modes.*

The proof of the theorem is omitted here, but it can be found in [129]. The GNC represents a necessary and sufficient condition for stability and, differently from the Nyquist criterion for scalar transfer functions, it requires the calculation of the eigenvalues (characteristic loci) $\lambda_i(\mathbf{L}(j\omega))$ of the loop transfer function. However, due to the limitations of eigenvalues in providing an useful measure of gain for MIMO systems [103], the applictaion of the theorem does not provide indications about stability margin in the same way as for a SISO system.

The most appealing aspect of the impedance-based approach is represented by its black-box nature. Indeed, the grid impedance can be estimated by means of suitable measurement systems without any prior knowledge of the grid configuration, or of the types of loads and generating units connected to the system [131], [132]. To this extent, methods have been proposed in the literature, in order to obtain the frequency behaviour of the grid impedance at the connection point, by performing signal injection at different frequencies, and reconstructing the estimated grid impedance by means of identification techniques for linear systems, e. g. the vector fitting approach [133], [134]. On the other hand, beside the aforementioned limitation of the GNC in calculating a stability margin for the system, one of the main limitations of the impedance-based approach is represented by the fact that it only allows assessing stability locally at the connection point of the converter, and it does not provide any information about the influence of parameters on the obtained results. However, a possible way for overcoming this drawback, might be represented by performing a wide amount of simulations, while varying parameters of interest within defined intervals. This represents the underlying principle behind the Monte-Carlo (MC) analysis briefly introduced in the following.

3.2.1 Monte-Carlo analysis

MC methods are probabilistic approaches based on simulations, representing an efficient solution for sensitivity assessment. They allow exploring the behaviour of a system for a broad range of possible scenarios, and are particularly suitable for investigating interactions between system variables, which cannot be easily assessed analytically. The MC analysis has been extensively used in the literature for various purposes, both by the power electronics community, e. g. for predicting the lifetime of power electronics devices [135]-[138], as well as by the power system community, in order to assess operational risks [139]. The underlying principle of the MC analysis is represented by the central limit theorem [139]. This states that, in some cases, adding independent random values not normally distributed, their normalized sum tends toward a normal distribution. Thus, the idea is to create a series of experimental samples using a random sequence number and, assuming a sufficiently large amount of samples, the mean of the sum of the obtained simulation results represents an estimate of the mathematical expectation.

Generating random samples is a key step in MC analysis, along with defining proper distributions of the random values adopted for representing the event of interest. The Cumulative Distribution Function (CDF) $F(x)$ indicates the probability of the random variable X being not larger than a real number x. This can be mathematically expressed as:

$$F(x) = \int_{-\infty}^{x} f(x)dx \tag{3.16}$$

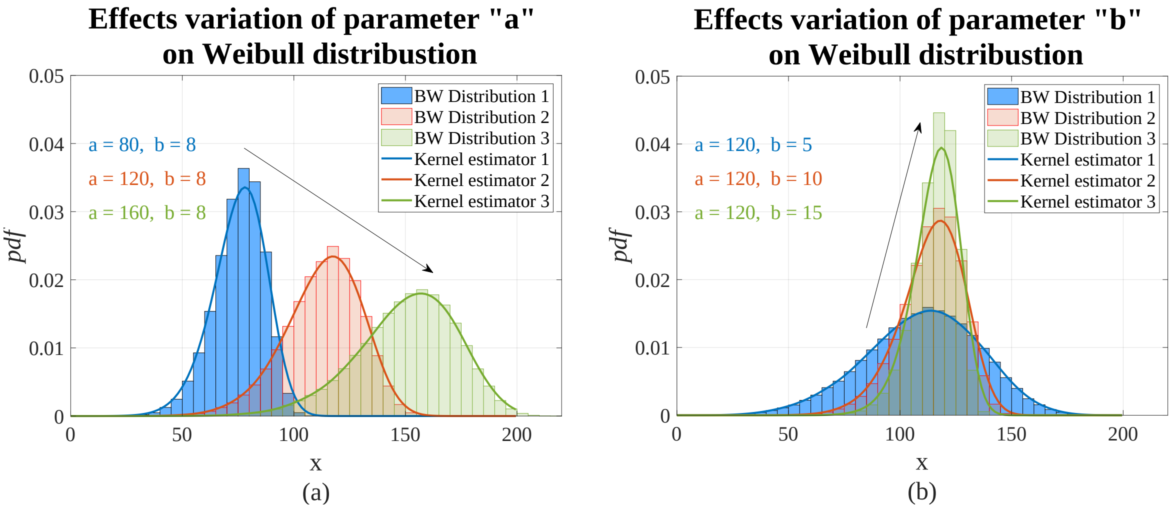

Figure 3.5: Effects of parameter variations on a Weibull distribution: (a) variation of parameter a maintaining b constant, (b) variation of parameter b maintaining a constant.

where $f(x)$ is the probability density function (pdf). In probability theory and statistics, the following pdfs are widely adopted: Exponential distribution, Normal (or Gaussian) distribution, Log-Normal distribution, Weibull distribution, Gamma distribution, and Beta distribution [139]. Among them, the Weibull distribution is largely used in many application fields. Indeed, this is very versatile and, compared to a standard normal distribution, data are not necessarily symmetrically distributed around the mean value. Its pdf is defined below:

$$f_W(x) = \frac{b}{a}\left(\frac{x}{a}\right)^{b-1} e^{-\left(\frac{x}{a}\right)^b} \quad (0 \leq x < \infty\,;\; a,b > 0) \tag{3.17}$$

where a is the so-called *scale parameter*, while b is the *shape parameter*. The first one has the effect of shifting the mean value of the distribution, while the latter tends to stretch out the pdf. Examples of the effects of these two parameters on a Weibull distribution are reported in Fig. 3.5, where the area of each bar is the relative number of observation, and the sum of the bar areas is ≤ 1. The continuous lines in the figures, are the *kernel density estimators*, representing non-parametric fitting curves of the resulting sample data, that become particularly useful in order to avoid errors caused by the mismatch between an assumption of theoretical distribution, and actual behaviour of sample data. The expression of a Kernel estimator is reported below [139]:

$$\hat{f}(x) = \frac{1}{nh}\sum_{i=1}^{n} K\left(\frac{x - x_i}{h}\right) \tag{3.18}$$

where x_i, with $i = [1, 2, \cdots, n]$, are random samples from the unknown distribution, n is the sample size , $K(\cdot)$ is the *kernel smoothing function* and h is the bandwidth. The introduced concepts will become useful for understanding the practical applications of the MC analysis presented in the next chapter.

3.3 Eigenvalue analysis

The impedance-based approach assesses locally the stability of a converter at the connection point. Nevertheless, for power system studies, where the holistic view of the system is of interest, eigenvalue analysis is often preferred [31]. In contrast to the impedance-based approach discussed in the previous subsection, eigenvalue analysis allows determining dominant system modes, and by means of modal analysis, the system states mainly affecting the relevant modes can be identified. These concepts are introduced in the following.

3.3.1 Eigenvalues and eigenvectors

The concept of eigenvalue of a $n \times n$ matrix $\mathbf{A}$ is introduced below [140].

Definition (Eigenvalue). *Let* $\mathbf{A} \in \mathbb{C}^{n \times n}$*, then the eigenvalues of* $\mathbf{A}$ *are the n roots of its characteristic polynomial* $p(\lambda) = det\,(\lambda I - A)$.

Eigenvalues may be real or complex and, if $\mathbf{A}$ is real, complex eigenvalues always occur in conjugate pairs. For any eigenvalue of the matrix $\mathbf{A}$ λ_i, the two $n-$column vectors $\boldsymbol{\Phi_i}$ and $\boldsymbol{\Psi_i}$ satisfying the following conditions:

$$\mathbf{A}\boldsymbol{\Phi}_i = \lambda_i\boldsymbol{\Phi}_i \qquad ; \qquad \boldsymbol{\Psi}_i\mathbf{A} = \lambda_i\boldsymbol{\Psi}_i \tag{3.19}$$

with $i = 1, 2, ..., n$; are respectively called *right* and *left eigenvectors*. These are of the form:

$$\boldsymbol{\Phi}_\mathrm{i} = \begin{bmatrix}\phi_{1i} & \phi_{2i} & \cdots & \phi_{ni}\end{bmatrix}^T \qquad ; \qquad \boldsymbol{\Psi}_i = \begin{bmatrix}\psi_{1i} & \psi_{2i} & \cdots & \psi_{ni}\end{bmatrix}^T \tag{3.20}$$

Left and right eigenvectors corresponding to different eigenvalues are orthogonal, hence [31]:

$$\boldsymbol{\Psi}_j\boldsymbol{\Phi}_i = 0 \tag{3.21}$$

for $i \neq j$, otherwise:

$$\boldsymbol{\Psi}_i\boldsymbol{\Phi}_i = \mathbf{C_i} \tag{3.22}$$

with $\mathbf{C_i}$ a non-zero constant. Due to the fact that eigenvectors are determined only with a scalar multiplier, the normalized notation for the eigenvectors is normally preferred, and therefore:

$$\boldsymbol{\Psi}_i\boldsymbol{\Phi}_i = 1 \tag{3.23}$$

Eigenvalues are sometimes called *characteristic gains*. The set of eigenvalues of $\mathbf{A}$ is called the *spectrum* of $\mathbf{A}$, while the largest of the absolute values of the eigenvalues of $\mathbf{A}$ is called *spectral radius*, defined as [140], [141]:

$$\rho(\mathbf{A}) \triangleq max_i|\lambda_i(\mathbf{A})| \tag{3.24}$$

Eigenvalue analysis is one of the most common ways for assessing closed-loop stability in linear control theory. Considering the linear system reported in (3.1), the system is stable *if and only if* all the closed-loop poles are in the open left-half plane (LHP). The poles are also equal to the eigenvalues of the state-space matrix **A**, and their calculation represents the common way for calculating the poles of the closed-loop system [103].

Let us consider the linearized system of eq. (3.8) (where $\mathbf{A}_j$ is indicated with **A** for simplicity), and assume that the input of the system is a zero vector (free motion condition), thus:

$$\Delta\dot{\mathbf{x}} = \mathbf{A}\ \Delta\mathbf{x} \tag{3.25}$$

The motion of the system can be decomposed in a linear combination of n dynamic modes, corresponding to the n eigenvalues of the state matrix **A**. Let us define the following matrix:

$$\mathbf{\Phi} = \begin{bmatrix}\mathbf{\Phi}_1 & \mathbf{\Phi}_2 & \cdots & \mathbf{\Phi}_n\end{bmatrix} = \begin{bmatrix}\phi_{11} & \dots & \phi_{1n} \\ \vdots & \ddots & \vdots \\ \phi_{n1} & \dots & \phi_{nn}\end{bmatrix} \tag{3.26}$$

It can be demonstrated that the time response of the i-th state variable is given by [31]:

$$\Delta x_i(t) = \phi_{i1}c_1e^{\lambda_1 t} + \phi_{i2}c_2e^{\lambda_2 t} + \cdots + \phi_{in}c_ne^{\lambda_n t} \tag{3.27}$$

where:

$$c_i = \mathbf{\Psi}_i\Delta\mathbf{x}(0) \tag{3.28}$$

is a scalar product representing the magnitude of the excitation of the i-th mode related to the initial condition. Eq. (3.27) reveals that the response of the system is obtained as the sum of n separated responses, indicated as *dynamic modes*, and each of the independent responses decays with a time constant related to the corresponding eigenvalue λ_i. The following considerations can be drawn:

- A *real eigenvalue* corresponds to a non-oscillatory mode.
  - A negative real eigenvalue corresponds to a decaying mode, whose decaying time is inversely proportional to the magnitude of the eigenvalue.
  - A positive real eigenvalue corresponds to an aperiodic unstable mode.

- *Complex eigenvalues* occur in conjugate pairs and correspond to oscillatory modes. Representing the complex conjugate eigenvalues with the following notation:

  $$\lambda_{1,2} = \sigma \pm j\omega \tag{3.29}$$

  the frequency of oscillation in Hz is:

  $$f = \frac{\omega}{2\pi} \tag{3.30}$$

  while the following quantity:

  $$\zeta = -\frac{\sigma}{\sqrt{\sigma^2 + \omega^2}} \tag{3.31}$$

  is normally indicated as *damping ratio*, and represents the decay rate of the oscillatory mode. Hence, the time constant of the amplitude decay can be calculated as:

  $$\tau = \frac{1}{|\sigma|} \tag{3.32}$$

  Finally, a negative value of ζ corresponds to an unstable undamped oscillatory mode, which is the case of a pair of complex eigenvalues with positive real part.

3.3.2 Modal analysis

As indicated in eq. (3.27), each state can be expressed as a linear combination of system modes. However, this relation can be observed from a more interesting perspective for the purpose of the analysis, and namely that each mode is affected by a combination of system states. This gives rise to the need for eliminating the cross-coupling between the states, in order to assess to which extent each of the modes of interest is affected by a specific state. This process is known as *modal analysis* [142], and it has been extensively used in the power system community since decades [31]. In fact, in a complex multivariable system, which might be the case of a large power system, modal analysis can provide indications about the influence of each component, or each generator on the damping of system modes, especially on the critical ones [143]. Here a distinction between *dominant modes* and *critical modes* is needed. Indeed, dominant modes are those mainly affecting the dynamic of the system, and therefore those eigenvalues whose real part is closer to the imaginary axis, whereas the critical modes are poorly damped eigenvalues, which under particular conditions might lead to system instability [144].

Let use define a state vector **z**, related to the state vector $\Delta\mathbf{x}$ through the following relation:

$$\Delta\mathbf{x} = \mathbf{\Phi}\mathbf{z} \tag{3.33}$$

where $\mathbf{\Phi}$ has been already introduced in (3.26). By substituting (3.33) in (3.25), the following can be written:

$$\dot{\mathbf{z}} = \mathbf{\Phi}^{-1}\mathbf{A}\,\mathbf{\Phi}\mathbf{z} = \mathbf{\Lambda}\mathbf{z} \tag{3.34}$$

where:

$$\mathbf{\Lambda} = diag\{\lambda_1, \lambda_2, \cdots, \lambda_n\} \tag{3.35}$$

The result of this transformation is that uncoupled state equations have been obtained, thus each of the variables $z_1, z_2, \cdots, z_n$ is associated only with a single mode. By considering the normalization (3.23), (3.33) can be written as:

$$\mathbf{z} = \mathbf{\Psi}\Delta\mathbf{x} \tag{3.36}$$

where:

$$\mathbf{\Psi} = \begin{bmatrix} \mathbf{\Psi}_1^T & \mathbf{\Psi}_2^T & \cdots & \mathbf{\Psi}_n^T \end{bmatrix}^T \tag{3.37}$$

Eq. (3.33) and (3.36) lead to the following conclusions:

- The *right eigenvector matrix* $\mathbf{\Phi}$ is known as *mode shape matrix* and describes the activity of the state variable when a particular mode is excited. More precisely, ϕ_{ki} measures the activity of the k-th state variable on the i-th mode.
- The *left eigenvector matrix* $\mathbf{\Psi}$ identifies the combination of original state variables that are present in the i-th mode. In the specific, ψ_{ik} indicates the weighted contribution of the k-th state variable to the i-th mode.

It is worth to notice that the elements of the aforementioned matrices are unit dependent, since directly related to the state variables, and therefore impossible to compare. In order to overcome this issue, the *participation factors* have been introduced [142]. These are calculated by multiplying right and left eigenvectors, obtaining dimensionless quantities associating state variables and system modes. The *participation matrix* **P** is defined as [31]:

$$\mathbf{P} = \begin{bmatrix} \mathbf{p_1} & \mathbf{p_2} & \cdots & \mathbf{p_n} \end{bmatrix} \tag{3.38}$$

where:

$$\mathbf{p_i} = \begin{bmatrix} p_{1i} & p_{2i} & \cdots & p_{ni} \end{bmatrix}^T = \begin{bmatrix} \phi_{1i}\psi_{i1} & \phi_{2i}\psi_{i2} & \cdots & \phi_{ni}\psi_{in} \end{bmatrix}^T \tag{3.39}$$

with $p_{ki} = \phi_{ki}\psi_{ik}$ called *participation factor*, and ϕ_{ki} indicating the k-th row and the i-th column of the modal matrix $\mathbf{\Phi}$, while ψ_{ik} indicates the i-th row and the k-th column of the modal matrix $\mathbf{\Psi}$.

Participation factors have been widely used in the power system literature, due to their characteristic of identifying participation of single machines or group of machines in critical modes. In view of the objectives of this work, this tool might become instead useful in order to quantify participation of control states on system stability, and therefore sensitivity to control parameters. To this extent, it might be interesting to identify the sensitivity of specific modes of interest to the elements of the state matrix **A**, a process usually indicated in the power system literature with the term *eigenvalue sensitivity analysis* [31], [145], [146].

This is achieved by differentiating eq. (3.19) with respect to an element a_{kj} of the system matrix **A**:

$$\frac{\partial \mathbf{A}}{\partial a_{kj}}\mathbf{\Phi}_i + \mathbf{A}\frac{\partial \mathbf{\Phi}_i}{\partial a_{kj}} = \frac{\partial \lambda_i}{\partial a_{kj}}\mathbf{\Phi}_i + \lambda_i \frac{\partial \mathbf{\Phi}_i}{\partial a_{kj}} \tag{3.40}$$

Then, premultiplying eq. (3.40) by $\mathbf{\Psi}_i$, yields:

$$\mathbf{\Psi}_i\frac{\partial \mathbf{A}}{\partial a_{kj}}\mathbf{\Phi}_i + \mathbf{\Psi}_i(\mathbf{A} - \lambda_i\mathbf{I})\frac{\partial \mathbf{\Phi}_i}{\partial a_{kj}} = \mathbf{\Psi}_i\frac{\partial \lambda_i}{\partial a_{kj}}\mathbf{\Phi}_i \tag{3.41}$$

According to eq. (3.23), and considering that $(\mathbf{A} - \lambda_i\mathbf{I}) = 0$, eq. (3.41) becomes:

$$\mathbf{\Psi}_i\frac{\partial \mathbf{A}}{\partial a_{kj}}\mathbf{\Phi}_i = \psi_{ik}\phi_{ji} = \frac{\partial \lambda_i}{\partial a_{kj}} \tag{3.42}$$

due to the fact that all the elements of $\frac{\partial \mathbf{A}}{\partial a_{kj}}$ are zero, except for the elements of the k-th row and the j-th column.

Though the sensitivity of a system mode to the element of the system matrix a_{kj} might provide useful indications, for controller tuning purposes, an explicit correlation between a critical mode λ_i and specific control parameters would actually represent a much useful indicator. In order to obtain such information from (3.42), further elaboration is needed, since an element a_{kj} of the system matrix might result from a combination of control parameters, or control parameters might appear in more than one element of **A**. Methods have been developed in the literature, in order to calculate the sensitivity of λ_i to a specific control parameter p_j [147], [148]. In this regard, a theorem is formulated in [148] (**Theorem** 2.2), which allows directly calculating the sensitivity of the mode λ_i to a parameter p_j, according to the following equation:

$$\frac{\partial \lambda_i}{\partial p_j} = \mathbf{\Psi}_i^H \frac{\partial \mathbf{A}}{\partial p_j}\mathbf{\Phi}_i \tag{3.43}$$

where $\mathbf{\Psi}_i^H$ is the complex conjugate transpose of $\mathbf{\Psi}_i$. Hence, differentiation of the state matrix **A** with respect to the parameter of interest p_j is required, which can be performed either numerically, or with the aid of programs allowing symbolic calculation, e.g. the "Symbolic Math Toolbox" of MATLAB.

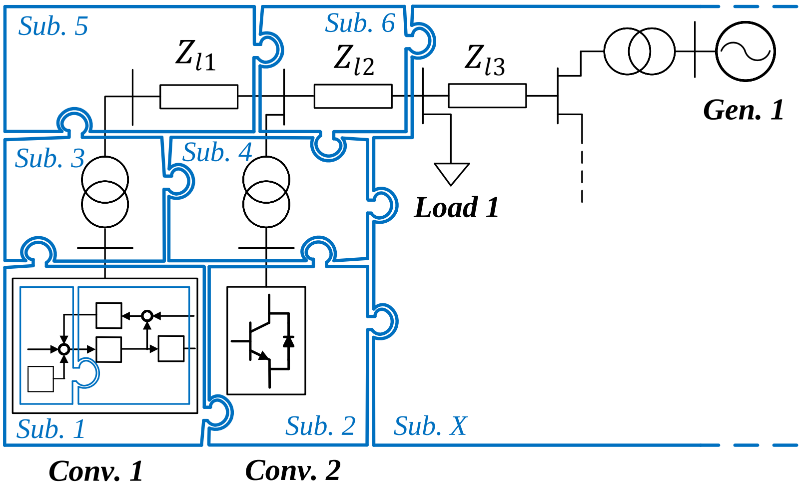

Figure 3.6: Conceptual explanation of the CCM principle.

3.3.3 The component connection method (CCM)

In order to perform eigenvalue analysis, the state-space representation of the system is required. For a simple system including only few components, this can be obtained by writing the system equations and, whether needed, linearizing around an operating point. Nevertheless, increasing the complexity of the system, this exercise might become quite tedious and time-consuming. More practical approaches have been proposed in the literature, in order to obtain the state-space representation of a complex system, such as the component connection method (CCM) [149], [150]. Initially developed for studying the dynamic stability of large power systems, it has been recently adopted by the power electronics community in order to investigate the stability of grid-connected converters [151], [152]. This simple and intuitive technique allows connecting the state-space representations of separated subsystems in a modular manner, so that the state-space representation of a complex system can be easily obtained. This principle is schematically explained in Fig. 3.6, where a system composed of converters, transformers, lines, and generators is shown. The objective is to obtain the state-space representation of the system in the following form:

$$\begin{cases} \dot{\mathbf{x}}_{sys} = \mathbf{F}_{int}\ \mathbf{x}_{sys} + \mathbf{G}_{int}\ \mathbf{u}_{sys} \\ \mathbf{y}_{sys} = \mathbf{H}_{int}\ \mathbf{x}_{sys} + \mathbf{J}_{int}\ \mathbf{u}_{sys} \end{cases} \tag{3.44}$$

The system is then split in N subsystems, whose state-space representations are known. Hence, indicating the generic representation of the subsystem X as:

$$\begin{cases} \dot{\mathbf{x}}_{subX} = \mathbf{A}_{subX}\ \mathbf{x}_{subX} + \mathbf{B}_{subX}\ \mathbf{u}_{subX} \\ \mathbf{y}_{subX} = \mathbf{C}_{subX}\ \mathbf{x}_{subX} + \mathbf{D}_{subX}\ \mathbf{u}_{subX} \end{cases} \tag{3.45}$$

with $X = \{1, 2, \cdots, N\}$, the vector $\mathbf{x}_{sys} = \left[\mathbf{x}_{sub1}\ \ \mathbf{x}_{sub2} \cdots\ \ \mathbf{x}_{subN}\right]^T$ contains all the states of the N subsystems, while the matrices $\mathbf{F}_{int}$, $\mathbf{G}_{int}$, $\mathbf{H}_{int}$ and $\mathbf{J}_{int}$ are obtained as a combination of the state-space matrices of the single subsystems as follows:

$$\begin{cases} \mathbf{F}_{int} = \mathbf{A}_d \; + \mathbf{B}_d \mathbf{L}_{11} (\mathbf{I} - \mathbf{D}_d \mathbf{L}_{11})^{-1} \mathbf{C}_d \\ \mathbf{G}_{int} = \mathbf{B}_d \mathbf{L}_{11} (\mathbf{I} - \mathbf{D}_d \mathbf{L}_{11})^{-1} \mathbf{D}_d \mathbf{L}_{12} \; + \mathbf{B}_d \mathbf{L}_{12} \\ \mathbf{H}_{int} = \mathbf{B}_d \mathbf{L}_{21} (\mathbf{I} - \mathbf{D}_d \mathbf{L}_{11})^{-1} \mathbf{C}_d \\ \mathbf{J}_{int} = \mathbf{L}_{21} (\mathbf{I} - \mathbf{D}_d \mathbf{L}_{11})^{-1} \mathbf{D}_d \mathbf{L}_{12} + \mathbf{L}_{22} \end{cases} \tag{3.46}$$

where $\mathbf{A}_d$, $\mathbf{B}_d$, $\mathbf{C}_d$ and $\mathbf{D}_d$ are sparse block diagonal matrices defined as:

$$\begin{cases} \mathbf{A}_d = diag\{\mathbf{A}_{sub1}, \mathbf{A}_{sub2}, \cdots, \mathbf{A}_{subN}\} \\ \mathbf{B}_d = diag\{\mathbf{B}_{sub1}, \mathbf{B}_{sub2}, \cdots, \mathbf{B}_{subN}\} \\ \mathbf{C}_d = diag\{\mathbf{C}_{sub1}, \mathbf{C}_{sub2}, \cdots, \mathbf{C}_{subN}\} \\ \mathbf{D}_d = diag\{\mathbf{D}_{sub1}, \mathbf{D}_{sub2}, \cdots, \mathbf{D}_{subN}\} \end{cases} \tag{3.47}$$

while $\mathbf{L}_{11}$, $\mathbf{L}_{12}$, $\mathbf{L}_{21}$ and $\mathbf{L}_{22}$ are sparse matrices called *interconnection matrices*, indicating how inputs and outputs of the subsystems are connected to each other. Thus, defining $\mathbf{u}_{sub}$ and $\mathbf{y}_{sub}$ the vectors containing respectively inputs and outputs of the N subsystems:

$$\mathbf{u}_{sub} = \left[\mathbf{u}_{sub1} \;\; \mathbf{u}_{sub2} \cdots \;\; \mathbf{u}_{subN}\right]^T \qquad ; \qquad \mathbf{y}_{sub} = \left[\mathbf{y}_{sub1} \;\; \mathbf{y}_{sub2} \cdots \;\; \mathbf{y}_{subN}\right]^T \tag{3.48}$$

the interconnection matrices relate inputs and outputs of the N subsystems according to the following relation:

$$\begin{cases} \mathbf{u}_{sub} = \mathbf{L}_{11} \, \mathbf{y}_{sub} + \mathbf{L}_{12} \, \mathbf{u}_{sys} \\ \mathbf{y}_{sys} = \mathbf{L}_{21} \, \mathbf{y}_{sub} + \mathbf{L}_{22} \, \mathbf{u}_{sys} \end{cases} \tag{3.49}$$

3.4 Robust stability analysis

Impedance-based analysis, as well as eigenvalue analysis, represent practical ways for stability assessment, and have been widely adopted in the power electronics community for investigating stability of grid-connected converters [115]. It is worth to remark that it is always possible to describe a state-space model by means of transfer functions, and vice versa, it is always possible to convert a system description by means of transfer functions into a state-space representation [153]. However, the process of converting transfer functions into state-space representation is not unique and, even though all the realization result equivalent, different representations might have advantages compared to others. Nevertheless, for the purposes of this work, it is only important to emphasize that the two representations are equivalent in practice, and it is always possible to convert a system state-space representation to a transfer functions description, and backwards. A practical example of such process is given in Section 4.3.2, where the state-space representations of the subsystems composing the model of a GFL converter are derived from their transfer function descriptions.

In the case of a MIMO system, impedance-based analysis, as well as eigenvalue analysis require the calculation of system eigenvalues. In the first case, in terms of the characteristic loci of the return ratio $\mathbf{L}(j\omega)$, in the latter case in terms of the eigenvalues of the system matrix $\mathbf{A}$. It is, however, known from multivariable control theory that eigenvalues do not provide a reliable estimation of stability margin for MIMO systems [103]. In fact, the main difference between a SISO and a MIMO system is represented by the concept of directions, and eigenvalues can only provide indications about the gains of the system when inputs and outputs are in the same direction, namely the direction of the eigenvectors. Hence, eigenvalues represent a *"poor measure of gain"* for a MIMO system [103], [143], where instead interactions among different channels generally take place. This aspect is in fact the underlying principle behind robust control theory, and numerous examples of the limitations occurring when analyzing the stability of MIMO systems by adopting standard SISO tools have been documented in the literature [103], [140], [141].

In this section, the concept of singular values and the tools for robust stability analysis adopted in this thesis are discussed, after having first introduced the following terminologies [140].

Definition (Nominal stability, robust stability, nominal performance, robust performance). *Given the description of an uncertainty model set* $\mathbf{\Pi}$ *and a set of performance objectives, suppose* $P \in \mathbf{\Pi}$ *is the nominal design model and* C *the resulting controller. Then the closed-loop feedback system is said to have*:

- ***Nominal Stability (NS)*** *if* C *stabilizes the nominal plant model* P .
- ***Robust Stability (RS)*** *if* C *stabilizes every plant* $P_x \in \mathbf{\Pi}$.
- ***Nominal Performance (NP)*** *if the performance objectives are satisfied for the nominal plant model* P .
- ***Robust Performance (RP)*** *if the performance objectives are satisfied for every plant* $P_x \in \mathbf{\Pi}$.

3.4.1 Singular values

The singular values are good measures of the size of a matrix because they provide information about the largest gain for any input direction, representing therefore a most suitable choice for the analysis of MIMO systems [140]. Defining an unitary matrix as [103]:

Definition (Unitary matrix). *A matrix* $\mathbf{U} \in \mathbb{C}^{n\times n}$ *is unitary if*

$$\mathbf{U}^H = \mathbf{U}^{-1}. \tag{3.50}$$

The following theorem explains the concept of singular value decomposition of a matrix [140].

Theorem 4 (Singular value decomposition (SVD)). *Let* $\mathbf{A} \in \mathbb{C}^{m\times n}$. *There exist unitary matrices*

$$\mathbf{U} = \left[\mathbf{u}_1, \mathbf{u}_2, \cdots, \mathbf{u}_m\right] \in \mathbb{C}^{m\times m} \qquad ; \qquad \mathbf{V} = \left[\mathbf{v}_1, \mathbf{v}_2, \cdots, \mathbf{v}_n\right] \in \mathbb{C}^{n\times n} \tag{3.51}$$

such that

$$\mathbf{A} = \mathbf{U}\boldsymbol{\Sigma}\mathbf{V}^H \qquad ; \qquad \boldsymbol{\Sigma} = \begin{bmatrix} \boldsymbol{\Sigma}_1 & 0 \\ 0 & 0 \end{bmatrix} \tag{3.52}$$

where

$$\boldsymbol{\Sigma}_1 = \begin{bmatrix} \sigma_1 & 0 & \cdots & 0 \\ 0 & \sigma_2 & \cdots & 0 \\ \vdots & \vdots & \ddots & \vdots \\ 0 & 0 & \cdots & \sigma_p \end{bmatrix} \tag{3.53}$$

and

$$\overline{\sigma} \triangleq \sigma_1 \geq \sigma_2 \geq \cdots \geq \sigma_p \triangleq \underline{\sigma} \geq 0, \qquad p = min\{m,n\}. \tag{3.54}$$

The proof of this theorem can be found in [140]. The quantities $\overline{\sigma}$ and $\underline{\sigma}$ are respectively indicated as *largest* and *smallest* singular values, $\mathbf{U}$ is the unitary matrix of output singular vectors $\mathbf{u}_i$, while $\mathbf{V}$ is the unitary matrix of input singular vectors $\mathbf{v}_i$. Singular values are sometimes called *principal gains*, and the associated directions are called *principal directions* [103]. They can be expressed as the positive roots of the eigenvalues of the symmetric matrix $\mathbf{A}^H\mathbf{A}$, and namely:

$$\sigma_i(A) = \sqrt{\lambda_i(\mathbf{A}^H\mathbf{A})} \tag{3.55}$$

The column vectors of $\mathbf{U}$ that have been denoted with $\mathbf{u}_i$ above, represent the *output directions*, which are orthogonal and of unit length (orthonormal):

$$\|\mathbf{u}_i\| = \sqrt{|u_{1i}|^2 + |u_{2i}|^2 + \cdots |u_{mi}|^2} = 1 \tag{3.56}$$

Similarly, the column vectors of $\mathbf{V}$ that have been denoted with $\mathbf{v}_i$ above, represent the *input directions*, which are also orthonormal. The following relation relates input and output directions to the singular values:

$$\mathbf{A}\mathbf{v}_i = \sigma_i\mathbf{u}_i \tag{3.57}$$

3.4.2 Matrix norms

The generalization of the magnitude of a SISO transfer function $|G(j\omega)|$ for the case when $\mathbf{G}$ is a matrix is the concept of *matrix norm*. Below the concept of norm for a vector or a matrix is introduced [103].

Definition (Norm) *A norm of e (which may be a vector, matrix, signal or system) is a real number, denoted* $||e||$*, that satisfies the following properties*:

(i) $||e|| \geq 0$ *(positivity)*;

(ii) $||e|| = 0$ *if and only if* $e = 0$ *(positive definiteness)*;

(iii) $||\alpha e|| = |\alpha| ||e||$, *for any scalar* α *(homogeneity)*;

(iv) *(triangle inequality)*:

$$||e_1 + e_2|| \leq ||e_1|| + ||e_2|| \tag{3.58}$$

More precisely, e is an element in a vector space $\mathbf{V}$ *over the field* $\mathbb{C}$*, and the properties above must be satisfied* $\forall e, e_1, e_2 \in \mathbf{V}$ *and* $\forall \alpha \in \mathbb{C}$*. Furthermore, a norm on a matrix* $||\mathbf{A}||$ *is a "matrix norm" if, in addition to the four properties listed above, it also satisfies the following property*:

(v) *(multiplicative property or consistency condition)*:

$$||\mathbf{AB}|| \leq ||\mathbf{A}|| \cdot ||\mathbf{B}|| \tag{3.59}$$

In sight of the considerations related to the concept of directions in MIMO systems, norms turn out to be very useful for the calculation of the maximum gains of a matrix. Assuming a system with input vector $\mathbf{w}$ and output vector $\mathbf{z}$, such that:

$$\mathbf{z} = \mathbf{Gw} \tag{3.60}$$

the maximum gain for all the possible directions is given by the *induced norm*, defined as:

$$||\mathbf{G}||_{ip} \triangleq \max_{w \neq 0} \frac{||\mathbf{z}||_p}{||\mathbf{w}||_p} \tag{3.61}$$

where:

$$||\mathbf{w}||_p \triangleq \left(\sum_i |w_i|^p \right)^{1/p} \tag{3.62}$$

and $p = 1, 2, \infty$. Considering the spectral radius defined in (3.24), the following theorem states an important relation between eigenvalues and singular values of a matrix.

Theorem 5. *For any matrix norm (and in particular for any induced norm):*

$$\rho(\mathbf{A}) \leq \|\mathbf{A}\| \tag{3.63}$$

The proof of the theorem is reported in [103]. It states an important relation between the eigenvalues of a matrix and a matrix norm, and namely that the largest eigenvalue of a matrix is not necessarily corresponding to the largest gain of the matrix itself, but rather the largest gain only in a specific direction.

The concepts reported above are particularly helpful for studying stability of multivariable systems. For a stable proper system described by $G(s)$, the $\mathcal{H}_2$ and the $\mathcal{H}_\infty$ norms are useful indicators, where $\mathcal{H}$ stands for *Hardy space*. $\mathcal{H}_2$ is the set of stable and strictly proper transfer functions, and the $\mathcal{H}_2$ norm represents a measure of the overall energy of the system, relating input disturbance with output response [143]. $\mathcal{H}_\infty$ represents instead the set of stable and proper transfer functions, and the $\mathcal{H}_\infty$ norm indicates the peak of the largest singular value within the whole frequency range [103]:

$$\|G(s)\|_\infty \triangleq \max_{\omega} \overline{\sigma}\,(G(j\omega)) \tag{3.64}$$

In a SISO system, the $\mathcal{H}_\infty$ norm is the peak value of the Bode plot, while in a MIMO system it indicates the maximum gain in the principal direction. At the basis of robust stability theory is the *small-gain theorem*, discussed in the following [103], [120], [140], [141].

3.4.3 Small-gain theorem and μ-analysis

The original formulation of the small-gain theorem represents a generalization of the Nyquist criterion for non-linear MIMO systems, as it will be recalled in the next chapter. It provides a sufficient condition for stability, resulting particularly useful in the context of input-output stability of feedback systems [120]. An appropriate use of that theorem is the main idea behind the robust stability theory; indeed, it might result too conservative if proper assumptions are not taken. Among the possible techniques for robust stability analysis, the structured singular value (SSV) analysis, commonly called μ-analysis, is an effective and mathematically accurate method for evaluating control robustness for MIMO applications. Widely adopted in the control engineering community, the μ-analysis is based on the formulation of the small-gain theorem reported below [140], [141], representing a necessary and sufficient condition for stability for a set of plants around a nominal plant.

Theorem 6 (Small-gain Theorem)**.** *Suppose $M(s) \in \mathcal{RH}_\infty$ (real rational subspace of $\mathcal{H}_\infty$), and let $\gamma > 0$. Then the interconnected system of Fig. 3.7 is well-posed and internally stable for all $\Delta(s) \in \mathcal{RH}_\infty$ with:*

(i) $\|\Delta\|_\infty \leq 1/\gamma$ *if and only if* $\|M\|_\infty < \gamma$

(ii) $\|\Delta\|_\infty < 1/\gamma$ *if and only if* $\|M\|_\infty \leq \gamma$

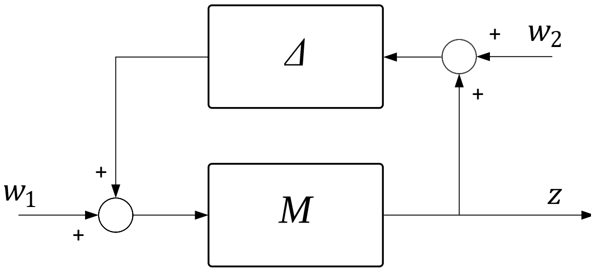

Figure 3.7: $M - \Delta$ loop for stability analysis.

The μ-analysis has been first introduced in [154], and it is based on the calculation of singular values rather than eigenvalues. It allows covering a set of possible system configurations identified by a frequency-dependent uncertainty function instead of assessing stability only for a particular condition. Thus, it avoids following a trial and error procedure based on checking stability and performance for a large number of candidate plants, representing instead the principle behind the MC analysis previously discussed.

Although well-known within the control engineering community, the μ-analysis has been seldom utilized by the power system or by the power electronics community. Few examples can be found in [155], [156], where the impact of constant power load behaviour of power electronics interfaced loads on the stability of the electrical power system has been addressed, whereas an application to power system studies can be found in [143]. Actually, this approach might become very useful for studying stability of grid-connected converters in the case of high power electronics-based penetration. In fact, the grid representation by means of a Thévenin equivalent with constant impedance is widely adopted in the power electronics community. The nature of the considered grid impedance is usually a resistive-inductive element, whose parameters are calculated according to the information usually provided by the SO, and related to the short-circuit power, and the X/R ratio of the fundamental component of the grid impedance at the point of connection.

It is, however, well-known that this representation might be rather inaccurate, since the characteristics of the grid can change substantially during the day [131]. Even though information related to the excursions of short-circuit power and of X/R ratio within defined limits could be in some cases provided by the SO, an accurate portrait of the grid impedance in frequency-domain is still unlikely to be obtained, due to the unknown behaviour of the generating units and loads connected to the grid. These, along with capacitors of underground cables and *LCL* filters of other converters operating nearby, may cause unexpected resonances in the equivalent grid impedance seen by the converter [152]. The μ-analysis tackles this problem by including plant uncertainties in the investigation, and is, therefore, suitable for assessing the robust stability of the converter in a grid with high-penetration of converter-based operating units, whose behaviour is generally unknown.

With the term *uncertainties*, the differences between the real plant and the adopted model is indicated. Causes for model uncertainties can be of different nature: neglected dynamics

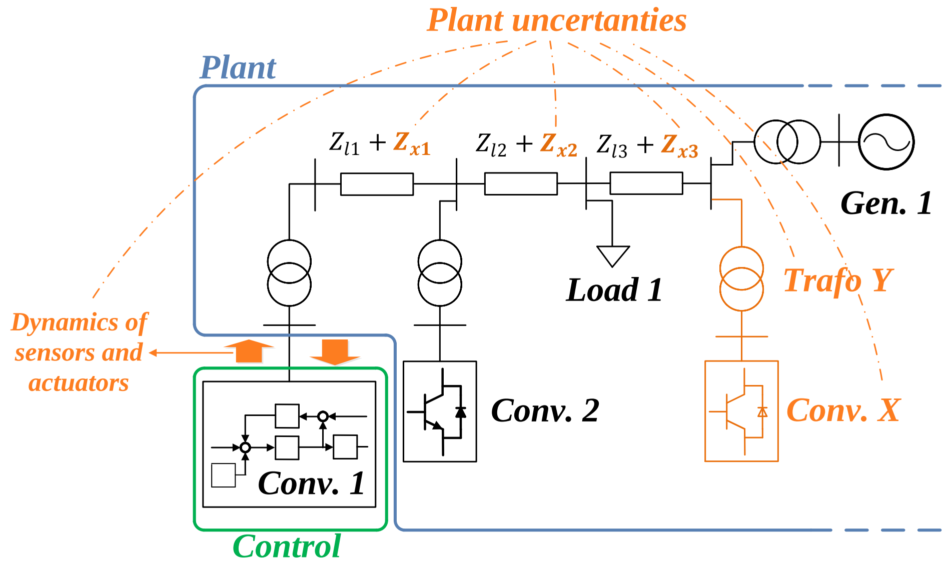

Figure 3.8: Example of common plant uncertainties for the case of a grid-connected converter.

of sensors or actuators, parameter uncertainties, or unknown behaviour of the system components. A practical example of source of uncertainties for the case of a grid-connected converter is schematically shown in Fig. 3.8. Inaccurate knowledge of cable lengths, the unknown or unmodeled presence of components like transformers or additional loads, or the presence of other converters with unknown controllers operating nearby, might substantially affect the frequency behaviour of grid impedance at the point of connection.

Inclusion of plant uncertainties

Including uncertainties in a model is equivalent to consider a model set rather than a specific configuration, and different techniques can be adopted in order to fulfill this purpose. An useful way is to assume that the uncertain behaviour is caused by an additive additional noise signal with bounded power spectrum. The additive, the multiplicative, and the coprime factor representations have been widely investigated in robust control theory [141], however the multiplicative representation is probably the most common one, since the numerical values of its weights result to be more informative [140]. It describes plant uncertainties by means of a frequency dependent function of the following form:

$$G_m = (1 + w_0 \Delta_0)\ G \quad ; \quad with\ \|\Delta_o\|_\infty \leq 1 \tag{3.65}$$

where Δ_o is a block diagonal normalized matrix including all the possible perturbations, $\|\Delta_o\|_\infty$ represents its $\mathcal{H}_\infty$ norm, w_o is the multiplicative weight and G is the nominal plant. A proper choice of the plant uncertainties allows including effects that are in fact certain, e. g. parameter variations within defined ranges [140]. A conceptual example for the case of a SISO transfer function representing the single-phase resistive-inductive impedance of a

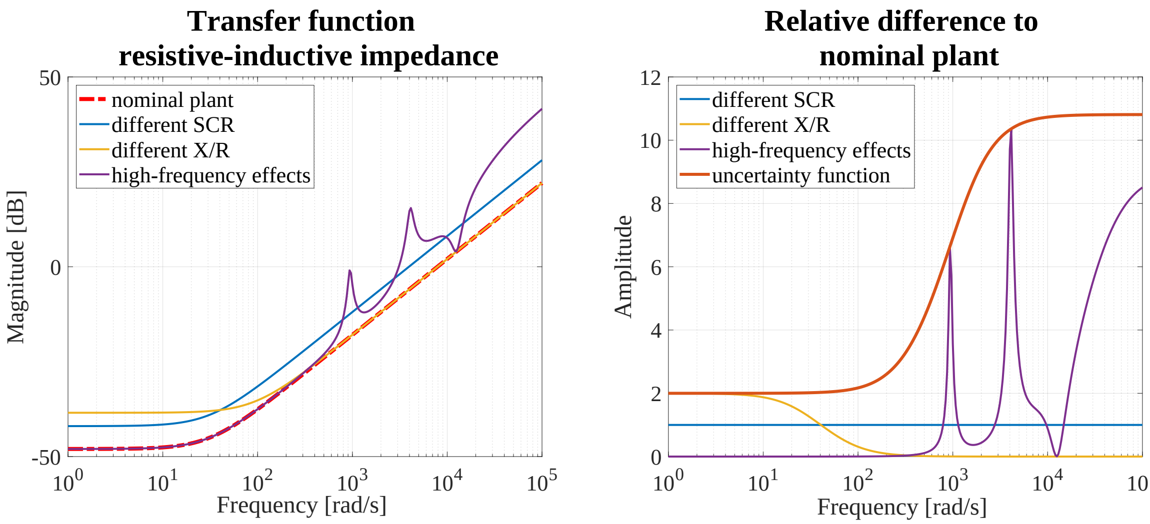

(a) (b)

Figure 3.9: Conceptual explanation of the uncertainty function. (a) Magnitude of the transfer function of a resistive-inductive impedance: (red dotted) nominal plant, (blue) increasing SCR, (yellow) varying X/R ratio, (violet) considering high-frequency effects. (b) Relative difference to nominal plant: (blue) increasing SCR, (yellow) varying X/R ratio, (violet) considering high-frequency effects, (red) possible weighting function.

hypothetical grid is shown in Fig. 3.9. Considering the impedance transfer function of the nominal plant:

$$G(j\omega) = (R_g + j\omega\, L_g) \tag{3.66}$$

where with R_g and L_g are indicated resistive and inductive values of the grid impedance, respectively. Fig. 3.9 (a) shows the comparison between the nominal plant (red-dotted line), the corresponding behaviour when a different SCR is considered (blue line), the magnitude when the X/R ratio is changed (yellow), and the frequency portrait of the impedance when additional resonant high-frequency effects are included (violet line). Indicating with G_p the perturbed plant, the blue, the yellow, and the violet lines in Fig. 3.9 (b) represent the relative difference D_{rel} between each of the aforementioned plants and the nominal one. These are calculated as follows [103]:

$$D_{rel}(j\omega) = \left| \frac{G_p(j\omega) - G(j\omega)}{G(j\omega)} \right| \tag{3.67}$$

The red-continuous line in Fig. 3.9 (b), represents a possible choice of the uncertainty function, which beside covering all the possible effects that have been considered in Fig. 3.9 (a), it would also include an additional degree of robustness to the analysis, due to the fact that a wider set of plants is actually considered. It should be noted that this behaviour is typical of real systems, and reflects the fact that the system is better understood at low frequency.

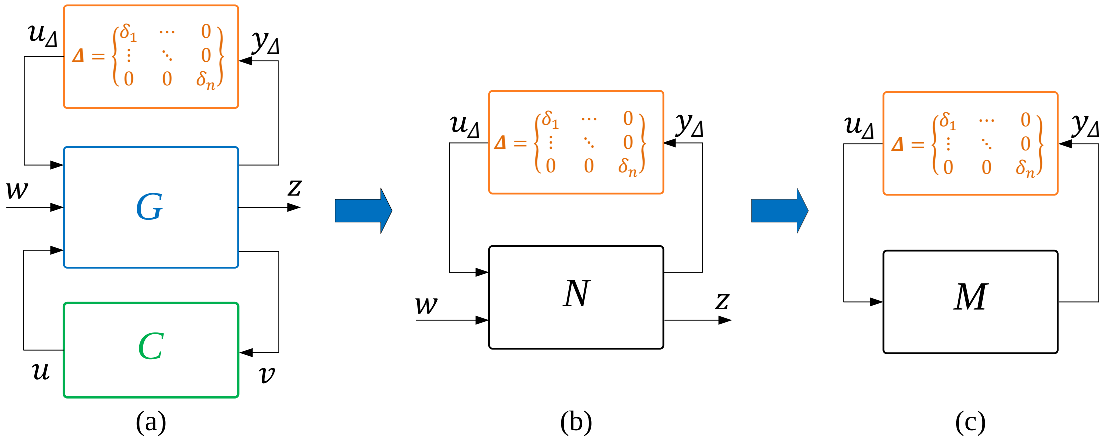

Figure 3.10: Steps for μ-analysis: (a) general control configuration including model uncertainties, (b) NΔ-structure, (c) MΔ-structure.

Calculation of the structured singular value μ

In order to perform the μ-analysis, the system has to be rearranged in the form shown in Fig. 3.10 (a), where with G is indicated the generalized plant, while with C the generalized controller. In order to obtain the structure of Fig. 3.10 (a), system uncertainties have to be *pulled out* from the generalized plant G and gathered together in a block-diagonal matrix indicated with Δ in the figure, including all the perturbations to the nominal plant, and usually normalized such that $\|\Delta\|_\infty \leq 1$. It is worth to notice, that a *structured* Δ is considered in the analysis, as emphasized in Fig. 3.10. In fact, a diagonal uncertainty usually arises from neglected dynamics in the individual input or output channels, which is always present [103]. Furthermore, by using a block-diagonal uncertainty matrix, couplings between some but not all channels can be represented, reflecting the fact that some MIMO uncertainties do have effects across channels, e.g. in the P/Q dynamics of a power converter, an aspect that will be further investigated in the following chapters. On the other hand, the use of an *unstructured uncertainty* introduces non-physical couplings between channels, with the risk of making the results of the robust stability analysis too conservative. Uncertainties can be located at the input or at the output of the plant, and practical examples of the derivation of the generalized plant considering system uncertainties will be shown in the next chapter. Then the $N\Delta$-structure shown in Fig. 3.10 (b) can be obtained by means of a matrix lower linear fractional transformation (LFT) between the generalized plant G and the controller C, defined as [140]:

$$N = \mathcal{F}_l(G,C) \triangleq G_{11} + G_{12}\,C(I - G_{22}\,C)^{-1}G_{21} \tag{3.68}$$

This represents a matrix function introduced by Doyle (1984) for the purpose of representing uncertainties in matrices and systems [140], [141], and can be calculated by means of the MATLAB command `starp` of the "Robust control" toolbox [157]. The $M\Delta$-structure shown in Fig. 3.10 (c), is then derived considering that $M = N_{11}$. The mathematical machinery behind this formalism is not explored in this chapter, and the interested reader is referred to [141] for a detailed derivation. Finally, the *SSV* μ is defined as follows [103].

Definition (Structured singular value (SSV or μ)) *Let M be a given matrix and let $\Delta = diag\{\Delta_i\}$ denote a set of complex matrices with $\overline{\sigma} \leq 1$ and with a given block-diagonal structure. The real non-negative function $\mu(M)$, called structured singular value, is defined as*:

$$\mu(M) \triangleq \frac{1}{\underset{\Delta}{min}\{\ \overline{\sigma} \mid det(I - M\Delta) = 0\ for\ structured\ \Delta\}}. \tag{3.69}$$

If no such structured Δ exists, then $\mu(M)$=0.

In other words, the *SSV* μ represents the smallest perturbation, or rather the smallest structured Δ (measured in terms of the largest singular value $\overline{\sigma}(\Delta)$), such that $det(I - M\Delta)$ = 0. The inverse of $\mu(M)$ can be interpreted as a stability margin with respect to the structured uncertainty set affecting M. Hence, indicating the peak of $\mu(M) = \beta$ across the frequency range ω, stability is guaranteed for all perturbations with appropriate structure and with respect to the chosen uncertainty, such that:

$$\underset{\omega}{max}\, \overline{\sigma}(\Delta) \leq \frac{1}{\beta} \tag{3.70}$$

meaning that, if the μ-factor exceeds the magnitude of 1 at a defined frequency, there exists a perturbation with $\overline{\sigma} = 1$, such that the system $I - M\Delta$ is singular. Therefore, there exists at least one plant among those identified by the defined uncertainty function for which the closed loop system is unstable. As a consequence, the calculated stability margin is closely related to the chosen uncertainty set, and it can be noted that it is generally more conservative compared to the results obtained by means of eigenvalue analysis. This is a consequence of the fact that the small-gain theorem is a necessary and sufficient condition for stability of an entire set of uncertain plants, hence the calculated stability margin takes into account a set of possible configurations, rather than just a particular condition. As a consequence, its results are more informative compared to eigenvalues, which can only state whether the system in its nominal configuration is stable or not.

In some cases, unstable plants may be located "very close" to stable plants, e.g. when stability is heavily dependent on knowing the precise frequencies of certain resonances. A stability margin takes account of such concerns by giving a measure of how much margin to instability remains in a particular choice of nominal plant and under the defined structure of the uncertainty. Furthermore, it represents a mathematically accurate calculation of the stability margin of a MIMO systems, which cannot be obtained by means of standard tools for SISO system analysis [103], [140], [141], [143].

4 Analysis of the interactions among converters

In the following, the approaches for stability analysis discussed in the previous chapter, are employed in order to study the stability of GFL and GFM converters, as well as the interactions among them, by giving particular emphasis to the effects caused by the synchronization principle adopted by the converter. It is therefore assumed that a GFL converter uses a PLL for synchronization purpose, whereas a VSM structure is considered in order to represent the behaviour of a generic GFM converter, which is able of self-synchronization to the grid without the need for a dedicated unit, due to the emulation of the power-synchronization principle. Indeed, it has been remarked in Chapter 2, that a VSM is a particular implementation of a GFM converter, and, by properly choosing control parameters, the results can be extended to several of the GFM converter structures discussed in Section 2.4.

A practical application of the impedance-based approach in order to study the interactions among synchronization units of GFL converters, is first presented. Then eigenvalue analysis is employed so as to investigate the stability of GFM converters, as well as their parallel operation. Finally, a robust stability analysis by means of SSVs of the interactions between GFL and GFM converters, along with the effects of the electrical distance between them, is performed in the last part of this chapter.

4.1 Impedance-based analysis of the interactions among PLLs

Harmonic stability has been thoroughly investigated in the last decade [115]. Early studies have been focusing on the resonance effects introduced by LCL converter filters, and the interactions between current control loops and filters of converters operating nearby [116], [117], [158]. However, the effects of synchronization loops of GFL converters, typically implemented by means of PLLs or similar filter structures, have been often neglected. In fact, due to the different bandwidths of the control loops typically employed by grid-connected converters, and depending on the phenomena of interest, the use of simplified models is generally allowed, without significantly affecting the accuracy of the results [159]. Nevertheless, recent studies have shown the importance of considering the synchronization mechanism of grid-connected converters in their stability assessment, especially when operating under weak grid conditions [66], [68], [69], [160]-[162].

Driven by the always more demanding grid code requirements introduced by SOs worldwide [6], enhanced performances for grid-connected converters are requested, in order to contribute to grid voltage stability by means of a prompt provision of reactive current in response to a grid fault. In order to achieve this purpose, GFL converters, whose controllers are often implemented in Synchronous Reference Frame (SRF) coordinates, require an accurate knowledge of the grid voltage characteristics at the connection point in terms of magnitude and phase. According to the aforementioned requirements, this translates in a need for increasing the bandwidth of the synchronization unit adopted by the converter.

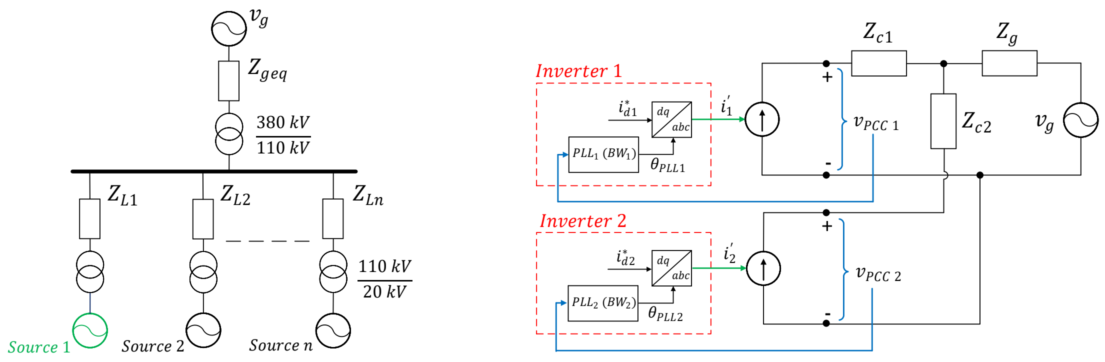

(a) (b)

Figure 4.1: Studied system for stability assessment of GFL converters operating nearby: (a) scheme of the system, (b) simplified representation showing control loops.

In the following, the effects of PLL-bandwidth variations, along with the interactions among synchronization units of GFL converters operating nearby, are investigated by means of impedance-based analysis. Considering the limitations of this approach in assessing influence of parameters on the obtained results, a MC analysis is also performed, in order to relate the aforementioned effects to the SCR of the grid at the point of connection. To this extent, and according to the MIMO formulation of the problem, a norm-based stability margin is calculated, which, for the particular case under study, does not suffer from excessive conservatism, thus providing a reliable estimation of the real system conditions.

4.1.1 Modeling of GFL converters for studying synchronization issues

The scheme of the studied system is reported in Fig. 4.1 (a). The case of an high-voltage grid is examined, and several converters operating nearby, sharing the same network bus, are considered. Seen from the bus, the grid is represented by means of a Thévenin equivalent, whose impedance is varied in order to emulate a weaker or a stronger connection point. It is assumed that each converter represents an aggregate model of several units having the same characteristics.

Due to the fact that interactions between the PLL and other converter control loops (current control, DC-link voltage/active power control, reactive power control, voltage feed-forward, etc..) have been thoroughly addressed in the literature in [66], [68], [69], and do not represent the goal of this investigation, the simplified model shown in Fig. 4.1 (b), is adopted in the following, which allows isolating the effects of the synchronization units from the other control loops. Indeed, the converters depicted in the figure, are supposed to behave as perfect current sources, whose output currents are calculated by transforming the given setpoints from the *dq* to the *abc* reference frame by means of the angle estimated by the PLL. The simplification of neglecting the other converter control loops is justified by the difference among the control bandwidths in question. In fact, the design guidelines for the current control of a grid-connected converter usually lead to a bandwidth of this control loop in a definitely higher range compared to the one of the synchronization loop [116], [117], whereas the bandwidths of the outer control loops (active/reactive power loops, DC-link voltage control, etc...) are

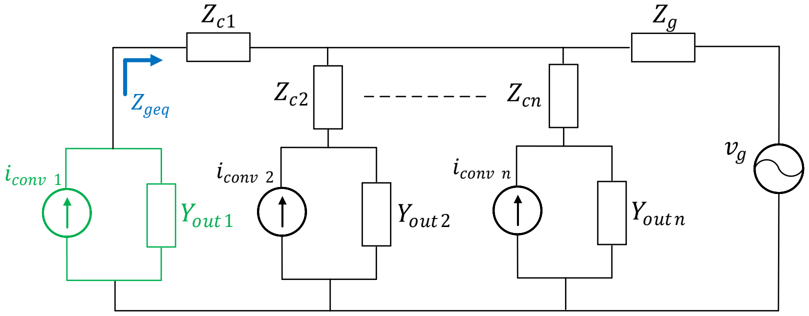

Figure 4.2: Equivalent system representation for impedance-based analysis.

usually way lower than it. Moreover, the simplification considered here has been adopted in the literature in several other works [163], [164], and to this extent, the Hysteresis Current Control (HCC) is among the current control implementations cited in the literature for modeling the performances of controllers for real industrial applications, which ensures an extremely high (ideally infinite) bandwidth [165]. Finally, the impedance Z_{c1} and Z_{c2} shown in Fig. 4.1 (b), account for the impedance of the medium-voltage/high-voltage transformer of each converter, along with those of the respective lines Z_{L1} and Z_{L2}.

Equivalent output admittance and equivalent grid impedance

Fig. 4.2 shows the equivalent representation of the system depicted in Fig. 4.1 (a), suitable for impedance-based analysis. Each converter is modeled by means of a Norton equivalent, while the grid by means of a Thévenin equivalent representation. According to the MIMO formulation necessary for considering the effects of the PLL, all the admittances and impedances are represented by matrix transfer functions. The equivalent grid impedance seen by the Converter 1 can be calculated as [166]:

$$\mathbf{Z}_{geq}(s) = \mathbf{Z}_{c1}(s) + \frac{1}{\frac{1}{\mathbf{Z}_g(s)} + \mathbf{Y}_{o2}(s) + \ldots + \mathbf{Y}_{on}(s)} \tag{4.1}$$

where $\mathbf{Y}_{on}(s)$ of the n-th converter is obtained from $\mathbf{Z}_{cn}(s)$ and $\mathbf{Y}_{outn}(s)$ as follows:

$$\mathbf{Y}_{on}(s) = \frac{1}{\mathbf{Z}_{cn}(s) + \frac{1}{\mathbf{Y}_{outn}(s)}} \tag{4.2}$$

Considering only the PLL and neglecting the other control loops of the converter, the output admittance of each converter is expressed by the following equation [66]:

$$\mathbf{Y}_{out}(s) = \begin{bmatrix} 0 & I_q H_{PLL}(s) \\ 0 & -I_d H_{PLL}(s) \end{bmatrix} \tag{4.3}$$

with I_d and I_q indicating respectively the d and q components of the converter current at the operating point, and $H_{PLL}(s)$ represents the transfer function of the detected angle $\Delta\theta_{PLL}$ according to a variation of the q component of the voltage Δv_q, already derived in Section 2.3, and reported below for simplicity [66]:

$$H_{PLL}(s) = \frac{\Delta\theta_{PLL}(s)}{\Delta v_q(s)} = \frac{LF(s)}{s + V_d LF(s)} \tag{4.4}$$

V_d in (4.4), represents the d component of the voltage at the operating point, while $LF(s)$ is the transfer function of the loop filter of the SRF-PLL, already given in eq. (2.8):

$$LF(s) = k_p + \frac{k_i}{s} \tag{4.5}$$

with k_p and k_i proportional and integral gains, respectively. Finally, indicating with ω_g the system frequency, the representation of a generic resistive-inductive impedance in dq-coordinates is reported below:

$$\mathbf{Z}_{RL}(s) = \begin{bmatrix} sL+R & -\omega_g L \\ \omega_g L & sL+R \end{bmatrix} \tag{4.6}$$

4.1.2 Norm calculation for stability margin assessment

According to the considerations about the GNC, and the limitations of system eigenvalues in providing a real measure of the stability margin for a MIMO system discussed in Section 3.4, methods have been proposed in the literature, defining a stability margin based on norm calculations of $\mathbf{Y}_{out}$ and $\mathbf{Z}_{geq}$ [130], [167]-[169]. However, even though a problem formulation suitable for design purposes can be achieved, the resulting margin might suffer from excessive conservatism. On the other side, if proper assumptions are verified, the norm calculation can provide a reliable estimation of system stability margin without the shortage of resulting too conservative. To this extent, let us consider the problem formulation of the impedance-based approach expressed by (3.15), and reported below for simplicity:

$$\mathbf{H}(s) = \big(\mathbf{I} + \mathbf{L}(s)\big)^{-1} \tag{4.7}$$

It has been observed in Section 3.2, that (4.7) resembles the closed loop transfer function of a negative feedback control system, where the forward gain is unity and the feedback gain is the return ratio $\mathbf{L}(s)$. In order to obtain a stability margin calculation consistent with the robust control theory discussed in the previous chapter, the original formulation of the small-gain theorem also valid for non-linear systems mentioned in Section 3.4.3, can be directly applied to the return ratio. This states that, given a system with a stable loop transfer function $\mathbf{L}(s)$, a sufficient condition that guarantees the stability of the closed-loop system is represented by $||\mathbf{L}|| < 1$ [103], being this valid for each matrix norm complying with the definition reported in Section 3.4.2. Thus, the following stability margin is introduced:

$$S_m \; = \; 20\, log\left(\frac{1}{||\mathbf{L}||_\infty}\right) \tag{4.8}$$

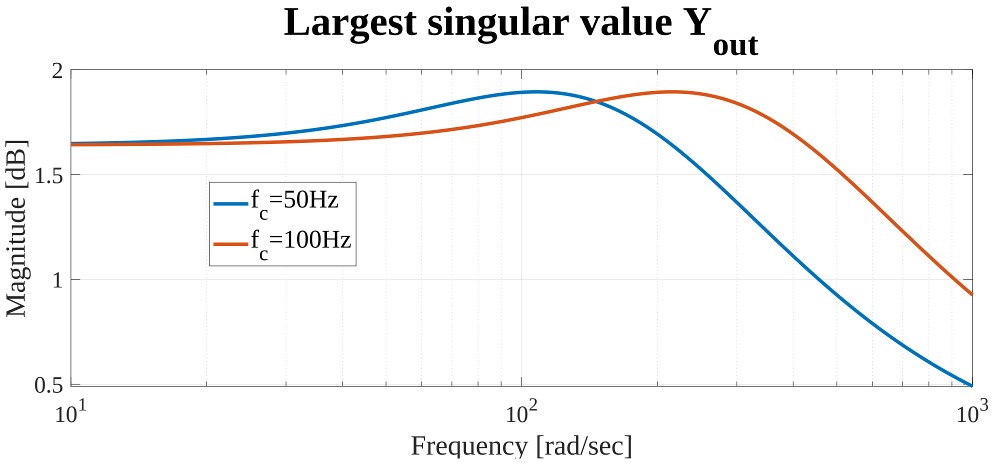

Figure 4.3: Largest singular value of $\mathbf{Y}_{out}$ calculated for two different values of the PLL-bandwidth. (Blue) f_c=50 Hz; (red) f_c= 100 Hz.

In fact, according to Theorem 5 reported in Section 3.4.2, which states that given a matrix $\mathbf{A}$, its largest singular value $\overline{\sigma}(\mathbf{A})$ is always $\geq \rho(\mathbf{A})$ (spectral radius of $\mathbf{A}$), the condition that the $\overline{\sigma} \leq 1 \; \forall\omega$, ensures that the characteristic loci of the return ratio $\lambda_i(\mathbf{L}(j\omega))$ will never encircle the point (-1, j0), simply due to the fact that the Nyquist contour will be always limited to the unit circle. A similar concept has been proposed in [169], where a stability margin calculation suitable for design purposes has been pursued. According to the property of a matrix norm (3.59), the following is valid:

$$||\mathbf{L}||_\infty = ||\mathbf{Z}_{geq}\mathbf{Y}_{out}||_\infty \leq ||\mathbf{Z}_{geq}||_\infty ||\mathbf{Y}_{out}||_\infty \tag{4.9}$$

The following stability margin calculation has been then proposed in [169]:

$$S_{m1} = 20\;log\left(\frac{1}{||\mathbf{Z}_{geq}||_\infty ||\mathbf{Y}_{out}||_\infty}\right) \tag{4.10}$$

The idea behind this proposal is that, given the equivalent output impedance $\mathbf{Z}_{geq}$, the converter output admittance $\mathbf{Y}_{out}$ can be designed accordingly, so as to satisfy the condition that the product of their norms will never exceed the unity. Nevertheless, such formulation noticeably increases the conservatism of the calculated norm. This is demonstrated by the example reported in Fig. 4.3, where the largest singular value of $\mathbf{Y}_{out}(s)$, the latter obtained according to (4.3), is calculated for two different values of the PLL-bandwidth, and namely for f_c = 50 Hz and f_c = 100 Hz. Here f_c indicates the cut-off frequency of the PLL open-loop transfer function according to [61]. This result indicates that the variation of the PLL-bandwidth only shifts the curve in the x-axis, while $\underset{\omega}{max}\;\overline{\sigma}(\mathbf{Y}_{out}(j\omega)) = ||\mathbf{Y}_{out}||_\infty$ is not affected by this variation, demonstrating that the calculated stability margin according to (4.10) is too conservative.

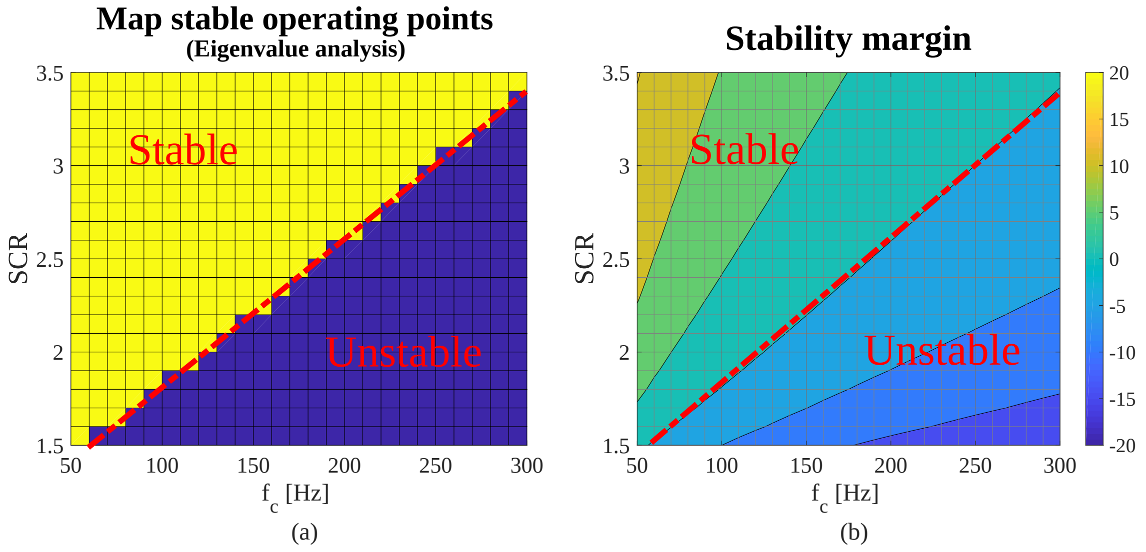

(a)

(b)

Figure 4.4: Map stable/unstable regions: (a) Eigenvalue analysis: (yellow) stable operating points, (blue) unstable operating points; (b) Stability margin according to 4.8.

Table 4.1: Simulation parameters

Description	Symbol	Value	Description	Symbol	Value
Short-circuit power	S_{sc}	100 MVA	Rated grid frequency	f_g	50 Hz
Line-to-line voltage	V_{LL}	110 kV (rms)	L connection impedance	L_c	$L_g/3$
X/R ratio	X/R	10	R connection impedance	R_c	$R_g/3$

Application to the studied case

The stability margin calculation proposed in (4.8), is now applied to the studied case. Let us consider the case of three converters of the same size operating nearby, and injecting their rated power. Settled the Short-Circuit Ratio (SCR) of the grid at the connection bus, and the short-circuit power S_{sc}, the rated power P_{rated} of each converter is calculated as:

$$P_{rated} = \frac{S_{sc}}{N_{con}\ SCR} \tag{4.11}$$

where N_{con} indicates the number of converters considered for the investigation. For sake of simplicity, the impedances between the converters and the connection bus, indicated with Z_{c1}, Z_{c2}, and Z_{c3} in Fig. 4.2, have been set to one-third of the grid impedance Z_g, assuming also the same X/R ratio. The PLL-bandwidths of the converters 2 and 3 are set to f_{c2} = 100 Hz, and f_{c3} = 50 Hz, respectively, while the PLL-bandwidth of Converter 1 is varied in the range f_{c1} = [50 ; 300] Hz. Then the SCR is varied within the range SCR = [1.5 ; 3.5], and converter stability is assessed first by calculating the eigenvalues of (4.7), used to identify stable and unstable operating points, and then by means of the stability margin S_m reported in (4.8). The results of these two calculations are shown in Fig. 4.4 (a) and (b), respectively, while system parameters are shown in Table 4.1. It can be noticed, that the stability borders between stable an unstable region perfectly match with both calculations, revealing the accuracy of the calculated stability margin.

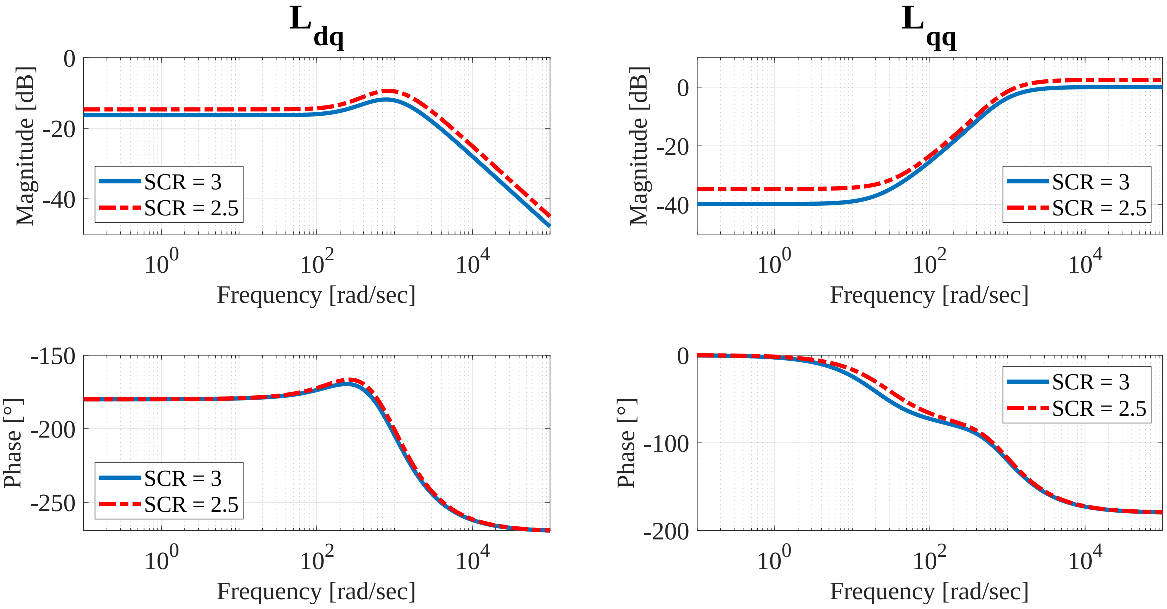

Figure 4.5: L_{dq} and L_{qq}: (Blue continuous line) SCR=3, (red dashed line) SCR=2.5.

Nevertheless, according to the considerations related to the conservatism of the norm calculation compared to the results of eigenvalue analysis, a certain discrepancy between the two calculations was expected, which is not visible from the results shown in Fig. 4.4. The reason for that accurate match for the particular case under study, is explained in the following. In fact, according to the expression of the return ratio:

$$\mathbf{L}(s) = \begin{bmatrix} L_{dd}(s) & L_{dq}(s) \\ L_{qd}(s) & L_{qq}(s) \end{bmatrix} = \begin{bmatrix} Z_{geq\ dd}(s) & Z_{geq\ dq}(s) \\ Z_{geq\ qd}(s) & Z_{geq\ qq}(s) \end{bmatrix} \begin{bmatrix} Y_{out\ dd}(s) & Y_{out\ dq}(s) \\ Y_{out\ qd}(s) & Y_{out\ qq}(s) \end{bmatrix} \tag{4.12}$$

It can be noticed that the resulting $\mathbf{L}(s)$ is given by:

$$\mathbf{L}(s) = \begin{bmatrix} 0 & Z_{geq\ dd}(s)Y_{out\ dq}(s) + Z_{geq\ dq}(s)Y_{out\ qq}(s) \\ 0 & Z_{geq\ qd}(s)Y_{out\ dq}(s) + Z_{geq\ qq}(s)Y_{out\ qq}(s) \end{bmatrix} \tag{4.13}$$

where the only two elements of the matrix different from zero are $L_{dq}(s)$ and $L_{qq}(s)$. Solving the characteristic equation of (4.13), the two eigenvalues of the matrix are given by $\lambda_1(s) = 0$, and $\lambda_2(s) = L_{qq}(s)$, meaning that one element of the matrix directly corresponds to the only eigenvalue different from zero. As a consequence, stability can be assessed by looking at the Nyquist plot or, equivalently, at the Bode plot of this quantity. For the condition SCR = 3 and $f_c = 250$ Hz, precisely at the border between stable and unstable region according to Fig. 4.4, magnitude and phase of $L_{dq}(j\omega)$ and $L_{qq}(j\omega)$ are shown in Fig. 4.5, and indicated by the continuous blue lines. The dashed red lines in the figure, indicate instead the same quantities calculated reducing the value of the SCR to 2.5, corresponding to an unstable operating condition according to Fig. 4.4. It is shown that in both cases, $L_{qq}(j\omega)$ approaches the unit circle (0 dB in the Bode plot) with a phase of $-180°$, corresponding exactly to the point (-1, j0) of the complex plane. Additionally, the magnitudes of $L_{dq}(j\omega)$ and $L_{qq}(j\omega)$ are shown

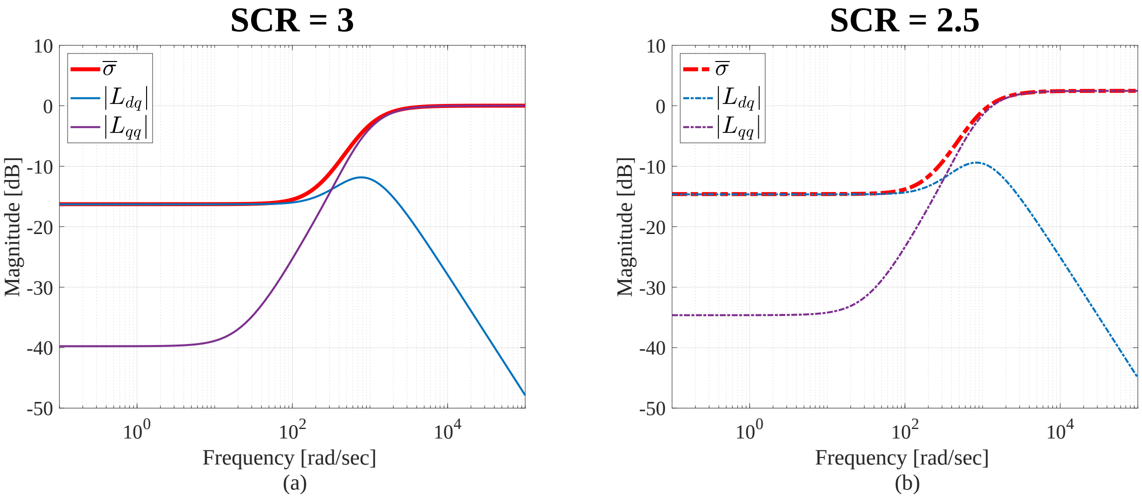

Figure 4.6: Magnitude of L_{dq} and L_{qq} vs. $\overline{\sigma}$: (a) SCR=3; (b) SCR=2.5.

in Fig. 4.6, along with the largest singular value $\overline{\sigma}(\mathbf{L}(j\omega))$ for the two examined cases. This figure indicates that the peak of the largest singular value of (4.13) always corresponds to the peak of the only eigenvalue different from zero. Thus, the following is valid:

$$\|\mathbf{L}\|_\infty = \|L_{qq}\|_\infty = \|\lambda_2\|_\infty \tag{4.14}$$

This result, along with the Bode plot shown in Fig. 4.5, demonstrates that, with the assumptions done for the specific case under study, eq. (4.8) provides an exact measure of the stability margin of the studied system without being conservative, due to the fact that the peak of the largest singular value of the matrix always corresponds to the peak of the only eigenvalue different from zero (Fig. 4.6), which always approaches the unit circle with a phase of $-180°$ (Fig. 4.5).

Simulation results

In order to validate the performed analysis, the studied system has been simulated in MATLAB/Simulink/PLECS. The converters have been modeled by means of controlled current sources as shown in Fig. 4.1, and the results of the stability map shown in Fig. 4.4, have been verified by means of time-domain simulations. An example is shown in Fig. 4.7. According to the stability map shown in Fig. 4.4, and for a SCR = 3, f_{c1} has to be increased over 250 Hz in order to cause instability, while decreasing the SCR to a value of 2.5, the critical PLL-bandwidth is reduced to $f_{c1} \approx 190$ Hz. Fig. 4.7 (a) shows the results of the performed simulations. The power of each converter is gradually increased up to its rated value, reaching a steady-state operating point after few periods. The SCR is set to 3 and the PLL parameters of converter 2 and 3 are set so as to obtain f_{c2} = 100 Hz and f_{c3} = 50 Hz, while the PLL-bandwidth of the first converter is varied from $f_{c1} = 180$ Hz to f_{c1} =200 Hz at time t = 0.4 s. The same simulation has been repeated varying the value of the impedances in the model so as to correspond to a value of SCR 2.5, and the results are shown in Fig. 4.7 (b). The three converters become unstable only in the second case, and for a value of the

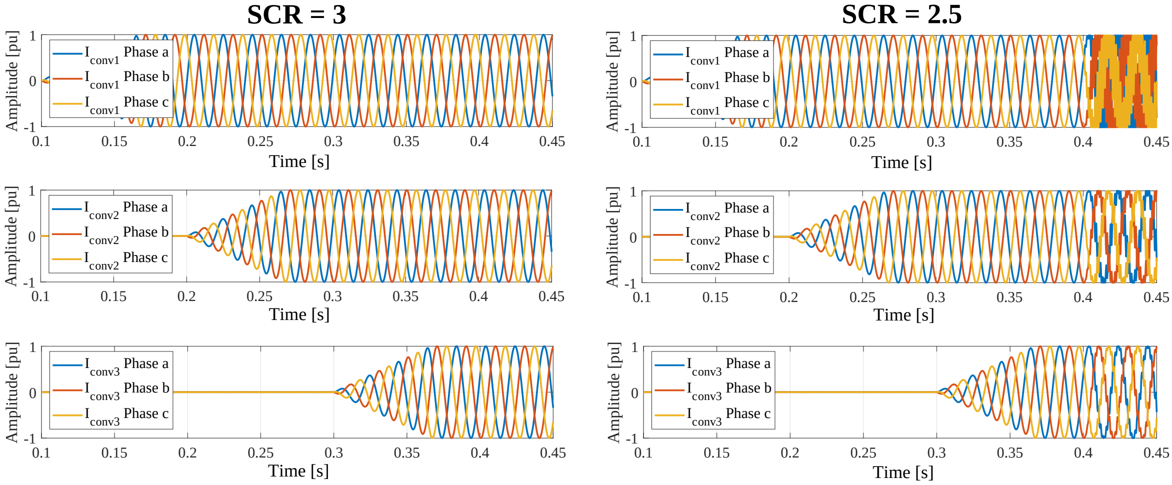

(a) (b)

Figure 4.7: Simulation results: f_{c1} from 180 Hz to 200 Hz at t = 0.4 s, f_{c2}= 100 Hz, f_{c3}= 50 Hz. (a) SCR=3; (b) SCR=2.5.

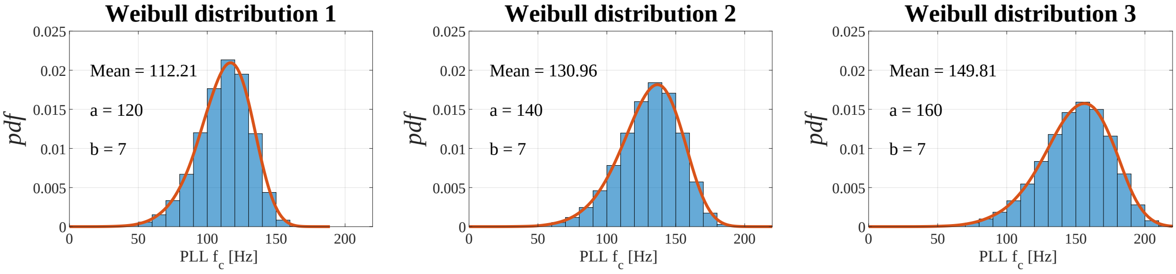

(a) (b) (c)

Figure 4.8: Probability density functions of PLL-bandwidths adopted for the MC analysis: (a) distribution 1, (b) distribution 2, (c) distribution 3.

PLL-bandwidth corresponding to the critical one reported in Fig. 4.4, hence confirming the results predicted by the performed frequency-domain analysis.

4.1.3 Monte-Carlo analysis

It has been shown in the previous subsections, that for the specific system configuration under study, it is possible to calculate a norm-based stability margin, whose lack of conservatism can be mathematically proven. The limitations of the impedance-based approach in assessing the effects of parameter variations on system stability, have been discussed in Section 3.2. To this extent, the stability margin calculation discussed in the previous sections, along with a MC simulation approach, can provide an useful insight into parameters sensitivity.

In the following, a MC analysis is performed in order to assess how the interactions between synchronization units of converters operating nearby are affected by the grid conditions. In order to generate the random samples needed for the analysis, three PLL-bandwidth distributions are first identified, and reported in Fig. 4.8. These represent three Weibull distributions, whose parameters are also reported in the respective figures. Similar to the example of Fig. 3.5 (a), the scale parameters a has been varied, while the shape parameter b has

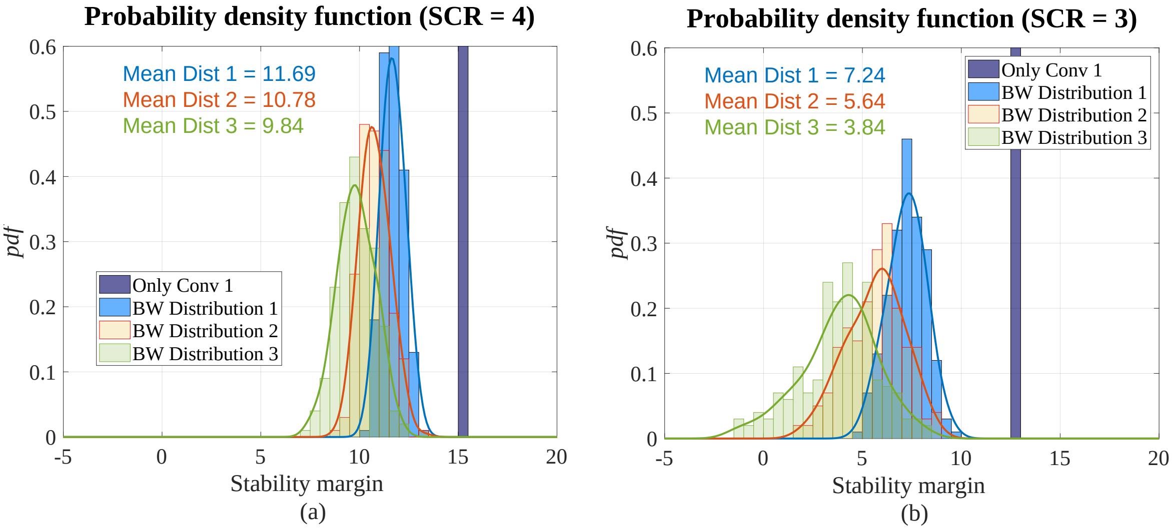

Figure 4.9: Simulation results: (a) SCR = 4, (b) = SCR = 3. (Violet bars) only Converter 1 in operation, (Blue bars) pdf from Weibull distribution 1, (blue line) pdf fitting from Weibull distribution 1, (red bars) pdf from Weibull distribution 2, (red line) pdf fitting from Weibull distribution 1, (green bars) pdf from Weibull distribution 3, (green line) pdf fitting from Weibull distribution 3.

been maintained constant, causing a shift of the distribution on the x-axis. The resulting mean value for each distribution is also reported in the figure, along with the kernel density estimators represented by the red lines. System parameters are reported in Table 4.1, with the exception of the impedances between converters, which have been set to constant values equal for the three converters. These represent the impedances of the corresponding transformers plus connection lines between the transformers and the network bus, whose inductive and resistive components are set to $L_c = 0.045\ pu$ and $R_c = 0.006\ pu$, respectively.

Fig. 4.9 shows the results of the performed MC analysis. The violet bars in the figure, correspond to the calculated stability margin when only one converter is in operation, injecting its rated power, and with a f_{c1} = 100 Hz, while it is assumed that the other two converters are switched OFF. Subsequently, maintaining f_{c1} constant to 100 Hz, random values for the PLL-bandwidths of the other two converters are drawn from each of the distributions shown in Fig. 4.8, and hundreds of simulations have been performed, also assuming that each converter injects its rated power. This process has been repeated for two different values of the grid SCR, namely for SCR = 4 and SCR = 3, and the results are reported in Fig. 4.9 (a) and (b), respectively, where the obtained pdfs are shown, along with the respective kernel approximations. Following conclusions can be drawn:

- The shift of the violet bar toward lower values of the x-axis, indicates a reduction of the converter stability margin when the converter operates alone and the grid SCR is reduced.
- The presence of other converters operating nearby further reduces the resulting stability margin, becoming this trend more accentuated when the average PLL-bandwidth of the converters operating nearby is increased.

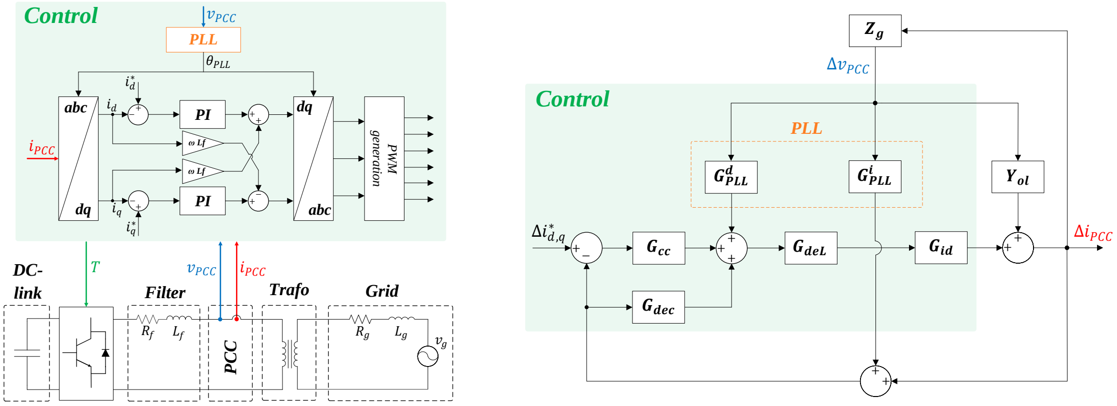

(a) (b)

Figure 4.10: Effects of the inner current control loop on the obtained results: (a) control structure considered for the analysis; (b) small-signal model of the converter including a PI-based inner current control loop.

- Each distribution results more spread in the x-axis, the lower the grid SCR becomes. This trend reveals that the effects of the interactions among synchronization units of converters operating nearby become stronger by reducing the grid SCR.

4.1.4 Effects of the inner current control loop

The converter control structure adopted for the analysis, and presented in Section 4.1.1, is strongly simplified, and the effects of several control loops have been neglected. However, these simplifications allow highlighting the effects of the interactions among synchronization units of converters operating nearby, yet obtaining qualitatively valid results. One of the assumptions made for the analysis, concerns the behaviour of the inner current control loop, which has been modeled as a unitary gain, resulting in an ideal current source behaviour of the converter. In the following, the effects due to the inclusion of an inner current control loop on the performed analysis are investigated.

To this extent, various current control techniques are employed in real industrial applications. Beside the standard current control approaches extensively mentioned in the academic literature, and based on PI or PR controllers [25], other non-linear techniques are also widely used. These comprise for example the already mentioned HCC [170], which directly controls the states of the converter without the need for a PWM modulation, as well as sliding mode controls [112], [171], or model predictive controllers [172], [173], also broadly adopted for wind applications [174]. Nevertheless, the modeling of PI current controllers in the SRF has been widely documented in the literature for the purposes of impedance-based analysis [66], [160], and is considered in the following.

In order to show the effects of an inner current control loop on the results of the stability analysis performed in this section, the case of a single converter connected to the grid by means of an inductive filter is considered. The considered control structure is shown in Fig. 4.10 (a), while the corresponding small-signal model including the effects of the PLL is shown in Fig. 4.10 (b). Beside $\mathbf{Z}_g$, seven 2×2 transfer function matrices appear in Fig. 4.10 (b), reported below for sake of clarity, but whose derivation has been comprehensively discussed in the literature [66], [68], [160], and thus not repeated here.

The transfer function matrix $\mathbf{G}^{d}_{PLL}(s)$ represents the effects of the PLL on the duty-cycle of the converter and is defined as:

$$\mathbf{G}^{d}_{PLL}(s) = \begin{bmatrix} 0 & -D_{cq}H_{PLL}(s) \\ 0 & D_{cd}H_{PLL}(s) \end{bmatrix} \tag{4.15}$$

where $H_{PLL}(s)$ has been reported in eq. (4.4), and D_{cd} and D_{cq} are the d and q components of the duty-ratio at the operating point, respectively [160]. $\mathbf{G}^{i}_{PLL}(s)$ corresponds to the matrix already defined in eq. (4.3), which, assuming a perfect current source bahviour of the converter, directly coincides with the equivalent output admittance, and represents instead the effects of the PLL on the measured converter currents in this case. Indicating with k_{pi}, and k_{ii} the proportional and the integral gain of the PI controller, respectively, the transfer function matrices $\mathbf{G}_{cc}(s)$, accounting for the current control, and $\mathbf{G}_{dec}(s)$, representing the contribution of the decoupling terms, are defined as follows:

$$\mathbf{G}_{cc}(s) = \begin{bmatrix} \frac{sk_{pi}+k_{ii}}{s} & 0 \\ 0 & \frac{sk_{pi}+k_{ii}}{s} \end{bmatrix} \tag{4.16}$$

$$\mathbf{G}_{dec}(s) = \begin{bmatrix} 0 & -\frac{3\omega_g L_f}{V_{DC}} \\ \frac{3\omega_g L_f}{V_{DC}} & 0 \end{bmatrix} \tag{4.17}$$

where L_f indicates the filter inductance, and V_{DC} the value of the converter DC-link voltage. Defining $T_{del} = 1.5/f_s$, with f_s converter switching frequency, the matrix $\mathbf{G}_{del}(s)$ models the effects of the delay introduced by the modulation:

$$\mathbf{G}_{del}(s) = \begin{bmatrix} \frac{1-s(T_{del}/2)}{1+s(T_{del}/2)} & 0 \\ 0 & \frac{1-s(T_{del}/2)}{1+s(T_{del}/2)} \end{bmatrix} \tag{4.18}$$

$\mathbf{Y}_{ol}(s)$ accounts for the open loop output admittance of the converter without considering the control:

$$\mathbf{Y}_{ol}(s) = \frac{1}{(sL_f+R_f)^2+(\omega_g L_f)^2} \begin{bmatrix} sL_f+R_f & \omega_g L_f \\ -\omega_g L_f & sL_f+R_f \end{bmatrix} \tag{4.19}$$

with R_f representing the resistive component of the filter impedance. $\mathbf{G}_{id}(s)$ is the transfer function between the duty-ratio of the converter and the inductor current, and is given by:

$$\mathbf{G}_{id}(s) = -V_{DC}\mathbf{Y}_{ol}(s) \tag{4.20}$$

Table 4.2: Simulation parameters

Description	Symbol	Value	Description	Symbol	Value
Converter nominal power	S_n	300 kVA	Filter inductance	L_f	0.1 pu
Line-to-line voltage	V_{LL}	400 V (rms)	Filter resistance	R_f	0.04 pu
Rated grid frequency	f_g	50 Hz	DC-link voltage	V_{DC}	750 V

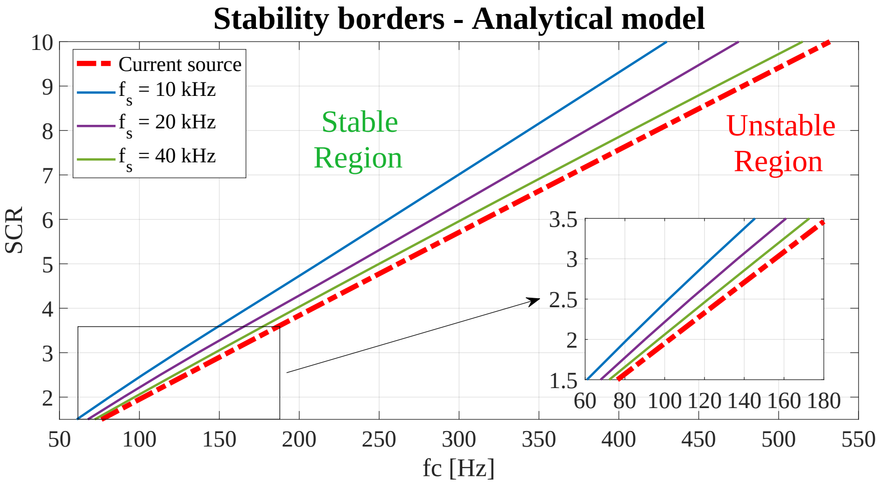

Figure 4.11: Stability borders calculated analytically. (Red-dashed) ideal current source model; (continuous-blue) f_s =10 kHz; (continuous-violet) f_s = 20 kHz; (continuous-green) f_s = 40 kHz.

The equivalent output impedance of the converter can be then calculated according to the following equation [66]:

$$\mathbf{Z}_{oCC}(s) = \Big(\mathbf{Y}_{ol}(s) + \mathbf{G}_{id}(s)\mathbf{G}_{del}(s)\mathbf{G}^{d}_{PLL}(s) + \mathbf{G}_{id}(s)\mathbf{G}_{del}(s)\big(-\mathbf{G}_{ci}(s)+\mathbf{G}_{dec}(s)\big)\mathbf{G}^{i}_{PLL}(s)\Big)^{-1} \times \Big(\mathbf{I}+\mathbf{G}_{id}(s)\mathbf{G}_{del}(s)\big(\mathbf{G}_{ci}(s)-\mathbf{G}_{dec}(s)\big)\Big) \tag{4.21}$$

Considering the system parameters reported in Table 4.2, the borders between stable and unstable operating regions are shown in Fig. 4.11, which have been obtained calculating the eigenvalues of (4.7). The control parameters of the PI current control have been tuned according to the technical optimum technique [25], while different switching frequencies of the converter have been taken into account. The red-dashed line represents the results obtained by considering the perfect current source behaviour of the converter, while the three continuous lines represent the results obtained considering different converter switching frequencies, and namely f_s = 10 kHz (blue line), 20 kHz (violet line), and 40 kHz (green line). Following conclusions can be drawn:

- The conditions proving the non-conservative nature of the results obtained by emplying the proposed norm calculation are not fulfilled when the full-model is considered, and the calculated stability margin by means of eq. (4.8) does not provide a reliable estimation of the real system conditions any longer. As a consequence, another stability margin calculation for MIMO systems should be adopted in order to perform a MC analysis similar to the one presented in Section 4.1.3.

- The calculation of the equivalent output admittance of the converter by means of eq. (4.21) noticeably increases the computational burden, especially when more than one converter is included in the analysis. The use of a software allowing symbolic calculation might help in this process, as also suggested in [68]. The results shown in Fig. 4.11, have been obtained with the aid of the symbolic toolbox of MATLAB.
- Compared to the results obtained by considering the perfect current source behaviour of the converter, instability tends to occur at lower PLL-bandwidths when the inner current control loop implemented by means of PI controllers is included in the analysis, becoming this effect more accentuated for higher values of the grid SCR. Nevertheless, Fig. 4.11 indicates that the use of a simplified converter model can still provide reliable results in view of the qualitative analysis pursued in this section, with the advantage of noticeably reducing model complexity.

4.2 Eigenvalue-based stability analysis of GFM converters

The interactions between synchronization units of GFL converters operating nearby have been investigated in the previous section, by employing the impedance-based approach. In this section, stability of GFM converters is investigated by means of eigenvalue analysis. According to the considerations reported in Section 2.4, several possible combinations of the inner and outer loops can be chosen in order to implement the control of a GFM converter. In the following, the VSM implementation labeled as synchronverter is adopted for the analysis [40], [41]. In fact, it has been discussed in Section 2.4, how by properly choosing the synchronverter parameters, several of the power-synchronization loops among those reported in the literature can be reproduced. Eigenvalue analysis is first applied to the case of a single GFM converter operating alone, and a simplified tuning procedure is proposed. Then the analysis is extended to the case of two GFM converters operating in parallel, and modal analysis is performed. This allows identifying the states mainly affecting critical system modes, and possible countermeasures for ensuring stable operation are evaluated.

4.2.1 Small-signal model of LCL filter-based synchronverter

The motivation behind the widespread use of the synchronverter in the GFM literature have been reported in Section 2.4.1. It became very popular in the last decade, due to its simple and intuitive working principle, and due to its capability of self-synchronization to the grid without the need of a dedicated unit, both for pre-synchronization purposes, as well as during normal operation. A significant amount of literature has been published regarding synchronverter stability analysis, and control parameter tuning [78], [79], [98], [175]-[177]. Some of the aforementioned works rely on strong assumptions, such as an high grid SCR [98], [175], whereas other works have presented approaches based on reduced-order models of the system, and propose pole placement at prescribed locations as optimal tuning procedure [78].

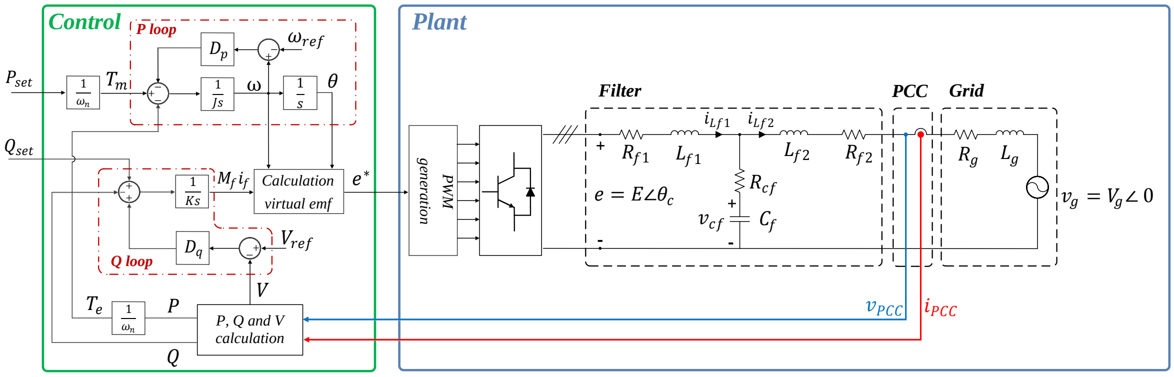

Figure 4.12: Scheme of the system under study: LCL filter-based synchronverter connected to the grid.

Eigenvalue analysis is often preferred for stability assessment and parameter tuning of synchronverters (and VSMs in general) [79], in comparison to the impedance-based approach, where only few examples are reported, e. g. in [176], and [178]. Due to the MIMO nature of the system caused by the coupling between active and reactive power loops, that cannot be neglected in many real applications, a multivariable approach for stability analysis is the most suitable choice, which will be addressed in the next section. Furthermore, the effects caused by the presence of a converter filter, usually implemented by LC or LCL structures, are often neglected in the mentioned literature.

In the following, the small-signal model of a synchronverter connected to the grid by means of an LCL filter is presented, along with a simple design procedure, introduced in order to choose realistic control parameters for the stability analysis performed in the next section.

Small-signal model

Fig. 4.12 shows the scheme of the studied system, namely a synchronverter connected to the grid through an output LCL filter. The linearized system model is obtained by splitting the system into two independent subsystems, namely the control C and the plant Π, composed of the filter and the grid. Fig. 4.13 shows the elements of the input and output vectors of the linearized subsystems, indicated respectively with $\mathbf{u}_c$ and $\mathbf{y}_c$ for the control subsystem, and $\mathbf{u}_\pi$ and $\mathbf{y}_\pi$ for the plant subsystem. The interconnected system, whose inputs and outputs are indicated in the figure by the dark blue and dark red arrows, respectively, is obtained by means of the CCM method, already introduced in Section 3.3.3.

The synchronverter structure presented in Fig. 4.12, is composed of two separated loops, one for the active power P, and the other one for the reactive power Q, which have been examined in detail in Section 2.4. The active power loop emulates the frequency droop mechanism of a SM, described by the well-known swing equation already reported in (2.16), and repeated here for simplicity:

$$J\dot{\omega} = T_m - T_e - D_p\omega \tag{4.22}$$

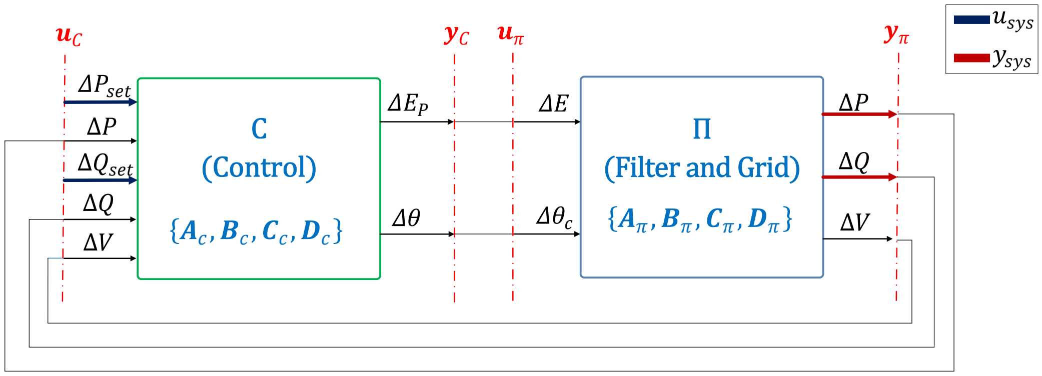

Figure 4.13: Inputs and outputs of the two linearized subsystems.

with J representing the mechanical (virtual) moment of inertia, ω the virtual rotor speed, D_p is the feedback gain accounting for the (virtual) mechanical friction of the machine, T_e is the electrical torque, and T_m is the mechanical one. As already pointed out in Section 2.4.1, D_p does not only represent the virtual mechanical friction, but it also accounts for the active power-frequency $P-f$ droop coefficient of the control. However, the modification to the synchronverter structure proposed in [80], elaborated in order to decouple the dynamic of the control from the droop coefficient, and compensate for the lack of this additional degree of freedom, is not considered here. Furthermore, it has been mentioned in Section 2.4.1 that the $P-f$ droop action can be disabled by means of a PI controller, yet it is assumed for simplicity that the droop control is always activated (PI action off).

The reactive power loop is conceptually similar to the active power loop. A reactive power-voltage droop $Q-V$ reacts to a voltage deviation ΔV from its nominal/reference value with a reactive power setpoint variation ΔQ, according to the following equation:

$$\Delta Q = -D_q \Delta V \tag{4.23}$$

The instantaneous reactive power measured at the converter terminals is then compared to its power setpoint Q_{set}, and added to the output of the $Q-V$ droop. An integrator with gain $1/K$ processes the sum of these quantities, producing the virtual mutual flux $M_f i_f$, which multiplied by the rotor speed ω, produces the amplitude of the virtual back-emf E_p. The linearization of this product yields:

$$\Delta E_p = M_f i_{f0}\, \Delta\omega + \Delta M_f i_f\, \omega_0 \tag{4.24}$$

where quantities with subscript "0" denote values at the operating point. As discussed in Section 2.4, the virtual back-emf voltages e^* are directly used for the PWM in the original synchronverter structure. Thus, the amplitude E and the phase θ_c of the converter voltage correspond to the amplitude of the virtual back-emf E_p, and the virtual rotor angle θ.

Defining with $\mathbf{x}_c = [\Delta M_f i_f \quad \Delta\omega \quad \Delta\theta]$ the state vector of the control subsystem, the state-space matrices $\mathbf{A}_c$, $\mathbf{B}_c$, $\mathbf{C}_c$, and $\mathbf{D}_c$ are given by:

$$\mathbf{A}_c = \begin{bmatrix} 0 & 0 & 0 \\ 0 & -\frac{D_p}{J} & 0 \\ 0 & 1 & 0 \end{bmatrix}; \qquad \mathbf{B}_c = \begin{bmatrix} 0 & 0 & \frac{1}{K} & -\frac{1}{K} & -\frac{D_q}{K} \\ \frac{1}{\omega_0 J} & -\frac{1}{\omega_0 J} & 0 & 0 & 0 \\ 0 & 0 & 0 & 0 & 0 \end{bmatrix};$$

$$\mathbf{C}_c = \begin{bmatrix} \omega_0 & M_f i_{f0} & 0 \\ 0 & 0 & 1 \end{bmatrix}; \qquad \mathbf{D}_c = \begin{bmatrix} 0^{2\times 5} \end{bmatrix}. \tag{4.25}$$

The state-space description of the plant is obtained by writing the equations in *dq* coordinates, and adding small perturbations:

$$\begin{cases} C_f \frac{d\Delta v_{cfd}}{dt} = \Delta i_{Lf1d} - \Delta i_{Lf2d} + \omega_0 C_f \Delta v_{cfq} \\ C_f \frac{d\Delta v_{cfq}}{dt} = \Delta i_{Lf1q} - \Delta i_{Lf2q} - \omega_0 C_f \Delta v_{cfd} \end{cases} \tag{4.26}$$

$$\begin{cases} L_{f1} \frac{d\Delta i_{Lf1d}}{dt} = -E_0 \sin\theta_0 \Delta\theta - \Delta E \cos\theta_0 - \Delta v_{cfd} + \\ \qquad -R_{f1} \Delta i_{Lf1d} - R_{cf}(\Delta i_{Lf1d} - \Delta i_{Lf2d}) + \omega_0 L_{f1} \Delta i_{Lf1q} \\ L_{f1} \frac{d\Delta i_{Lf1q}}{dt} = E_0 \cos\theta_0 \Delta\theta + \Delta E \sin\theta_0 - \Delta v_{cfq} + \\ \qquad -R_{f1} \Delta i_{Lf1q} - R_{cf}(\Delta i_{Lf1q} - \Delta i_{Lf2q}) - \omega_0 L_{f1} \Delta i_{Lf1d} \end{cases} \tag{4.27}$$

$$\begin{cases} (L_{f2} + L_g) \frac{d\Delta i_{Lf2d}}{dt} = \Delta v_{cfd} + R_{cf}(\Delta i_{Lf1d} - \Delta i_{Lf2d}) + \\ \qquad -(R_{f2} + R_g) \Delta i_{Lf2d} + \omega_0 (L_{f2} + L_g) \Delta i_{Lf2q} \\ (L_{f2} + L_g) \frac{d\Delta i_{Lf2q}}{dt} = \Delta v_{cfq} + R_{cf}(\Delta i_{Lf1q} - \Delta i_{Lf2q}) + \\ \qquad -(R_{f2} + R_g) \Delta i_{Lf2q} - \omega_0 (L_{f2} + L_g) \Delta i_{Lf2d} \end{cases} \tag{4.28}$$

linearization is required in order to calculate active and reactive power, as well as the amplitude of the voltage V measured at the connection point. In fact, according to [56], P and Q can be calculated from the *dq* components of voltages and currents as:

$$\begin{cases} P = \frac{3}{2}(i_{Lf2d} v_{PCCd} + i_{Lf2q} v_{PCCq}) \\ Q = \frac{3}{2}(i_{Lf2d} v_{PCCq} - i_{Lf2q} v_{PCCd}) \end{cases} \tag{4.29}$$

where v_{PCCd} and v_{PCCq} are the d and q components of the voltages at the PCC respectively, while i_{Lf2d} and i_{Lf2q} are the components of the current flowing into the grid, which in this case corresponds to the current flowing through L_{f2} and L_g. Linearizing eq.(4.29) yields:

$$\begin{cases} \Delta P = \frac{3}{2}(I_{Lf2d0} \Delta v_{PCCd} + V_{PCCd0} \Delta i_{Lf2d} + V_{PCCq0} \Delta i_{Lf2q} + I_{Lf2q0} \Delta v_{PCCq}) \\ \Delta Q = \frac{3}{2}(V_{PCCq0} \Delta i_{Lf2d} + I_{Lf2d0} \Delta v_{PCCq} - V_{PCCd0} \Delta i_{Lf2q} + I_{Lf2q0} \Delta v_{PCCd}) \end{cases} \tag{4.30}$$

where V_{PCCd0}, V_{PCCd0}, I_{Lf2d0}, and I_{Lf2d0} indicate voltages and currents at the operating point, and:

$$\begin{cases} \Delta v_{PCCd} = \Delta v_{cfd} + R_{cf}(\Delta i_{Lf1d} - \Delta i_{Lf2d}) - R_{f2}\Delta i_{Lf2d} - L_{f2}\frac{di_{Lf2d}}{dt} + \omega_0 L_{f2}\Delta i_{Lf2q} \\ \Delta v_{PCCq} = \Delta v_{cfq} + R_{cf}(\Delta i_{Lf1q} - \Delta i_{Lf2q}) - R_{f2}\Delta i_{Lf2q} - L_{f2}\frac{di_{Lf2q}}{dt} - \omega_0 L_{f2}\Delta i_{Lf2d} \end{cases} \tag{4.31}$$

The amplitude of the voltage at the PCC can be obtained as follows:

$$V = \sqrt{v_{PCCd}^2 + v_{PCCq}^2} \tag{4.32}$$

Indicating with $\Delta_{dq0} = \left(V_{PCCd0}^2 + V_{PCCq0}^2\right)$, the linearization of (4.32) produces:

$$\Delta V = \frac{V_{PCCd0}\Delta v_{PCCd} + V_{PCCq0}\Delta v_{PCCq}}{\sqrt{\Delta_{dq0}}} \tag{4.33}$$

Defining with $\mathbf{x}_\pi = [\Delta v_{cfd} \quad \Delta v_{cfq} \quad \Delta i_{Lf1d} \quad \Delta i_{Lf1q} \quad \Delta i_{Lf2d} \quad \Delta i_{Lf2q}]$ the state vector of the plant subsystem, the state-space matrices $\mathbf{A}_\pi$, $\mathbf{B}_\pi$, $\mathbf{C}_\pi$, and $\mathbf{D}_\pi$ are given by:

$$\mathbf{A}_\pi = \begin{bmatrix} 0 & \omega_0 & \frac{1}{C_f} & 0 & -\frac{1}{C_f} & 0 \\ -\omega_0 & 0 & 0 & \frac{1}{C_f} & 0 & -\frac{1}{C_f} \\ -\frac{1}{L_{f1}} & 0 & -\frac{R_{f1}+R_{cf}}{L_{f1}} & \omega_0 & \frac{R_{cf}}{L_{f1}} & 0 \\ 0 & -\frac{1}{L_{f1}} & -\omega_0 & -\frac{R_{f1}+R_{cf}}{L_{f1}} & 0 & \frac{R_{cf}}{L_{f1}} \\ \frac{1}{L_g+L_{f2}} & 0 & \frac{R_{cf}}{L_g+L_{f2}} & 0 & -\frac{R_{cf}+R_{f2}+R_g}{L_g+L_{f2}} & \omega_0 \\ 0 & \frac{1}{L_g+L_{f2}} & 0 & \frac{R_{cf}}{L_g+L_{f2}} & -\omega_0 & -\frac{R_{cf}+R_{f2}+R_g}{L_g+L_{f2}} \end{bmatrix};$$

$$\mathbf{B}_\pi^T = \begin{bmatrix} 0 & 0 & \frac{\cos\theta_0}{L_{f1}} & \frac{\sin\theta_0}{L_{f1}} & 0 & 0 \\ 0 & 0 & -\frac{V_0\sin\theta_0}{L_{f1}} & \frac{V_0\cos\theta_0}{L_{f1}} & 0 & 0 \end{bmatrix}; \quad \mathbf{D}_\pi = \left[0^{3\times 2}\right];$$

$$\mathbf{C}_\pi^T = \frac{3}{2}\begin{bmatrix} I_{Lf2d0}\frac{L_g}{L_g+L_{f2}} & -I_{Lf2q0}\frac{L_g}{L_g+L_{f2}} & \frac{2}{3}\frac{V_{PCCd0}}{\sqrt{\Delta_{dq0}}}\frac{L_g}{L_g+L_{f2}} \\ I_{Lf2q0}\frac{L_g}{L_g+L_{f2}} & I_{Lf2d0}\frac{L_g}{L_g+L_{f2}} & \frac{2}{3}\frac{V_{PCCq0}}{\sqrt{\Delta_{dq0}}}\frac{L_g}{L_g+L_{f2}} \\ I_{Lf2d0}\frac{R_{cf}L_g}{L_g+L_{f2}} & -I_{Lf2q0}\frac{R_{cf}L_g}{L_g+L_{f2}} & \frac{2}{3}\frac{V_{PCCd0}}{\sqrt{\Delta_{dq0}}}\frac{R_{cf}L_g}{L_g+L_{f2}} \\ I_{Lf2q0}\frac{R_{cf}L_g}{L_g+L_{f2}} & I_{Lf2d0}\frac{R_{cf}L_g}{L_g+L_{f2}} & \frac{2}{3}\frac{V_{PCCq0}}{\sqrt{\Delta_{dq0}}}\frac{R_{cf}L_g}{L_g+L_{f2}} \\ \left[I_{Lf2d0}\frac{L_{f2}R_g-L_gR_{f2}-R_{cf}L_g}{L_g+L_{f2}} + V_{PCCd0}\right] & \left[V_{PCCq0} - I_{Lf2q0}\frac{L_{f2}R_g-L_gR_{f2}-R_{cf}L_g}{L_g+L_{f2}}\right] & \frac{2}{3}\frac{V_{PCCd0}}{\sqrt{\Delta_{dq0}}}\frac{R_gL_{f2}-R_{f2}L_g-R_{cf}Lg}{L_g+L_{f2}} \\ \left[I_{Lf2q0}\frac{L_{f2}R_g-L_gR_{f2}-R_{cf}L_g}{L_g+L_{f2}} + V_{PCCq0}\right] & \left[I_{Lf2d0}\frac{L_{f2}R_g-L_gR_{f2}-R_{cf}L_g}{L_g+L_{f2}} - V_{PCCd0}\right] & \frac{2}{3}\frac{V_{PCCq0}}{\sqrt{\Delta_{dq0}}}\frac{R_gL_{f2}-R_{f2}L_g-R_{cf}Lg}{L_g+L_{f2}} \end{bmatrix}. \tag{4.34}$$

The general state-space representation of the interconnected system has been reported in (3.44), and is shown below for simplicity:

$$\begin{cases} \dot{\mathbf{x}}_{sys} = \mathbf{F}_{int}\,\mathbf{x}_{sys} + \mathbf{G}_{int}\,\mathbf{u}_{sys} \\ \mathbf{y}_{sys} = \mathbf{H}_{int}\,\mathbf{x}_{sys} + \mathbf{J}_{int}\,\mathbf{u}_{sys} \end{cases} \tag{4.35}$$

where $\mathbf{u}_{sys} = [\Delta P_{set}\ \Delta Q_{set}]^T$, $\mathbf{y}_{sys} = [\Delta P\ \Delta Q]^T$, and $\mathbf{x}_{sys} = [\mathbf{x}_c\ \mathbf{x}_\pi]^T$. The matrices $\mathbf{F}_{int}$, $\mathbf{G}_{int}$, $\mathbf{H}_{int}$ and $\mathbf{J}_{int}$ are calculated according to (3.46), with $\mathbf{A}_d$, $\mathbf{B}_d$, $\mathbf{C}_d$ and $\mathbf{D}_d$ given by:

$$\begin{cases} \mathbf{A}_d = diag\{\mathbf{A}_c, \mathbf{A}_\pi\} \\ \mathbf{B}_d = diag\{\mathbf{B}_c, \mathbf{B}_\pi\} \\ \mathbf{C}_d = diag\{\mathbf{C}_c, \mathbf{C}_\pi\} \\ \mathbf{D}_d = diag\{\mathbf{D}_c, \mathbf{D}_\pi\} \end{cases} \tag{4.36}$$

Finally, defining the following vectors $\mathbf{u}_{sub} = [\mathbf{u}_c\ \mathbf{u}_\pi]^T$, and $\mathbf{y}_{sub} = [\mathbf{y}_c\ \mathbf{y}_\pi]^T$, the interconnection matrices for the considered case study are given below:

$$\mathbf{L}_{11} = \begin{bmatrix} 0&0&0&0&0 \\ 0&0&1&0&0 \\ 0&0&0&0&0 \\ 0&0&0&1&0 \\ 0&0&0&0&1 \\ 1&0&0&0&0 \\ 0&1&0&0&0 \end{bmatrix};\quad \mathbf{L}_{12} = \begin{bmatrix} 1&0 \\ 0&0 \\ 1&0 \\ 0&0 \\ 0&0 \\ 0&0 \\ 0&0 \end{bmatrix};\quad \mathbf{L}_{21}^T = \begin{bmatrix} 0&0 \\ 0&0 \\ 1&0 \\ 0&1 \\ 0&0 \end{bmatrix};\quad \mathbf{L}_{22} = \begin{bmatrix} 0^{2\times 2} \end{bmatrix}. \tag{4.37}$$

The initial operating conditions can be obtained by solving the following system of equations obtained from the linearization process of (4.26)-(4.28):

$$\begin{cases} V_g = V_{PCCd0} - R_g I_{Lf2d0} + \omega_0 L_g I_{Lf2q0} \\ 0 = V_{PCCq0} - R_g I_{Lf2q0} - \omega_0 L_g I_{Lf2d0} \\ E_0 \cos\theta_0 = V_{cd0} + (R_{cf} + R_{f1}) I_{Lf1d0} - R_{cf} I_{Lf2d0} - \omega_0 L_{f1} I_{Lf1q0} \\ E_0 \sin\theta_0 = V_{cq0} + (R_{cf} + R_{f1}) I_{Lf1q0} - R_{cf} I_{Lf2q0} + \omega_0 L_{f1} I_{Lf1d0} \\ 0 = I_{Lf1d0} - I_{Lf2d0} + \omega_0 C_f V_{cq0} \\ 0 = I_{Lf1q0} - I_{Lf2q0} - \omega_0 C_f V_{cd0} \\ V_g = V_{cd0} + R_{cf} I_{Lf1d0} - R_{sum} I_{Lf2d0} + \omega_0 (L_g + L_{f2}) I_{Lf2q0} \\ 0 = V_{cq0} + R_{cf} I_{Lf1q0} - R_{sum} I_{Lf2q0} - \omega_0 (L_g + L_{f2}) I_{Lf2d0} \end{cases} \tag{4.38}$$

where V_g is the amplitude of the grid voltage, and R_{sum} accounts for the sum of R_{cf}, R_{f2}, and R_g.

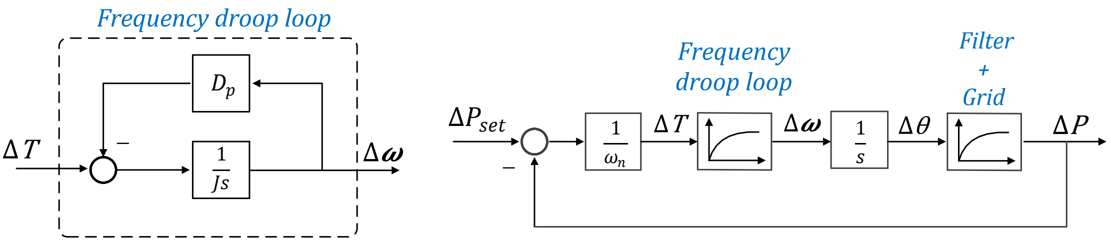

(a) (b)

Figure 4.14: (a) Simplified frequency droop loop, (b) simplified active power loop.

4.2.2 Parameter tuning and eigenvalue analysis

In order to investigate the behaviour of the synchronverter under different grid conditions, a simple and intuitive approach for tuning the control parameters is adopted in the following. It aims to the optimization of the step response of the converter in terms of rise-time, overshoot, and settling-time. Active and reactive power loops are considered separately, and the transfer functions of each loop are approximated to second-order equations. Control parameters are then calculated in order to obtain a damping ratio of the resulting approximated transfer function of $1/\sqrt{2}$ which, according to control theory [67], represents the optimal parameter tuning of a second-order system. It is, however, worth to notice, that the adopted simplifications might result in design errors, with possible repercussions on control performances. In fact, even if the full-order model of the system would be considered, separating the two loops might lead to erroneous results due to the cross-coupling between active and reactive power taking place in the real system. Thus, the tuning procedure presented below will be refined in the next section, in order to consider the MIMO nature of the system.

According to the control structure shown in Fig. 4.12, four parameters need to be tuned, and namely the $P-f$ droop coefficient D_p, and the virtual moment of inertia J of the active power loop, along with the $Q-V$ droop coefficient D_q, and the K factor of the reactive power loop. However, droop coefficients are usually fixed in order to comply with grid code requirements, and typical values are in the range of 5 % [31]. Considering this indication as a design guideline, only J and K can be adjusted in order to improve the dynamic behaviour of the system. Nevertheless, the procedure reported below can be also adopted for the case that the four parameters are freely adjustable. Furthermore, the design of the filter hardware components is not explicitly addressed in this work, yet it is assumed that filter parameters are tuned according to the filter design procedure reported in [179].

The simplified scheme of the synchronverter frequency droop loop is shown in Fig. 4.14 (a), and it is described by the following first-order transfer function:

$$\frac{\Delta\omega}{\Delta T}(s) = \frac{\frac{1}{D_p}}{1+s\,\frac{J}{D_p}} = \frac{K_f}{1+s\,\tau_f} \tag{4.39}$$

Fig. 4.14 (b) shows the simplified scheme of the active power closed-loop. A first-order transfer function is adopted in order to account for the filter and the grid, which is given

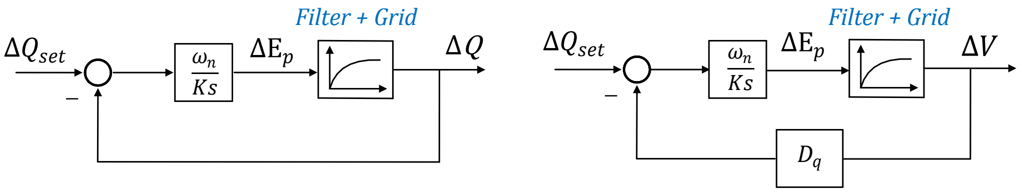

(a) (b)

Figure 4.15: (a) Simplified reactive power loop scheme, (b) simplified $Q-V$ loop scheme.

by the $\frac{\Delta P}{\Delta\theta}$ transfer function of the plant Π. This represents a second-order transfer function with two poles, whose time constants are indicated with τ_1 and τ_2, respectively. The transfer function $\frac{\Delta P}{\Delta\theta}$ approximation is given by:

$$PT1_P(s) = \frac{S_{sp}}{1+s\ \tau_{refp}} \tag{4.40}$$

where S_{sp} is the steady-state value of $\frac{\Delta P}{\Delta\theta}$, and τ_{refp} is the time constant of its dominant pole. Under the assumption that the virtual moment of inertia J is chosen sufficiently small (e. g. $\tau_f \approx \tau_{refp}/10$), the dynamic of the frequency droop loop can be neglected, and the power loop is approximated to the following second-order transfer function:

$$P_{app}(s) = \frac{1}{T_p^2 s^2 + 2\zeta_p T_p s + 1} \tag{4.41}$$

where T_p and ζ_p represent the inverse natural frequency and the damping ratio of the approximated transfer function, respectively:

$$T_p = \sqrt{\frac{\tau_{refp}\,\omega_n D_p}{S_{sp}}} \quad ; \quad \zeta_p = \frac{1}{2}\sqrt{\frac{D_p\,\omega_n}{\tau_{refp}\,S_{sp}}} \tag{4.42}$$

Therefore, assuming that D_P is already set in order to comply with the steady-state performance requirements, the damping of the simplified second-order active power loop cannot be influenced otherwise [80]. If instead D_P is freely adjustable, it can be tuned so as to obtain a resulting $\zeta_p = 1/\sqrt{2}$. It is worth to remark, that the choice of J indicated above, makes the control behaving similarly as the droop controller already discussed in Section 2.4, while the effects of this parameter on the converter dynamic, as well as on its stability are investigated in the following of this chapter.

A similar approach is proposed here for the tuning of the reactive power loop. Nevertheless, due to the $Q-V$ droop, two separated loops are identified, and namely a reactive power and a voltage control loop, respectively shown in Fig. 4.15 (a) and (b). Also in this case, the transfer functions $\frac{\Delta Q}{\Delta E_p}$ and $\frac{\Delta V}{\Delta E_p}$ of the plant Π are approximated to first-order transfer functions, indicated as $PT1_Q$ and $PT1_V$, respectively:

$$PT1_Q(s) = \frac{S_{sq}}{1+s\ \tau_{refq}} \quad ; \quad PT1_V(s) = \frac{S_{sv}}{1+s\ \tau_{refv}} \tag{4.43}$$

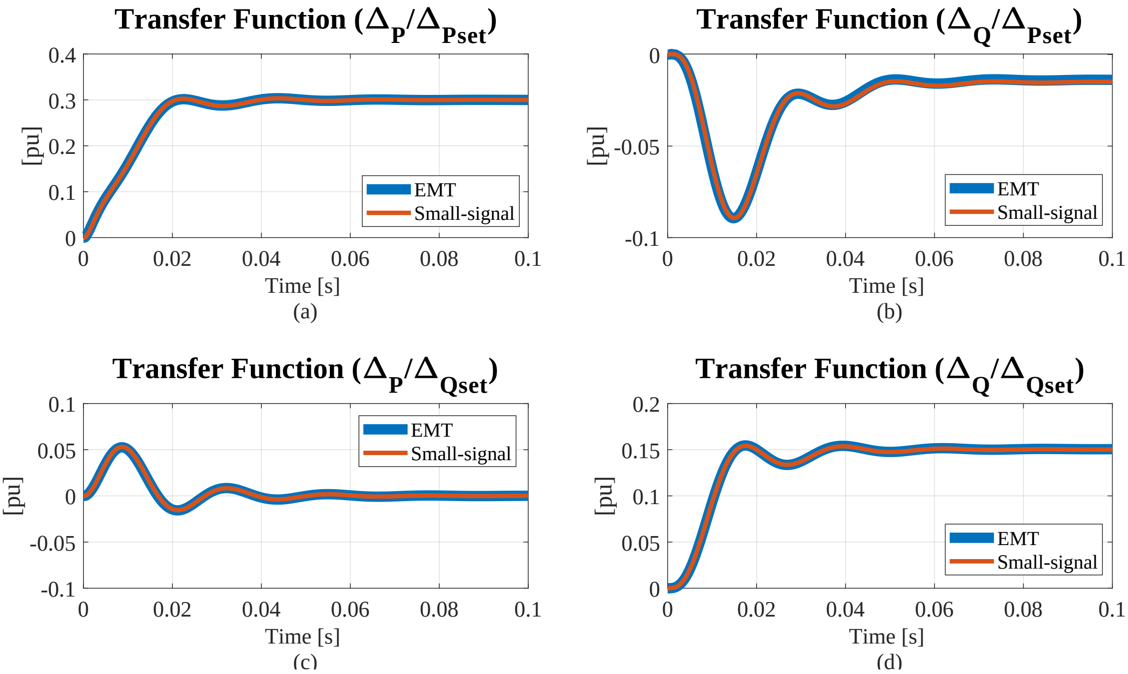

Figure 4.16: Model validation: (blue) EMT simulations, (red) linearized model. (a) $\frac{\Delta_P}{\Delta_{Pset}}$, (b) $\frac{\Delta_Q}{\Delta_{Pset}}$, (c) $\frac{\Delta_P}{\Delta_{Qset}}$, (d) $\frac{\Delta_Q}{\Delta_{Qset}}$.

where S_{sq} and S_{sv} are the steady-state values of $\frac{\Delta_Q}{\Delta E_p}$ and $\frac{\Delta V}{\Delta E_p}$, respectively, while τ_{refQ} and τ_{refV} are the time constants of the respective dominant poles. The resulting damping factors of the two approximated transfer functions are reported below:

$$\zeta_q = \frac{1}{2}\sqrt{\frac{K}{\tau_{refq}\,\omega_n\,S_{sq}}} \quad ; \quad \zeta_v = \frac{1}{2}\sqrt{\frac{K}{\tau_{refv}\,\omega_n\,D_q\,S_{sv}}} \tag{4.44}$$

In case that D_q can be arbitrarily modified, K and D_q can be selected such that $\zeta_q = \zeta_v = 1/\sqrt{2}$. Otherwise, the highest value of K resulting from the two calculations is chosen.

Simulation results

In order to test the performances of the converter when the parameters are tuned by adopting the presented procedure, a real case of study is considered, whose parameters are reported in

Table 4.3: Parameters of the simulated system

Description	Symbol	Value	Description	Symbol	Value
Rated converter power	S_n (kVA)	300	Grid resistance	R_g (pu)	0.005
Grid short-circuit ratio	SCR	20	Filter resistance	$R_{f1} = R_{f2}$ (pu)	0.02
X/R ratio grid impedance	X/R	10	Damping resistance	R_{cf} (pu)	0.18
Lint-to-line voltage	V_{LL} (V rms)	400	Capacitor filter	C_f (pu)	0.05
Rated grid frequency	f_g (Hz)	50	P Droop coefficient	D_p (5%)	60.8
Grid inductance	L_g (pu)	0.05	Q droop factor	D_q (5%)	18371
Converter-side inductance	L_{f1} (pu)	0.08	Virtual moment of inertia	J_{opt}	0.0638
Grid-side inductance	L_{f2} (pu)	0.02	K factor	K_{opt}	37459

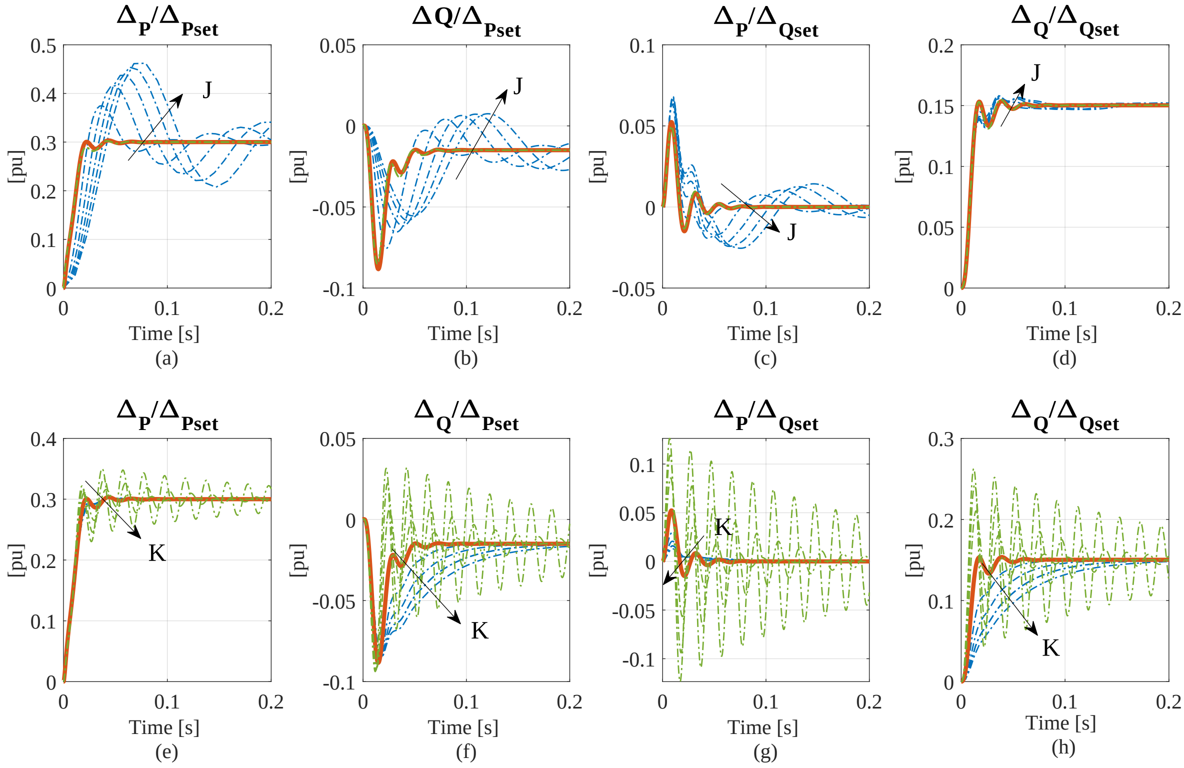

Figure 4.17: Effects of parameter variations on the dynamic response of the system. Variation of parameter J within the range $\left[J_{opt}/50\ ;\ 50\ J_{opt}\right]$: (a) $\frac{\Delta_P}{\Delta_{Pset}}$, (b) $\frac{\Delta_Q}{\Delta_{Pset}}$, (c) $\frac{\Delta_P}{\Delta_{Qset}}$, (d) $\frac{\Delta_Q}{\Delta_{Qset}}$. Variation of parameter K within the range $\left[K_{opt}/4\ ;\ 4\ K_{opt}\right]$: (e) $\frac{\Delta_P}{\Delta_{Pset}}$, (f) $\frac{\Delta_Q}{\Delta_{Pset}}$, (g) $\frac{\Delta_P}{\Delta_{Qset}}$, (h) $\frac{\Delta_Q}{\Delta_{Qset}}$.

Table 4.3. The LCL filter parameters are chosen according to the design procedure reported in [179], while the control parameters result from the tuning procedure described above.

Firstly, the linearized model of Fig. 4.13 is validated against time-domain simulations. The system shown in Fig. 4.12 has been implemented in MATLAB/Simulink/PLECS, where the converter has been replaced by means of controlled voltage sources reproducing the signal e^* calculated by the control, thus neglecting the high-frequency switching effects of the converter. The comparison between EMT simulations and the results of the linearized model to steps of active and reactive power setpoints of 0.3 *pu* are shown in Fig. 4.16. A good match between the two models for the direct transfer functions $\frac{\Delta_P}{\Delta_{Pset}}$ and $\frac{\Delta_Q}{\Delta_{Qset}}$, as well as for the cross-coupling effects $\frac{\Delta_Q}{\Delta_{Pset}}$ and $\frac{\Delta_P}{\Delta_{Qset}}$ can be appreciated in the figure. It is worth to notice, that the reactive power in Fig. 4.16 (d), does not reach the given setpoint of 0.3 *pu* due to the effect of the droop control, which modifies the reactive power injection according to the measured voltage at the PCC.

Fig. 4.17 shows the effects of parameter variations on the step response of the converter. The red curves indicate the dynamic responses of the system when the parameters correspond to those indicated in Table 4.3. Then the factor J is varied within the range $\left[J_{opt}/50\ ;\ 50\ J_{opt}\right]$, while the parameter K is maintained constant and equal to K_{opt}. The results are reported in Fig. 4.17 (a)-(d), where green curves indicate the response when the corresponding parameter

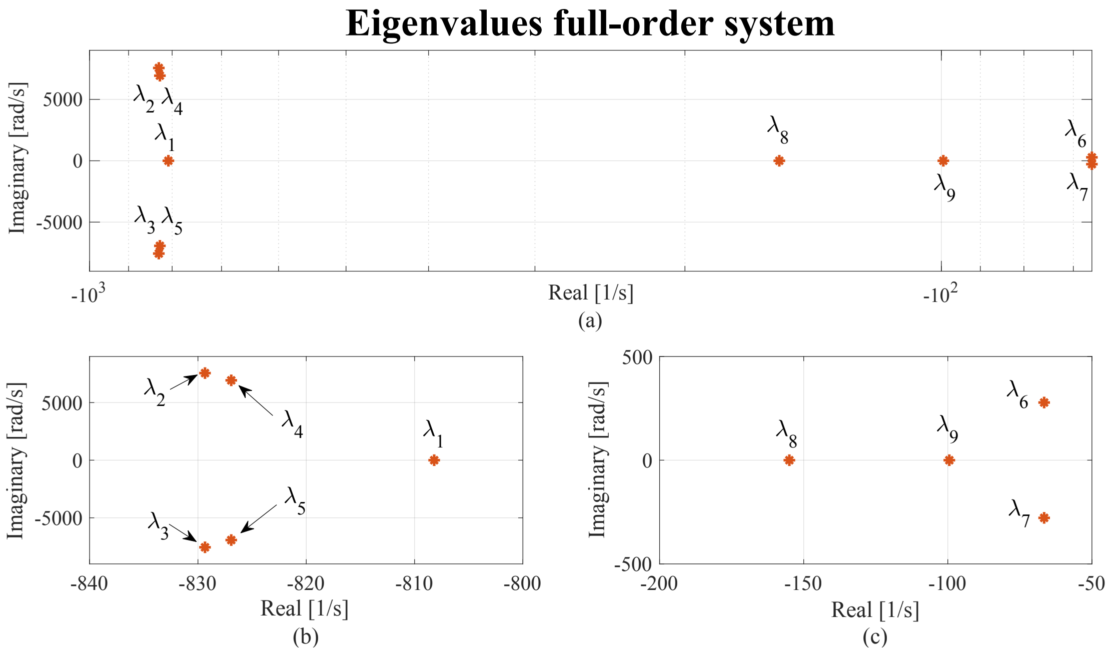

Figure 4.18: Location of system eigenvalues for nominal operating conditions: (a) overview, (b) zoom in the range of λ_1-λ_5, (c) zoom in the range of λ_6-λ_9.

is lower than the estimated optimal value, whereas blue curves when the parameter is chosen to be higher than it. Similarly, the effects due to the variation of the parameter K on the dynamic response of the converter are shown in Fig. 4.17 (e)-(h), where K is varied in the range $\left[K_{opt}/4 \ ; \ 4\ K_{opt}\right]$, while $J = J_{opt}$. It can be noticed, that though the simplified tuning procedure, the chosen control parameters provide acceptable results, according to the initial objective of achieving a satisfying dynamic response of the system in terms of rise-time, settling time, and overshoot. It can be also noticed, that the increase of the parameter J tends to introduce low-frequency oscillations in the response, while an increase of the parameter K increases system damping, effects that will be further investigated in the following by means of eigenvalue analysis. Finally, the results shown in the figure, also emphasize the cross-coupling effects between control loops, since variations of control parameters of one control loop generally affect the whole system dynamic.

Eigenvalue analysis

In the following, the effects of parameter variations on system stability are studied by means of eigenvalue analysis. The linearized system model developed above contains nine eigenvalues which, under nominal operating conditions, are located in the complex plane as shown in Fig. 4.18. These can be grouped into two clusters: the eigenvalues λ_1-λ_5 far from the imaginary axis, and λ_6-λ_9, located closer to the origin, and representing therefore the dominant system modes, as discussed in Section 3.3. The easiest way for assessing the effects of parameter variations on system eigenvalues is to perform sweeps of the parameters of interest and observe the migration of system eigenvalues. Due to the simple system configuration, this approach is adopted in the following, in order to investigate the effects of the control parameters J and K, along with the variation of the grid SCR, on system stability.

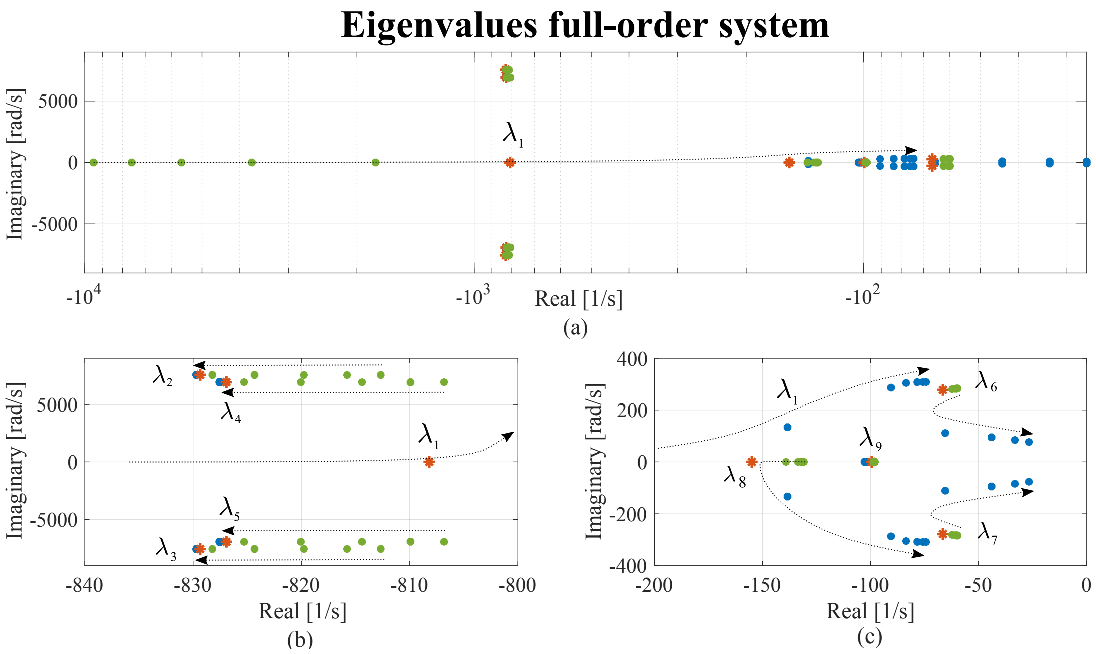

Figure 4.19: Migration of system eigenvalues for a sweep of J within the range $\left[J_{opt}/20\ ;\ 20\ J_{opt}\right]$: (a) overview, (b) zoom in the range of λ_1-λ_5, (c) zoom in the range of λ_6-λ_9.

Fig. 4.19 shows the migration of the nine eigenvalues of the system for a sweep of the parameter J in the range $\left[J_{opt}/20\ ;\ 20\ J_{opt}\right]$. Colors have the same meaning as in Fig. 4.17, hence, red dots indicate nominal conditions and correspond to the positions indicated in Fig. 4.18, green points correspond to the location of the eigenvalues for lower values of the corresponding parameter, blue points for higher values, and the direction of the arrows indicate the migration of the eigenvalues for an increase of the corresponding parameter. It can be noticed, that an increase of the parameter J causes a migration of the eigenvalues λ_2-λ_5 leftwards. The real eigenvalue λ_1 is particularly sensitive to this variation, and together with λ_8, they become a couple of complex conjugated poles when the parameter J is increased above the chosen value J_{opt}. Indeed, this parameter has been calculated so as to approximate the active power loop by means of a second-order transfer function. Therefore, the chosen value would basically correspond to an inertia factor close to zero, while an increase of this parameter over the indicated J_{opt} introduces additional oscillatory modes in the dynamic response of the system. Particularly interesting is the behaviour of the complex conjugate pair λ_6-λ_7, which might become critical for a further increase of the parameter J over J_{opt}, and correspond to the low frequency modes that have been observed in Fig. 4.17 (a).

Fig. 4.20 shows the migration of the system eigenvalues for a variation of the parameter K within the range $\left[K_{opt}/5\ ;\ 5\ K_{opt}\right]$. Fig. 4.20 (a) shows that the eigenvalues of the first identified group move leftwards according to an increase of the parameter K, and tend to cluster to an area not far from the red dots, corresponding to the nominal conditions. On the contrary, the two real poles λ_8 and λ_9 move rightwards for an increase of the parameter, and the latter becomes the dominant pole when K approaches the maximum value of the chosen range of variation. Nevertheless, the most interesting result is that an increase of K tends

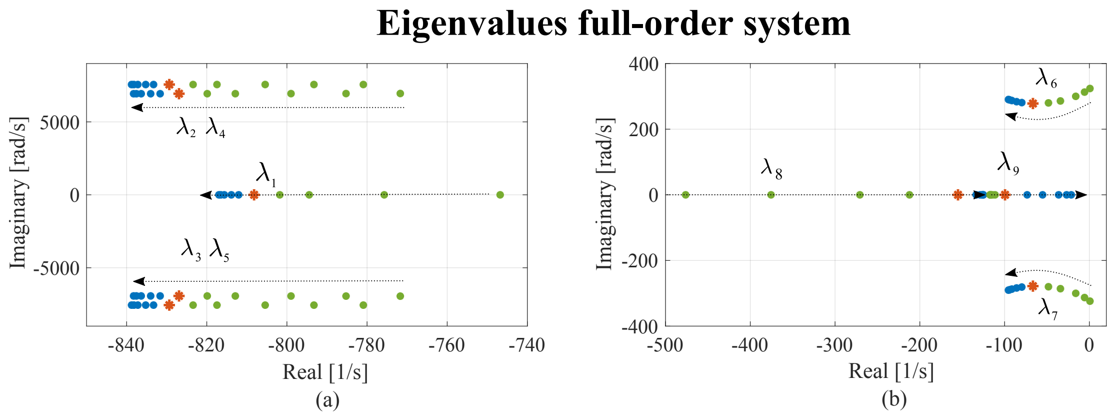

(a) (b)

Figure 4.20: Migration of system eigenvalues for a sweep of K within the range $\left[K_{opt}/5\ ;\ 5\ K_{opt}\right]$: (a) zoom in the range of λ_1-λ_5, (b) zoom in the range of λ_6-λ_9.

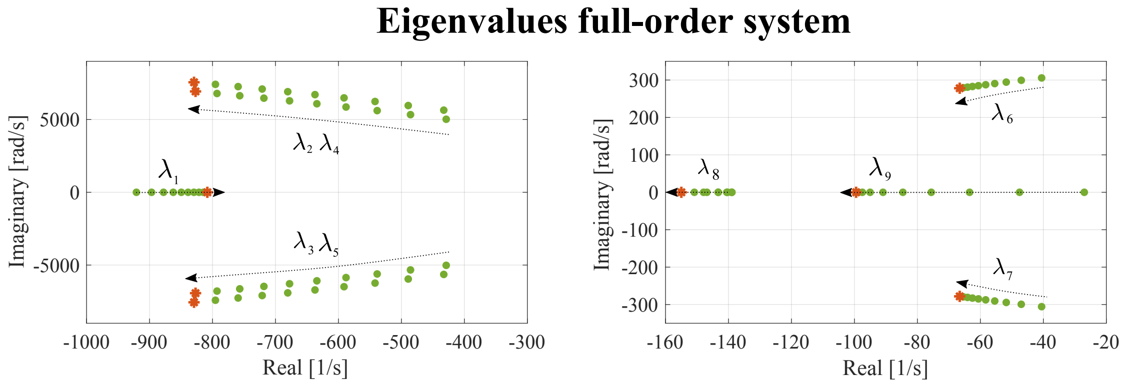

(a) (b)

Figure 4.21: Migration of system eigenvalues for a sweep of SCR within the range $\left[2\ ;\ 20\right]$: (a) zoom in the range of λ_1-λ_5, (b) zoom in the range of λ_6-λ_9.

to stabilize the system, since the pair of complex conjugate poles λ_6 and λ_7 become critical for lower values of K, and destabilize the system when K becomes lower than $K_{lim} \approx 8500$, effects that can be clearly observed in Fig. 4.17.

Finally, Fig. 4.21 shows the effects of the variation of the grid SCR on system eigenvalues, whose nominal value (SCR=20) represents the case of a strong grid. The parameter is varied in the range $\left[2\ ;\ 20\right]$, and the migration of all system eigenvalues is reported in the figure. Except from λ_1, an increase of the grid SCR causes the movement of all system eigenvalues leftwards. Limiting the stability analysis to system eigenvalues, this result would lead to the conclusion that the system becomes less stable for operation under weak grid conditions. To this extent, such conclusions have been drawn in [180], where similar effects as those shown in Fig. 4.21 have been observed, according to a stability investigation of a synchronverter-dominated microgrid. Nevertheless, it is interesting to notice that the system remains stable even for the lowest SCR considered here, while the robust stability analysis performed in the following of this chapter, will reveal some interesting aspects related to this operating condition, which cannot be explicitly deduced by means of eigenvalue analysis.

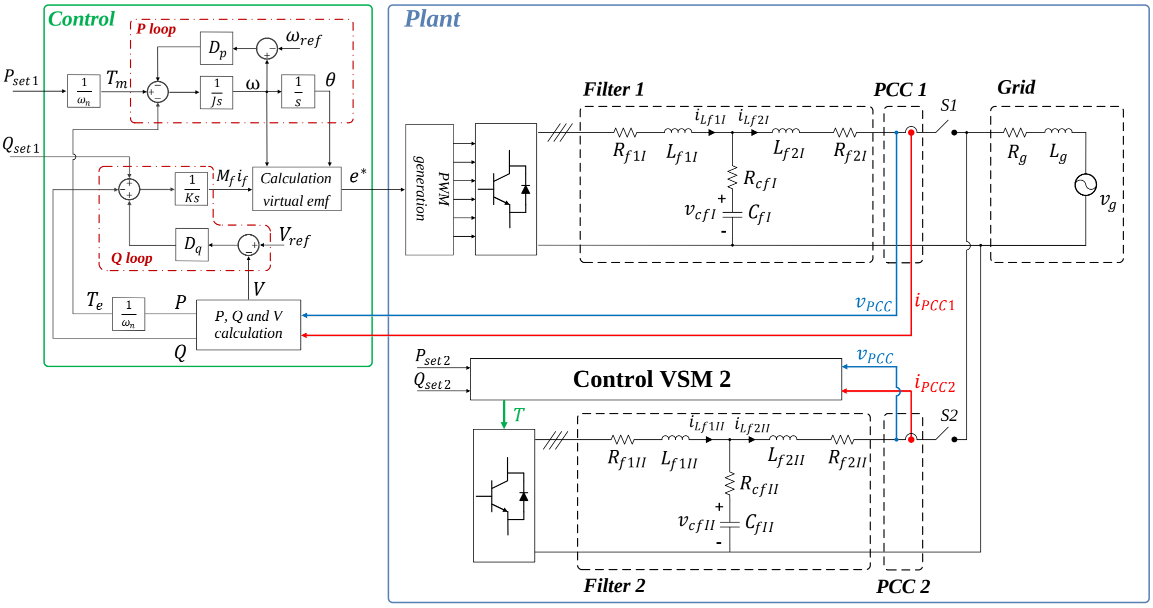

Figure 4.22: Scheme of the system under study: two LCL filter-based synchronverters operating in parallel.

4.2.3 Parallel operation of GFM converters

In the following, the eigenvalue analysis reported above for one synchronverter, is extended to the case of two synchronverters operating in parallel. The system under study is the one shown in Fig. 4.22, while the state-space description of the interconnected system is obtained as in the previous case, namely by dividing the overall system into a control subsystem and the plant, as shown in Fig. 4.13. However, apart from the control subsystem, whose state-space equations remain unchanged, obtaining the state-space representation of the new plant by writing down the equations, and linearizing around an operating point, might become a quite tedious exercise. Therefore, the CCM method is again employed here, however in order to obtain the state-space description of the new plant, while the process for obtaining the interconnected system, described in the previous subsection, remains unvaried. The scheme of the whole system suitable for applying the CCM is reported in Fig. 4.23, while the subsystems composing it are described in the following.

LCL filter

Choosing the inductor currents i_{Lf1} and i_{Lf2}, along with the capacitor voltage v_c as state-variables, the state-space equations of the LCL filter subsystem are obtained similarly as in (4.26)-(4.28). However, in this case, not only the control outputs, but also the measured voltage at the PCC is among the inputs of this subsystem, while the output is represented by the grid-side current i_{Lf2}. Writing the equations in dq coordinates, the input and output vectors are therefore $\mathbf{u}_{LCL} = [\Delta E_p\ \Delta\theta\ \Delta v_{PCCd}\ \Delta v_{PCCq}]^T$, and $\mathbf{y}_{LCL} = [\Delta i_{Lf2d}\ \Delta i_{Lf2q}]^T$, respectively, while the resulting state-space matrices are reported below:

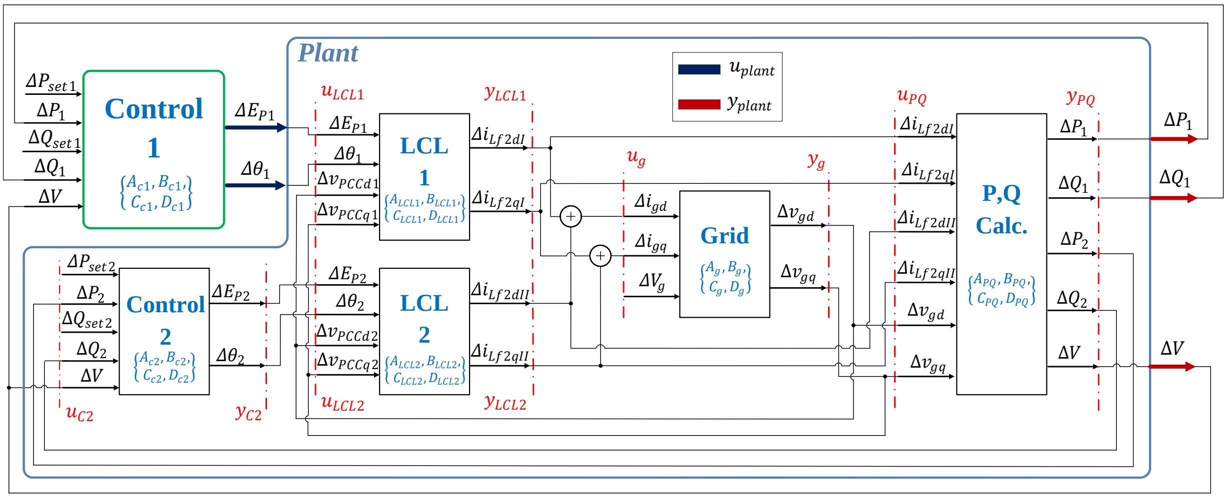

Figure 4.23: Equivalent system representation for applying CCM.

$$
\mathbf{A}_{LCL} = \begin{bmatrix}
\frac{-R_{cf}-R_{f1}}{L_{f1}} & \omega_0 & -\frac{1}{L_{f1}} & 0 & \frac{R_{cf}}{L_{f1}} & 0 \\
-\omega_0 & \frac{-R_{cf}-R_{f1}}{L_{f1}} & 0 & -\frac{1}{L_{f1}} & 0 & \frac{R_{cf}}{L_{f1}} \\
\frac{1}{C_f} & 0 & 0 & \omega_0 & -\frac{1}{C_f} & 0 \\
0 & \frac{1}{C_f} & -\omega_0 & 0 & 0 & -\frac{1}{C_f} \\
\frac{R_{cf}}{L_{f2}} & 0 & \frac{1}{L_{f2}} & 0 & \frac{-R_{cf}-R_{f2}}{L_{f2}} & \omega_0 \\
0 & \frac{R_{cf}}{L_{f2}} & 0 & \frac{1}{L_{f2}} & -\omega_0 & \frac{-R_{cf}-R_{f2}}{L_{f2}}
\end{bmatrix} ; \quad \mathbf{D}_{LCL} = \begin{bmatrix} 0^{2\times 4} \end{bmatrix} ;
$$

$$
\mathbf{B}_{LCL} = \begin{bmatrix}
\frac{\cos\theta_0}{L_{f1}} & -\frac{V_0 \sin\theta_0}{L_{f1}} & 0 & 0 \\
\frac{\sin\theta_0}{L_{f1}} & -\frac{V_0 \cos\theta_0}{L_{f1}} & 0 & 0 \\
0 & 0 & 0 & 0 \\
0 & 0 & 0 & 0 \\
0 & 0 & -\frac{1}{L_{f2}} & 0 \\
0 & 0 & 0 & -\frac{1}{L_{f2}}
\end{bmatrix} ; \quad \mathbf{C}_{LCL} = \begin{bmatrix}
0 & 0 & 0 & 0 & 1 & 0 \\
0 & 0 & 0 & 0 & 0 & 1
\end{bmatrix} . \qquad (4.45)
$$

Grid

The grid model is represented by a Thévenin equivalent at the PCC. The input of this subsystem is the sum of the two converter currents, while the voltage at the PCC represents its output. In order to obtain the information about the voltage at the connection point, another state has been introduced in the model, by adding a shunt capacitor at the input terminal, as shown in Fig. 4.24. In fact, choosing very high values for the shunt components R_s and C_s, it can be assumed that the input current i_g flows entirely into the grid, and the PCC voltage is represented by the voltage v_{cs} across the shunt capacitor. This expedient is equivalent to the solution commonly adopted by EMT simulation software, and namely equipping a current

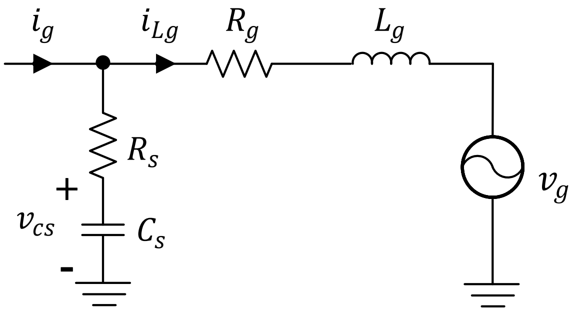

Figure 4.24: Equivalent grid subsystem model for CCM.

source element with a large parallel impedance, in order to ensure simulation convergence. Analogously, the ”dummy” capacitor introduced in Fig. 4.24, does not have a physical meaning, but it only serves as a mean for introducing an additional state in the subsystem. Similar solutions have been also reported in the literature, e. g. in [152] or in [181], where, however, an additional inductor has been also introduced in the shunt branch, increasing the order of the subsystem model. The equations of the grid subsystem are given below:

$$\begin{cases} L_g \frac{di_{Lg}}{dt} = R_s(i_g - i_{Lg}) + v_{cs} - v_g - R_g i_{Lg} \\ C_s \frac{dv_{cs}}{dt} = i_g - i_{Lg} \end{cases} \tag{4.46}$$

Writing (4.46) in dq coordinates, and defining the following input and output vectors:

$$\begin{cases} \mathbf{u}_g = [\Delta i_{gd}\ \Delta i_{gq}\ \Delta V_g]^T \\ \mathbf{y}_g = [\Delta v_{gd}\ \Delta v_{gq}]^T \end{cases} \tag{4.47}$$

the state-space matrices of the grid subsystem are reported below:

$$\mathbf{A}_g = \begin{bmatrix} \frac{-R_s-R_g}{L_g} & \omega_0 & \frac{1}{L_g} & 0 \\ -\omega_0 & \frac{-R_s-R_g}{L_g} & 0 & \frac{1}{L_g} \\ -\frac{1}{C_s} & 0 & 0 & \omega_0 \\ 0 & -\frac{1}{C_s} & -\omega_0 & 0 \end{bmatrix} ; \quad \mathbf{B}_g = \begin{bmatrix} \frac{R_s}{L_g} & 0 & -1 \\ 0 & \frac{R_s}{L_g} & 0 \\ \frac{1}{C_s} & 0 & 0 \\ 0 & \frac{1}{C_s} & 0 \end{bmatrix} ;$$

$$\mathbf{C}_g = \begin{bmatrix} 0 & 0 & 1 & 0 \\ 0 & 0 & 0 & 1 \end{bmatrix} ; \quad \mathbf{D}_g = \begin{bmatrix} 0^{2\times 3} \end{bmatrix} . \tag{4.48}$$

P, Q, and V calculation

Calculation of active and reactive power of each converter, along with the amplitude of the PCC voltage have been reported in (4.30)-(4.33). These involve algebraic equations and, in order to obtain a state-space description of the subsystem, first-order low-pass filters with a cut-off frequency ω_{cf} are employed. Hence, eq. (4.30), (4.32), and (4.33) become:

$$\begin{cases} \Delta P = \left(\frac{\omega_{cf}}{s+\omega_{cf}}\right)\frac{3}{2}(I_{Lf2d_0}\Delta v_{gd} + I_{Lf2q_0}\Delta v_{gq} + V_{gd_0}\Delta i_{Lf2d} + V_{gq_0}\Delta i_{Lf2q} \\ \Delta Q = \left(\frac{\omega_{cf}}{s+\omega_{cf}}\right)\frac{3}{2}(-I_{Lf2q_0}\Delta v_{gd} + I_{Lf2d_0}\Delta v_{gq} + V_{gq_0}\Delta i_{Lf2d} - V_{gd_0}\Delta i_{Lf2q}) \\ \Delta V = \left(\frac{\omega_{cf}}{s+\omega_{cf}}\right)\frac{V_{gd_0}\Delta v_{gd}+V_{gq_0}\Delta v_{gq}}{\sqrt{\Delta_{dq0}}} \end{cases} \tag{4.49}$$

where $\Delta_{dq0} = (V_{gd0}^2 + V_{gq0}^2)$, and $i_{Lf2dq} = \left\{i_{Lf2dqI},\, i_{Lf2dqII}\right\}$. Values at the operating point, indicated with the subscript "0", can be calculated with a similar procedure as reported in (4.38). Choosing a proper value for ω_{cf} ensures that this element does not affect the system dynamic. Defining input and output vectors of the subsystem as:

$$\begin{cases} \mathbf{u}_{PQ} = [\Delta i_{Lf2dI}\ \Delta i_{Lf2qI}\ \Delta i_{Lf2dII}\ \Delta i_{Lf2qII}\ \Delta v_{gd}\ \Delta v_{gq}]^T \\ \mathbf{y}_{PQ} = [\Delta P_1\ \Delta Q_1\ \Delta P_2\ \Delta Q_2\ \Delta V]^T \end{cases} \tag{4.50}$$

the corresponding state-space matrices are given by:

$$\mathbf{A}_{PQ} = -\omega_{cf}\left[I^{(5)}\right]; \quad \mathbf{C}_{PQ} = \left[I^{(5)}\right]; \quad \mathbf{D}_{PQ} = \left[0^{5\times6}\right];$$

$$\mathbf{B}_{PQ} = \omega_{cf}\frac{3}{2}\begin{bmatrix} V_{gd0} & V_{gq0} & 0 & 0 & I_{Lf2dI_0} & I_{Lf2qI_0} \\ V_{gq0} & -V_{gd0} & 0 & 0 & -I_{Lf2qI_0} & I_{Lf2dI_0} \\ 0 & 0 & V_{gd0} & V_{gq0} & I_{Lf2dII_0} & I_{Lf2qII_0} \\ 0 & 0 & V_{gq0} & -V_{gd0} & -I_{Lf2qII_0} & I_{Lf2dII_0} \\ 0 & 0 & 0 & 0 & \frac{V_{gd0}}{\sqrt{\Delta_{dq0}}} & \frac{V_{gq0}}{\sqrt{\Delta_{dq0}}} \end{bmatrix}. \tag{4.51}$$

Interconnected system

The state-space matrices of the interconnected system $\mathbf{F}_{int}$, $\mathbf{G}_{int}$, $\mathbf{H}_{int}$ and $\mathbf{J}_{int}$ are obtained as reported in (3.46), where, for the specific case under study, the required matrices $\mathbf{A}_d$, $\mathbf{B}_d$, $\mathbf{C}_d$, and $\mathbf{D}_d$, are given by:

$$\begin{cases} \mathbf{A}_d = diag\{\mathbf{A}_{c2}, \mathbf{A}_{LCL1}, \mathbf{A}_{LCL2}, \mathbf{A}_g, \mathbf{A}_{PQ}\} \\ \mathbf{B}_d = diag\{\mathbf{B}_{c2}, \mathbf{B}_{LCL1}, \mathbf{B}_{LCL2}, \mathbf{B}_g, \mathbf{B}_{PQ}\} \\ \mathbf{C}_d = diag\{\mathbf{C}_{c2}, \mathbf{C}_{LCL1}, \mathbf{C}_{LCL2}, \mathbf{C}_g, \mathbf{C}_{PQ}\} \\ \mathbf{D}_d = diag\{\mathbf{D}_{c2}, \mathbf{D}_{LCL1}, \mathbf{D}_{LCL2}, \mathbf{D}_g, \mathbf{D}_{PQ}\} \end{cases} \tag{4.52}$$

Defining the following vectors:

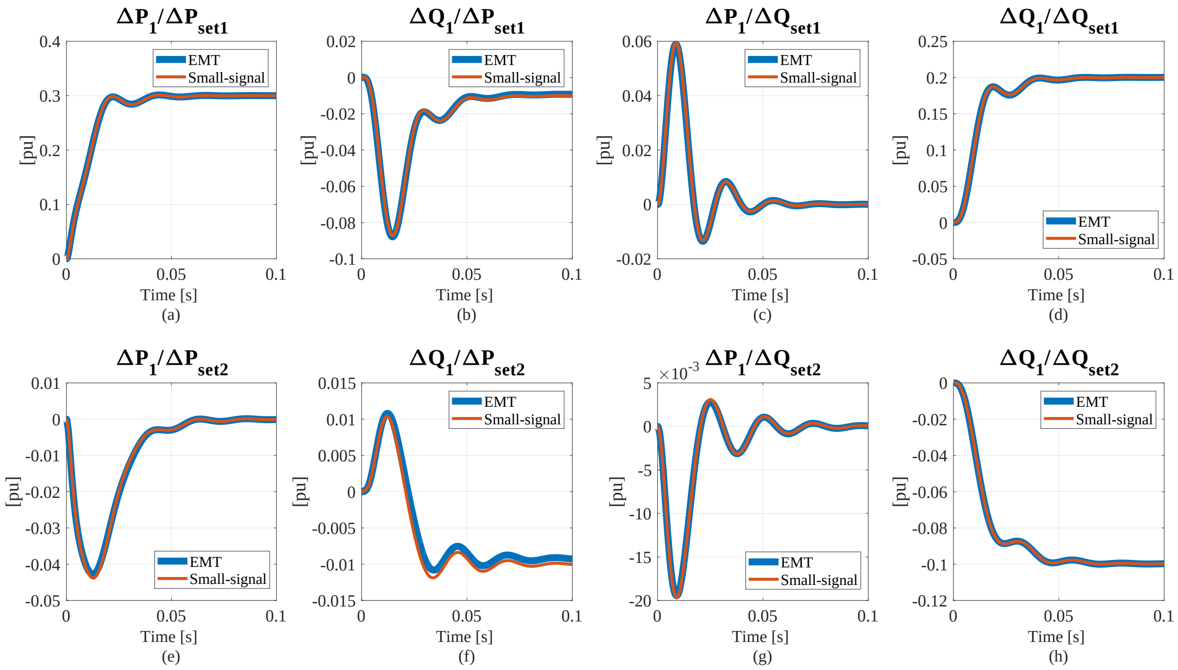

Figure 4.25: Model validation: (blue) EMT simulations, (red) linearized model. (a) $\frac{\Delta_{P1}}{\Delta_{Pset1}}$, (b) $\frac{\Delta_{Q1}}{\Delta_{Pset1}}$, (c) $\frac{\Delta_{P1}}{\Delta_{Qset1}}$, (d) $\frac{\Delta_{Q1}}{\Delta_{Qset1}}$, (e) $\frac{\Delta_{P1}}{\Delta_{Pset2}}$, (f) $\frac{\Delta_{Q1}}{\Delta_{Pset2}}$, (g) $\frac{\Delta_{P1}}{\Delta_{Qset2}}$, (h) $\frac{\Delta_{Q1}}{\Delta_{Qset2}}$.

$$\begin{cases} \mathbf{u}_{sub} = \left[\mathbf{u}_{c2}\ \mathbf{u}_{LCL1}\ \mathbf{u}_{LCL2}\ \mathbf{u}_{g}\ \mathbf{u}_{PQ}\right]^{T} \\ \mathbf{y}_{sub} = \left[\mathbf{y}_{c2}\ \mathbf{y}_{LCL1}\ \mathbf{y}_{LCL2}\ \mathbf{y}_{g}\ \mathbf{y}_{PQ}\right]^{T} \\ \mathbf{u}_{plant} = \left[\Delta E_{p1}\ \Delta\theta_{1}\right]^{T} \\ \mathbf{y}_{plant} = \left[\Delta P_{1}\ \Delta Q_{1}\ \Delta V\right]^{T} \end{cases} \tag{4.53}$$

The interconnection matrices $\mathbf{L}_{11}$, $\mathbf{L}_{12}$, $\mathbf{L}_{21}$, and $\mathbf{L}_{22}$ satisfy the following equations:

$$\begin{cases} \mathbf{u}_{sub} = \left[\mathbf{L}_{11}\right]^{22\times 13}\mathbf{y}_{sub} + \left[\mathbf{L}_{12}\right]^{22\times 2}\mathbf{u}_{plant} \\ \mathbf{y}_{plant} = \left[\mathbf{L}_{21}\right]^{3\times 13}\mathbf{y}_{sub} + \left[\mathbf{L}_{22}\right]^{3\times 2}\mathbf{u}_{plant} \end{cases} \tag{4.54}$$

These are reported in the Appendix (Section 9.1) for sake of completeness. In the following, the derived model is validated against time-domain EMT simulations.

Model validation

In order to validate the obtained linearized model of the two synchronverters operating in parallel, the system depicted in Fig. 4.22 has been simulated in MATLAB/Simulink/PLECS, and the results are shown in Fig. 4.25. As for the case of one synchronverter operating alone, average models for the two converters have been employed. It is assumed that the two converters have the same parameters, shown in Table 4.3, and steps of active and reactive

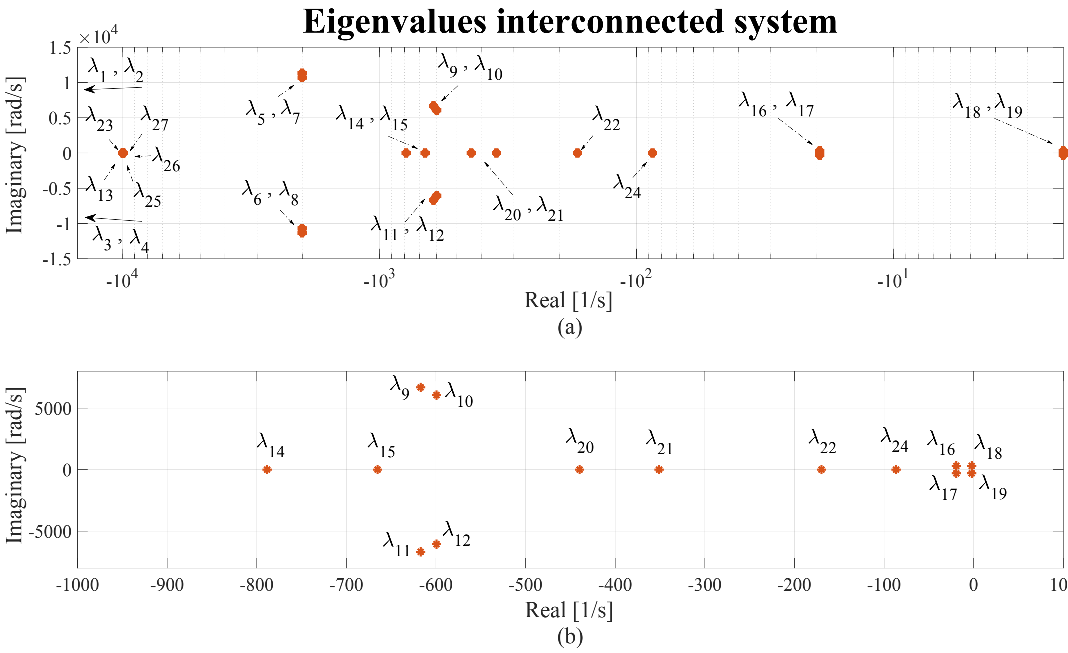

Figure 4.26: Location of system eigenvalues when the K parameter of the two converters is K_1=K_2=12000. (a) Overview, (b) zoom.

power setpoints of Converters 1 and 2 of 0.3 *pu* have been simulated. Fig. 4.25 shows the comparison between the results obtained with the two models, where the cross-coupling effects between active and reactive power within the same converter, as well as the cross-coupling between the two converters are depicted. The results shown in Fig. 4.25 (a)-(d) account for the transfer functions relating quantities within Converter 1, and are similar to the results already shown in Fig. 4.16. Fig. 4.25 (e)-(h) show the cross-coupling effects between quantities in the two converters, concluding that a satisfying match between the two models can be observed also in this case.

4.2.4 Modal analysis

According to the eigenvalue analysis reported above, the converter is apparently far from an unstable operating condition when the control parameters are chosen by adopting the presented tuning procedure. The effects of parameter variations on system eigenvalues have been investigated, indicating how control parameters can influence the stability of the converter when operating alone. In the following, eigenvalue analysis is performed in order to study the parallel operation between two synchronverters. Under the assumption that the two converters are identical, they are also tuned with the same parameters, reported in Table 4.3. However, the value of the parameter K of both converters is reduced, so as to bring the system to an operating condition close to the stability borders.

The location of the twenty-seven system eigenvalues of the resulting interconnected system for the case when the two converters have the same parameter $K_1 = K_2$ =12000, are shown in Fig. 4.26, with the exception of the eigenvalues λ_1-λ_4, located far from the imaginary axis.

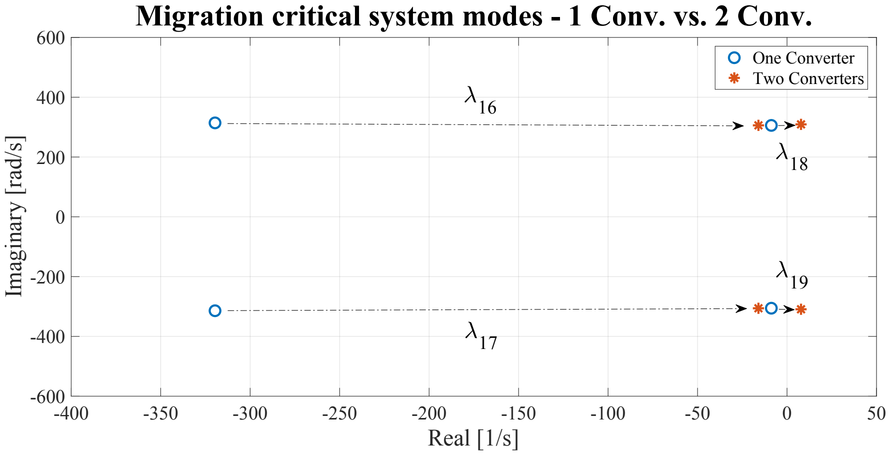

Figure 4.27: Migration of critical system modes λ_{16}-λ_{19}, (green) one synchronverter, (red) two synchronverters, $K_1 = K_2 = 10500$.

As it can be better appreciated in Fig. 4.26 (b), the critical system modes are represented by the two couples of complex conjugated poles λ_{16}-λ_{17}, and λ_{18}-λ_{19}. According to the analysis performed for the synchronverter operating alone, it has been revealed that the system becomes unstable for values of $K < K_{lim} \approx 8500$. However, when the second synchronverter is connected in parallel, the new K value causing instability becomes $K_{lim} \approx 11800$. This condition is clearly shown in Fig. 4.27, where the location of the critical system modes for the case when only one converter is in operation (blue circles), is compared to the case when the second converter is connected in parallel (red dots). The figure has been obtained by setting the factor K of both converters to a value of 10500, which is not critical when only one converter is in operation, but causes system instability when the second converter is connected in parallel.

Participation factors

It has been emphasized in Section 3.3.2, that participation factors allow assessing the contribution of system states to system modes. In the following, a modal analysis is performed, in order to identify the states mainly affecting the pairs of complex conjugated poles λ_{16}-λ_{17}, and λ_{18}-λ_{19}, identified here as critical system modes. It is still worth to remark, that participation factors do not explicitly provide indications about influence of control or system parameters on the modes of interest. To this extent, the *eigenvalue sensitivity analysis*, which can be performed according to (3.42), and which allows calculating the influence of a precise element of the state-matrix **A** on a specific mode, might become helpful. However, since elements of the state matrix are generally obtained by combinations of parameters, more precise information can be gained by means of the differentiation of the elements of the system matrix with respect to a particular parameter of interest, according to eq. (3.43). Either way, an explicit representation of the state matrix is needed, which might not be always available, especially when increasing the size of the system under study, and approaches like the one adopted here become necessary. In fact, the state matrix of the interconnected system has been obtained by adopting the CCM and, therefore, the explicit representation of the matrix

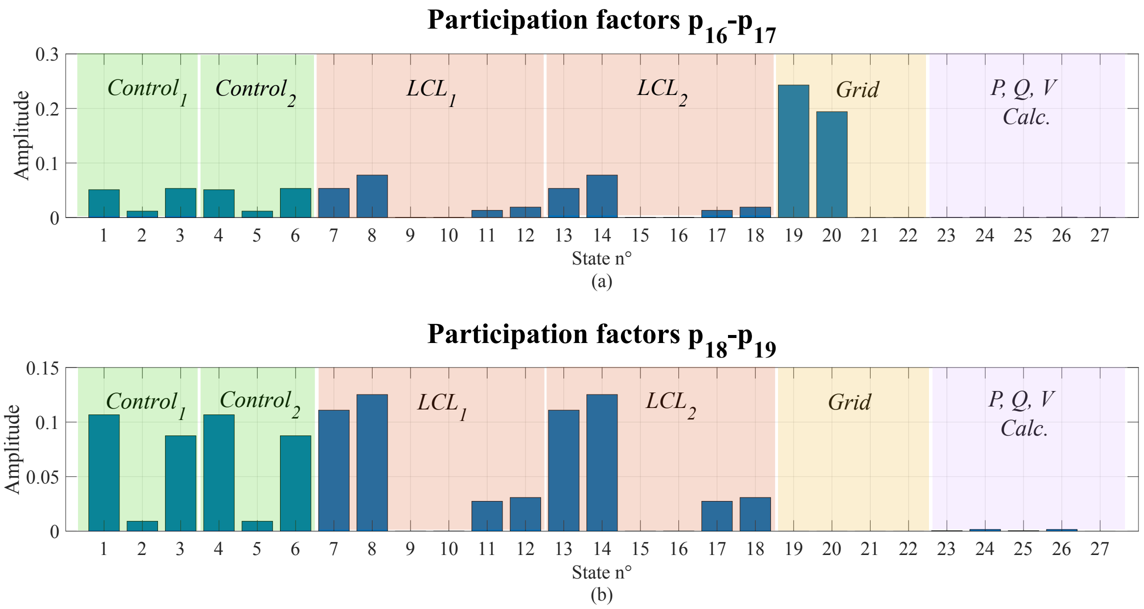

Figure 4.28: Participation factors: (a) $\mathbf{p}_{16}$-$\mathbf{p}_{17}$; (b) $\mathbf{p}_{18}$-$\mathbf{p}_{19}$.

Table 4.4: Participation factors

State n^o	Description	Subsystem	$\mathbf{p}_{16}$-$\mathbf{p}_{17}$	$\mathbf{p}_{18}$-$\mathbf{p}_{19}$
1, 4	$\Delta M_f i_f 1, \Delta M_f i_f 2$	*Control* 1	0.0511	0.1067
2, 5	$\Delta\omega_1, \Delta\omega_2$	and	0.0118	0.0091
3, 6	$\Delta\theta_1, \Delta\theta_2$	*Control* 2	0.0534	0.0875
7, 13	$\Delta i_{Lf1dI}, \Delta i_{Lf1dII}$		0.0534	0.1109
8, 14	$\Delta i_{Lf1qI}, \Delta i_{Lf1qII}$	*LCL* 1	0.0779	0.1252
9, 15	$\Delta v_{cfdI}, \Delta v_{cfdII}$	and	0	0
10, 16	$\Delta v_{cfqI}, \Delta v_{cfqII}$	*LCL* 2	0.0001	0.0001
11, 17	$\Delta i_{Lf2dI}, \Delta i_{Lf2dII}$		0.0132	0.0274
12, 18	$\Delta i_{Lf2qI}, \Delta i_{Lf2qII}$		0.0192	0.0309
19	Δi_{gd}		0.2429	0
20	Δi_{gq}	*Grid*	0.01941	0
21	Δu_{sd}		0	0
22	Δu_{sq}		0	0
23	ΔP_1		0.0006	0.0005
24	ΔQ_1		0.0008	0.0016
25	ΔP_2	P, Q, V	0.0006	0.0005
26	ΔQ_2	Calc.	0.0008	0.0016
27	ΔV		0.0001	0

is not necessarily available, unless a toolbox allowing symbolic calculation is employed.

Multiplying the elements of the left and the right eigenvectors, as reported in (3.39), participation factors can be calculated. However, since for the case under study the eigenvalues of interest are represented by couples of complex conjugated poles, the participation factors are calculated according to the following equation [182]:

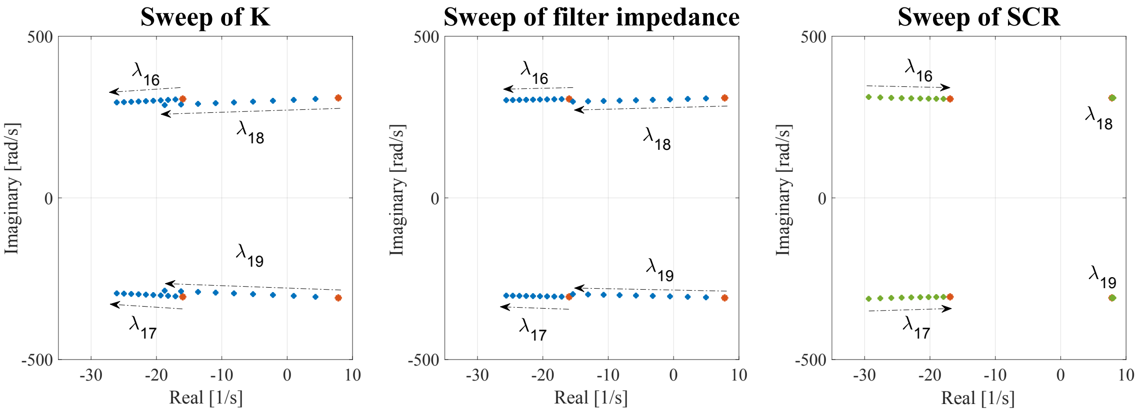

(a) (b) (c)

Figure 4.29: Migration of critical system modes according to parameter sweeps: (a) $K_1 = K_2 = \left[10500\,;\ 15000\right]$; (b) Increase filter parameters by 30%, $K_1 = K_2 = 10500$; (c) SCR variation in the range $\left[2\,;\ 20\right]$, $K_1 = K_2 = 10500$.

$$p_{ki} = \frac{|\psi_{ik}||\phi_{ki}|}{\sum_{i=1}^{n} |\psi_{ik}||\phi_{ki}|} \tag{4.55}$$

where the same notations as in (3.39) apply. Other techniques have been proposed for calculating participation factors in case of complex eigenvalues, which take into account only the real part of the elements of the eigenvectors [183], but those methods are not considered here. The calculated participation factors $\mathbf{p}_{16} - \mathbf{p}_{19}$ are shown in Fig. 4.28, specifying also to which subsystem each element is related, while their amplitudes are reported in Table 4.4.

A careful analysis of the obtained results reveals that the states mainly affecting λ_{16} and λ_{17} are those of the grid subsystem Δi_{gd} and Δi_{gq}, while the modes λ_{18} and λ_{19} are particularly susceptible to the control states $\Delta M_f i_f$, and the converter side filter currents Δi_{Lf1d} and Δi_{Lf1q}. This suggests that, whether it would be possible to identify parameters directly related to the aforementioned states, it could be assumed that the participation factors can be somehow directly related to those parameters. Aided by the particularly simple control configuration of the synchronverter examined here, it is reasonable to assume that the parameter K can be directly related to the state $\Delta M_f i_f$, and namely an increase of this parameter can provide some damping to the aforementioned state. Similarly, the filter impedance, as well as the grid impedance, can be directly related to the states Δi_{Lf1d}-Δi_{Lf1q}, and Δi_{gd}-Δi_{gq}, respectively. To confirm these assumptions, Fig. 4.29 shows the migration of the critical system modes λ_{16}-λ_{17}, and λ_{18}-λ_{19} according to variations of the aforementioned parameters. Colors have the same meaning as in Fig. 4.19 - 4.21, namely red dots account for the location of the eigenvalues at the considered operating condition, blue points are obtained for higher values of the parameter of interest, green points for lower values, and the arrows indicate the increase of the parameter. By examining these results, following conclusions can be drawn:

- As expected, an increase of the parameter K of both converters moves the critical modes leftwards, bringing the system into a stable operating condition. Furthermore, the influence of this parameter is stronger for λ_{18}-λ_{19} than for λ_{16}-λ_{17}, in accordance with the participation factors shown in Fig. 4.28.

- An increase of the filter impedance causes a significant migration of all the critical eigenvalues leftwards, ensuring again a stable operating condition. This represents an important aspect, which will be further investigated in the next section.
- A reduction of the SCR, hence an increase of the grid impedance, provides additional damping to the modes λ_{16}-λ_{17}. However, as predicted by the participation factors, it does not affect the λ_{18}-λ_{19} , which are barely influenced by this variation, and remain on the right half plane.

4.3 Robust stability analysis of the interactions among GFL and GFM converters

In this section, interactions between GFM and GFL converters are investigated. Differently from Section 4.1, where the interactions between synchronization units of GFL converters have been investigated by means of impedance-based analysis, and Section 4.2, where the stability of GFM converters has been addressed by means of eigenvalue analysis and modal analysis, in this section, the robust stability of GFL and GFM converters is examined by performing the μ-analysis introduced in Section 3.4.3. It is however worth to remark, that the impedance-based approach adopted in Section 4.1, has been formulated in terms of a norm calculation, which allows assessing a stability margin for the MIMO system under study according to the small-gain theorem, thus complying with robust control theory. On the contrary, the analysis performed for GFM converters has been solely based on eigenvalue analysis, and therefore the μ-approach is first applied to this case study.

4.3.1 Robust stability of GFM converters

In order to perform the μ-analysis, the state-space representation of the system is required. For GFM converters, this has been already obtained in the previous section, both for the case of a single converter, as well as for the case of two converters operating in parallel. Furthermore, the adopted system representation shown in Fig. 4.13, where the system under study is split into a control part and the plant, results particularly suitable for the purposes of the investigation. In fact, according to the steps for the μ-analysis discussed in Section 3.4.3, and reported in Fig. 3.10, the general control configuration including model uncertainty is necessary, whose structure for the particular case under study is depicted in Fig. 4.30.

Two multiplicative input uncertainties are included in the generalized plant G at the input channels u_1 and u_2, indicated with $W_{\delta 1}$ and $W_{\delta 2}$ in the figure. These represent frequency dependent functions, properly chosen so as to include a desired uncertain behaviour of the plant in the analysis. Yet, it has been explained in Section 3.4.3, that a proper choice of

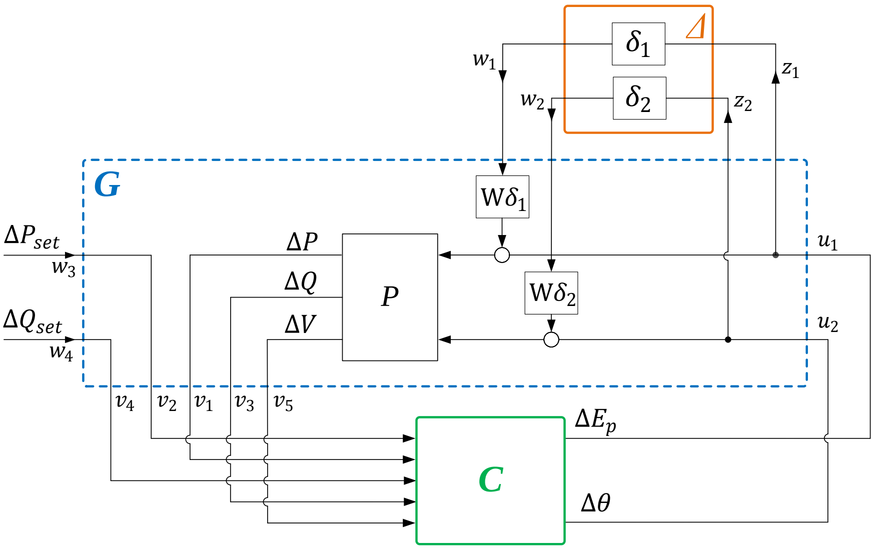

Figure 4.30: Construction of the generalized plant for robust stability analysis of GFM converters.

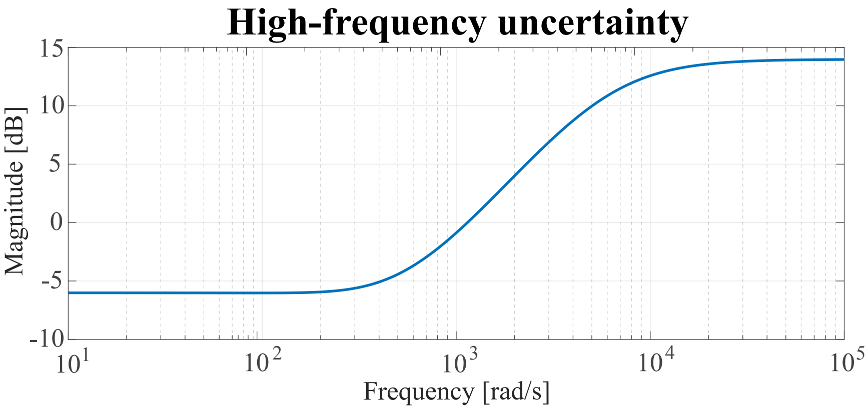

Figure 4.31: Frequency behaviour of the uncertainty function chosen for the analysis.

the uncertainty function is fundamental for the purposes of the μ-analysis, due to the fact that the obtained results are strongly related to it. Fig. 4.31 shows the chosen uncertainty function considered in the following. As already explained in the example of Fig. 3.9, it presents the typical behaviour of multiplicative uncertainties, namely lower amplitude at lower frequencies, rising up to higher values in the high-frequency range. In the specific, the chosen uncertainty presents an amplitude of 50% in the low-frequency range, accounting for eventual parameter uncertainties, increasing till 500 % at very high frequencies, in order to consider the effects caused by the presence of other converters operating nearby, as discussed in Section 3.4.3. Furthermore, the chosen uncertainty, along with the diagonal structure adopted here, allows addressing, among others, the effects due to neglected dynamics in the input channels (sensors), or in the individual output channels (actuators) of the considered plant, which have not been explicitly included in the model, but are always present in a real system [103]. The outputs of the generalized plant G are the inputs of the control subsystem, and are represented by the vector $\mathbf{v} = \begin{bmatrix} v_1 & v_2 & v_3 & v_4 & v_5 \end{bmatrix}$, which also include the active and reactive power setpoints P_{set} and Q_{set}, respectively.

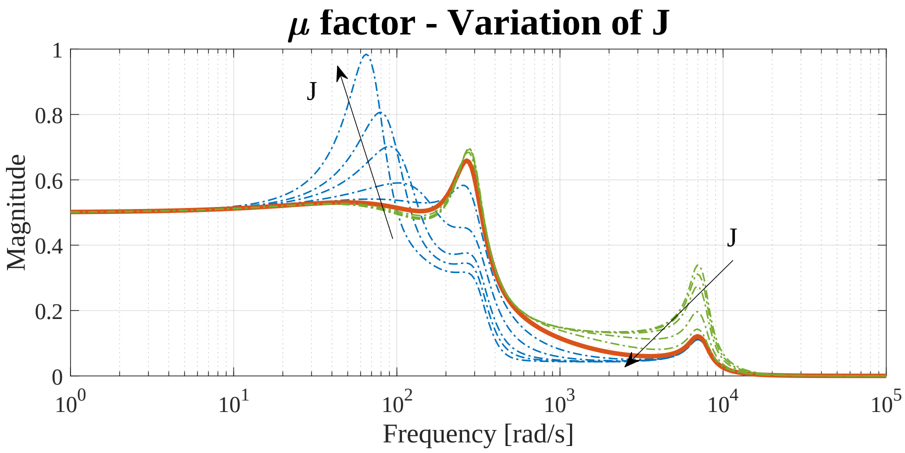

Figure 4.32: Effects of the variation of the parameter J within the range $\left[J_{opt}/20\ ;\ 20\ J_{opt}\right]$ on the robust stability of the converter.

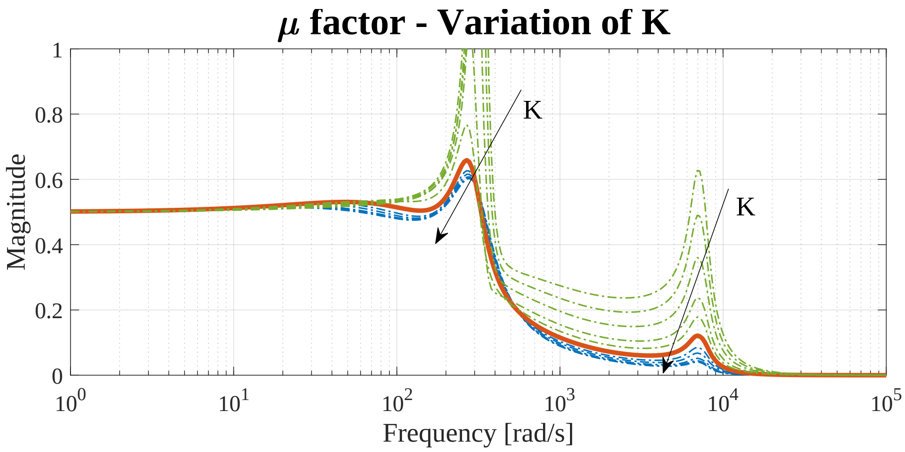

Figure 4.33: Effects of the variation of the parameter K within the range $\left[K_{opt}/5\ ;\ 5\ K_{opt}\right]$ on the robust stability of the converter.

Robust stability analysis of LCL filter-based synchronverter

In the following, the μ-analysis is performed to the case study examined in Section 4.2.1, represented by a single LCL filter-based synchronverter connected to the grid. Analogously to the eigenvalue analysis performed in Section 4.2.2, effects of control parameter variations, as well as grid conditions on the robust stability of the converter are investigated.

Fig. 4.32 shows the results of the μ-analysis according to the variation of the factor J of the power control loop. Colors have the same meaning as in Fig. 4.19 - 4.21, hence the red curve represents the μ-factor calculated under nominal operating conditions, and corresponding to the parameters reported in Table 4.3. The highest peak of $\mu = 0.658$ is reached for a frequency of $\approx 270\ rad/s$, showing a satisfying stability margin according to the chosen uncertainty description. Even though an increase of the parameter tends to augment the robustness of the control at higher frequencies, an excessive increase of this parameter causes an increase of the μ-factor in the low frequency range, and reaches almost the unity for a value of $J = 20\ J_{opt}$, indicating a reduction of the stability margin in the sub-synchronous region. This is consistent with the results of the eigenvalue analysis shown in Fig. 4.19,

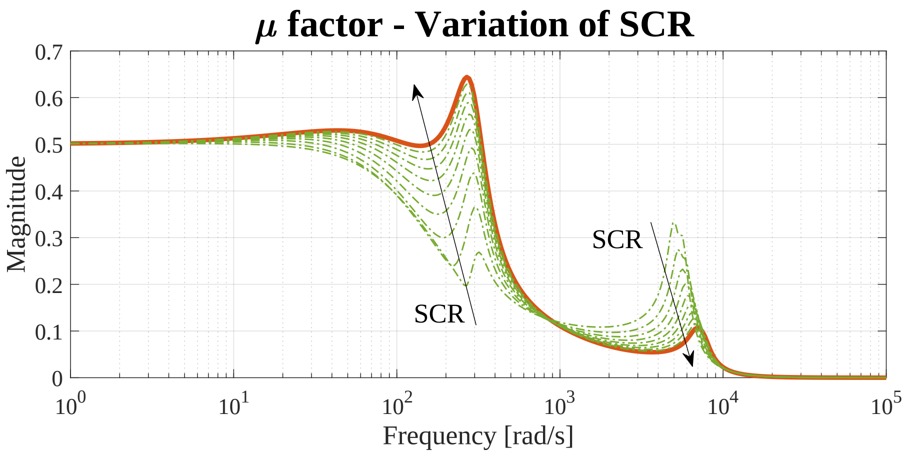

Figure 4.34: Effects of the variation of the SCR within the range $\left[2;\ 20\right]$ on the robust stability of the converter.

where it has been shown that the increase of the parameter J reduces the damping of two low-frequency poles, which move toward the imaginary axis and become dominant. This represents an important aspect that needs to be considered during the design procedure, and will be further discussed in the following.

The effects of the parameter K on the robust stability of the synchronverter are shown in Fig. 4.33. An increase of the parameter K above the value calculated by means of the proposed tuning procedure, does not substantially enhance the robustness of the control, which is instead noticeably worsened by a decrease of the parameter below the calculated K_{opt}. This result is again consistent with the results of the eigenvalue analysis shown in Fig. 4.20. However, the limit of μ =1 is reached for a value of $K \approx$ 18000, which is more conservative compared to the $K_{lim} \approx$ 8500 identified by means of eigenvalue analysis. As already pointed out in Section 3.4.3, this is a consequence of the fact that the μ-analysis provides information for a set of possible plants, instead of assessing stability only for a specific configuration.

Finally, Fig. 4.34 shows the effects of the reduction of the grid SCR on the robust stability of the synchronverter. Contrary to what has been deduced by means of the eigenvalue analysis performed in Section 4.2.2, where, according to Fig. 4.21, a reduction of the SCR causes a migration of all system eigenvalues toward the imaginary axis, the results of the robust stability analysis performed here reveal that the synchronverter is actually suitable for operation under weak grid conditions, since the reduction of the SCR causes a decrease of the highest peak of the calculated μ-factor. This can be intuitively explained considering the operating principle of a synchronverter, and generally of GFM converters, that makes the converter reproducing the behaviour of a voltage source behind impedance. Hence, small grid perturbations can cause significant variations of converter currents if the impedance between the ideal voltage source and the grid is relatively small, whereas an high impedance provides additional damping to the effects caused by such perturbations. To this extent, it is worth to notice that typical values of stator reactances of real SMs are generally much higher (in the range of 1.5-2 *pu* [31]), compared to typical filter impedance of grid connected converters,

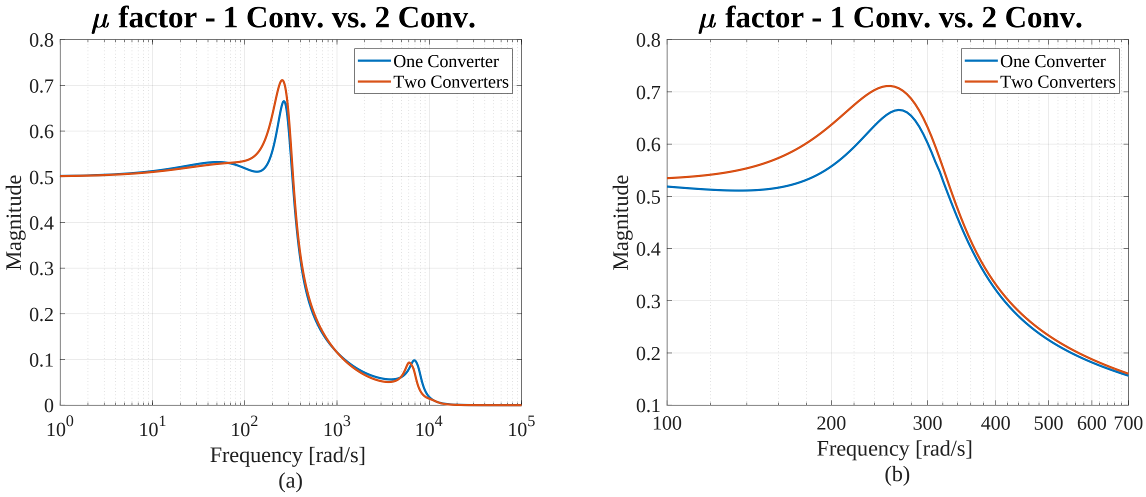

Figure 4.35: Effects of the presence of the second synchronverter operating in parallel on the μ-factor: (a) overview; (b) zoom.

usually in the range of 0.1 *pu* [25], and designed so as to optimize the trade-off between power quality and size of filter components. Similar conclusions have been drawn in [99], where the proposed approach for the virtual increase of the output converter impedance of a synchronverter discussed in Section 2.4.3, has been motivated by the fact that a VSM should reproduce as close as possible the characteristics of a real SM.

It is necessary to remark here that, while GFM converters result suitable for operation under weak grid conditions, exactly the opposite trend has been observed in Section 4.1 for the case of GFL converters, where it has been instead demonstrated that these converters are particularly susceptible to such operating conditions.

Robust stability of two synchronverters operating in parallel

The μ-analysis performed in the previous subsection, for the case of a single LCL filter-based synchronverter connected to the grid, is now extended to the case of two synchronverters operating in parallel. The derivation of the state-space model of the system under study has been already discussed in Section 4.2.3 which, according to Fig. 4.30, is already in a form suitable for performing the μ-analysis. Hence, the plant constituted by the filter and the grid adopted for the analysis when the single converter is in operation, is substituted by the plant of Fig. 4.23, and the analysis is performed again. Assuming that the two converters have the same parameters, and namely those of Table 4.3, Fig. 4.35 compares the μ-factor calculated when only one synchronverter is in operation (blue curve), against the resulting μ-factor when the second syncronverter is connected in parallel (red line). The outcome of this analysis is consistent with the results obtained by means of eigenvalue analysis, and shown in Fig. 4.27, where the migration of the critical system modes due to the presence of the second synchronverter is reported. Nevertheless, in order to obtain the results of Fig. 4.27, additional steps were needed, and namely the control parameters have been first modified so as to bring the system close to an unstable operating condition, then the critical system modes under the specific operating conditions have been identified, and finally their movement has been

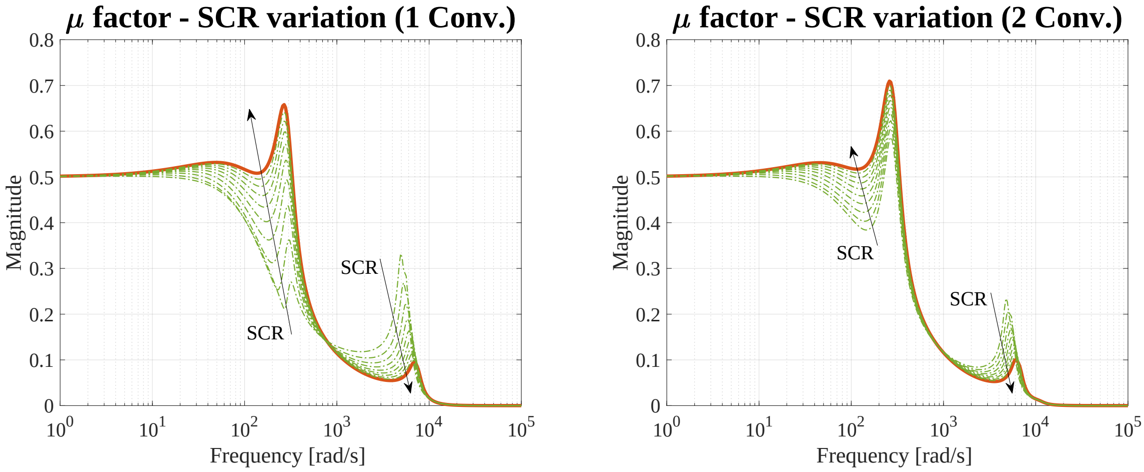

(a)

(b)

Figure 4.36: Effects of SCR variation within the range $[2;\ 20]$ on the robust stability of the converter: (a) one synchronverter; (b) two synchronverters in parallel.

observed. The calculation of the μ-factor, instead, highlights the reduction of the system stability margin without the need for any additional steps.

Fig. 4.36 compares the effects of the SCR variation on the μ-factors for the case when the synchronverter operates alone, and when the second synchronverter is connected in parallel. Fig. 4.36 (a) is equivalent to Fig. 4.34, and the reason for the reduction of the highest peak of the μ-factor has been already discussed. It can be observed in Fig. 4.36 (b), that the beneficial effects deriving from the increase of the grid impedance are noticeably reduced when the two synchronverters operate in parallel. This result can be explained considering that the second synchronverter operating in parallel, which emulates the behaviour of a voltage source behind impedance, becomes in this case the (electrically) closest voltage source. As a consequence, the reduction of the grid SCR does not produce the same effects that have been examined in Fig.4.36 (a), and Fig. 4.34. It can be then concluded, that the robust stability of the synchronverter, and generally of a GFM converter, is enhanced when the electrical distance between the converter and the closest voltage source, which might be represented by a strong grid, or by another GFM converter, is increased. These results are again consistent with the eigenvalue analysis performed in Section 4.2.4, where the stabilizing effects on the parallel operation of two synchronverters due to the increase of the filter impedance of both converters have been shown in Fig.4.29 (b).

Motivated by these findings, an optimal combination of filter parameters enhancing the robust stability of synchornverters operating in parallel is pursued in the following. Fig. 4.37 shows the μ-factor calculated for different combinations of inductive and resistive components of the converter filter impedance. The blue line represents nominal operating condition, namely when the inductance and the resistance of the two converter filters coincide with the values reported in Table 4.3. The red curve has been obtained increasing L_{f1} and L_{f2} of both converters of 100 %, while the resistance is maintained constant, causing a general reduction of the μ factor in the whole frequency range, however maintaining a significant peak around $\approx 300\ rad/s$. Analogously, the yellow curve in Fig. 4.37, has been obtained

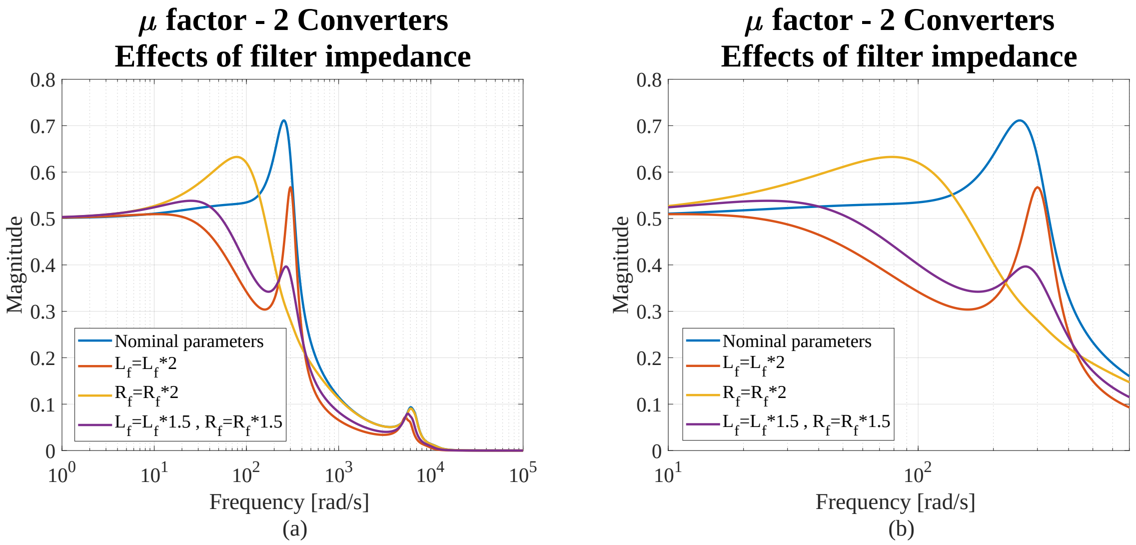

(a)

(b)

Figure 4.37: Effects due to the variation of the converter filter impedance on the μ-factor: (a) overview; (b) zoom.

by increasing the resistance of the filter impedance of both converters of 100 %, while the inductance is maintained unchanged. This modification causes a shift of the resonance peak toward lower frequencies. Finally, the violet curve shows the corresponding μ factor when both resistive and inductive components of the converter filter impedances are increased of 50 %, which, according to the obtained results, represents the best compromise among the examined conditions.

Refinement of the tuning procedure for a GFM converter

The synchronverter tuning procedure introduced in Section 4.2.2, does not consider the MIMO nature of the system, and control parameters have been tuned considering active and reactive power control loops independently. The dynamic performances of the converter have been tested by performing time-domain simulations, while stability has been assessed by means of eigenvalue analysis. Additional information have been gained by means of the robust stability analysis performed in this section, especially regarding the increase of the robust stability of a GFM converter when operating under weak grid conditions, along with indications about tuning of filter parameters. The results of these analysis can be combined in a comprehensive design procedure for a GFM converter, aiming to find the best compromise between dynamic performances and stability margin. To this extent, an example of such design process is reported in Fig. 4.38, and the most significant findings obtained in this section, are summarized below:

- In this work, control parameters have been initially tuned without considering any requirements on virtual inertia. In fact, according to the design procedure presented in Section 4.2.2, the virtual moment of inertia J has been set to a low value, properly chosen so as to allow neglecting the dynamic of the frequency droop loop in the

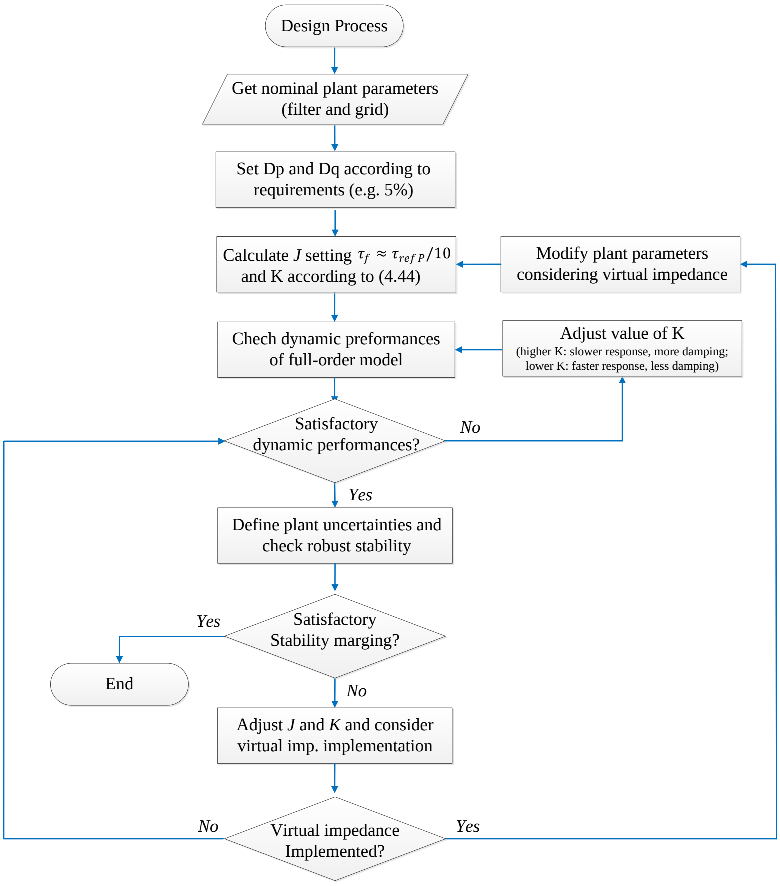

Figure 4.38: Steps of the proposed design procedure including robust stability considerations.

active power control loop. Considering the different implementations of the power-synchronization loop of a GFM converter discussed in Section 2.4, this condition would correspond to the droop control of Fig. 2.15, but can be generally extended to other among the considered implementations by properly choosing the virtual moment of inertia J. As it could be interpreted by looking at the results of the eigenvalue analysis in Fig. 4.19, and that becomes evident from the results of the robust stability analysis shown in Fig. 4.32, while an increase of this parameter can provide a certain degree of damping at higher frequencies, a significant increase of the aforementioned parameter might become instead detrimental for the robust stability of the converter in the sub-synchronous frequency range. Nevertheless, it is common thought that VSMs should reproduce the inertia of a real SM of the same size, requiring therefore the use of additional energy storage in the DC-link of the converter, thus increasing sizes and costs. Hence, it is instead important to point out that high values of the virtual moment of inertia J do not always correspond to an increment of the stability margin of the converter, if damping is not increased accordingly.

- The parameter K of the reactive power loop significantly affects the stability of the converter. To comply with the design procedure presented in Section 4.2.2, it has been suggested to choose the highest value of K resulting from (4.44) as K_{opt}. However,

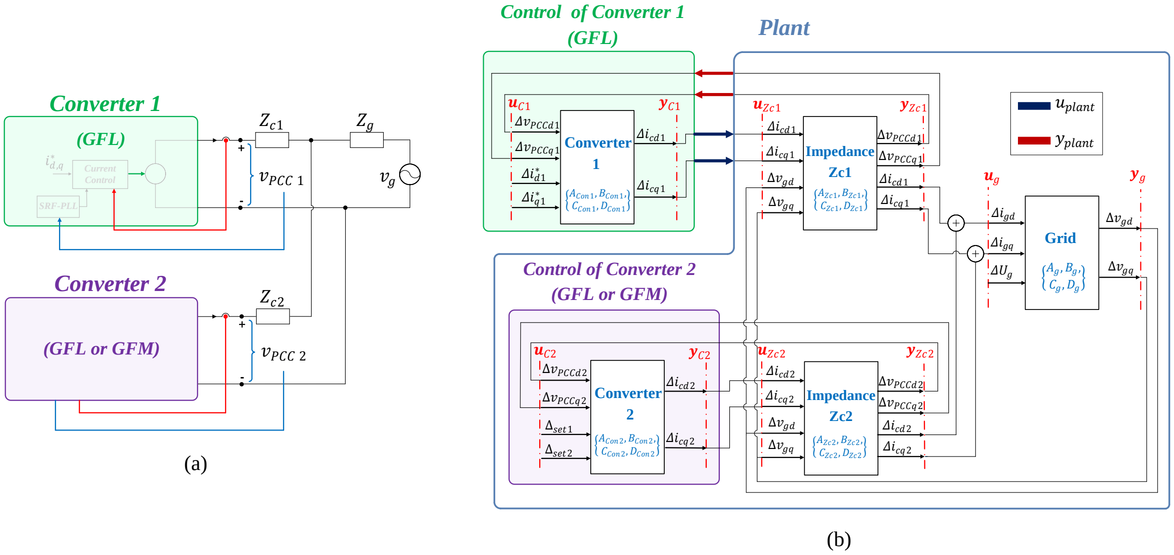

(a)

(b)

Figure 4.39: System under study: (a) equivalent scheme; (b) representation for CCM.

according to the results of the robust stability analysis performed in this section, along with the time-domain simulations shown in Fig. 4.17, an excessive increase of K over a certain limit simply worsen the dynamic performances of the converter, without significantly contributing to an increase of the stability margin.

- The μ-analysis performed for the case of a single synchronverter connected to the grid indicates that the robust stability of the converter against high-frequency uncertainties is augmented by the presence of a high impedance between the converter and the grid. This result has been extended to the case of two synchronverters operating in parallel, revealing that the robust stability of the synchronverter is generally enhanced by increasing the electrical distance between the converter and any other GFM unit operating nearby, which might be represented either by the grid, or by another GFM converter. Methods for virtually increasing the output impedance of a GFM converter without necessarily increasing the size of its hardware components, have been discussed in 2.4, and practical applications will be shown in the following chapters. According to the results shown in Fig. 4.37, it is recommended to choose the parameters of the virtual impedance so that the corresponding total filter resistance $R_f = R_{f1} + R_{f2} =$ [0.06 ; 0.1] *pu*, while the the total filter inductance $L_f = L_{f1} + L_{f2} =$ [0.15 ; 0.25] *pu*.

4.3.2 Model for studying interactions between GFL and GFM converters

In the following, the μ-analysis is performed in order to study effects of proximity of other converters on the robust stability of a GFL converter. The structure of the system under study is shown in Fig. 4.39. It is composed of two converters operating nearby, and connected to the same grid, resembling the structure shown in Fig. 4.1 (b). The state-space representation of the plant is obtained again by adopting the CCM, and the subsystem decomposition is

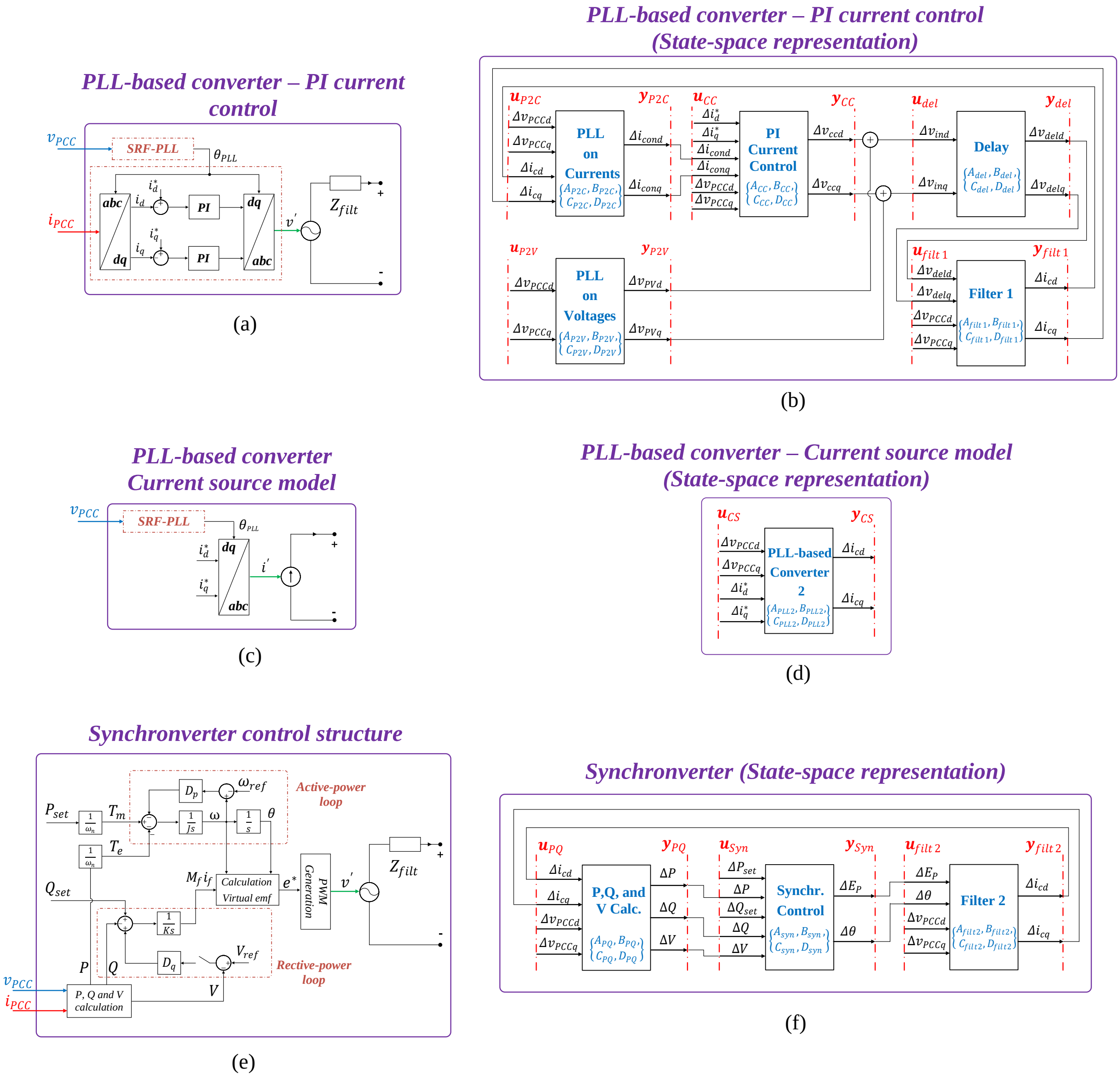

PLL-based converter – PI current control

PLL-based converter – PI current control (State-space representation)

PLL-based converter Current source model

PLL-based converter – Current source model (State-space representation)

Synchronverter control structure

Synchronverter (State-space representation)

(a)

(b)

(c)

(d)

(e)

(f)

Figure 4.40: Control structures: (a) GFL with PI current control, (c) GFL current source model, (e) GFM. Subsystem decomposition for CCM: (b) GFL with PI current control, (d) GFL current source model, (f) GFM.

depicted in Fig. 4.39 (b). Also in this case, impedances between converters, indicated with Z_{c1} and Z_{c2}, are introduced, which are modified so as to vary the electrical distance between the operating units, namely the impedance between their respective PCCs and the connection bus. It is assumed that the converter labeled as ”Converter 1” is a GFL unit, whereas the second converter can be either a GFL or a GFM converter. The control structures for the GFL and the GFM converter considered for the analysis are shown in Fig. 4.40 (a), (c), and (e). Two different implementations of GFL converters are investigated in the following, respectively depicted in Fig. 4.40 (a) and (c), and both equipped with a SRF-PLL for the estimation of the grid angle. In the control structure shown in Fig. 4.40 (a), a PI-based inner current control loop in the dq reference frame is implemented, while the structure shown in Fig. 4.40 (b), is the one already adopted in Section 4.1, where the perfect current source behaviour of the converter is assumed. The GFM converter control is again represented by the synchronverter structure already adopted for the stability analysis of GFM converters in the previous sections, and shown in Fig. 4.40 (e).

The subsystem decompositions of each of the aforementioned control structures are reported in Fig. 4.40 (b), (d), and (f). The state-space representation of each subsystem depicted in the figure is discussed in the following, with only few exceptions that have been already presented in the previous sections, and namely the ”*Grid*” subsystem, the ”*Synchronverter control*”, and ”*P, Q, and V calculation*”. The three control subsystems are formulated so as to have the same input and output vectors:

$$\begin{cases} \mathbf{u}_c = [\Delta v_{PCCd}\ \Delta v_{PCCq}\ \Delta_{set1}\ \Delta_{set2}]^T \\ \mathbf{y}_c = [\Delta i_{cd}\ \Delta i_{cq}]^T \end{cases} \tag{4.56}$$

where i_{cd} and i_{cq} represent the output converter currents, v_{PCCd} and v_{PCCq} the voltages measured at the respective PCCs, and $[\Delta_{set1}\ \Delta_{set2}] = [\Delta i_d^*\ \Delta i_q^*]$, for the case of a GFL converter, while $[\Delta_{set1}\ \Delta_{set2}] = [\Delta P_{set}\ \Delta Q_{set}]$ otherwise.

Filter 1 and Filter 2

In order to reduce model complexity, inductive converter output filters are considered in the following. For convenience, two slightly different formulations are adopted, in order to fit with the subsystem decomposition of the different control models. These are indicated in Fig. 4.40 (b) and (f) as "*Filter 1*" and "*Filter 2*", and only differ for their input vectors:

$$\begin{cases} \mathbf{u}_{filt1} = [\Delta v_{deld}\ \Delta v_{delq}\ \Delta v_{PCCd}\ \Delta v_{PCCq}]^T \\ \mathbf{u}_{filt2} = [\Delta E_p\ \Delta\theta\ \Delta v_{PCCd}\ \Delta v_{PCCq}]^T \\ \mathbf{y}_{filt1} = \mathbf{y}_{filt2} = [\Delta i_{cd}\ \Delta i_{cq}]^T \end{cases} \tag{4.57}$$

The corresponding input matrices $\mathbf{B}_{filt1}$ and $\mathbf{B}_{filt2}$ are defined as:

$$\mathbf{B}_{filt1} = \begin{bmatrix} \frac{1}{L_f} & 0 & -\frac{1}{L_f} & 0 \\ 0 & \frac{1}{L_f} & 0 & -\frac{1}{L_f} \end{bmatrix}; \qquad \mathbf{B}_{filt2} = \begin{bmatrix} \frac{\cos\theta_0}{L_f} & -\frac{V_0\sin\theta_0}{L_f} & -\frac{1}{L_f} & 0 \\ \frac{\sin\theta_0}{L_f} & \frac{V_0\cos\theta_0}{L_f} & 0 & -\frac{1}{L_f} \end{bmatrix}; \tag{4.58}$$

whereas the state-space matrices $\mathbf{A}_{filt}$, $\mathbf{C}_{filt}$ and $\mathbf{D}_{filt1}$ are equal for both subsystems:

$$\mathbf{A}_{filt} = \begin{bmatrix} -\frac{R_f}{L_f} & \omega_0 \\ -\omega_0 & -\frac{R_f}{L_f} \end{bmatrix}; \qquad \mathbf{C}_{filt} = \begin{bmatrix} I^{(2)} \end{bmatrix}; \qquad \mathbf{D}_{filt} = \begin{bmatrix} 0^{2\times 4} \end{bmatrix}. \tag{4.59}$$

R_f and L_f indicate the resistive and inductive component of the filter, respectively, whereas the quantities with subscript "0" represent values at the operating point.

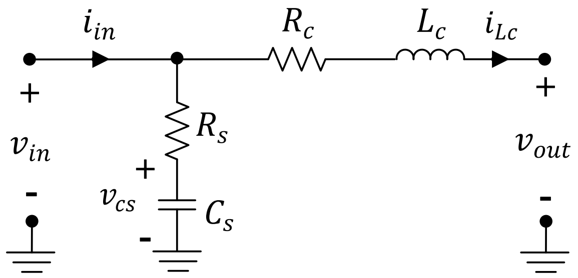

Figure 4.41: Model of the additional impedance Z_c.

Additional impedance Zc

The additional impedance is modeled by means of a resistive-inductive element, whose equivalent model is shown in Fig. 4.41. A similar solution as the one adopted in the previous section for modeling the grid is used, hence the auxiliary shunt components R_s and C_s are introduced in order to create the additional state of the capacitor voltage v_{cs}, obtaining the information about the voltage at the connection point. The equations describing this subsystem are reported below:

$$\begin{cases} L_c\frac{di_{Lc}}{dt} = R_s(i_{in}-i_{Lc})+v_{cs}-v_{out}-R_c i_{Lc} \\ C_s\frac{dv_{cs}}{dt} = i_{in}-i_{Lc} \end{cases} \tag{4.60}$$

which transformed in dq coordinates, yield the following state-space matrices:

$$\mathbf{A}_{Zc} = \begin{bmatrix} 0 & \omega_0 & -\frac{1}{C_s} & 0 \\ -\omega_0 & 0 & 0 & -\frac{1}{C_s} \\ \frac{1}{L_c} & 0 & \frac{-R_s-R_c}{L_c} & \omega_0 \\ 0 & \frac{1}{L_c} & -\omega_0 & \frac{-R_s-R_c}{L_c} \end{bmatrix}; \quad \mathbf{B}_{Zc} = \begin{bmatrix} \frac{1}{C_s} & 0 & 0 & 0 \\ 0 & \frac{1}{C_s} & 0 & 0 \\ \frac{R_s}{L_c} & 0 & -\frac{1}{L_c} & 0 \\ 0 & \frac{R_s}{L_c} & 0 & -\frac{1}{L_c} \end{bmatrix};$$

$$\mathbf{C}_{Zc} = \left[I^{(4)}\right]; \qquad \mathbf{D}_{Zc} = \left[0^{4\times4}\right], \tag{4.61}$$

while input and output vectors are:

$$\begin{cases} \mathbf{u}_{Zc} = [\Delta i_{cd}\ \Delta i_{cq}\ \Delta v_{gd}\ \Delta v_{gq}]^T \\ \mathbf{y}_{Zc} = [\Delta v_{PCCd}\ \Delta v_{PCCq}\ \Delta i_{cd}\ \Delta i_{cq}]^T \end{cases} \tag{4.62}$$

PLL on Currents and PLL on Voltages

The effects of the PLL on the measured converter currents are represented by means of the subsystem labeled in the figure as ”*PLL on Currents*”, whose equations have been presented in [66]. Indicating with i_{cond} and i_{conq} the d and q components of the measured currents including the effects of the PLL and propagated in the control, respectively, input and output vectors of this subsystem are:

$$\begin{cases} \mathbf{u}_{P2C} = [\Delta v_{PCCd}\ \Delta v_{PCCq}\ \Delta i_{cd}\ \Delta i_{cq}]^T \\ \mathbf{y}_{P2C} = [\Delta i_{cond}\ \Delta i_{conq}]^T \end{cases} \tag{4.63}$$

Then the effects of the PLL on the measured currents are modeled by means of the following equations:

$$\mathbf{y}_{P2C} \approx \begin{bmatrix} 0 & I_q H_{PLL}(s) & 1 & 0 \\ 0 & -I_d H_{PLL}(s) & 0 & 1 \end{bmatrix} \mathbf{u}_{P2C} \tag{4.64}$$

where I_q and I_d respectively indicate the d and the q components of the converter currents at the operating point, while $H_{PLL}(s)$ is the PLL transfer function already defined in (4.4). According to the considerations reported in Section 3.4, and namely that it is always possible to convert transfer-functions into state-space form [153], the state-space matrices of this subsystem have been obtained from (4.64) by means of the MATLAB command `ss`.

Similarly, the effects of the PLL on the reproduced converter voltages are modeled by means of the subsystem "*PLL on voltages*", associated with the matrix transfer function already reported in (4.15). Input and output vectors of this subsystem are:

$$\begin{cases} \mathbf{u}_{P2V} = [\Delta v_{PCCd}\ \Delta v_{PCCq}]^T \\ \mathbf{y}_{P2V} = [\Delta v_{PVd}\ \Delta v_{PVq}]^T \end{cases} \tag{4.65}$$

and the state-space description of this subsystem is again obtained from the matrix transfer function (4.15), by means of the MATLAB command `ss`.

PI Current Control

Inputs and outputs of the "*PI current control*" subsystem are given below:

$$\begin{cases} \mathbf{u}_{CC} = [\Delta i_d^*\ \Delta i_q^*\ \Delta i_{cond}\ \Delta i_{conq}\ \Delta v_{PCCd}\ \Delta v_{PCCq}]^T \\ \mathbf{y}_{CC} = [\Delta v_{ccd}\ \Delta v_{ccq}]^T \end{cases} \tag{4.66}$$

The equations describing the subsystem are:

$$\mathbf{y}_{CC} = \begin{bmatrix} \frac{k_{pi}\ s+k_{ii}}{s} & 0 & -\frac{k_{pi}\ s+k_{ii}}{s} & 0 & 1 & 0 \\ 0 & \frac{k_{pi}\ s+k_{ii}}{s} & 0 & -\frac{k_{pi}\ s+k_{ii}}{s} & 0 & 1 \end{bmatrix} \mathbf{u}_{CC} \tag{4.67}$$

where k_{pi} and k_{ii} have the same meaning as in (4.16), and indicate respectively the proportional and the integral gain of the PI controller. The state-space matrices are obtained from (4.67) by means of the MATLAB command `ss`.

Delay

The subsystem "*Delay*" takes into account the effects introduced by the PWM modulation and the digital control, and is represented by the matrix transfer function reported in eq. (4.18). Indicating input and output vectors of the subsystem as:

$$\begin{cases} \mathbf{u}_{del} = [\Delta v_{ind} \ \Delta v_{inq}]^T \\ \mathbf{y}_{del} = [\Delta v_{deld} \ \Delta v_{delq}]^T \end{cases} \tag{4.68}$$

the state-space matrices are obtained applying the MATLAB command `ss` to eq. (4.18).

PLL-based converter (current source model)

The equations describing the subsystem accounting for the PLL-based converter with current source behaviour are obtained again from [66], and are similar to those already adopted for describing the effects of the PLL on the measured currents in (4.64). Defining input and output vectors as:

$$\begin{cases} \mathbf{u}_{CS} = [\Delta v_{PCCd} \ \Delta v_{PCCq} \ \Delta i_d^* \ \Delta i_q^*]^T \\ \mathbf{y}_{CS} = [\Delta i_{cd} \ \Delta i_{cq}]^T \end{cases} \tag{4.69}$$

The matrix transfer function of this subsystem is reported below:

$$\mathbf{y}_{CS} \approx \begin{bmatrix} 0 & -I_q H_{PLL}(s) & 1 & 0 \\ 0 & I_d H_{PLL}(s) & 0 & 1 \end{bmatrix} \mathbf{u}_{CS} \tag{4.70}$$

which slightly differs from (4.63) for the sign of some elements. As for the previous case, the state-space matrices are obtained from (4.70) by means of the MATLAB command `ss`.

4.3.3 Interactions between GFL and GFM converters - μ-analysis

Two GFL converters in parallel

Once the state-space representation of the control and of the plant are obtained, the system is brought into a form suitable for performing the μ-analysis. The construction of the generalized plant for the examined case is depicted in Fig. 4.42, where differently from the case of

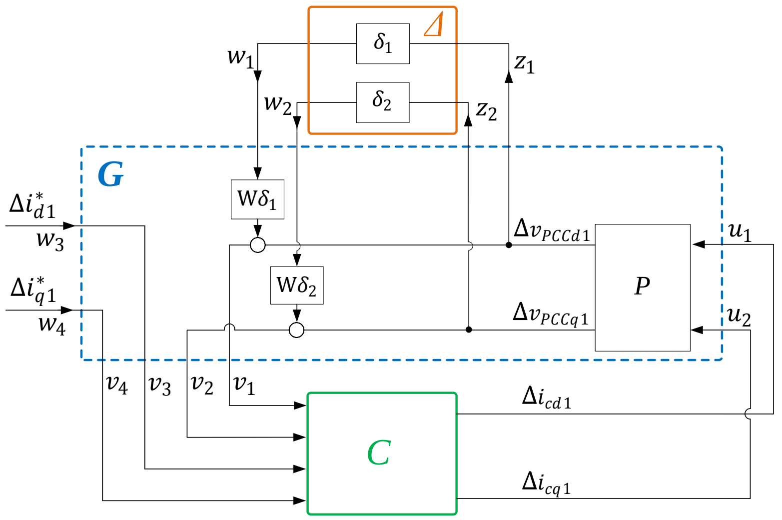

Figure 4.42: Construction of the generalized plant for the study of the interactions between GFL and GFM converters.

GFM converters, two multiplicative uncertainties $W_{\delta 1}$ and $W_{\delta 2}$ have been located at the output channels v_1 and v_2. This choice is motivated by the fact that, compared to multiplicative input uncertainties, which are suitable for representing the effects of neglected actuators dynamic, output uncertainties can better model the uncertain behaviour of input channels [140], [141]. In fact, for the case of GFM converters examined in the previous section, the effects of the modulation on the reproduced output voltage of the converter have been neglected in the model, but have been instead included in the analysis by means of the chosen plant uncertainties. On the contrary, the two GFL converter models considered for the analysis, either assume the perfect current source behaviour of the converter, or the effects of the delay are explicitly included in the model. Furthermore, the effects of the PLL on the stability of the control are mainly due to the measured converter voltages, hence it is much more convenient for the purpose of this investigation to locate plant uncertainties at the output channels.

Considering first the case of two GFL converters operating in parallel ($Z_{c1} = Z_{c2} = 0$), and both injecting their rated power, Fig. 4.43 (a) shows the effects due to the variation of the PLL-bandwidth of the two converters on the calculated μ-factor. The results are obtained assuming that the two converters are exactly identical in terms of hardware and control parameters. The blue curves are obtained using the GFL converter model shown in Fig. 4.40 (c), hence assuming the current source behaviour of the converter. The SCR of the grid is set to 2.5, and the bandwidth of the two PLLs has been increased within the range

Table 4.5: Parameters of the simulated system

Description	Symbol	Value	Description	Symbol	Value
Converter rated power	S_n	300 kVA	DC-link voltage	V_{DC}	750 V
X/R ratio	X/R	10	Converter switching frequency	f_s	30 kHz
Line-to-line voltage	V_{LL}	400 Vrms	Converter filter inductance	L_f	0.1 (pu)
Grid frequency	f_g	50 Hz	Converter filter resistance	R_f	0.04 (pu)

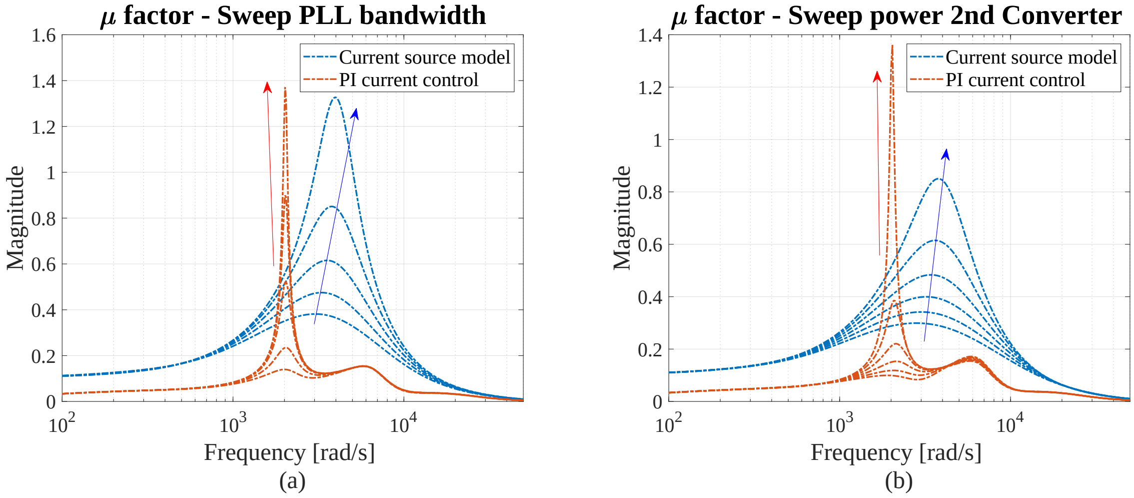

Figure 4.43: Two GFL converters in parallel, (blue) converter modeled as a current source, (red) converter model with PI-based inner current control loop: (a) variation of the μ-factor for a sweep of PLL-bandwidths of the two converters; (b) variation of the μ-factor for a sweep of power of the second Converter $P_2 = [0.5\ ;\ 1]pu$.

$f_{c1} = f_{c2} = [100\ ;\ 120]$ Hz. The peak of the μ-factor reaches higher values by increasing the PLL-bandwidth of the converter, overcoming the unity for $f_{c1} = f_{c2} \approx 118$ Hz. As expected, this result is more conservative compared to the value calculated by means of eigenvalue analysis, according to which the PLL-bandwidth causing instability under such operating condition is $f_{c1} = f_{c2} \approx 129$ Hz.

The same calculation is performed by modeling the two converters by means of the GFL control structure shown Fig. 4.40 (a), hence considering the presence of a PI-based inner current control loop, and the results are represented by the red curves in Fig. 4.43. As for the case studied in Section 4.1.4, the control parameters of the PI current controllers are tuned according to the technical optimum technique [25]. Under these conditions, the PLL-bandwidths of the two converters causing instability calculated by means of eigenvalue analysis, are slightly lower compared to the previous examined case, where the current source behaviour of the converter is assumed, resulting in a critical PLL-bandwidth of $f_{c1} = f_{c2} \approx 118$ Hz. The red curves shown in Fig. 4.43 (a), are obtained by varying the bandwidth of the two PLLs in the range $f_{c1} = f_{c2} = [100\ ;\ 115]$ Hz, resulting in a μ-factor reaching the unity for $f_{c1} = f_{c2} \approx 111$ Hz, thus confirming the expected trend.

The results shown in Fig. 4.43 (b), have been instead obtained by setting the PLL-bandwidth of the two converters with both converter models to fixed values, namely $f_{c1} = f_{c2} = 115$ Hz. Then the power of the first converter is set to its rated value, while the power of Converter 2 is varied within the range $P_2 = [0.5\ ;\ 1]$ pu. This condition can be interpreted as a variation of the SCR, and the results shown in the figure, again confirm the expected trend, namely that a decrease of the SCR (higher power injected by Converter 2) causes a decrease of the converter stability margin (higher μ-factor). It can be then concluded that the outcomes of the performed μ-analysis for case of two GFL converters operating in parallel, are consistent with the results obtained in Section 4.1.

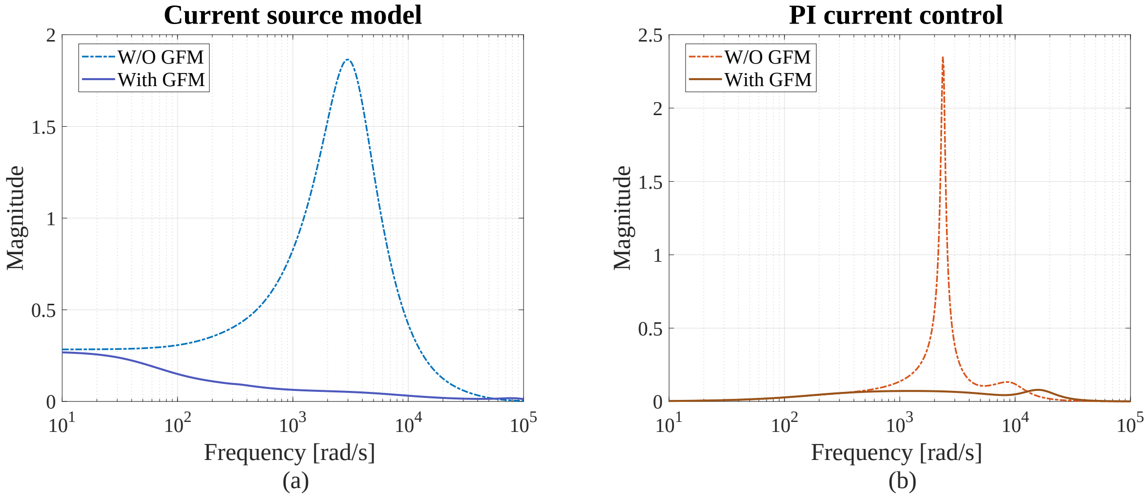

(a) (b)

Figure 4.44: Effects of a GFM converter on the robust stability of a GFL converter when the two converters are connected in parallel: (a) converter modeled as a current source, (b) converter model with PI-based inner current control loop.

Paralell operation between GFL and GFM converters

Fig. 4.44 shows the effects of the proximity of a GFM converter on the robust stability of a GFL converter. Assuming that Converter 1 is connected to a grid with SCR = 2.5, and injects its rated power, the dashed curves shown in Fig. 4.44 are obtained by fixing the PLL-bandwidth of the converter to a value of f_c =120 Hz for the currents source model (Fig. 4.44(a)), and f_c =115 Hz for the model with inner current control loop (Fig. 4.44(b)).

The continuous dark red and dark blue lines in the respective figures, are obtained connecting a GFM converter in parallel, tuned according to the procedure presented in Section 4.2.2, while the grid impedance is maintained constant. It can be clearly noticed in the figure that, independently from the adopted GFL converter model, the μ-factor is substantially reduced, indicating an increase of the robust stability margin. This effect can be intuitively explained observing that the presence of a GFM converter operating in parallel, which is stable and properly tuned, overcomes to certain extents the lack of a stiff grid, a condition required by a GFL converter in order to operate properly.

Effects of the distance on the obtained results

The results reported above, indicate that the robust stability of a GFL converter operating under weak grid conditions can be enhanced by locating a GFM converter in its electrical proximity. This conclusion suggests that a strategical distribution of converters operating with different working principles in the actual power system could aid integration of power electronics-based generation, thus without the necessity for a radical replacement of all existing units. To this extent, it is interesting to investigate how the electrical distance between converters affect the results obtained above. Assuming that the impedance between converters is mainly due to the presence of cables and transformers, the term electrical distance used here can be directly related to the physical distance between the units. However, this is not

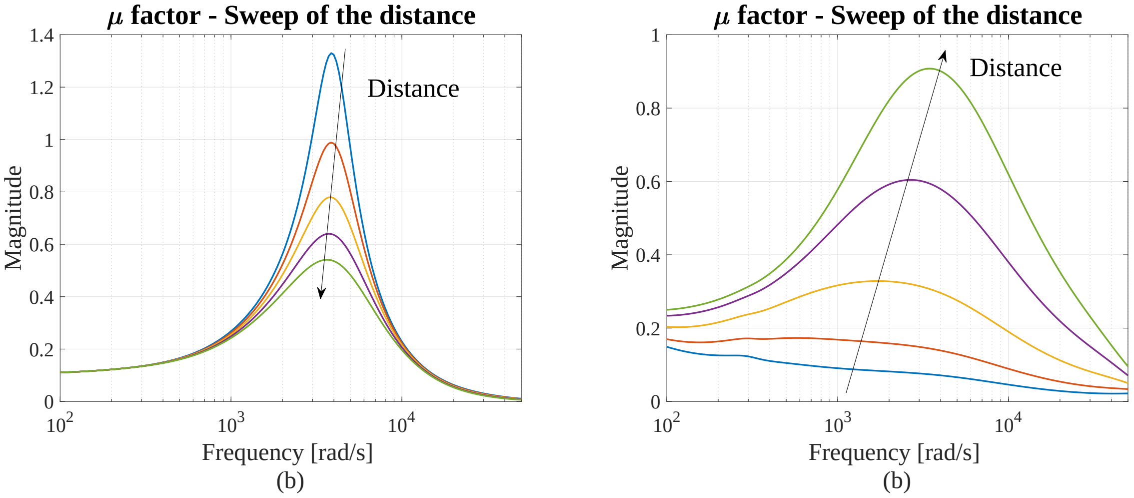

Figure 4.45: Effects of the electrical distance on the robust stability of converters operating nearby: (a) two GFL converters, sweep of $k_{dist} = [1\ ;\ 0.8]$; (b) GFL and GFM converter sweep of $k_{dist} = [1\ ;\ 0.5]$.

a general statement, since the value of determined impedances might be properly increased in practical cases, so as to provide a certain degree of decoupling between electrical parts of a complex system, e.g. in order to reduce circulating currents among converters operating nearby.

In the following, the effects due to the variation of the electrical distance between a GFL converter and other converters operating nearby, on the results obtained assuming parallel operation between the units are examined. For the purpose of the investigation, the factor k_{dist} is introduced. Thus, indicating with L_{gb} and R_{gb} inductive and resistive components of the grid, calculated considering for the respective cases a SCR of 2.5 and a X/R ratio of 10, resistive and inductive elements of the impedances Z_{c1} and Z_{c2} are calculated as follows:

$$\begin{cases} L_{c1} = L_{c2} = L_{gb} \cdot \left(1 - k_{dist}\right); \quad L_g = L_{gb} \cdot k_{dist} \\ R_{c1} = R_{c2} = R_{gb} \cdot \left(1 - k_{dist}\right); \quad R_g = R_{gb} \cdot k_{dist} \end{cases} \tag{4.71}$$

A value of $k_{dist} = 1$ corresponds to the case of converters operating in parallel examined in the previous paragraphs. A decrease of this parameter increases the value of the impedance between the two, however maintaining the sum of the total impedance $Z_c + Z_g$ for each converter unchanged. Since it has been demonstrated in the previous two paragraphs, that the two investigated GFL models provide qualitatively similar results, in the following, only the GFL converter model with current source behaviour is adopted for this analysis, gaining reduction of model complexity. Fig. 4.45 (a) shows the variation of the μ-factor for a sweep of k_{dist} within the range [1 ; 0.8] for the case of two GFL converters operating nearby. Although the sum of the two impedances $Z_{c1} + Z_g$ for Converter 1, and $Z_{c2} + Z_g$ for Converter 2 are maintained constant, the increase of the electrical distance between the two GFL converters causes a significant reduction of the μ-factor, indicating an increase of the converter robust stability margin. The same analysis is then performed for the case of a GFL and a GFM

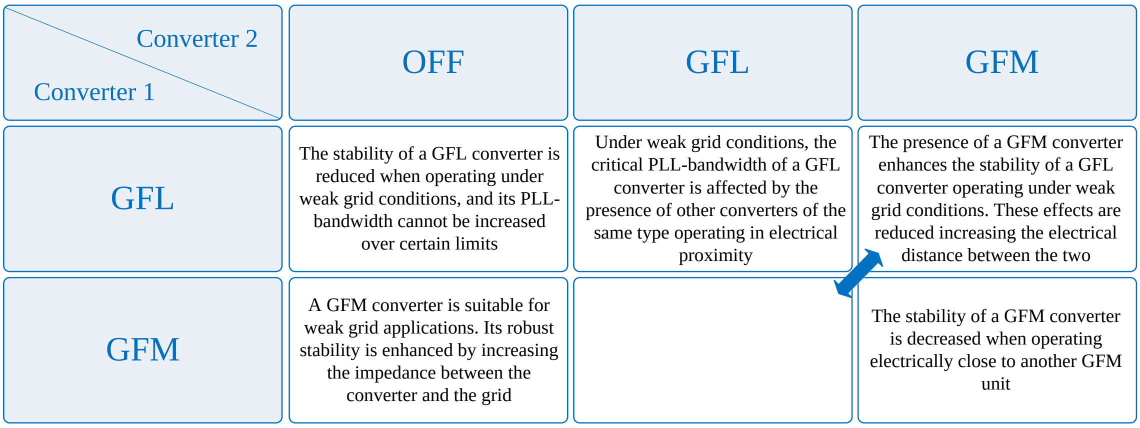

Converter 2 / Converter 1	OFF	GFL	GFM
GFL	The stability of a GFL converter is reduced when operating under weak grid conditions, and its PLL-bandwidth cannot be increased over certain limits	Under weak grid conditions, the critical PLL-bandwidth of a GFL converter is affected by the presence of other converters of the same type operating in electrical proximity	The presence of a GFM converter enhances the stability of a GFL converter operating under weak grid conditions. These effects are reduced increasing the electrical distance between the two
GFM	A GFM converter is suitable for weak grid applications. Its robust stability is enhanced by increasing the impedance between the converter and the grid		The stability of a GFM converter is decreased when operating electrically close to another GFM unit

Figure 4.46: Summary of the results related to stability analysis of the interactions between GFL and GFM converters.

converter operating nearby. k_{dist} is varied within the range [1 ; 0.5], and the modification of the μ-factor according to this variation is reported in Fig. 4.45 (b). An opposite trend compared to the case of two GFL converters can be observed in the figure, indicating that an increase of the electrical distance between the converters is responsible for the decrease of the converter stability margin.

4.4 Summary of the chapter

In the table shown in Fig. 4.46, an overview of the results related to the stability analysis of GFL anf GFM converters performed in this chapter, and focusing on the synchronization principles employed by the two examined converter types, is reported. These are summarized below:

- The stability of GFL converters has been investigated by means of impedance-based analysis in Section 4.1. In order to address the effects of the interactions among synchronization units of GFL converters operating nearby, a simplified model including only the PLL, and assuming the current source behaviour of the converter has been considered. The simplified system configuration allowed the calculation of a non-conservative norm-based stability margin, which has been adopted in order to perform a MC-based analysis. The outcome of this analysis showed that a GFL converter is particularly susceptible to weak grid operating conditions, and it has been demonstrated that there are limitations for the maximum allowable PLL-bandwidth of such converters. Furthermore, it has been shown that interactions between synchronization units of GFL converters operating nearby further reduce the value of the highest achievable PLL-bandwidth, being these effects accentuated by weaker grid conditions.

  The effects of additional control loops, e. g. the current control loop, on the results of the performed impedance-based stability analysis, have been subsequently included in the investigation. It has been demonstrated that the simplified model assuming the current source behaviour of the converter can still provide qualitatively reliable results, yet by reducing model complexity. On the contrary, the proposed norm calculation adopted for the MC analysis cannot be applied anymore when the additional loops are included in the model, due to the fact that the conditions for proving that the obtained results are non-conservative cannot be fulfilled. Finally, the robust stability analysis performed in Section 4.3.3, has shown that a stability margin consistent with the results obtained in Section 4.1, can be calculated independently on the adopted GFL model by means of μ-analysis.

- The eigenvalue analysis performed in Section 4.2 for GFM converters, along with the robust stability analysis performed in Section 4.3.1, have shown that a GFM converter operating alone is particularly suitable for applications under weak grid conditions, since its robust stability is enhanced by increasing the impedance between the converter and the voltage source representing an ideal strong grid. The investigation has been extended to the case of two GFM converters operating in parallel, showing how the robust stability of the GFM converter is negatively affected by the presence of another converter of the same type operating in close electrical proximity. This result has been generalized saying that the robust stability of a GFM converter is enhanced when the electrical distance between the converter and any other GFM unity, which might be represented by the grid or by another GFM converter, is increased. The implementation of a virtual impedance in the control of GFM converter has been proposed as a possible solution, in order to enhance the stability of GFM converters operating electrically close, an aspect that will be further investigated in the following chapters.
- The effects of the parallel operation between GFL and GFM converters have been addressed in Section 4.3.3. The results of the performed robust stability analysis have shown the beneficial effects on the stability of a GFL converter operating under weak grid conditions deriving from the presence of a GFM converter located in electrical proximity. The way how the electrical distance between converters affects the robust stability of a GFL has been addressed in the same section. The outcome of this investigation shows that small variations of the distance might substantially modify the results obtained when the converters operate in parallel, and that the increase of the electrical distance between two GFL converters has opposite effects compared to the case when the GFL converter operates in proximity to a GFM unit.

5 Fault ride-Through (FRT) of GFM converters

The operating principles of GFM converters have been discussed in Chapter 2, and a comprehensive literature overview on the possible implementations of the different subsystems composing the general control structure of a GFM converter has been presented in the same chapter. In the following, some of the most relevant challenges related to the implementation of GFM converters are addressed, which are represented by the synchronization stability, and the currents limitation during faults. These two aspects, typical of SMs, are inherent in the behaviour of GFM converters, as it will be demonstrated in the following. Thus, after having analyzed the causes for these two phenomena, and the consequent challenges for a GFM related to them, a proper Fault Ride-Through (FRT) strategy for GFM converters is proposed, whose efficacy is first demonstrated by means of hardware-in-the-loop (HIL) simulations in this chapter, then by means of experimental tests in Chapter 6.

5.1 Challenges for GFM converters

The characteristics of GFM converters, and their conceptual differences compared to GFL converters have been discussed in Chapter 2. The stability analysis performed in the previous chapter has demonstrated that, contrary to their counterpart, GFM converters are particularly suitable for operation under weak grid conditions, a situation that converters in the power system of the future are supposed to face rather frequently. Furthermore, due to the possibility of virtually modifying the equivalent output impedance of the converter according to the operating condition, when operating close to another GFM converter or connected to a stiff grid, the equivalent output impedance could be increased, so as to artificially increase the electrical distance between the GFM units, while when connected to a grid with low SCR, its output impedance could be instead reduced, enhancing the stability of the GFL converters operating nearby.

Although from the conceptual point of view GFM converters are highly appealing due to their capability of solving several shortcomings of GFL converters, there are, however, several issues related to their practical implementation. Among them, the transition between islanded mode and grid-connected mode still represents a topic of research [184], even though it has been extensively investigated in the last decade in the context of microgrids [185]-[188]. Beside that, other aspects have gained particular attention in recent years, and mainly concern the behaviour of GFM during fault conditions when operating in wide interconnected networks, rather than in an isolated system or in a microgrid. Among them, the synchronization stability and the current limitation during faults are surely noteworthy, two phenomena that GFM converters inherit from the emulation of certain aspects of real SMs. Indeed, the first one is directly related to the power-synchronization principle reproduced by many GFM implementations, while a proper handling of short-circuit currents in order to provide support to grid stability, yet preventing the converter from hardware damages, is directly related to the emulated behaviour of a voltage source behind impedance.

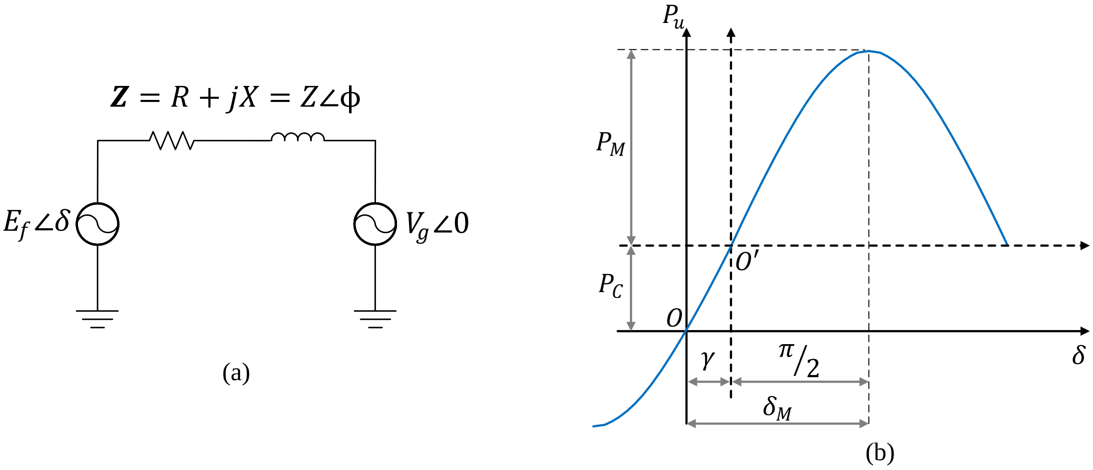

Figure 5.1: SM connected to an infinite bus: (a) equivalent single-line diagram; (b) power-angle curve.

In the following, these two aspects are first discussed from the conceptual point of view, then their consequences on the behaviour of a GFM converter are examined. Finally, proper solutions to handle their occurrence are proposed.

5.1.1 Rotor angle stability

Most of the GFM implementations presented in the literature, which have been examined in Section 2.4, reproduce the power-synchronization mechanism of a SM for grid synchronization purposes. The effects on the small-signal stability of the converter deriving from this synchronization principle compared to the process adopted by GFL converters, and commonly achieved by means of dedicated units (e. g. PLLs or similar structures), have been thoroughly exposed in the previous section. Nevertheless, reproducing this mechanism in the control of a converter might give rise to instability phenomena typical of a classical power system, e. g. *rotor angle stability*. Already introduced in Section 3.1.2, this phenomenon is commonly indicated as *loss of synchronism* in power system theory [70], and is succinctly explained in the following.

Let us consider the case of a SM connected to an infinite bus through a transmission line, schematically shown in the single-line diagram of Fig. 5.1 (a). Assuming the most generic case of a resistive-inductive impedance $\mathbf{Z} = R + jX$, the power exchange between the synchronous machine and the infinite bus is given by the following equation:

$$P_u = \frac{1}{Z}\left[E_f^2 \cos\phi + E_f V_g \cos(\phi - \delta)\right] \tag{5.1}$$

Defining the angle $\gamma = \phi - \frac{\pi}{2}$, eq. (5.1) can be rewritten as [70]:

$$P_u = \frac{1}{Z}\left[E_f^2 \sin\gamma + E_f V_g \sin(\delta - \gamma)\right] = P_C + P_M \sin(\delta - \gamma) \tag{5.2}$$

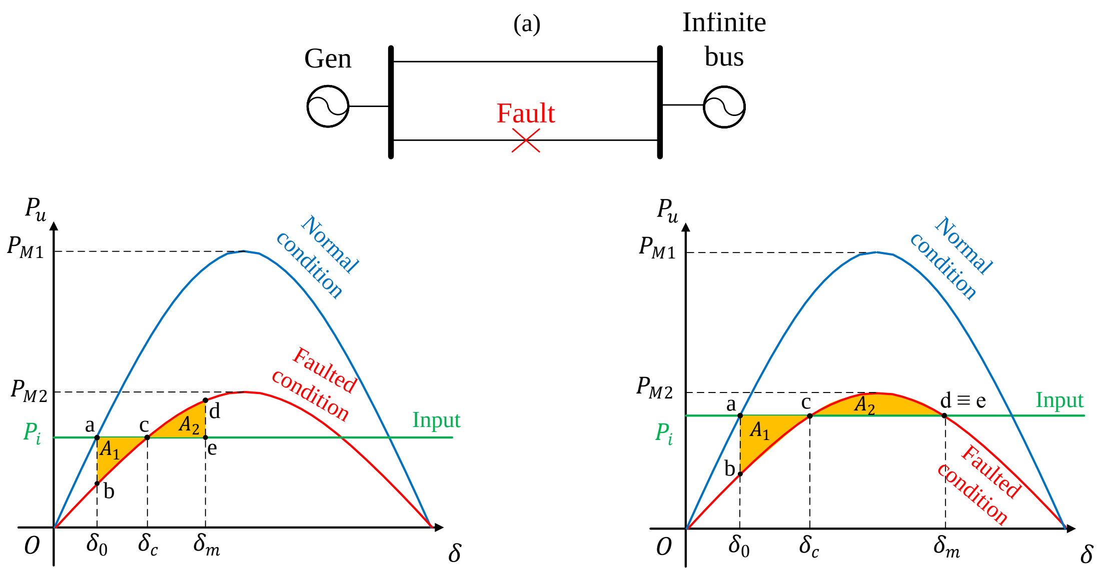

(b)

(c)

Figure 5.2: (a) Generator connected to an infinite bus through a double-circuit line; (b) graphical explanation of the equal-area criterion; (c) limit condition for stability.

A graphical explanation of eq. (5.2) is reported in Fig. 5.1 (b), showing that the power-angle curve is generally a displaced sinus, where δ_M indicates the angle displacement between the two voltage sources corresponding to the maximum power transfer. However, for the case of a purely inductive transmission line, $\mathbf{Z} = jX$, $\gamma = 0$, and the following is valid:

$$\begin{cases} P_u = \frac{E_f V_g}{X} \sin \delta \\ \delta_M = \frac{\pi}{2} \end{cases} \tag{5.3}$$

Let us now consider the condition depicted in Fig. 5.2 (a), where the generator is connected to the infinite bus through a double-line circuit. The input to the generator is the mechanical power P_i, and the initial operating point is defined by the intersection between the blue curve and the green horizontal line, hence the point a = (P_i , δ_0) in Fig. 5.2 (b). Assuming that at a certain instant in time a fault causes the opening of one of the two lines, the equivalent impedance between the generator and the infinite bus is suddenly increased, modifying the power-angle curve as depicted in Fig. 5.2 (b). Since the angle between the generator and the infinite bus δ_0 is initially unchanged, the operating point suddenly drops to point b, directly below the initial operating point a. According to the simplified expression of the swing equation, the *accelerating power* P_a is defined as follows [70]:

$$J\dot{\delta}\ddot{\delta} = P_i - P_u = P_a \tag{5.4}$$

At the instant when the fault occurs, the accelerating power $P_a = P^+_{a_{MAX}}$, corresponding to the vertical line ab in the figure. This causes an acceleration of the machine that shifts the operating point along the curve from b to c. In c, the accelerating power $P_a = 0$, but the speed of the machine reaches its maximum value $\dot{\delta}_{MAX}$, hence the angle δ continues increasing.

Table 5.1: Equal-area criterion

Point	P_a	$\ddot{\delta}$	$\dot{\delta}$	δ
b	$P^+_{aMAX} > 0$	$\ddot{\delta}^+_{MAX} > 0$	0	δ_0
c	0	0	$\dot{\delta}_{MAX}$	δ_c
d	$P^-_{aMAX} < 0$	$\ddot{\delta}^-_{MAX} < 0$	0	δ_m

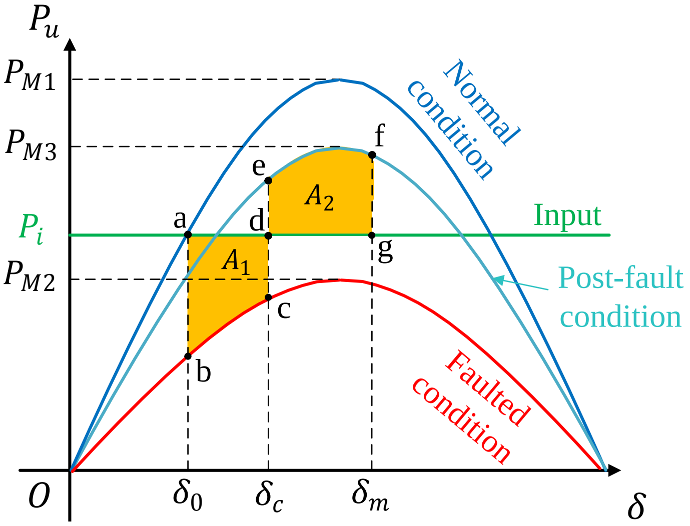

Figure 5.3: Equal-area criterion for the case of a fault cleared at angle δ_c.

As a consequence, the operating point further moves along the curve, reaching the point d characterized by $\dot{\delta}$ =0, and whose position in the curve can be calculated according to the *equal-area criterion*. In fact, due to the kinetic energy stored in the rotor of the machine, the value δ_m in Fig. 5.2 (b) satisfies the following condition:

$$\int_{\delta_0}^{\delta_m} P_a \, d\delta = 0 \tag{5.5}$$

determining the equality of the two areas $A_1 = abc$ and the area $A_2 = cde$. Therefore, the maximum displacement δ_m is reached at point d, but the accelerating power at that point on the curve is $P_a = P^-_{aMAX} < 0$. This produces a deceleration of the machine, that moves the operating point from d toward c, and then to b. The operating point continues oscillating between b and d, converging into point c due to the damping of the machine. Table 5.1 summarizes the conditions at the points b, c, and d for the process described above. Finally, Fig. 5.2 (c) shows the border between stable and unstable operation, represented by the condition $d = e$. Indeed, overcoming this limit, a δ_m satisfying (5.5) cannot be found, and the machine continues accelerating without finding a stable operating point.

Fig. 5.3 shows the equal-area criterion applied to the case of a fault cleared after a time interval. The light-blue line in the figure represents the power-angle curve after fault clearance, resulting from a new system configuration after disconnection of the faulted line. Compared to the previous two cases depicted in Fig. 5.2, P_{M2} lies below the horizontal line indicating the input power P_i, so that the machine does not have any chance to maintain the synchro-

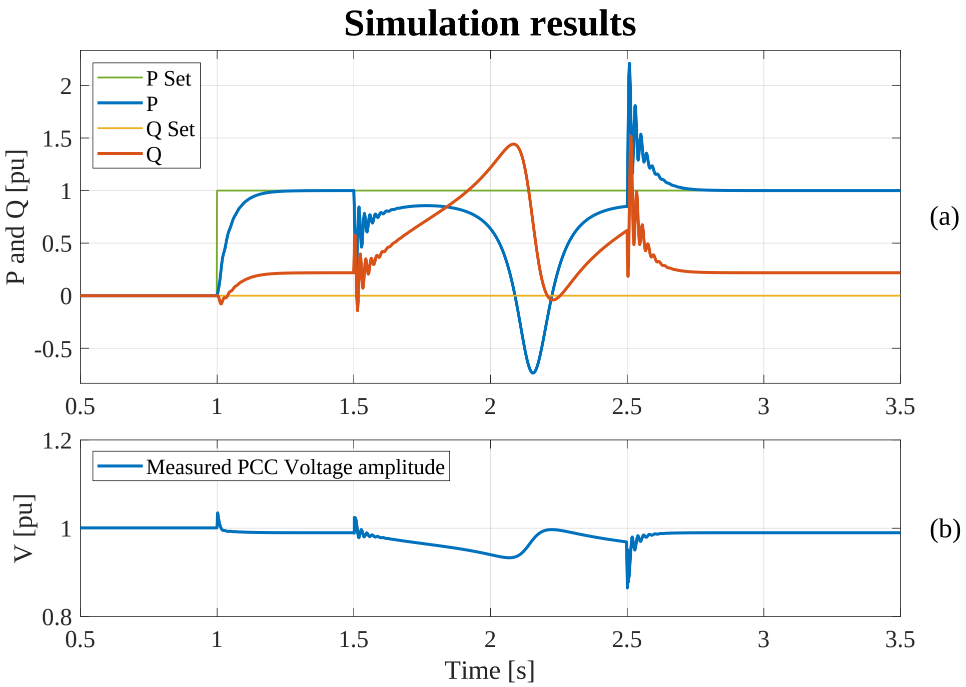

Figure 5.4: Simulation results showing the angle instability phenomena for a synchronverter when no measures are adopted: (a) active and reactive power; (b) measured amplitude of the grid voltage at the PCC.

nism to the grid if the fault is sustained. Yet, instability can be avoided if the fault is cleared before the angle δ reaches a critical angle δ_{cr}, corresponding to the condition $f = g$. The clearing angle is usually not known directly, but a clearing time can be estimated from the sum of relays and breakers delays [70]. Methods for calculating the Critical Fault Clearing Time (CFCT), namely the longest faulted condition that can be tolerated by the machines of a power system without falling out of step, have been developed, and usually involve non-linear analysis and numerical calculations [189]. These are needed in order to design the protections systems, and usually adopted in order to verify whether generators comply with the specifications defined by the Network Code on Requirements for Generators (NC-RfG) [190] given by SOs.

Consequences for the behaviour of GFM converters

The phenomenon described above is a consequence of the power-synchronization mechanism, which causes a SM falling out of step if the equilibrium betweem mechanical and electrical power cannot be reached. Thus, GFM converters adopting the same synchronization principle might be subjected to similar instability conditions. To confirm this statement, simulations for a GFM converter performed in Matlab/Simulink/PLECS, are reported in Fig. 5.4. The synchronverter model used for the simultations shown in the previous chapter, whose parameters are reported in Table 4.3, has been connected to an infinite bus through two identical lines as shown in Fig. 5.2 (a), with a resulting SCR=1.7, and X/R ratio of 10. Only for demonstration purposes, it is assumed that the converter does not have any current limitation algorithm implemented in the control, and it can sustain currents higher than 1 *pu*

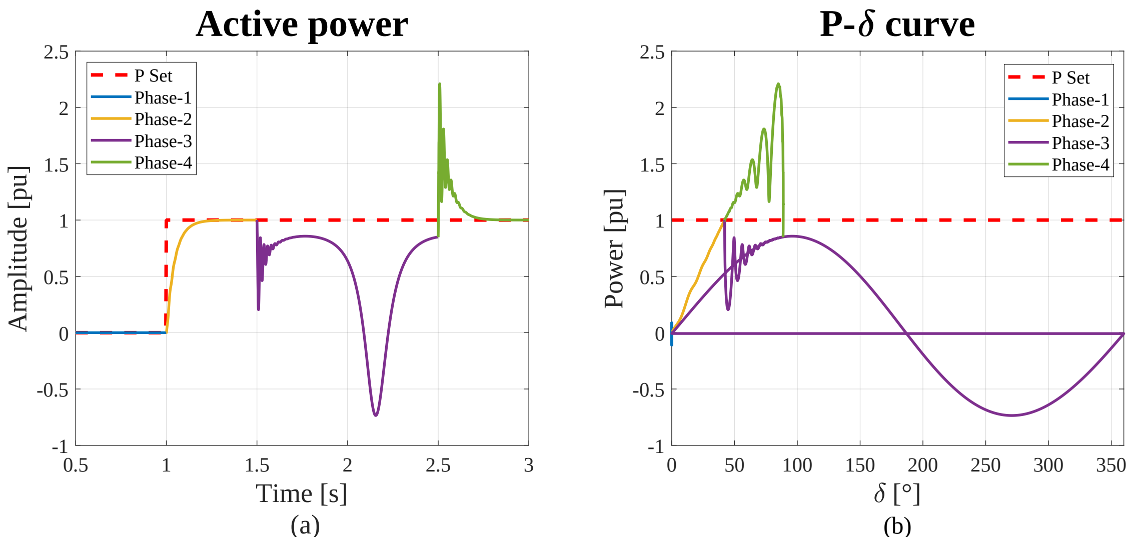

(a)

(b)

Figure 5.5: (a) Converter output power for the simulated event; (b) $P-\delta$ curve drawn from instantaneous simulated converter output power and power angle δ.

during a fault. At $t=1$ *sec*, the power setpoint P_{set} of the converter is set to its rated value, namely $P_{set}=1$ *pu*, which is reached after a transient. At $t=1.5$ *sec*, the disconnection of one line is emulated, resulting in a SCR below 1. The control tries to restore the power to the given setpoint increasing the power angle δ, by producing an acceleration of the virtual rotor. However, it loses synchronism with the grid after few hundreds of milliseconds falling out of steps. At $t = 2.5$ *sec*, the fault is cleared and the original condition is restored, so that the converter synchronizes again to the grid after a transient. The reactive power droop control has been activated for the simulations, and the voltages measured at the converter terminals are shown in Fig. 5.4(b), highlighting that the simulated voltage at the PCC is still maintained within its operating range considered as normal operation [0.9 *pu*, 1.1 *pu*], which might complicate a prompt detection of such critical condition.

The sequence of events described above is further analyzed in Fig. 5.5, where four different phases are distinguished and marked by using different colors. For each of the identified phases, the output converter power against the angle between the virtual back-emf e^* of the converter and the voltage of the ideal infinite bus is shown in Fig. 5.5 (b). This provides a similar plot as the power-angle curve shown in Fig. 5.2, which is, however, obtained from the quasi steady-state equations reported in (5.2). The first phase, indicated by the blue curve in Fig. 5.5 (a), represents the inizialization of the converter, where the power sepoints $P_{set} = 0$ *pu*. At the beginning of the second phase, indicated by the yellow curve, a step of the power setpoint $P_{set} = 1$ *pu* is performed, and the angle δ is increased from 0° to $\approx 40°$. At the occurrence of the fault, the operating point jumps on a new curve maintaining initially the same δ, which is slowly increased in order to reach the power setpoint P_{set}. However, the converter further increases the angle δ, yet without being able to reach a new equilibrium point, so that the virtual rotor further accelerates and loses synchronism with the grid. This effect is clearly visible in Fig. 5.5 (b), and is represented by the violet sinus. At $t=2.5$ *sec*, when the fault is cleared, the operating point jumps back to the original curve, as indicated by the green line in the figure, and pre-fault conditions are restored.

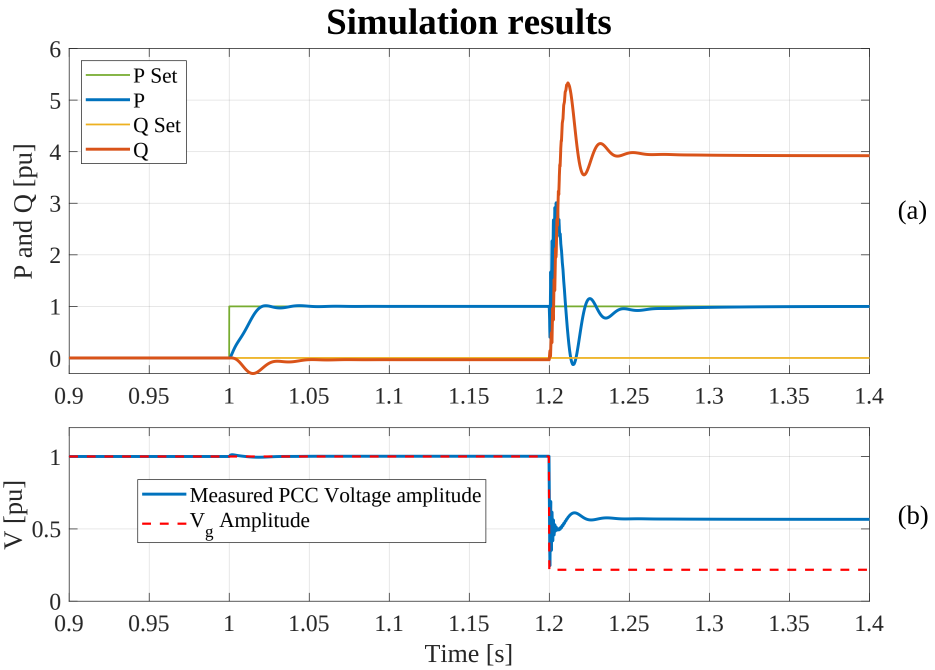

Figure 5.6: Simulation results showing the behaviour of a synchronverter subjected to a symmetrical three-phase fault. (a) Active and reactive power; (b) simulated voltages: (red-dashed) grid voltage amplitude, (blue-continuous) voltage amplitude at the PCC.

5.1.2 Short-circuit currents

The second aspect examined in this chapter, is represented by the handling of Low-Voltage Ride-Through (LVRT) scenarios, or commonly Fault Ride-Through (FRT). As already introduced in Section 2, one of the main differences between GFM converters and their counterparts GFL converters is their reaction to a grid fault. A GFL converter, whose reaction to a grid fault is strongly dependent on the dynamic of its synchronization unit, needs to detect first the new magnitude and phase of the grid voltage in order to inject properly the required fault currents, while an outer power control loop will adjust active and reactive current setpoints in order to comply with the grid codes of the country where the plant is installed. This measurement-based reaction usually requires several tens of milliseconds, and just to have an idea of the time constants at stake, actual German grid codes require injection of reactive power within 30 *ms* after fault detection [191]. On the contrary, a GFM converter that behaves as a voltage source behind impedance is able to react to a grid fault almost instantaneously without the need for detecting first the fault condition. This is a consequence of the emulated behaviour of voltage source behind impedance proper of a GFM converter, whose injected currents are then directly resulting from the characteristics of the impedance between the emulated voltage source and the grid. Therefore, similarly to a SM, and assuming that the impedance between the two voltage sources is mainly inductive, a GFM converter is able to inject almost instantaneously reactive power at the occurrence of a fault, hence overcoming the necessity for an accurate estimation of the new grid voltage angle.

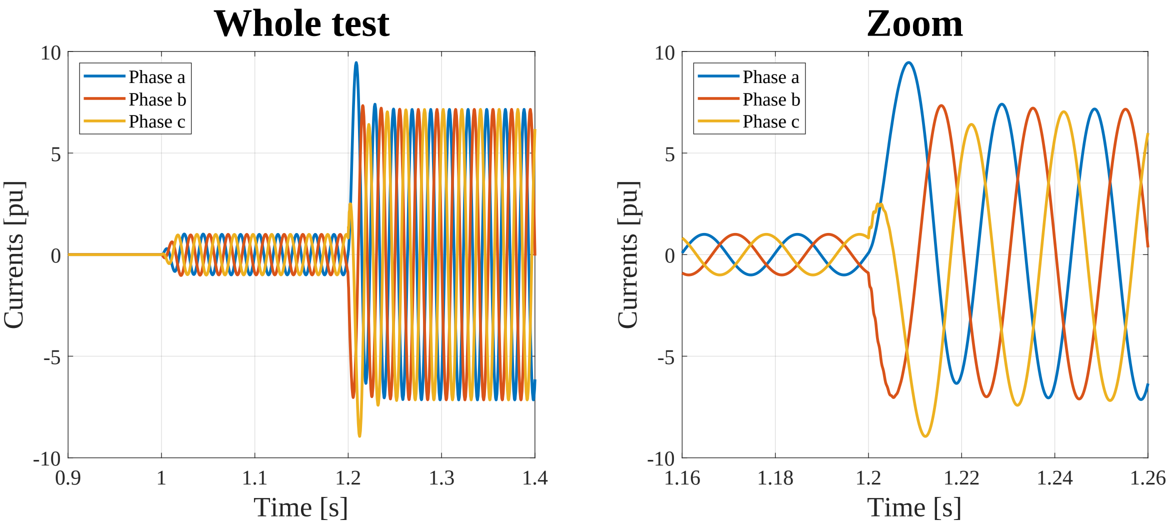

(a) (b)

Figure 5.7: Converter currents in case of a symmetrical three-phase fault: (a) whole event; (b) zoom at the time instant when the fault occurs.

Consequences for the behaviour of GFM converters

Only for demonstration of concepts, simulations results showing the ideal behaviour of a synchronverter in case of a symmetrical three-phase fault are reported in Fig. 5.6. A current limitation strategy is not implemented in the control, and it is assumed that the converter is able to sustain currents up to several times their rated values without incurring in hardware damages. Converter control and hardware parameters are shown in Table 4.3, and the grid SCR is set to 20, while the X/R ratio to 10. A step of the power setpoint P_{set} =1 *pu* is performed at $t = 1$ *sec*, and the converter dynamic response according to this event corresponds to the one already shown in Fig. 4.17. Then a three-phase short-circuit is simulated at $t = 1.2$ *sec* by suddenly decreasing the amplitude of the ideal voltage source V_g of the equivalent grid model from 1 *pu* to 0.2 *pu*. The simulations results reported in Fig. 5.6-5.8 are discussed in the following:

- As shown in Fig. 5.6, the significant amount of reactive power injected by the converter almost instantaneously, and without the need for any grid angle estimation, helps boosting the PCC voltage providing a significant contribution to the retained voltage. This aspect is highlighted in Fig. 5.6 (b), where the measured voltage at the converter terminals indicated by the continuous blue line is compared against the simulated amplitude of the ideal voltage source V_g of the equivalent grid model.

- Since the converter currents are only limited by the impedance between the converter and the ideal voltage source, which for the simulated case is mainly represented by the converter output filter due to the high SCR, the converter currents can reach up to several times their rated values within few milliseconds, as shown in Fig. 5.7. This behaviour typical of real SMs [192], and also useful in a classical power system for fault detection purposes (e. g. zone selective interlocking) [193], cannot be reproduced in practice by a real converter, unless it is massively oversized.

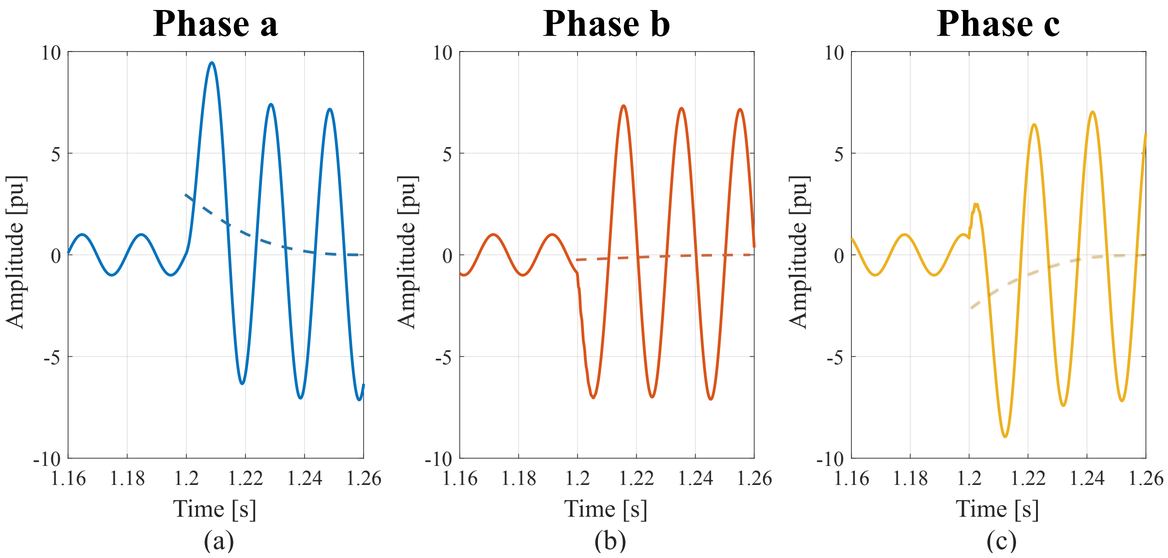

(a) (b) (c)

Figure 5.8: DC-components of the short-circuit currents for the simulated case: (a) phase a; (b) phase b; (c) phase c.

- As highlighted in Fig. 5.8, unidirectional components of the short-circuit currents with a decaying time constant $\tau = L/R$ can be observed. This behaviour typical of any RL circuit, is caused by the fact that the currents cannot change instantaneously. DC currents are also useful in power systems for fault detection purposes. Nevertheless, trying to reproduce these DC components of the currents would cause the saturation of the converter isolating transformer.

Taking into account the effects highlighted above, proper countermeasures should be taken so as to keep the advantages of GFM converters during faults in terms of fast reaction to a grid event, however by ensuring integrity of the converter hardware components without requiring significant converter oversizing.

5.1.3 Literature overview on FRT techniques for GFM converters

In the following, a literature overview on the solutions proposed in the literature in order to overcome the possible issues for GFM converters highlighted above, is reported. Even though the two phenomena are both related to the converter behaviour during faults, a distinction between solutions mainly related to avoidance of angle instability, and solutions for limiting converter overcurrents is done.

Avoidance of angle instability

The issue related to angle instability of converters working according to the power-synchronization principle of SMs has been recently investigated in the literature in several works [194]-[202]. In [195] and [196], a non-linear analysis for power-synchronization based control algorithms is presented, showing that, contrary to real SMs, these controllers are able to re-synchronize with the grid after one cycle of oscillation, even if the fault-clearing time is beyond the CFCT. Other works have addressed the issue of angle stability related to a grid fault that causes the reduction of the voltages at the connection point, so that the critical condition can be easily recognized. In that case, proper countermeasures can be taken, and [197] proposes a modification of the power setpoint proportional to the measured voltage depression, whereas [198] and [199] modify control parameters at the occurrence of a grid fault, namely the virtual damping factor in the first case, or the droop control gain in the latter case. If from one side the reduction of the grid voltage allows easily to detect a fault condition, this might provoke a sudden increase of the converter currents up to several times their rated values, which needs to be properly handled in order to prevent from hardware damages. As a consequence, current limitation during faults can also give rise to angle instability, an aspect that has been addressed in [200]-[202], and reveals that the two phenomena are closely related to each other. Nevertheless, the simulation results reported in Fig. 5.4 (b), show that a potential angle instability condition might not be necessarily recognized measuring the voltages at the converter terminals, and therefore, additional safety measures should be adopted, which preferably not only rely on voltage measurements. To this extent, no solutions are currently proposed in the literature in order to overcome this limitation, and a possible strategy is discussed in the next section.

Handling of short-circuit currents

The FRT of GFM converters has been also widely discussed in the literature, and various solutions have been proposed. Nevertheless, due to the lack of clear specifications regarding the behaviour of such converters during faults, in most of the cases, the proposed techniques mainly aim on preventing the converter from hardware damages and from instability issues, however without fully exploiting the potentials of GFM converters during fault conditions. Typical examples are the solutions adopted in [52], [73], [74], where the converter switches from GFM operating mode to a vector controlled mode as soon as a fault is detected, requiring therefore a back-up PLL. Other works have proposed the introduction of a cascaded inner current control loop for achieving converter currents limitation [203], [204], however without explicitly preventing from the risk of instability issues, since proper techniques in order to avoid the classical phenomena of ”wind-up” or ”latch-up” should be adopted [205].

A valuable alternative to saturation of PI controllers for limiting the fault currents of a GFM converter is represented by virtual impedances, and different techniques for virtual impedance implementation have been discussed in Section 2.4. These allow limiting the fault currents of a GFM converter by adapting the value of the reproduced impedance to the operating mode, hence avoiding the generation of excessively high current setpoints for the inner current control loop [206], [207]. To this extent, interesting studies showing the beneficial effects of virtual impedance implementation for improving the stability of GFM converters during grid faults when working in parallel to SMs have been reported in [93].

Early studies addressing FRT of VSMs have been presented in [208]. In [209], a non-linear approach for limiting the control states of a synchronverter is proposed, which ensures boundedness of frequency and voltage without the need for implementing anti wind-up techniques, yet without directly solving the issue related to limitation of converter currents during faults. Detailed calculations of synchronverter inrush currents during symmetrical and asymmetrical faults, according to the grid and the control parameters have been presented in [210] and [211], respectively. Nevertheless, a solution for limiting synchronverter currents has been proposed only for symmetrical faults in [210], which consists of activating an hysteresis inner current control loop as soon as the fault is detected. The converter currents setpoints are calculated by means of the information on the grid voltage angle, so that the required amount of reactive power according to the grid codes can be injected, thus requiring a PLL or a similar structure. The FRT of GFM converters in case of asymmetrical faults has been discussed in [212]. An auxiliary control regulating the negative sequence component of the converter currents to zero is activated at the occurrence of the fault, resulting therefore inappropriate for fulfilling some of the most stringent grid codes worldwide, which also require negative sequence current injection during asymmetrical fault conditions [191]. The work presented in [213], covers this gap considering both symmetrical and asymmetrical faults, and proposes to add an inner current control loop in the synchronverter structure, composed of a virtual impedance and a positive and negative sequence PI-based current control loop. This allows implementing the FRT strategies for GFL converters presented in [25], however without fully utilizing the potentials of GFM converters during faults, but simply reproducing the classical behaviour of a GFL converter.

Recent works have addressed the problems related to the coordination between outer and inner loops of GFM converters in order to avoid instability during grid faults, e. g. the angle stability phenomenon previously discussed. Beside [202], already mentioned in the last subsection and where, however, only symmetrical faults are considered, [214] proposes a current limitation strategy based on virtual impedances, where converter currents are properly limited by restraining positive and negative sequence components of the current setpoints. Nevertheless, several filters are implemented in the proposed control, degrading the dynamic performances of the converter. Furthermore, only simulation results are shown, lacking from an experimental proof of the proposed strategy.

5.1.4 Actual status draft grid codes for GB

The current status of the discussions among SOs and manufacturers at European level, and related to the development of specifications for GFM converters, has been introduced in Section 1.1.1. It has been pointed out that, at present time, grid code requirements including GFM characteristics have not yet been officially released. Nevertheless, the activities currently ongoing in Great Britain, and driven by the British SO NGESO, seem to represent the closest approach to a concrete development of grid codes including such characteristics, becoming probably Great Britain the first country worldwide to introduce such requirements in the grid codes.

According to these considerations, in the following, the current status of the draft grid codes elaborated within the EG on VSM is taken into account as a guideline for defining the behaviour of a GFM converter during faults [7], so that proper solutions can be developed accordingly. Indeed, it has been specified in Section 1.1.1, that the draft specifications elaborated within the EG phase, are currently under discussion within a ”working group”, so that they will be refined in order to approve a final proposal by the end of 2021. At the end of the second stage of the EG (December 2019), the following requirements were included in the draft GFM specifications for Great Britain (GFC-GB) [7], [215]:

(i) *The converter shall be capable of operating as a voltage source behind a reactance over a frequency band of 5 Hz to 1 kHz before, during, and after the fault.*

(ii) *The converter shall have a short-circuit current contribution of at least 1.5 pu of converter rating.*

(iii) *During a fault or voltage depression below 0.85 pu, the phase, magnitude and frequency of the voltage source will remain fixed at the pre-fault values. In the event that the resulting fault current would exceed 1.5 pu, a reduced fault current limited to 1.5 pu can be supplied, however its phase angle relative to the voltage source must be equivalent to the phase angle of the higher fault current.*

(iv) *In the event of a fault, the converter shall be able of supplying reactive power as soon as possible and within 5 ms of the voltage disturbance.*

(v) *The converter shall be capable of absorbing an unbalanced current of up to 2% without modifying the voltage source waveform.*

The lower frequency band indicated in **(i)**, was chosen according to the IEEE guide for excitation systems [216], so as to prevent from interactions with conventional machine rotor resonances, whereas the upper bandwidth of 1 kHz can be considered as an indication for the eventual implementation of an inner current control loop, an aspect that will be further discussed in the following. The short-circuit current contribution mentioned in **(ii)**, reflects the consideration reported in Section 5.1.2 related to the overcurrent capability of SMs during faults, which cannot be reproduced by a converter without additional oversizing. Hence, a compromise has been proposed with a short-circuit current up to 1.5 pu which, however, has been highly debated. Point **(iii)** provides instead a clear indication on the required converter behaviour during the fault, the latter defined as a voltage depression below 0.85 *pu*, and is therefore considered as a guideline for the FRT strategy proposed in the following section. Furthermore, this requirement is directly related to the dynamic behaviour of the converter requested in **(iv)**, being the latter point inherently achieved by fulfilling the requirement of point **(iii)**. Point **(iv)** also emphasizes the need for a measurement-less reaction of the converter to a grid event, which is otherwise difficult to achieve with a standard GFL converter. Finally, point **(v)** allows limiting the inherent contribution on negative sequence imbalances below a given threshold, since this might impact on lifetime and costs of the converter hardware components, e .g on the converter DC-link capacitors [217], [218].

5.2 Proposed solutions for overcoming the highlighted issues

In this section, solutions in order to overcome the issues previously highlighted are proposed. First, the angle instability phenomenon is addressed, proposing a method for the estimation of a potential critical operating condition. Then the limitation of converter currents during faults is investigated, and a proper implementation of an inner control loop for a GFM converter is proposed.

5.2.1 Estimation of angle instability condition

Contrary to a real SM, where occurrence of angle instability can be guaranteed only when the fault clearance within the CFCT is ensured, angle instability can be avoided in a GFM converter by detecting the potential critical operating condition, and taking proper control countermeasures. A possible solution might be represented by the direct calculation of the power angle δ according to the following equation [197], [198]:

$$\frac{d\delta}{dt} = \omega - \omega_g \tag{5.6}$$

Hence, the power angle δ could be theoretically obtained by integrating (5.6), however requiring an almost exact knowledge of the grid frequency at any time. To this extent, several algorithms can be implemented for the estimation of the grid frequency ω_g, e. g. the use of a Frequency-Locked-Loop (FLL) represents a well-established technique for grid-connected applications [25]. Nevertheless, these algorithms usually provide an accurate estimation of the grid frequency only at steady-state operating conditions, deviating from the real value during transients. Furthermore, even assuming that a perfect calculation of δ can be somehow achieved, the critical angle δ_M should be known. In fact, as indicated in Fig. 5.1, this may vary according to the characteristics of the grid impedance $\mathbf{Z}$, thus requiring a precise estimation of this quantity.

In order to overcome the need for such detailed information, a simple and intuitive solution is proposed in the following. This is based on the calculation of the *synchronizing-power coefficient* defined below [192]:

$$S_{PC} = \frac{\partial P_u}{\partial \delta} \tag{5.7}$$

where P_u has been defined in (5.1), as the power exchanged between a SM and an infinite bus. This coefficient has been introduced in [192], as a conservative stability criterion for multi-machine systems. It is based on the observation that on the stable side of the $P-\delta$ curve, an increase of the power angle δ caused by an acceleration of the rotor $\dot{\omega}$ >0, corresponds to an increase of the power exchanged between the machine and the infinite bus, resulting in the opposite behaviour on the unstable side of the curve, where an increase of the angle δ over δ_M provokes a decrease of the power P_u. Intuitively, in a multi-machine system, the synchronizing-power coefficient S_{PC} indicates that if one machine is advanced in phase,

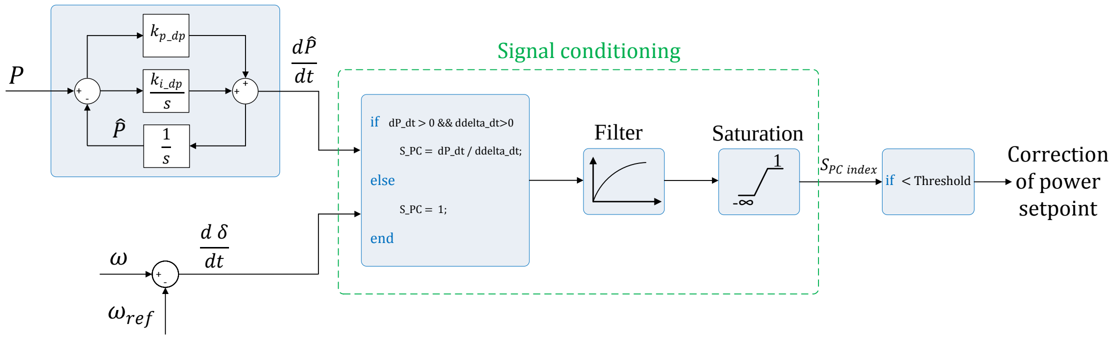

Figure 5.9: Subsystem in charge of the calculation of the $S_{PC\ index}$.

while the others are constant in phase, its electrical power output should increase. So if each machine in the system meets this requirement, the system is stable [192]. In accordance to power system theory, the calculation of a factor based on the S_{PC} could be integrated in the control algorithm of a GFM converter in order to estimate in which side of the $P-\delta$ curve the converter is currently operating. Thus, eq. (5.7) can be rewritten as:

$$S_{PC} = \frac{\partial P_u / \partial t}{\partial \delta / \partial t} \tag{5.8}$$

An exact calculation of this factor is not necessarily needed, but rather of an index, whose magnitude can provide an indication about the actual operating condition of the GFM converter. Hence, the $S_{PC\ index}$ is introduced, whose calculation is performed by means of the structure shown in Fig. 5.9.

According to the consideration about the exact estimation of the grid frequency, which is almost impossible in practice, the quantity $d\delta/dt$ cannot be easily obtained. Yet, considering the synchronverter structure depicted in Fig. 4.12, and assuming transient operating conditions, this calculation might be approximated to the difference between the actual ω and ω_{ref}. On the other side, an observer is introduced in order to perform the derivative of the measured power, and calculate the numerator of (5.8). In fact, it is well-known from control theory that the discrete derivative of a measured signal is highly sensitive to measurement noise [219]. The derivative of the measured power is then obtained by using the observer structure shown in Fig. 5.9, resembling the one of a PLL. The state $d\hat{P}/dt$ is generated by processing the difference between the measured power P and the estimated power $\hat{P}$ by means of a PI controller, whose proportional and integral gains are indicated as k_{p_dp} and k_{i_dp}, respectively. In order to identify the condition where the power angle δ slowly moves from the stable operating region toward the unstable side of the $P-\delta$ curve, the $S_{PC\ index}$ is calculated dividing $d\hat{P}/dt$ by $d\delta/dt$. However, this calculation is only performed when the two signals are simultaneously positive, being the factor set to a constant value otherwise. This signal is further scaled, processed through a first-order filter, and limited by means of a saturation block, so that during normal conditions the resulting $S_{PC\ index} = 1$.

This procedure allows identifying the transition from the left-hand side of the $P-\delta$ curve, to the right-hand side, where an increase of the power angle δ provokes a reduction of the

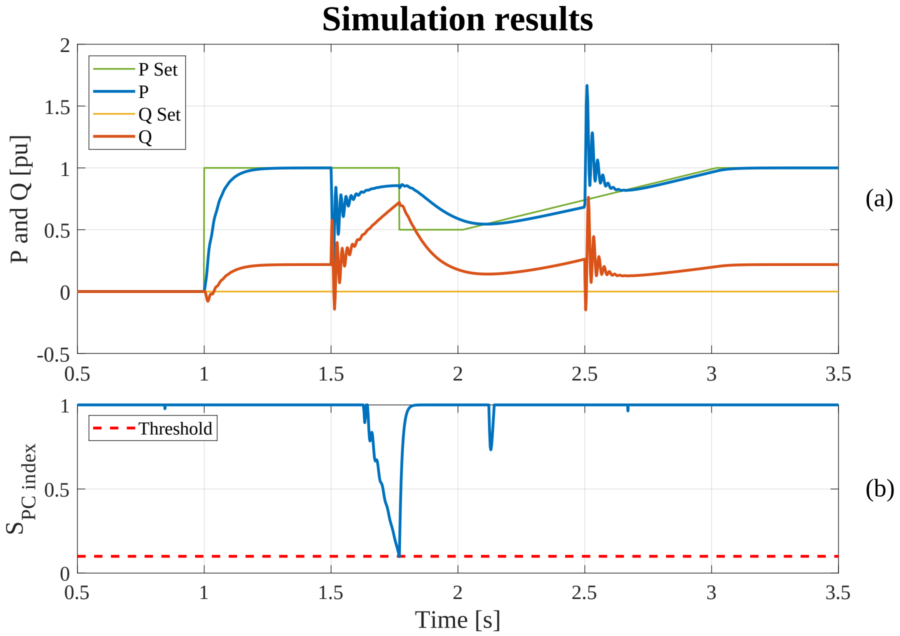

Figure 5.10: Simulation results showing the behaviour of the synchronverter when the proposed countermeasures for avoiding angle instability are adopted: (a) active and reactive power; (b) calculated $S_{PC\ index}$.

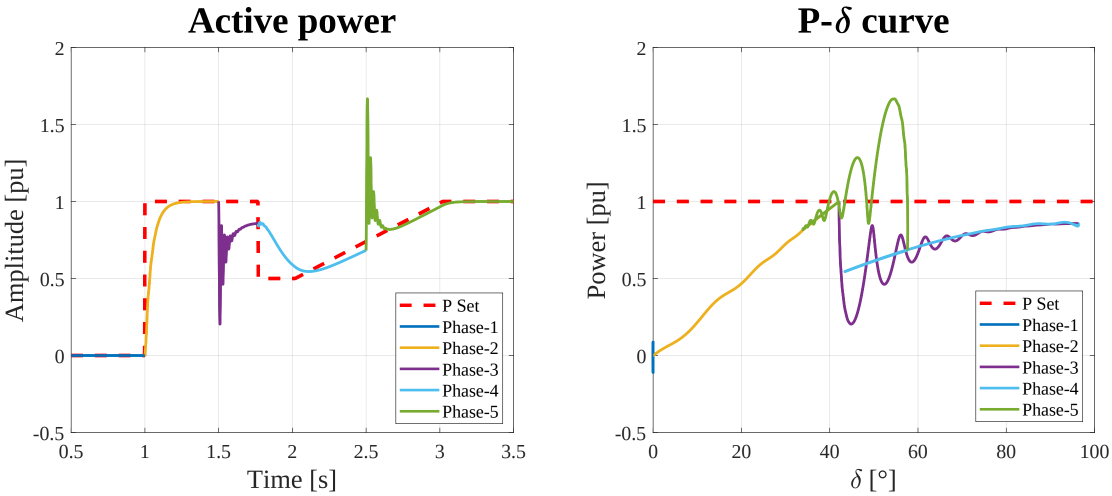

(a)

(b)

Figure 5.11: (a) Converter output power for the simulated event; (b) $P-\delta$ curve drawn from instantaneous simulated converter output power and power angle δ.

converter output power. Once the $S_{PC\ index}$ hits a lower threshold, further countermeasures can be employed. A possible solution might be a temporary reduction of the power setpoint, which is then slowly ramped up to its pre-fault value, waiting for the protections to isolate the fault. The simulations results in Fig. 5.10, show the behaviour of the converter under the same conditions simulated in Fig. 5.4, where the calculation of the $S_{PC\ index}$ is implemented. Few tens of milliseconds after fault occurrence, the $S_{PC\ index}$ slowly becomes lower than 1, hitting a lower threshold of 0.1 at $t \approx 1.8\ sec$. Merely for demonstration purposes, the power setpoint of the converter is reduced to 50 % of P_{set} for 200 ms, and then slowly ramped up to its pre-fault value within 1 sec. A comparison to Fig. 5.5 is shown in Fig. 5.11, where the

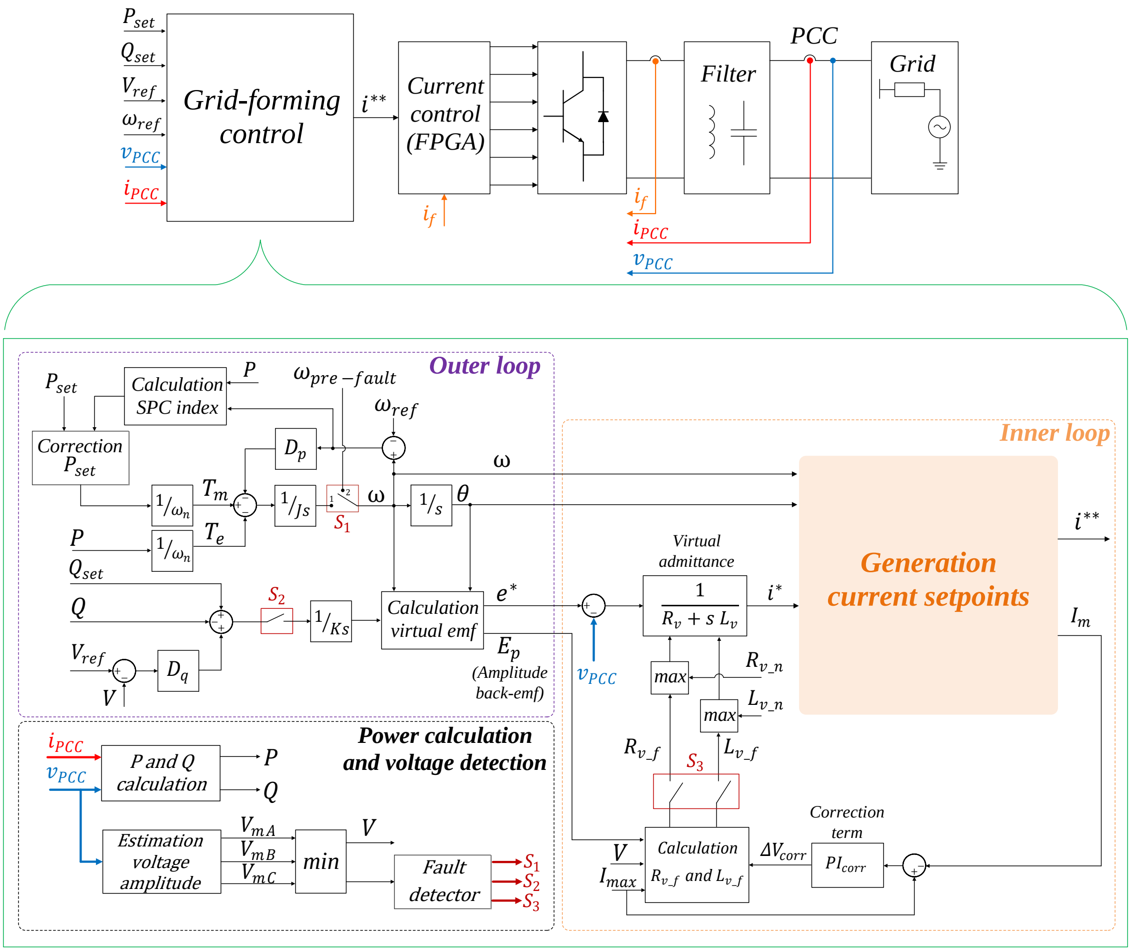

Figure 5.12: Overview structure of the proposed control scheme including calculation of the $S_{PC\ index}$ in the outer loop, and limitation of the short-circuit converter currents by means of the introduced inner control loop.

$P-\delta$ curve corresponding to the simulated condition is reported. Five phases are identified, and, compared to Fig. 5.5, the additional phase indicated by the cyan lines in Fig. 5.11 (a) and (b) can be seen, in which the operating point moves leftwards in the $P-\delta$ curve, and then slowly upwards until the fault is cleared, when it jumps back on the pre-fault curve.

5.2.2 Limitation of short-circuit currents

In order to prevent the converter from the risk of overcurrents during grid faults, an inner control loop based on a variable virtual admittance implementation is proposed [43], [44]. The virtual admittance concept has been already described in Section 2.4, in the context of possible implementations of the inner control loop of a GFM converter. This allows a direct control of the converter currents, yet ensuring highly dynamic performances, so that the behaviour of a voltage source behind impedance before, during, and after the fault can be reproduced.

The proposed control structure combining the two main modifications discussed in this chapter, is reported in Fig. 5.12. The outer loop is represented by the synchronverter structure already shown in Fig. 4.12, where additionally the calculation of the S_{PC} stability index discussed above, and reported in Fig. 5.9 is introduced, and which can eventually modify the power setpoint P_{set} if a critical operating condition leading to angle instability is recognized. A dedicated unit detects a fault by estimating the amplitude of the measured voltages v_{PCC} at the connection point. According to point **(iii)**, as soon as the lowest voltage among the three phases drops below the threshold of 0.85 pu, the switch S_1 connects to position 2, while S_2 will be opened, so that the magnitude and the frequency of the reference back-emf voltage e^* calculated by the outer loop are locked to their pre-fault values. The pre-fault frequency, indicated in the figure as $\omega_{pre-fault}$, can be obtained either by means of a dedicated unit, e. g. a FLL [25], or by means of a proper feedback of the internal quantity ω calculated in the outer loop.

A variable virtual admittance is implemented in the inner control loop of the proposed structure. Its inductive and resistive components, indicated respectively with L_v and R_v, are dynamically modified according to the operating conditions. To this extent, the effects of the virtual impedance implementation on the stability of a GFM converter have been thoroughly investigated in the previous Chapter, and design indications have been provided in Section 4.3.1. Hence, the virtual admittance implementation can reproduce the desired behaviour during normal operation, while it can be used in order to limit the converter currents during the fault.

Variable virtual admittance

The virtual admittance concept allows calculating independently single-phase currents directly from the comparison between the instantaneous measured voltages at the PCC and the virtual back-emf voltages e^* calculated in the outer loop according to eq. (2.33), reported below for simplicity:

$$i^*(s) = \frac{e^* - v_{PCC}}{R_v + s\,L_v} \tag{5.9}$$

The currents calculated above would correspond to those flowing into the grid when the converter is replaced by ideal three-phase voltage sources behind an impedance $Z_v(s) = R_v + s\,L_v$. Hence, under normal operating conditions, L_v and R_v are set to their nominal values L_{v_n} and R_{v_n}, properly chosen during the design procedure. At the occurrence of a fault, the switch indicated in the figure with S_3 is closed, and a dedicated subsystem calculates the quantities L_{v_f} and R_{v_f} limiting the amplitude of the highest single-phase current to the maximum allowable value I_{max}, according to the following equations:

$$\begin{cases} Z_{v\_f} = \left(E_p - V + \Delta V_{corr}\right)/I_{max}; \\ R_{v\_f} = Z_{v\_f}/\sqrt{X_{ratio}^2 + 1}; \\ L_{v\_f} = \left(X_{ratio} \cdot R_{v\_f}\right)/\omega_n; \end{cases} \tag{5.10}$$

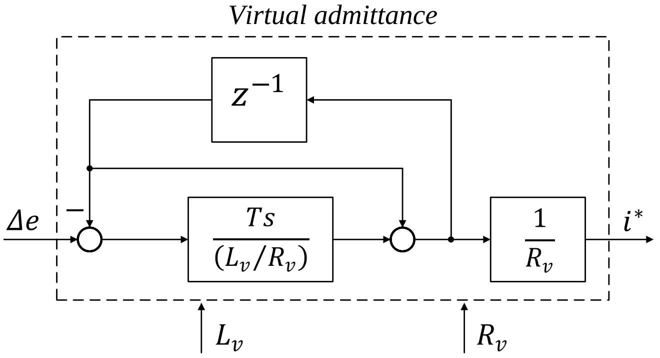

Figure 5.13: Discrete implementation of the variable virtual admittance.

where X_{ratio} indicates the X/R of the virtual admittance, ω_n is the nominal grid frequency, and, in order to calculate V, the lowest amplitude among the three phases estimated in the outer loop is considered. Since for the calculation of Z_{v_f} the phase displacement between the two phasors of the back-emf voltage and of the measured voltage at the PCC is not taken into account, a PI controller calculates the quantity ΔV_{corr} in order to compensate for the lack of this information, according to the following equation:

$$\Delta V_{corr} = \left(k_{p\_corr} + \frac{k_{i\_corr}}{s}\right)\left(I_{max} - I_m\right) \tag{5.11}$$

where k_{p_corr} and k_{i_corr} respectively indicate proportional and integral gain, and the quantity I_m represents the maximum instantaneous amplitude among the three phases of the current setpoints i^*. Finally, the variable virtual admittance is discretized as:

$$Y_v(z) = \frac{T_s}{z\,L_v - (L_v - R_v T_s)} \tag{5.12}$$

where T_s indicates the control sample time, and a scheme of the discrete implementation of the virtual admittance is reported in Fig. 5.13. This implementation allows easily modifying the value of the virtual admittance/impedance according to the operating condition.

It has been highlighted in Section 5.1.2, that the short-circuit currents of a GFM converter can reach up to several times their rated values within few milliseconds. Hence, before the action of the virtual admittance loop can actively limit them, the currents calculated according to eq. (5.9) are processed through a subsystem, indicated in the figure as *Generation current setpoints*, and which calculates the setpoints i^{**} for the most inner current control loop. This intermediate stage has the task of properly limiting the currents during the fault, so as to comply with the requirement **(iii)**, and prevent the converter from hardware damages.

To this extent, two approaches for the implementation of this subsystem are examined in the following. The first one is based on the decomposition of the three-phase currents i^* calculated by the virtual admittance subsystem into $\alpha\beta$ coordinates, an then into positive and negative sequence rotating vectors. Hence, the limitation of the single-phase currents is achieved by properly restraining the magnitudes of these two vectors. The second approach

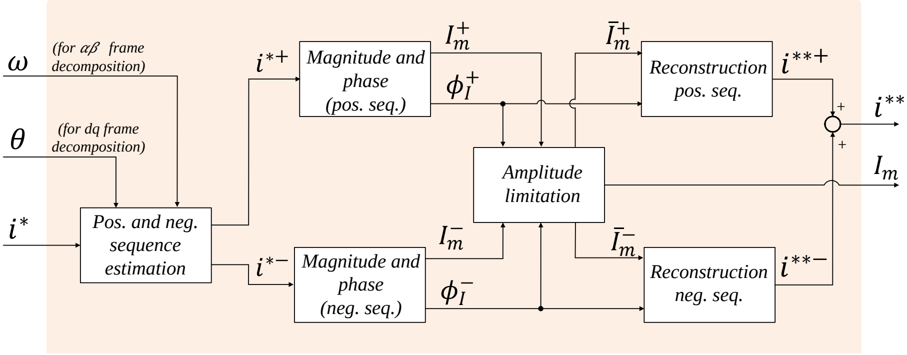

Figure 5.14: First examined implementation of the subsystem generating the converter current setpoints (*Concept 1*).

handles instead the three-phase currents i^* separately, so that each phase is treated as an independent vector, whose magnitude and phase can be properly manipulated so as to respect the hardware limitations, while complying with the specifications.

Generation of converter current setpoints - Concept 1

The first examined solution for the implementation of the subsystem in charge of the calculation of the converter current setpoints i^{**}, is schematically depicted in Fig. 5.14, and is referred in the following as *Concept 1*. This is based on a transformation of the currents i^* from the *abc* to the dq or $\alpha\beta$ reference frame and, in order to handle both symmetrical and asymmetrical faults, a decomposition in positive and negative sequence components is further required. This resembles the approach commonly adopted in the literature, for the estimation of positive and negative sequence components of the grid voltages during a fault, for which several techniques have been proposed, e. g. the Decoupled Double Synchronous Reference Frame structure (DDSRF) when working in dq coordinates [64], or the Double Second-Order Generalized Integrator (DSOGI) in $\alpha\beta$ coordinates [220], representing these two approaches the actual state of the art [25], [221]. Nevertheless, the equivalence between the DDSRF and the DSOGI has been mathematically proven in [25], and therefore only the formulation in $\alpha\beta$ coordinates is discussed in the following.

The frequency ω or the angle θ needed for the transformations are calculated in the outer control loop and, in contrast to a GFL converter, these represent internal control quantities, which do not need to be estimated from the measured converter voltages at the PCC, e. g. by means of a DDSRF-PLL or a DSOGI-FLL [25]. Considering then a formulation in $\alpha\beta$ coordinates, positive and negative sequence currents $\mathbf{i}_{\alpha\beta}^{*+}$ and $\mathbf{i}_{\alpha\beta}^{*-}$ can be calculated as:

$$\mathbf{i}_{\alpha\beta}^{*+} = \frac{1}{2}\begin{bmatrix} 1 & -q_L \\ q_L & 1 \end{bmatrix} \mathbf{i}_{\alpha\beta}^{*}; \qquad \mathbf{i}_{\alpha\beta}^{*-} = \frac{1}{2}\begin{bmatrix} 1 & q_L \\ -q_L & 1 \end{bmatrix} \mathbf{i}_{\alpha\beta}^{*}; \tag{5.13}$$

where $q_L = e^{-j\pi/2}$ is a 90° lagging phase shift. Assuming a constant frequency, this quadrature signal can be obtained by means of the quarter cycle delayed version of the input signal [214]. However, this approach works in practice only if the input signal is a perfect sinus

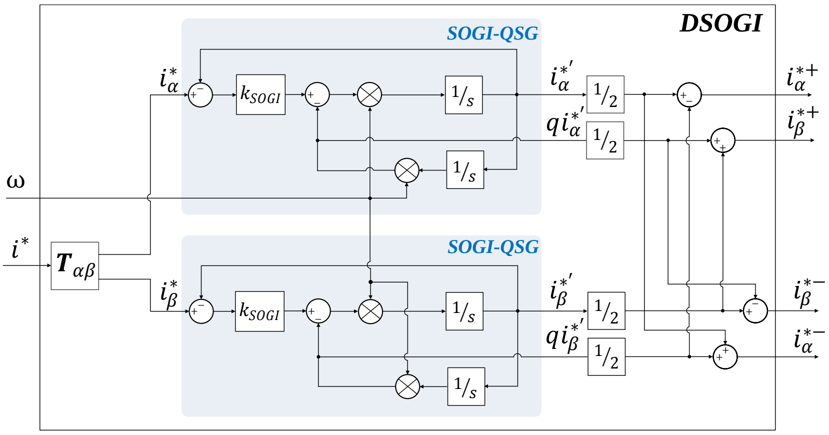

Figure 5.15: DSOGI structure for the calculation of positive and negative sequence components in $\alpha\beta$ coordinates.

at rated frequency [25], and therefore other techniques are better suited for generating a quadrature signal. Among them, the Second-Order Generalized Integrator-Quadrature Signal Generator (SOGI-QSG) [220], is widely adopted and represents the core of the DSOGI previously discussed, whose structure is shown in Fig. 5.15, and which is described by the following equations:

$$\mathbf{i}_{\alpha\beta}^{*+} = \frac{1}{2}\begin{bmatrix} D(s) & -Q(s) \\ Q(s) & D(s) \end{bmatrix} \mathbf{i}_{\alpha\beta}^{*}; \qquad \mathbf{i}_{\alpha\beta}^{*-} = \frac{1}{2}\begin{bmatrix} D(s) & Q(s) \\ -Q(s) & D(s) \end{bmatrix} \mathbf{i}_{\alpha\beta}^{*}; \tag{5.14}$$

where:

$$D(s) = \frac{i_{\alpha\beta}^{*'}}{i_{\alpha\beta}^{*}} = \frac{s\, k_{SOGI}\ \omega}{s^2 + s\, k_{SOGI} + \omega^2}; \qquad Q(s) = \frac{qi_{\alpha\beta}^{*'}}{i_{\alpha\beta}^{*}} = \frac{k_{SOGI}\ \omega^2}{s^2 + s\, k_{SOGI} + \omega^2}; \tag{5.15}$$

Here k_{SOGI} indicates the gain of the SOGI-QSG, whose tuning procedure has been widely covered in the literature [25]. Magnitude and phase of positive and negative sequence components are then calculated as follows:

$$I_m^+ = \sqrt{(i_\alpha^{*+})^2 + (i_\beta^{*+})^2}\,; \qquad I_m^- = \sqrt{(i_\alpha^{*-})^2 + (i_\beta^{*-})^2} \tag{5.16}$$

$$\phi_I^+ = \arctan\left(\frac{i_\beta^{*+}}{i_\alpha^{*+}}\right); \qquad \phi_I^- = \arctan\left(\frac{i_\beta^{*-}}{i_\alpha^{*-}}\right) \tag{5.17}$$

According to (5.16) and (5.17), the current setpoints $\mathbf{i}^* = [i_a^*\ i_b^*\ i_c^*]$ can be expressed as:

$$\begin{cases} i_a^* = I_m^+ \cos(\phi_I^+) + I_m^- \cos(\phi_I^-) \\ i_b^* = I_m^+ \cos(\phi_I^+ - \frac{2}{3}\pi) + I_m^- \cos(\phi_I^- - \frac{2}{3}\pi) \\ i_c^* = I_m^+ \cos(\phi_I^+ + \frac{2}{3}\pi) + I_m^- \cos(\phi_I^- + \frac{2}{3}\pi) \end{cases} \tag{5.18}$$

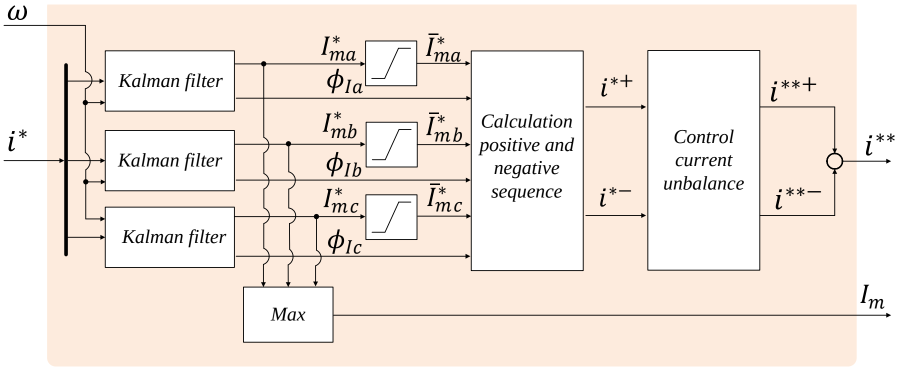

Figure 5.16: Second examined implementation of the subsystem generating the converter current setpoints (Concept 2).

The amplitude of each phase current can be calculated from the the quantities I_m^+, I_m^-, ϕ_I^+, and ϕ_I^-, according to the following equations [222]:

$$\begin{cases} I_{ma} = \sqrt{(I_m^+)^2 + (I_m^-)^2 + 2\, I_m^+\, I_m^- \cos(\gamma)} \\ I_{mb} = \sqrt{(I_m^+)^2 + (I_m^-)^2 + 2\, I_m^+\, I_m^- \cos(\gamma - \frac{2}{3}\pi)} \\ I_{mc} = \sqrt{(I_m^+)^2 + (I_m^-)^2 + 2\, I_m^+\, I_m^- \cos(\gamma + \frac{2}{3}\pi)} \end{cases} \tag{5.19}$$

where $\gamma = -(\phi_I^+ + \phi_I^-)$. Then a proper technique needs to be implemented in order to limit the amplitude of the current setpoints $I_m = max\{I_{ma}, I_{mb}, I_{mc}\} \leq I_{max}$. Hence, an approach similar to the one proposed in [214] is adopted here, and is briefly explained in the following. It consists of multiplying both positive and negative sequence current components $\mathbf{i}^{*+}_{\alpha\beta}$ and $\mathbf{i}^{*-}_{\alpha\beta}$ by a proportional factor k_{lim}, calculated as follows:

$$\begin{cases} k_{lim} = 1; \quad if \quad I_m \leq I_{max} \\ k_{lim} = \frac{I_{max}}{I_m}; \quad if \quad I_m > I_{max} \end{cases} \tag{5.20}$$

Then $\bar{I}_m^+ = I_m^+ \cdot k_{lim}$ and $\bar{I}_m^- = I_m^- \cdot k_{lim}$, which ensures the limitation of the instantaneous value of the reconstructed positive and negative sequence current setpoints $i^{**+}_{\alpha\beta}$ and $i^{**-}_{\alpha\beta}$, such that the resulting current setpoints i^{**} in each phase do not exceed the maximum allowable amplitude I_{max}.

Generation of converter current setpoints - Concept 2

The scheme of the second investigated approach, referred in the following as *Concept 2*, is shown in Fig. 5.16. Compared to the previous implementation, each phase is considered separately, and three independent Kalman filters are employed in order to detect the magnitude and the phase of each current, respectively indicated in the figure as I^*_{mx} and ϕ_{Ix}, with $x = \{a, b, c\}$. Kalman filters, along with their formulation for non-linear applications, Extended Kalman Filters (EKFs), are based on a recursive estimation of the states of a process

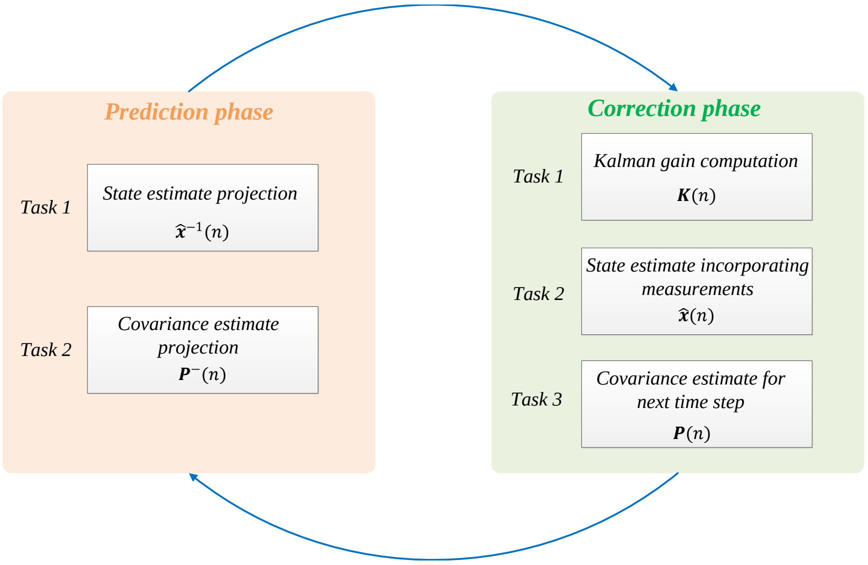

Figure 5.17: Graphical explanation of the Kalman filter workflow.

and are widely adopted in control applications, e. g. in Linear Quadratic Gaussian (LQG) controllers [103], [141]. Kalman filter theory has been subjected to extensive research in the past decades, becoming nowadays broadly used in practical engineering applications, e. g. in sensor-less drives [223]-[226], or for grid impedance estimation purposes [227], to name a few examples.

The estimation process of the Kalman filter can be divided into two distinct phases: *prediction* and *correction*. The first one is responsible for projecting forward the current state in order to obtain *a priori* estimate of the next step, whereas the correction phase involves the measurement in the process, and corrects the estimation for the following time step. The Kalman filter process is schematically shown in Fig. 5.17, and described in the following. For the specific application under study, the system model is given by the following equations:

$$\mathbf{x}(n+1) = \Phi(n)\mathbf{x}(n) + \mathbf{w}(n) \tag{5.21}$$

where $\mathbf{x}(n)$ is the state-vector, while $\Phi(n)$ is the state transition matrix defined as [228]:

$$\Phi(n) = \begin{bmatrix} \cos(\omega T_s) & -\sin(\omega T_s) \\ \sin(\omega T_s) & \cos(\omega T_s) \end{bmatrix} \tag{5.22}$$

with ω representing the frequency of the input signal and T_s the time step. The observation (or measurement) model is instead assumed to be of the form given below:

$$\mathbf{z}(n) = \mathbf{H}(n)\mathbf{x}(n) + \mathbf{v}(n) \tag{5.23}$$

where $\mathbf{H}(n) = [1\ \ 0]$ represents the measurement matrix, and $\mathbf{w}(n)$ and $\mathbf{v}(n)$ are the model and the measurement error vectors, respectively. These are considered to be white sequence with known covariance matrices $\mathbf{Q}(n) = Q_0\ \mathbf{I}$ and $\mathbf{R}(n) = R_0\ \mathbf{I}$, respectively, with $\mathbf{I}$ representing the identity matrix. Indicating with the superscript "-" calculations using information at the instant $n-1$, the prediction equations of the filter are given below:

$$\widehat{\mathbf{x}}^-(n) = \Phi(n-1)\widehat{\mathbf{x}}(n-1) \tag{5.24}$$

$$\mathbf{P}^-(n) = \Phi(n-1)\mathbf{P}(n-1)\Phi^T(n-1) + \mathbf{Q}(n) \tag{5.25}$$

These equations project the state and the covariance estimate from the step $n-1$ to the step n. Then the measurement update equations (correction phase) are given by:

$$\mathbf{K}(n) = \mathbf{P}^-(n)\mathbf{H}^T(n)\left[\mathbf{H}(n)\mathbf{P}^-(n)\mathbf{H}^T(n) + \mathbf{R}(n)\right]^{-1} \tag{5.26}$$

$$\widehat{\mathbf{x}}(n) = \widehat{\mathbf{x}}^-(n) + \mathbf{K}(n)\left[\mathbf{z}(n) - \mathbf{H}(n)\widehat{\mathbf{x}}^-(n)\right] \tag{5.27}$$

$$\mathbf{P}(n) = \left[\mathbf{I} - \mathbf{K}(n)\mathbf{H}(n)\right]\mathbf{P}^-(n) \tag{5.28}$$

The first task is represented by the calculation of the Kalman gain $\mathbf{K}(n)$, while measurements are involved in the second task, in order to produce a state estimate $\widehat{\mathbf{x}}(n)$. Then the last task calculates the covariance matrix of the estimation error $\mathbf{P}(n)$, for the next prediction step.

The setpoints currents i^{**} forwarded to the most inner current control loop are calculated reconstructing the three single-phase signals from the information about the respective magnitude and phase. First, the magnitude of each current is limited to the value I_{max} by means of a saturation unit. Then positive and negative sequence components of the three-phase signals are calculated as follows:

$$\begin{bmatrix} \mathbf{I}^{*+} \\ \mathbf{I}^{*-} \end{bmatrix} = \frac{1}{3} \begin{bmatrix} 1\ \alpha\ \alpha^2 \\ 1\ \alpha^2\ \alpha \end{bmatrix} \begin{bmatrix} \overline{I}^*_{ma} e^{j\phi_{Ia}} \\ \overline{I}^*_{mb} e^{j\phi_{Ib}} \\ \overline{I}^*_{mc} e^{j\phi_{Ic}} \end{bmatrix} \tag{5.29}$$

where $\alpha = e^{j2/3\pi}$ is the Fortescue operator [25], and $\overline{I}^*_{mx}$, with $x = \{a, b, c\}$, represents the saturated amplitude of the respective single-phase current. It can be noticed, that the calculation of positive and negative sequence current components is performed by means of algebraic equations, which do not involve any calculation time delay. The structure reported in Fig.5.16, also allows employing additional measures in order to limit the magnitude of negative sequence component, according to point **(v)** of the draft specifications.

Finally, a similar approach adopting three independent Kalman filters, one for each phase of the measured grid voltages, is implemented in the fault detection subsystem depicted in

Fig. 5.12 and located in the outer control loop. This estimates the amplitude of each phase separately and compares it to the threshold indicated by the specifications in **(iii)**, in order to trigger the FRT operating mode.

Inner current control loop

In order to fulfill the requirements on the control bandwidth specified in **(i)**, an extremely fast current control implemented on a FPGA board, and directly generating the converter pulses without the need of a modulation signal, is employed. In fact, in order to reproduce the desired behaviour of a voltage source behind impedance up to the frequency specified by point **(i)**, it is reasonable to design the inner current control loop so as to have a bandwidth in a range of at least twice the required frequency indicated by the specifications. Hence, this can be translated into an indication about the rise-time of the current control, considering the relation between rise-time t_r and bandwidth BW of a first-order system [67]:

$$t_r = \frac{ln\,9}{BW} \tag{5.30}$$

According to (5.30), the rise-time of the inner current control loop should be in the range of $< 1ms$. Therefore, in order to enhance the performances of the current control and reduce the time delay, different solutions can be employed.

Model predictive control approaches, e. g. deadbeat control [25], might represent good candidates [172]-[174]. However, due to the susceptibility of this category of controllers to uncertainties in filter and grid parameters, an adaptive hysteresis current control has been implemented by means of an FPGA board [229], which allows achieving extremely high bandwidth, and ensures that the converter currents do not overcome the limitations imposed the hardware components, under the assumption that their setpoints are properly generated. Hence, the advanced tracking capability of the implemented current control drastically reduces the time delay introduced by this control loop, necessary in order to reproduce the required behaviour of a voltage source behind impedance in the range specified by the requirements, and achieve an almost instantaneous reaction of the converter within the first 5 ms after fault occurrence.

5.3 HIL simulation results

In order to show the operating principle of the proposed control, in the following, the results of a hardware-in-the loop (HIL) test campaign are reported. The HIL test bench adopted for the simulations is depicted in Fig. 5.18. The control structure shown in Fig. 5.12, has been implemented on a Speedgoat real-time target machine, running with a time step $T_s = 200$ μs. The calculated current setpoints i^{**} are forwarded to a FPGA board, where an adaptive hysteresis current control generating the gate signals of the converter is implemented. A real-time digital simulator Typhoon HIL 602 has been adopted in order to emulate the converter and the grid with a simulation time step of 1 μs. The model implemented in the real-time

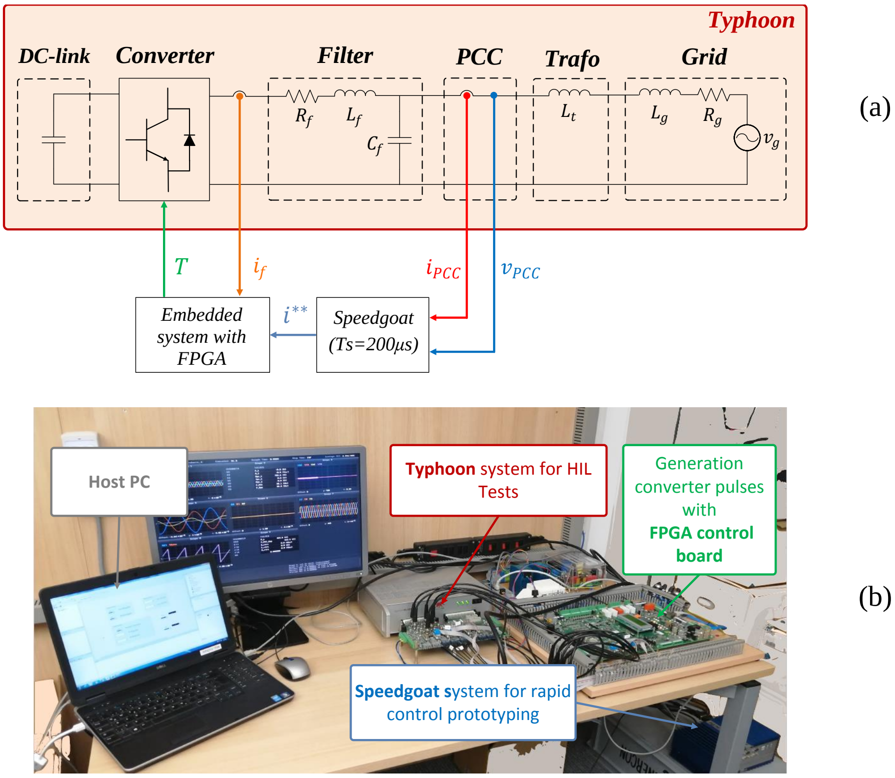

Figure 5.18: (a) Scheme of the HIL setup adopted for real-time simulations; (b) picture of the setup.

HIL simulator is shown in Fig. 5.18, while the characteristics of the simulated system, along with the control parameters are reported in Table 5.2. These correspond also to the system parameters of the laboratory setup used for the experiments presented in the next chapter.

In the following, simulation results performed by using the described setup show the behaviour of the proposed control during fault conditions. In order to show the impact of the introduced modifications to the structure of a GFM converter on the behaviour during faults, the action of each of the introduced subsystems is examined separately, so that starting from the generation of the current setpoints for the most inner current control loop and going backwards, the contribution of each subsystem can be appreciated.

Table 5.2: Parameters of the simulated system

Description	Symbol	Value	Description	Symbol	Value
Converter rated power	S_n	1.55 kVA	Integral gain correction	k_{i_corr}	200
Line-to-line voltage	V_{LL}	400 Vrms	Virtual moment of inertia	J	4e-4
Rated grid frequency	f_g	50 Hz	K factor	K	800
Filter inductance	L_f	0.13pu	P-Droop coefficient	D_p	0.8
Filter resistance	R_f	0.015pu	Q-Droop coefficient	D_q	90
Filter capacitor	C_f	0.033pu	Model error covariance (I)	Q_{0I}	0.5
Transformer inductance	L_T	0.02pu	Measurement error covariance (I)	R_{0I}	1
Virtual filter inductance	L_{v_n}	0.26pu	Model error covariance (V)	Q_{0V}	0.5e-3
Virtual filter resistance	R_{v_n}	0.013pu	Measurement error covariance (V)	R_{0V}	1
Proportional gain correction	k_{p_corr}	10	Proportional factor DSOGI	k_{SOGI}	2

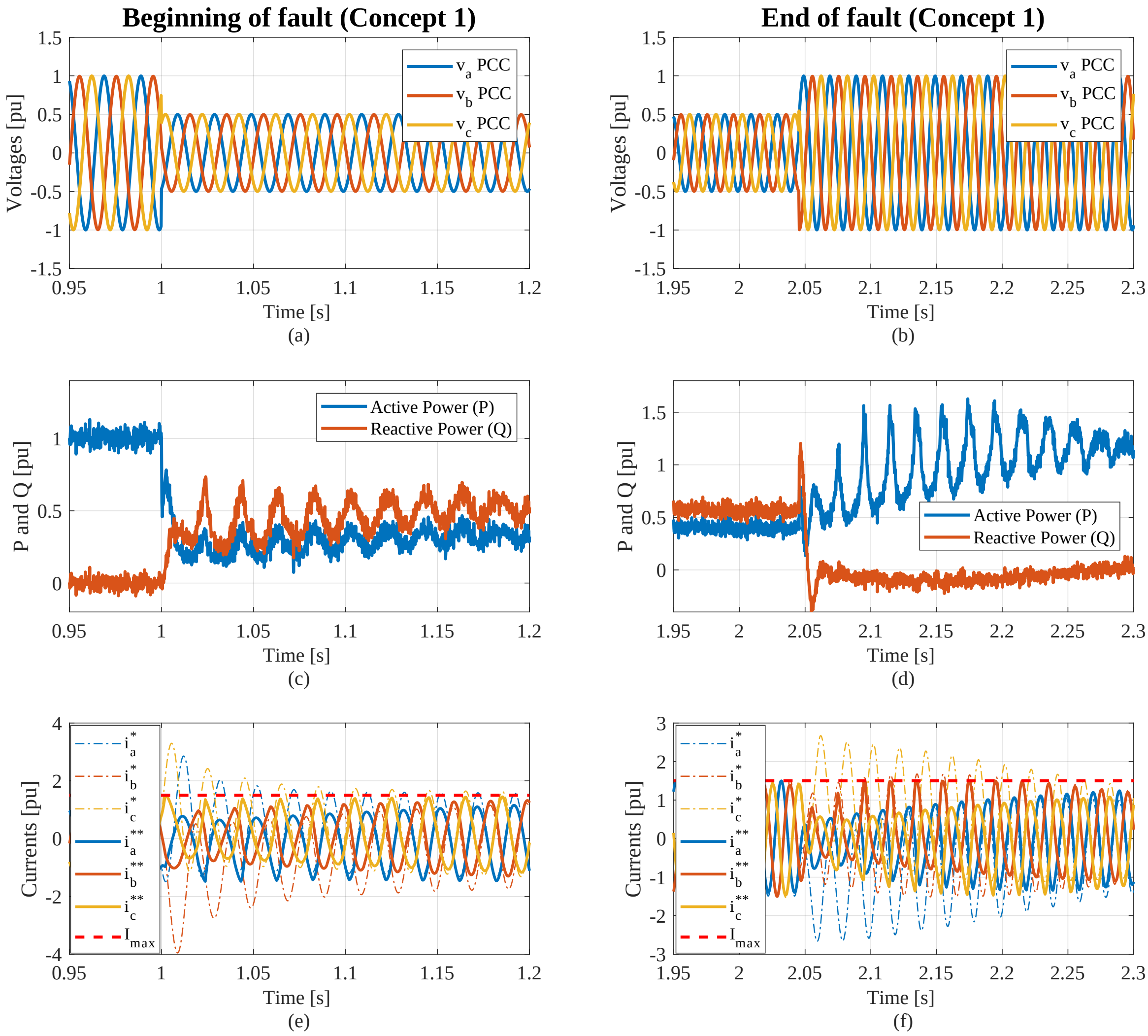

(a) (b) (c) (d) (e) (f)

Figure 5.19: HIL simulations. Symmetrical fault and generation of current setpoints employing *Concept 1*. Simulated grid voltages: (a) beginning of fault, (b) end of fault; active and reactive power: (c) beginning of fault, (d) end of fault; comparison current setpoints before current limitation and after current limitation: (e) beginning of fault, (f) end of fault.

5.3.1 Action of the inner control loop

In the following, the dynamic response of the converter by adopting the two concepts described in the previous section for the generation of the current setpoints i^{**}, are compared under symmetrical and asymmetrical fault conditions.

Generation of converter current setpoints - Concept 1

Fig. 5.19 shows the dynamic response of the converter for the case of a symmetrical fault when the current setpoints i^{**} are generated according to the strategy labeled as *Concept 1*, where the control parameter k_{SOGI} has been chosen according to the indications provided in [25]. The converter active and reactive power setpoints are respectively set to $P_{set} = 1$ pu, and Q_{set} =0 pu at pre-fault conditions. Then a symmetrical fault is simulated at $t = 1$ sec, and the

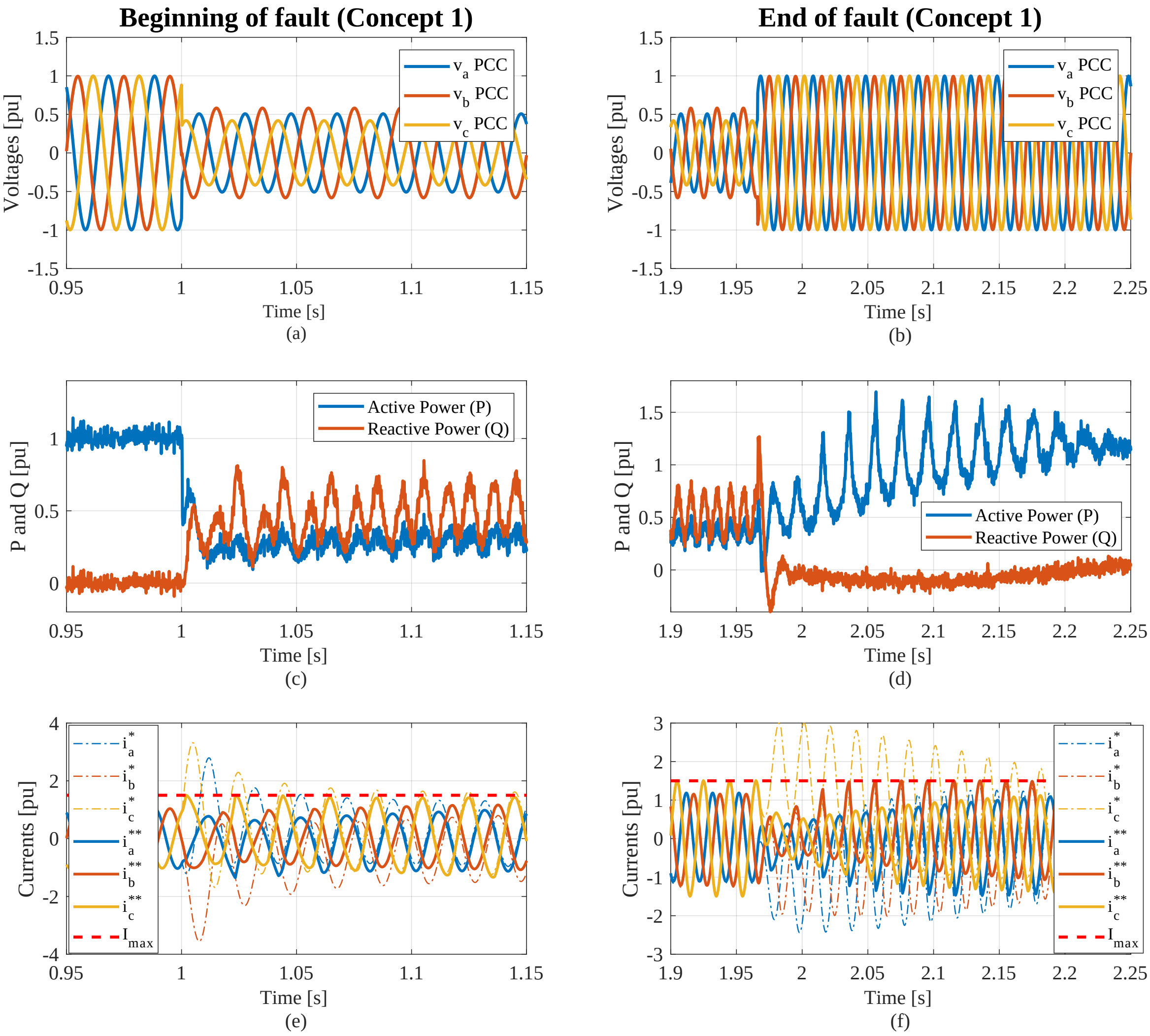

Figure 5.20: HIL simulations. Asymmetrical fault and generation of current setpoints employing *Concept 1*. Simulated grid voltages: (a) beginning of fault, (b) end of fault; active and reactive power: (c) beginning of fault, (d) end of fault; comparison current setpoints before current limitation and after current limitation: (e) beginning of fault, (f) end of fault.

measured voltages at the converter terminals at the beginning and at the end of the fault are shown in Fig. 5.19 (a) and (b), respectively. Simulated active and reactive power are reported in Fig. 5.19 (c) and (d). As expected, the converter reacts with an almost instantaneous injection of reactive power at the occurrence of the fault, while the instantaneous active power is suddenly reduced. At $t \approx 2.045$ *sec* the fault is cleared, and a re-synchronization phase takes place, so that the converter restores the operating conditions prior the fault after a transient. Oscillations in the simulated active and reactive power can be observed in Fig. 5.19 (c) and (d), which can be explained looking at the converter current setpoints i^{**} generated in the inner loop, and shown Fig. 5.19 (e) and (f). Indeed, the adopted strategy is able to limit the maximum instantaneous amplitude of the current setpoints i^{**} to the value of I_{max}, however, these are highly distorted during the transients (beginning of the fault, as well as end of the fault) as a consequence of the poor rejection capability of the decaying DC-component present in the currents i^{*}. Similar conclusions can be drawn by looking at Fig. 5.20, where

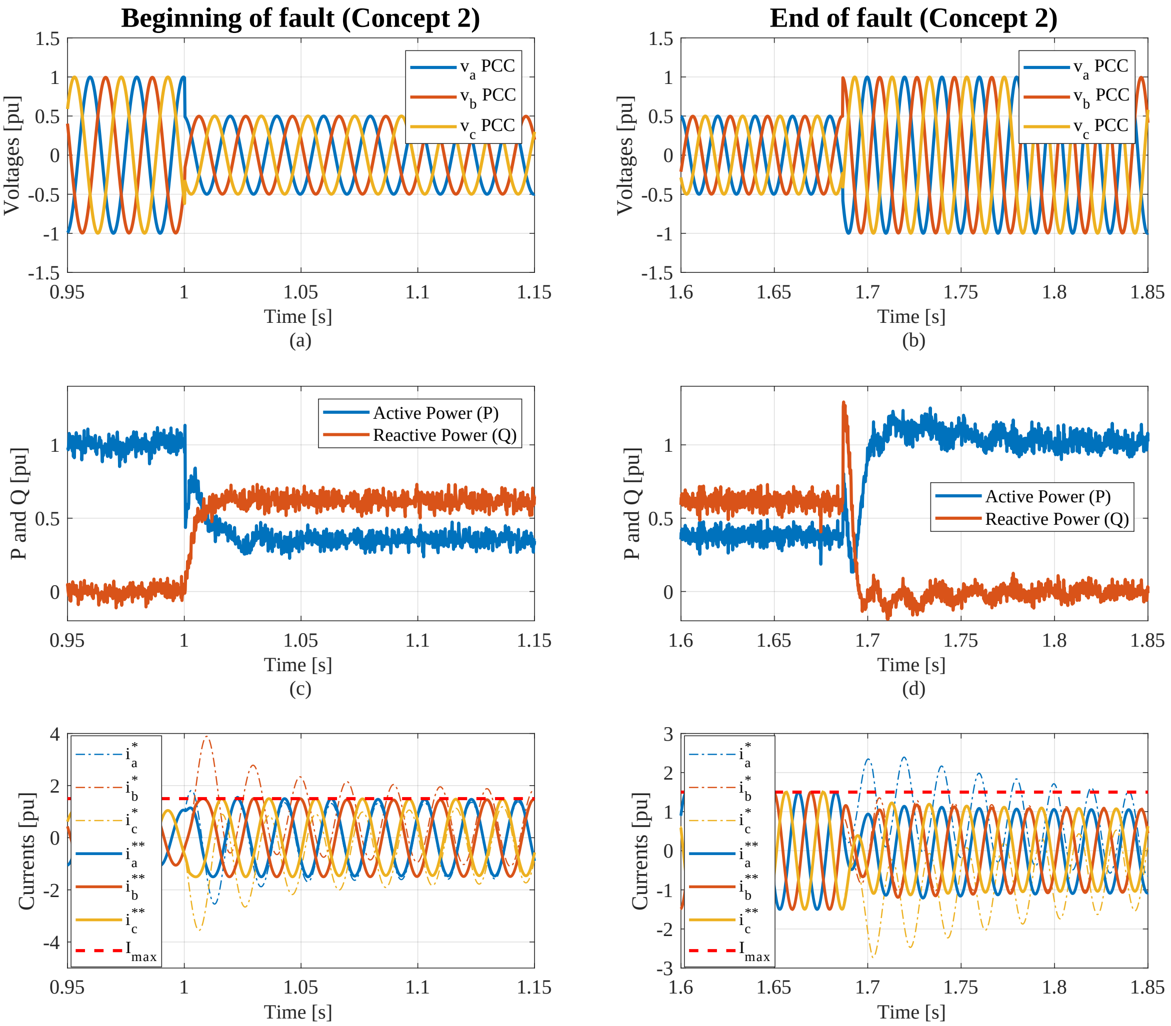

(a) (b) (c) (d) (e) (f)

Figure 5.21: HIL simulations. Symmetrical fault and generation of current setpoints employing *Concept 2*. Simulated grid voltages: (a) beginning of fault, (b) end of fault; active and reactive power: (c) beginning of fault, (d) end of fault; comparison current setpoints before current limitation and after current limitation: (e) beginning of fault, (f) end of fault.

the simulation results for the case of an asymmetrical fault are shown. Also in this case, significant oscillations in the power caused by the current setpoints i^{**} can be observed, especially during the re-synchronization phase of the converter after fault clearance.

Generation of converter current setpoints - Concept 2

The same events have been simulated by performing the generation of the converter current setpoints i^{**} by means of the control structure depicted in Fig. 5.16, and labeled here as *Concept 2*. Fig. 5.21 shows the converter behaviour according to a symmetrical fault. Comparing active and reactive power in Fig. 5.21 (c) and (d), against the results of Fig. 5.19 (c) and (d), a smoother dynamic behaviour can be observed, both at the occurrence of the fault, as well during the re-synchronization to the grid after fault clearance. These effects can be linked to the superior performances of the adopted current limitation approach, which are clearly

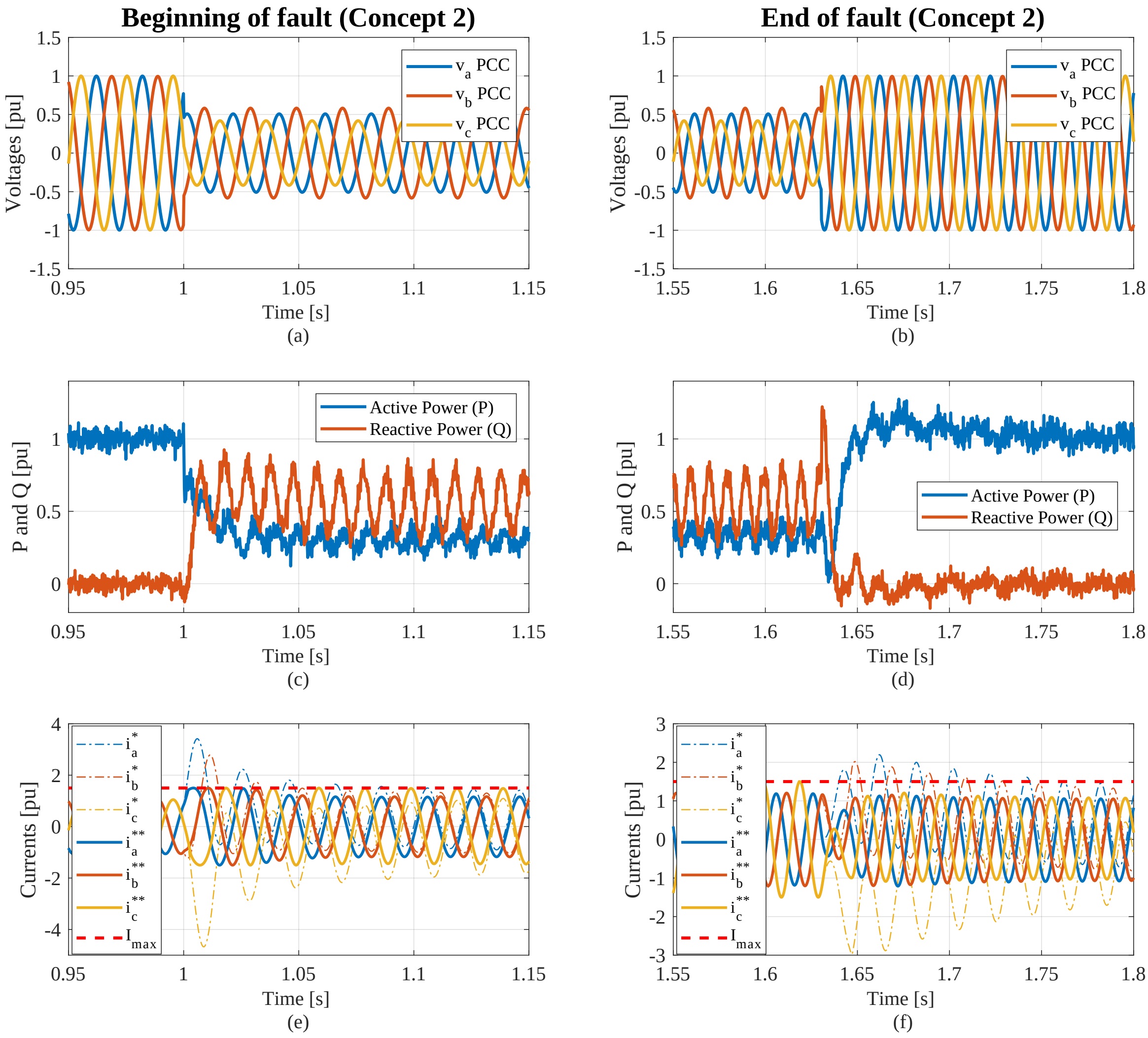

Figure 5.22: HIL simulations. Asymmetrical fault and generation of current setpoints employing *Concept 2*. Simulated grid voltages: (a) beginning of fault, (b) end of fault; active and reactive power: (c) beginning of fault, (d) end of fault; comparison current setpoints before current limitation and after current limitation: (e) beginning of fault, (f) end of fault.

visible comparing the results of Fig. 5.21 (e) and (f), against those of Fig. 5.19 (e) and (f). Furthermore, it can be noticed that the adopted approach allows better fulfilling the indications provided by the specifications at point (**iii**), requiring that when the resulting converter currents deriving from the emulated behaviour of voltage source behind impedance (represented here by the currents i^*) exceed the maximum amplitude I_{max}, a reduced fault current is allowed, which, however, should maintain the same phase of i^*, but with a maximum amplitude limited to 1.5 *pu*. Hence, compared to *Concept 1*, *Concept 2* can better avoid current distortion deriving from the limitation of the converter current setpoints, thus reducing oscillations in the output power.

The main reason for that can be found in the capability of this approach of better removing the decaying DC-components from the setpoint currents i^*, which, as discussed in Section 5.1.2, are typical of short-circuit currents and do not contribute to power injection, but would

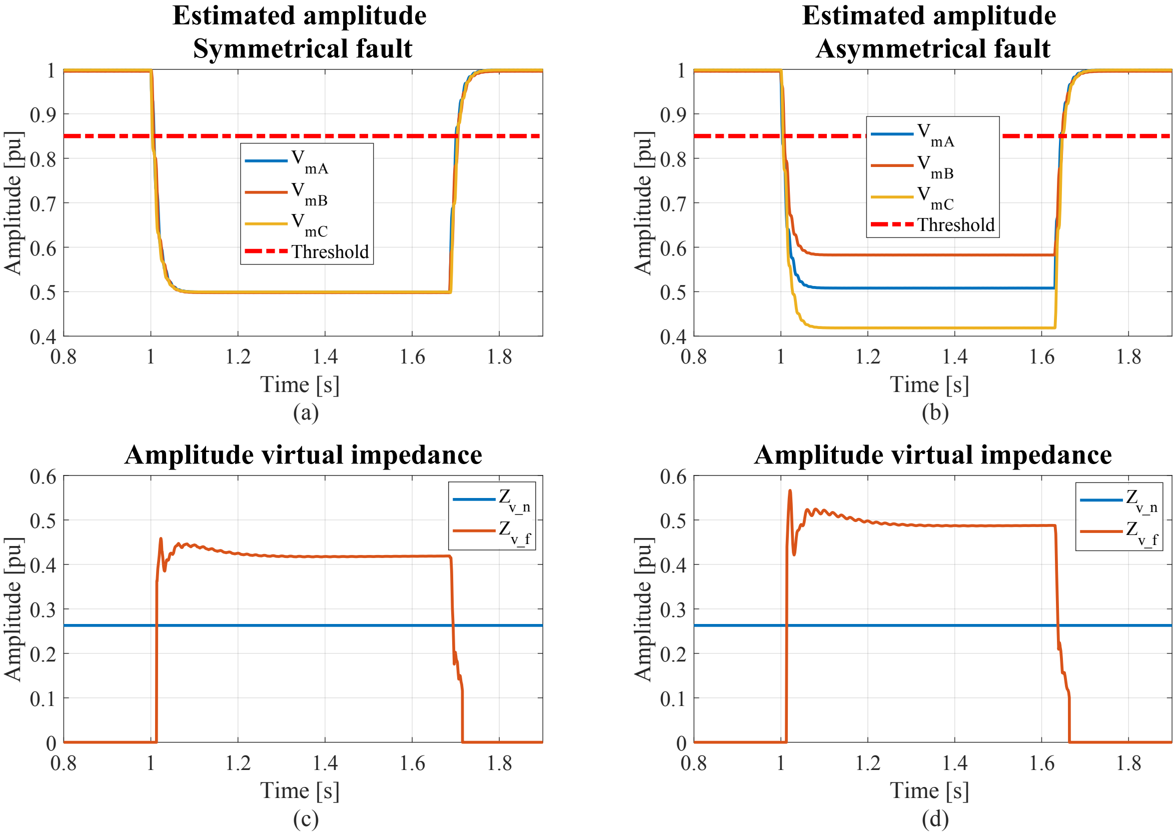

(a) (b) (c) (d)

Figure 5.23: HIL simulation. Symmetrical fault: (a) estimated single-phase voltages, (b) calculated amplitude of the virtual impedance. Asymmetrical fault: (c) estimated single-phase voltages, (d) calculated amplitude of the virtual impedance.

rather saturate the transformer. To this extent, the limitations of PLLs, and similar filter structures as the one adopted here for the implementation of *Concept* 1, in estimating sequence components of a three-phase system in presence of DC-offset are well-known in the literature, and methods for overcoming this inconvenient have been proposed, at the cost of higher complexity and degradation of the dynamic performances [230], [231]. Finally, similar considerations regarding the comparison between the two approaches can be drawn for the case of an asymmetrical fault, whose results are reported in Fig. 5.22.

Virtual admittance loop

Fig. 5.23 shows the virtual admittance calculation performed by the adaptive control loop described in Section 5.2.2. The results are related to the events shown in Fig. 5.21 and Fig. 5.22, and namely when the converter currents limitation is implemented by means of *Concept 2*. Since the action of this subsystem is triggered by the fault detection unit located in the outer loop, the estimation of the single-phase voltage amplitudes by means of three separated Kalman filters implemented in the outer loop are reported in Fig. 5.23 (a) and (b), for the two examined cases, respectively. The filter parameters are reported in Table 5.2, and have been tuned so as to result in a lower bandwidth compared to those employed in the inner loop. This allows enhancing harmonic rejection capability, while it avoids triggering

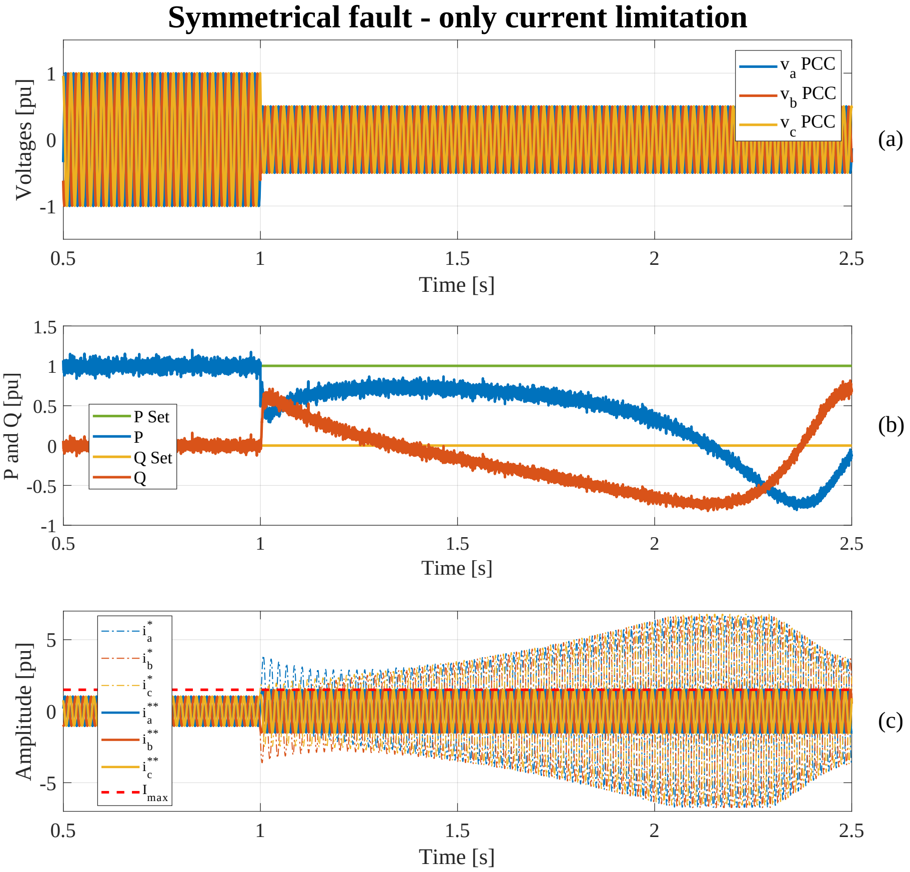

Figure 5.24: HIL simulation: behaviour of the converter for a symmetrical grid fault when only the current limitation control is activated. (a) Simulated voltages, (b) active and reactive power, (c) converter currents.

the FRT operating mode when only voltage disturbances occur, e. g. line connections or switching of capacitor banks. As soon as the lowest among the estimated single-phase amplitudes falls below the threshold indicated by the specifications at point (**iii**), the calculation of the impedance Z_{v_f} limiting the maximum amplitude of the converter currents to the values I_{max} is activated. In Fig. 5.23 (c) and (d), the calculated value Z_{v_f} according to (5.10), is compared to the default value Z_{v_n} adopted for normal operation. Only for demonstration purposes, and in order to maximize the reactive power injection during the fault, Z_{v_n} has been chosen so as to comply with the indications provided in Section 4.3.1, however the factor X_{ratio} defining the X/R ratio of the virtual impedance has been maintained constant to a value of 20 before and during the fault. Nevertheless, the implemented procedure allows easily modifying the X/R ratio of the virtual impedance according to the operating condition.

5.3.2 Action of the outer control loop

In order to show the importance of the measures adopted in the outer control loop, Fig. 5.24 shows the converter behaviour for a symmetrical fault when only the current limitation control is activated, the latter implemented by means of *Concept 2*. The fault detector is deac-

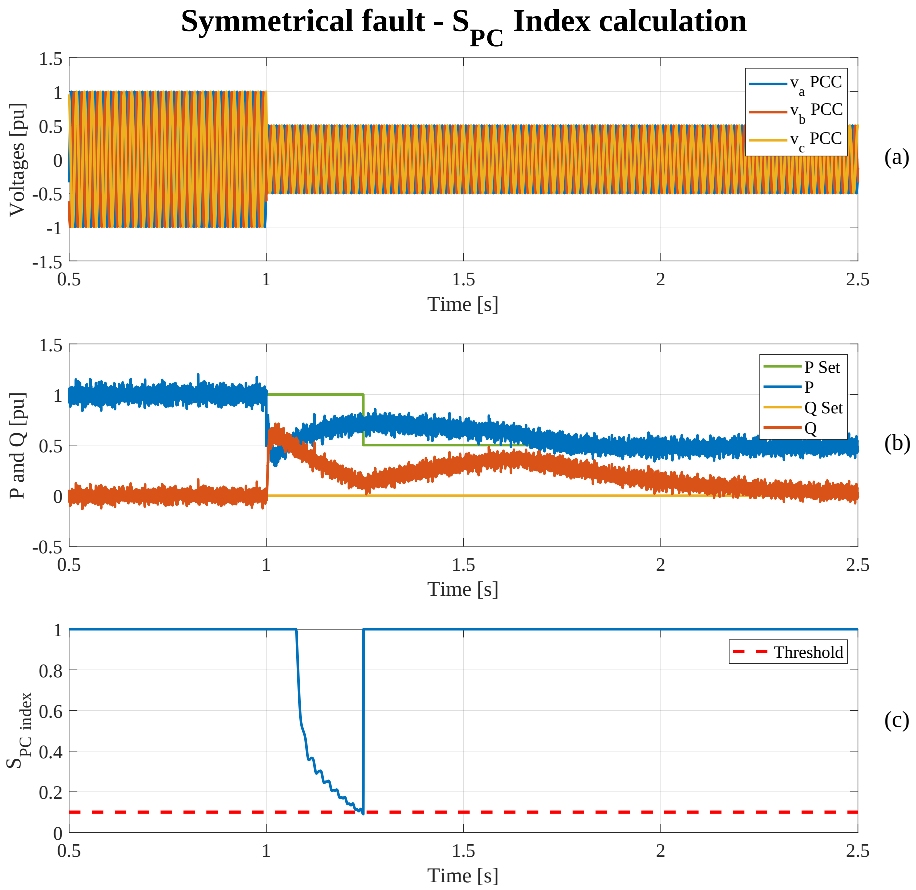

Figure 5.25: HIL simulation: behaviour of the converter for a symmetrical grid fault when the power correction according to the $S_{PC\ index}$ is activated. (a) Simulated voltages, (b) active and reactive power, (c) $S_{PC\ index}$.

tivated, as well as the additional security measure modifying the power setpoint according to the calculated $S_{PC\ index}$. The prompt reactive power injection of the converter can be observed in Fig. 5.24 (b), which is intrinsic in the control behaviour, and does not require a fault detection to be achieved. Nevertheless, the simulations show that, if within the first tens of milliseconds no further actions are taken, the control tries to regulate the converter power to the defined setpoint P_{Set} by increasing the power angle δ, however without being able to reach it due to the limitation of the maximum converter currents. Hence, a similar behaviour as the one examined in Fig. 5.4, and typical of the angle instability phenomenon can be observed in Fig. 5.24 (b).

The same simulation is repeated by activating the correction of the power setpoint based on the calculation of the $S_{PC\ index}$, while the fault detection loop remains deactivated. The simulation results reported in Fig. 5.25, show that the potential angle instability can be avoided by adopting this strategy, which represents the main objective of this control loop. The calculated $S_{PC\ index}$ is reported in Fig. 5.25 (c) for the simulated case, while output active and reactive power of the converter are shown in Fig. 5.25 (b). Only for demonstration of concepts, the action taken in the simulation is to reduce the power setpoint P_{Set} to 50% of the pre-fault condition as soon as the $S_{PC\ index}$ hits a lower threshold. Even though this measure would prevent the converter from possible angle instability, it is evident that further measures are needed in order to fulfill the requirements listed in Section 5.1.4.

These results highlight the effects deriving from the activation of the fault detection system, that controls the switches $S1$ and $S2$ in order to fix the amplitude and the phase of the virtual back-emf voltage e^* during the fault. Hence, the contribution of this control action can be summarized in the following two aspects:

- It intrinsically avoids occurrence of possible angle instability phenomena caused by the reduction of the maximum achievable converter output power, induced by the voltage drop in combination with the limitation of the converter currents.
- It allows sustaining for the whole duration of the fault the almost instantaneous reactive power injection intrinsic in the GFM behvaiour, without the need for the calculation of a reactive power setpoint according to the magnitude of the voltage depression.

5.4 Summary of the chapter

In this chapter, the behaviour of GFM converters during faults, and the critical aspects related to this operating condition have been investigated. The transient angle stability, and the sudden increase of converter currents in case of a short-circuit have been examined, which represent typical phenomena of real SMs, yet intrinsic in the behaviour of a GFM converter. Each of the examined aspects has been first introduced from the theoretical point of view by reviewing electrical machines theory, then simulation results have been reported, so as to show their impact on the behaviour of a GFM converter.

For each of the investigated issues, a literature overview has been first presented, then solutions have been proposed in order to overcome the limitations of the existing approaches. In the specific, the calculation of an index signalizing a possible angle instability condition has been proposed, whose motivation has been supported by simulation results showing the possible benefits deriving from its implementation. Then the limitation of short-circuit currents has been addressed, and the current state-of-the art has been critically reviewed. It has been pointed out that most of the FRT strategies for GFM converters presented in the literature, mainly aim on preventing the converter from the risk of hardware damages and instability issues, but do not explicitly reproduce the behaviour of a voltage source behind impedance also during faults. To this extent, the draft grid codes elaborated within the EG established by the British SO NGESO on GFM converters have been taken as a reference, so as to elaborate a proper FRT strategy for preventing the converter from possible instability issues, and which allows reproducing a GFM behaviour also during the fault.

To fulfill this purpose, a modification to a standard GFM control structure has been proposed, which is primarily based on a particular implementation of a variable virtual admittance in the inner control loop, along with additional modifications in the outer loop. This enables a direct control on the converter currents, yet ensuring the required behaviour of a voltage source behind impedance before, during, and after the fault, under the assumption that the most inner current control loop is adequately implemented. To this extent, two different approaches for the generation of the converter current setpoints during the fault have been investigated, and their performances have been compared by means of an extensive simulation campaign using a HIL test bench. The function of each of the introduced subsystems composing the proposed control is motivated and explained by means of simulation results, giving particular emphasis to the necessity for a proper coordination between outer and inner control loops. The efficacy of the proposed solution and the converter dynamic performances deriving from its implementation will be further investigated in the next chapter, where experimental tests performed in a laboratory environment are reported.

6 Experimental validation

This chapter presents the experimental results performed for validating the theoretical analysis presented in Chapter 4, regarding the stability of GFL and GFM converters and the interactions among the two converter types, as well as the experimental tests assessing the FRT capabilities of the control strategy proposed in Chapter 5. For the purposes of the tests, two different setups have been used, which will be described in the following. Hence, in order to validate the theoretical analysis concerning small-signal stability of GFL and GFM converters, a setup at the laboratory of the Chair of Power Electronics at the University of Kiel, Germany, has been used, while the measurement campaign performed in order to test the FRT capabilities of the proposed GFM strategy has been carried out at the Energy Systems laboratory facilities of the company WRD GbmH in Aurich, Germany.

6.1 Setups descriptions

6.1.1 Setup 1

The setup adopted for stability analysis purposes is the one shown in Fig. 6.1, and labeled in the following as *Setup 1*. Two converters Danfoss Series FC-302 (4 kVA rated power), operating with a switching frequency of 10 kHz, are equipped with output LCL filters and additional output transformers, so as to provide galvanic isolation. As indicated in the figure, the point of connection of each converter is defined as the primary side of the respective transformer. The hardware components of the two converters are identical, and the setup parameters are reported in Table 6.1. Both converters are connected to a four-quadrant linear power amplifier PAS 15000 from the company Spitzenberger & Spies (single-phase rated power 15 kVA, total three-phase rated power 45 kVA), controlled by means of a RTDS real-time digital simulator. The control of the two converters is instead implemented on a dSPACE control Desk DS1202 MicroLabBox running with a time step of 100 μs, generating the gate signals T_1 and T_2 for the two converters.

The setup configuration allows performing power-hardware-in-the-loop (PHIL) tests, an efficient way for testing the converter performances under different operating conditions. The interface algorithm adopted for the tests is the so-called Ideal Transformer Method (ITM),

Table 6.1: Parameters of Setup 1

Description	Symbol	Value	Description	Symbol	Value
Converters rated power	S_n	4 kVA	Additional inductance	L_{add}	0.016 pu
Line-to-line voltage	V_{LL}	400 V (rms)	Transformer inductance	L_T	0.004 pu
Rated grid frequency	f_g	50 Hz	Filter capacitor	C_f	0.019 pu
Switching frequency	f_s	10 kHz	Converter-side resistance	R_{f1}	0.04 pu
Converter-side inductance	L_{f1}	0.04 pu	Grid-side resistance	R_{f2}	0.025 pu
Grid-side filter inductance	L_{f2}	0.004 pu	Damping resistance	R_{cf}	0.05 pu

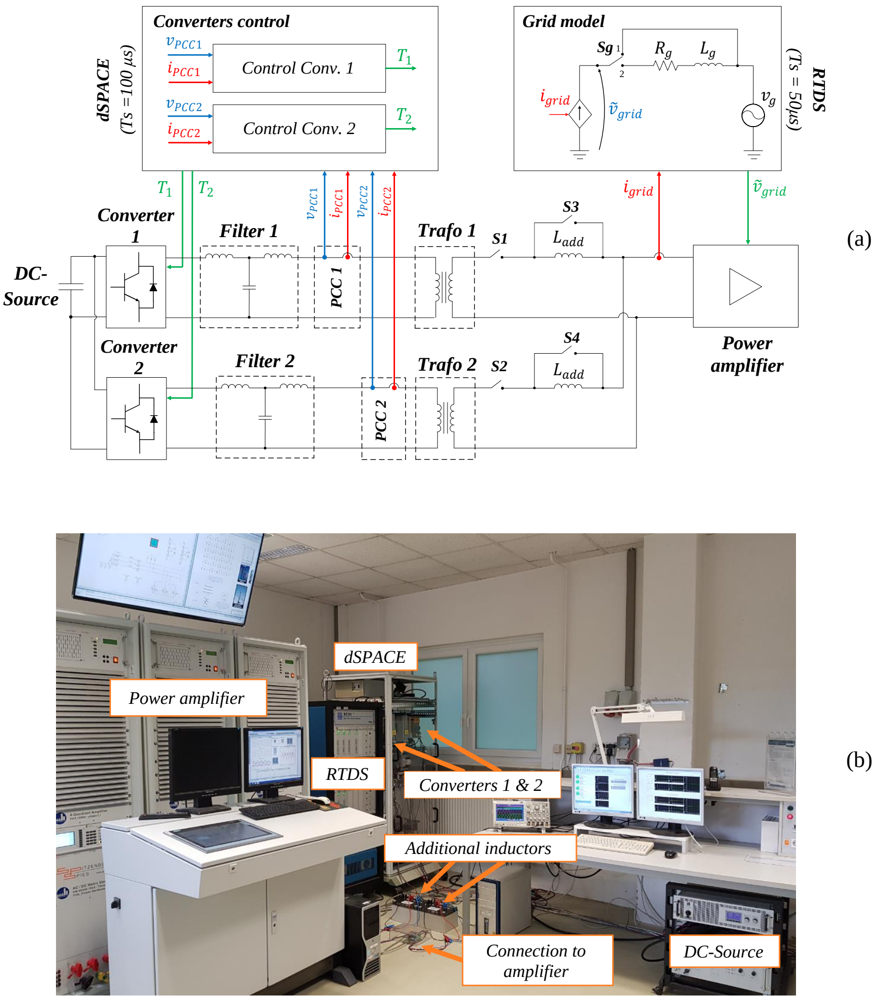

Figure 6.1: (a) Schematic of the laboratory *Setup 1*; (b) picture of the laboratory setup.

well-known in the literature [232], and whose principle is succinctly explained in the following. A grid model, represented for the specific case under study by a Thévenin equivalent, is simulated in real-time in the RTDS system, with a time step of 50 μs. The single-phase equivalent circuit of the grid model is shown in the scheme of Fig. 6.1 (a), where the values of the resistive and inductive components of the grid impedance, respectively indicated with R_g and L_g, can be varied in order to emulate a weaker or a stronger connection point. The input currents of the power amplifier i_{grid} are measured and forwarded to the simulator, which calculates the voltages at the virtual grid entry point resulting from the injection of the measured currents. The simulated voltages, indicated with $\tilde{v}_{grid}$ in the figure, are then forwarded as setpoint to the linear power amplifier, which is able to reproduce them at its terminals with an extremely high bandwidth (slew-rate > 52 V/μs). The switch indicated with S_g in the grid model, is implemented so as to allow the possibility of activating or deactivating the closed-loop tests. Hence, when the switch S_g is connected to position 1, the grid voltage reproduced at the terminals of the power amplifier is not affected by the currents injected by the converters, emulating the condition of a connection to an infinite bus.

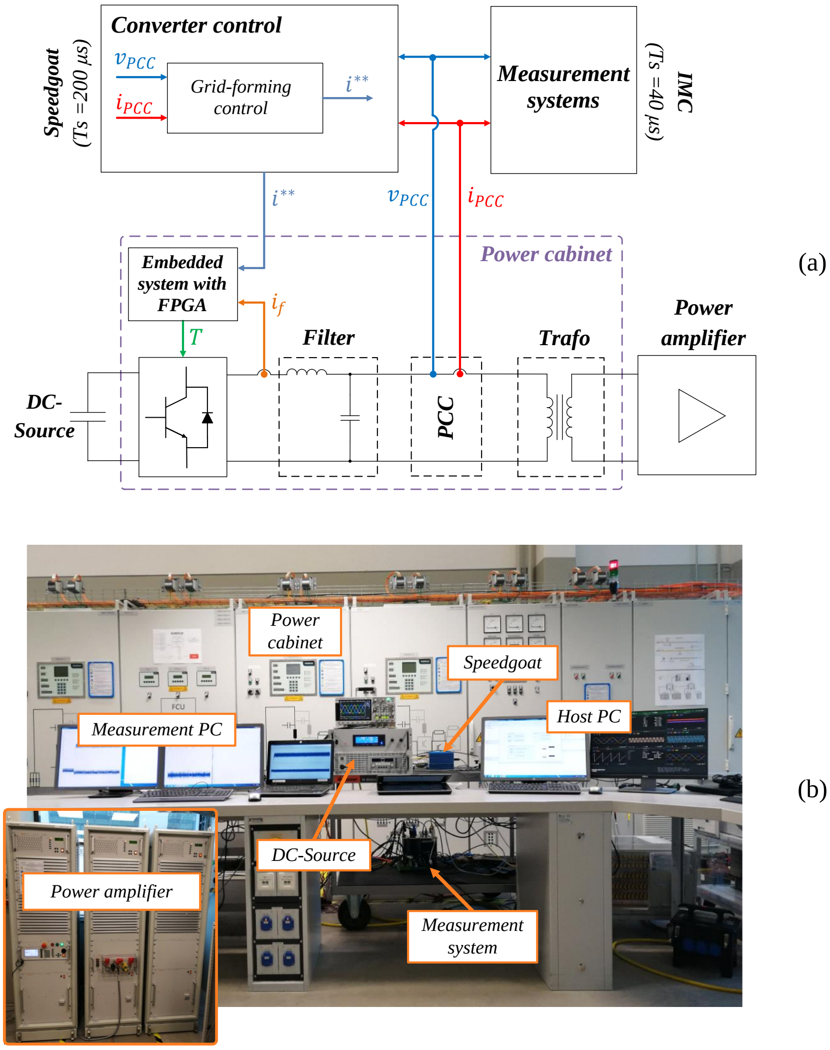

Figure 6.2: (a) Schematic of the laboratory *Setup 2*; (b) picture of the laboratory setup.

6.1.2 Setup 2

The second setup is depicted in Fig. 6.2, and its parameters are reported in Table 6.2. A two-level converter with 1.55 kVA rated power, equipped with an output LC filter and isolating transformer, has been connected to a power amplifier of the same type as the one described above for the Setup 1. The control of the converter has been instead implemented on the Speedgoat real-time target machine combined with the FPGA board used for the HIL tests, as already discussed in Section 5.3. Additionally, an IMC measurement system is used for data monitoring, sampling voltages and currents with a time step of 40 μs.

Table 6.2: Parameters of Setup 2

Description	Symbol	Value	Description	Symbol	Value
Converter rated power	S_n	1.55 kVA	Filter inductance	L_f	0.13 pu
Line-to-line voltage	V_{LL}	400 V (rms)	Filter resistance	R_f	0.015 pu
Rated grid frequency	f_g	50 Hz	Filter capacitor	C_f	0.033 pu
Max switching frequency	f_s	10 kHz	Transformer inductance	L_T	0.02 pu

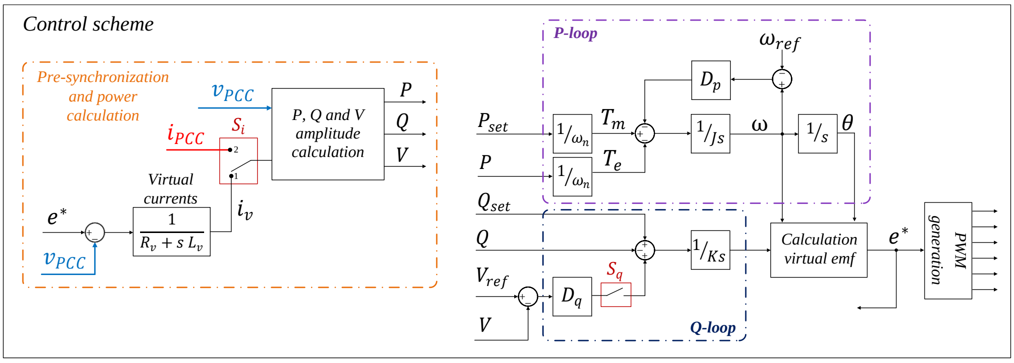

Figure 6.3: Scheme of the implemented GFM control structure for the experimental tests regarding small-signal stability analysis.

Since the main goal of the tests was to verify the FRT capabilities of the proposed GFM control structure, the power amplifier has been adopted in this case in order to simulate grid faults. This has been achieved by programming magnitude and duration of the events directly at the device interface.

6.2 Interactions among converters

This section presents the experimental results performed in order to validate the small-signal stability analysis performed in Chapter 4. First the case of GFM converters is addressed, validating the linearized model obtained in Section 4.2, both for the case of a single converter, as well as for the case of two GFM converters operating in parallel. Subsequently, the case of GFL converters is investigated, testing the instability caused by the PLL-bandwidth variation when only one converter is in operation and when two GFL converters operate in parallel. Finally, the interactions between the two types of converters and the effects of the electrical distance among them are investigated, according to the results shown in Section 4.3.3.

6.2.1 GFM converters

Implemented control structure

The GFM control structure adopted for the tests is depicted in Fig. 6.3. This is represented by the synchronverter structure already described in Section 4.2.1, and shown in Fig. 4.12, where additionally a pre-synchronization loop has been introduced. The latter has been proposed in [41], and it allows pre-synchronization to the grid, in order to avoid potential overcurrents during the connection process.

The procedure presented in [41], emulates the synchronization process of a real SM, whose back-emf needs to be perfectly synchronized with the grid voltage phasor in terms of magnitude and phase before connection. Considering the equivalent single-line diagram of a SM

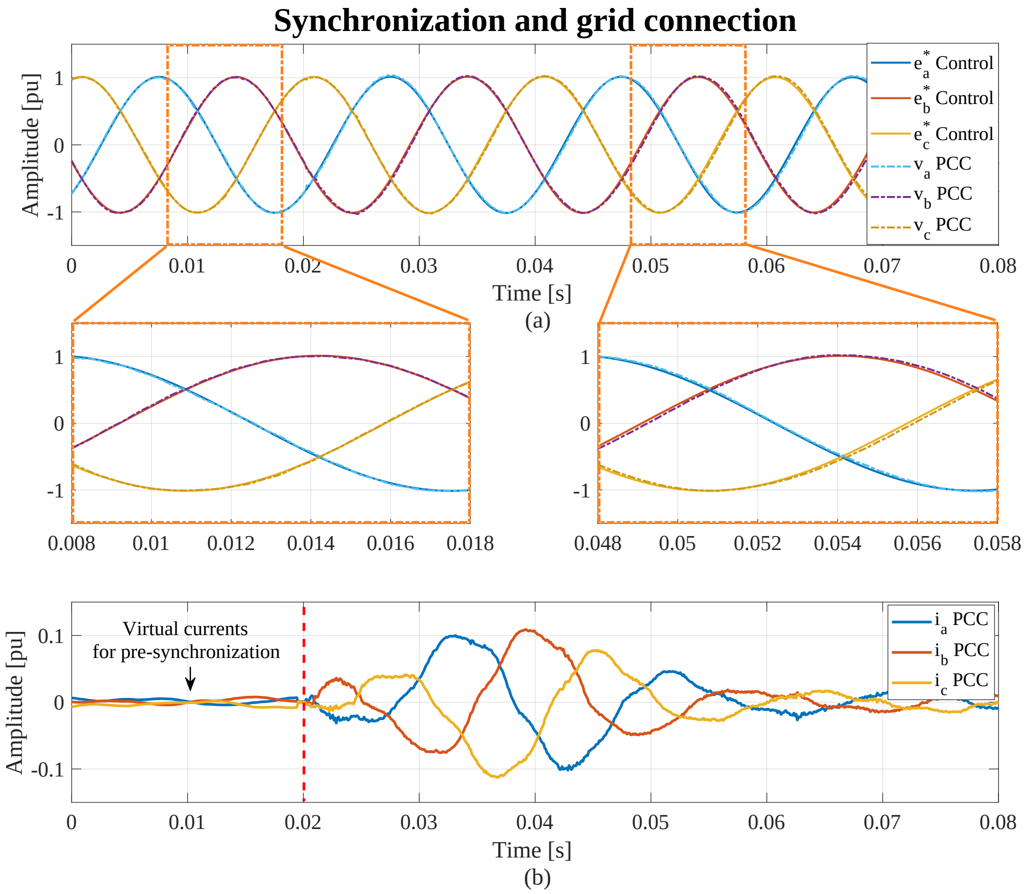

(a)

(b)

Figure 6.4: Experimental results showing the pre-synchronization phase of a synchronverter: (a) comparison between control internal voltages and measured grid voltages at the PCC, (b) currents fed into the control for power calculation purposes.

connected to an infinite bus reported in Fig. 5.1, and assuming a mainly inductive transmission line, active and reactive power exchanged between the machine and the grid can be expressed by means of the quasi steady-state equations reported below:

$$\begin{cases} P = \frac{E_g V_g}{X}\sin(\delta) \\ Q = \frac{E_f}{X}\left[E_f - V_g \cos\delta\right] \end{cases} \tag{6.1}$$

where E_f and V_g respectively indicate the amplitudes of the back-emf voltage of the SM and of the infinite bus, X represents the inductance of the transmission line, and δ is the phase displacement between the two phasors. According to (6.1), the pre-synchronization of the synchronverter is achieved by setting active and reactive power setpoints $P_{set} = Q_{set} = 0$, and by calculating virtual converter currents i_v according to the scheme shown in Fig. 6.3. It can be noticed, that this structure represents the virtual admittance implementation already discussed in the previous chapter. However, in this case, the calculated virtual currents are only adopted during the pre-synchronization phase for performing active and reactive power calculation, so that the control can adjust its inner voltage vector in order to nullify the virtual power exchange.

A practical example of the process described above is given in Fig. 6.4, where experimental

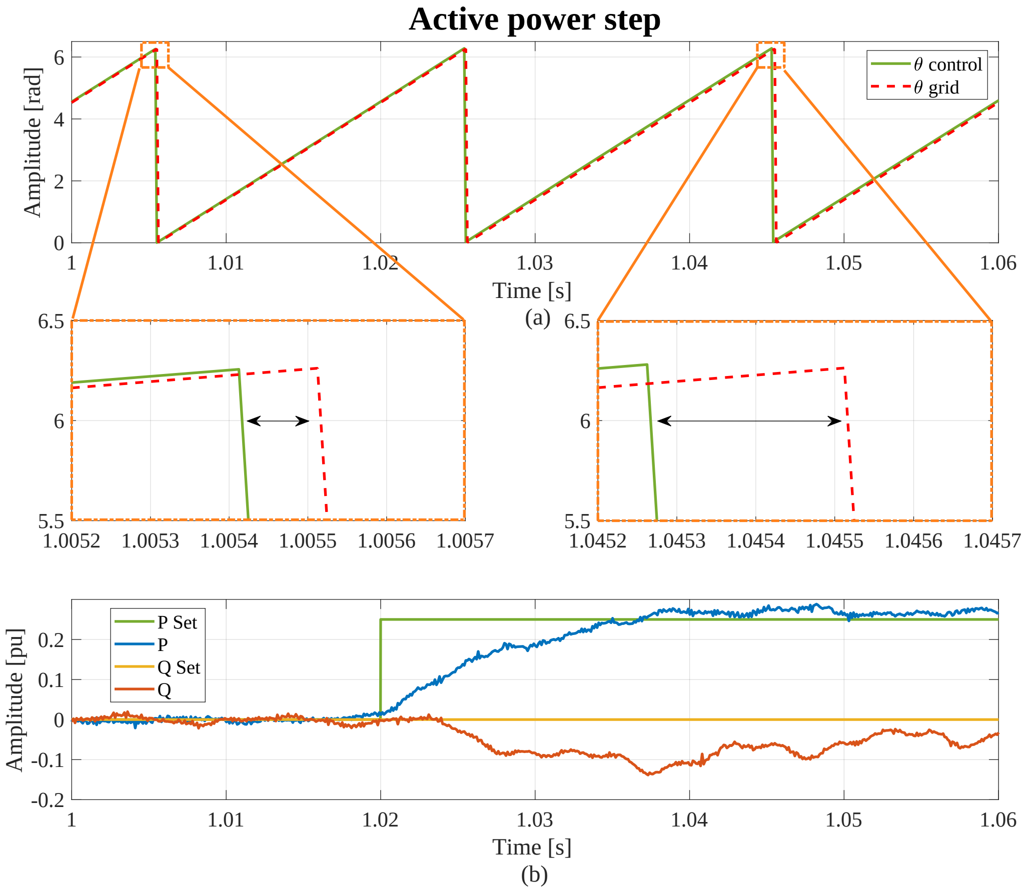

(a)

(b)

Figure 6.5: Experimental results showing the active power control principle of a power-synchronization-based control algorithm: (a) comparison between internal control voltage angle and measured grid voltage angle, (b) measured active and reactive power.

results regarding the connection of the synchronverter to the grid are shown. Fig. 6.4 (a) shows the comparison between the inner voltages e_a^*, e_b^*, and e_c^* calculated by the control and the measured grid voltages at the connection point, while Fig. 6.4 (b) shows the currents fed into the control for the power calculation. As indicated in the figure, the currents before connection are the virtual currents i_v calculated by the virtual admittance loop, so that the inner voltage results perfectly synchronized to the grid. At $t = 0.02\ sec$, the converter is connected to the grid by activating the converter pulses, while simultaneously switching S_i shown in Fig. 6.3 to position 2, thus feeding the real measured currents at the PCC to the power calculation subsystem. Even though the inner voltages of the converter are perfectly synchronized to the grid before connection, a transient in the converter currents can be observed, which is mainly caused by the delay introduced by the control sampling and the PWM. As it can be deduced from the slight slip of the inner voltages compared to the measured grid voltages shown in the zoom of Fig. 6.4, the converter reacts by adjusting its inner voltage vector so that the resulting power at the PCC corresponds to the given setpoint.

Finally, Fig. 6.5 further clarifies the working principle of a synchronverter, and generally of a power-synchronization-based control algorithm, regarding the regulation of the active power injection. Once the converter is connected to the grid according to the process described

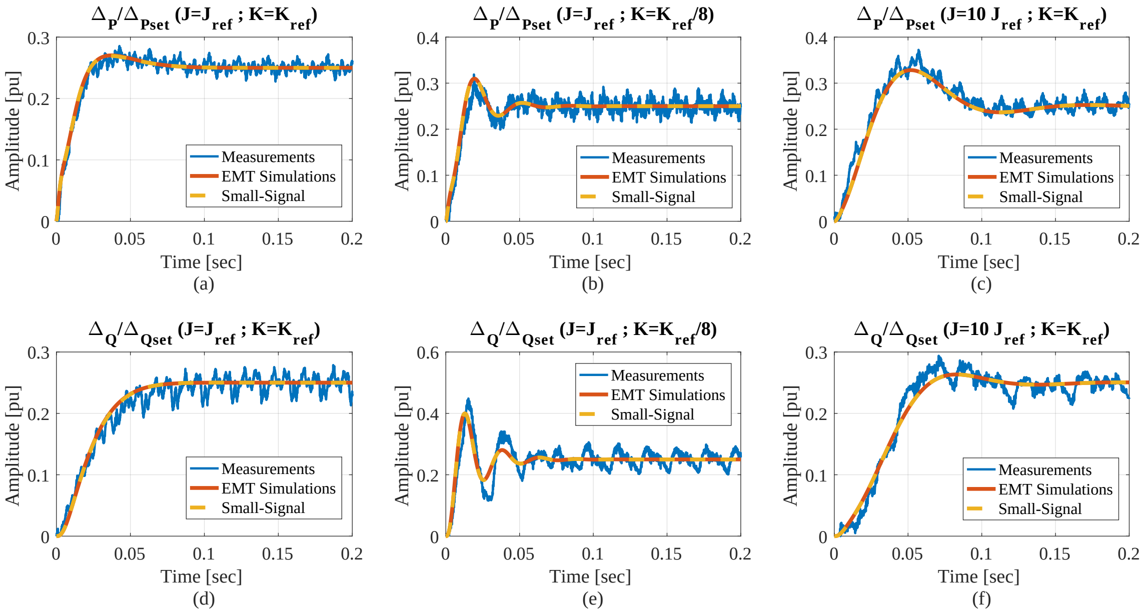

Figure 6.6: Grid SCR = 20, Q-V droop off, X/R=10. Dynamic behaviour of $\frac{\Delta_P}{\Delta P_{set}}$, step of 0.25 pu: (a) J=J_{ref}, K=K_{ref}; (b) J=J_{ref}, K=$K_{ref}/8$; (c) J=10 J_{ref}, K=K_{ref}. Dynamic behaviour of $\frac{\Delta_Q}{\Delta Q_{set}}$, step of 0.25 pu: (d) J=J_{ref}, K=K_{ref}; (e) J=J_{ref}, K=$K_{ref}/8$; (f) J=10 J_{ref}, K=K_{ref}.

above, a step of the power setpoint $P_{set} = 0.25$ pu is given at $t = 1.02$ *sec*, and the dynamic behaviour of the injected active and reactive power are shown in Fig. 6.5 (b). A comparison between the inner voltage angle indicated by the green line, and the grid angle represented by the red-dashed line, is shown in Fig. 6.5 (a). The latter is obtained by means of a PLL, and is only shown for demonstration purpose, thus it is not fed into the control. As it can be noticed from the zoom of Fig. 6.5 (a) before and after the power step, the control adapts the angle of the inner voltage, so that the resulting power angle δ is increased, however without requiring any knowledge about the actual grid voltage angle.

Model validation - One GFM converter

The linearized synchronverter model adopted for stability analysis purposes developed in Section 4.2.1, is validated in the following by means of experimental tests. First the case of a single synchronverter connected to the grid is investigated. The control parameters adopted for the tests are reported in Table 6.3, and steps of active and reactive power setpoints of 0.25 *pu* have been performed. The parameters of the simulated grid are also reported in the table, and correspond to the case of a strong grid condition (SCR = 20). Fig. 6.6 (a) and

Table 6.3: Control parameters adopted for the test

Description	Symbol	Value	Description	Symbol	Value
Virtual moment of inertia	J	4e-4	P-droop coefficient	D_p	0.81
Q-loop inverse integrator gain	K	800	Q-droop coefficient	D_q	245
Simulated grid inductance	L_g	0.0497 pu	Simulated grid resistance	R_g	0.00497 pu

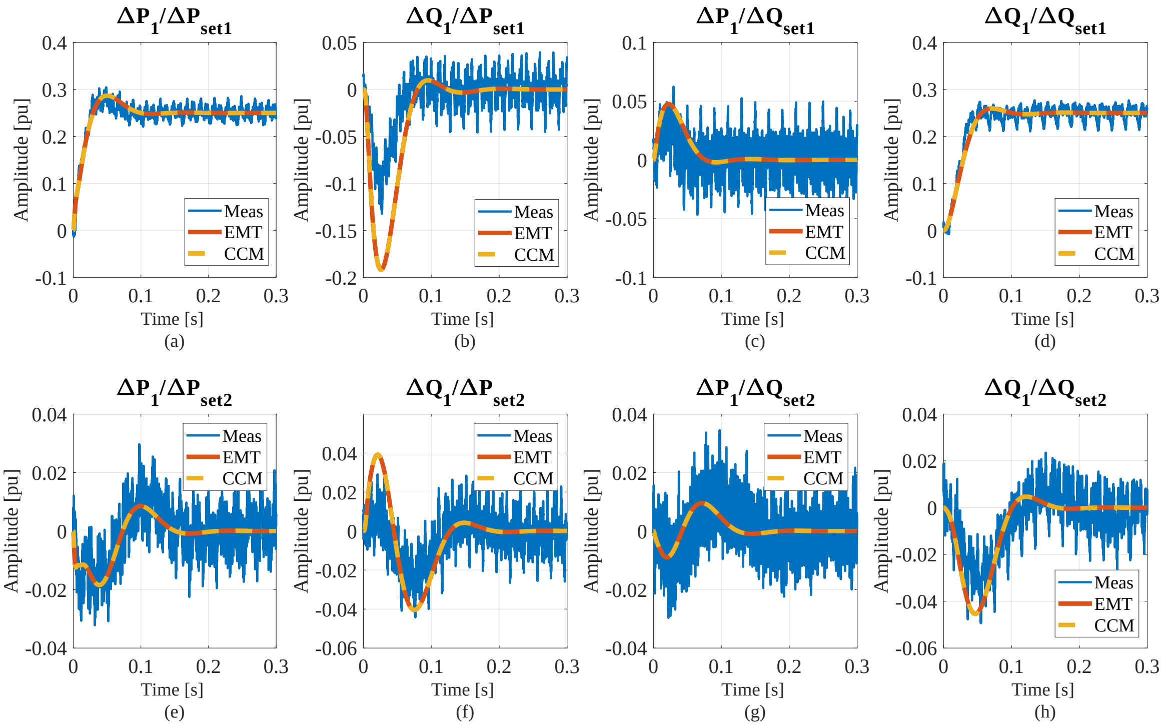

Figure 6.7: Comparison experimental results (blue), EMT simulations (red), linearized model (yellow). (a) $\frac{\Delta_{P1}}{\Delta_{Pset1}}$, (b) $\frac{\Delta_{Q1}}{\Delta_{Pset1}}$, (c) $\frac{\Delta_{P1}}{\Delta_{Qset1}}$, (d) $\frac{\Delta_{Q1}}{\Delta_{Qset1}}$, (e) $\frac{\Delta_{P1}}{\Delta_{Pset2}}$, (f) $\frac{\Delta_{Q1}}{\Delta_{Pset2}}$, (g) $\frac{\Delta_{P1}}{\Delta_{Qset2}}$, (h) $\frac{\Delta_{Q1}}{\Delta_{Qset2}}$.

(d) show the dynamic behaviour of the converter according to a step of active and reactive power setpoints, for the direct transfer functions $\frac{\Delta_{P}}{\Delta P_{set}}$ and $\frac{\Delta_{Q}}{\Delta Q_{set}}$, respectively. Measurements are compared to simulations results obtained by means of the average model described in Section 4.2.2, as well as against the results of the developed analytical model.

The same procedure has been repeated by setting first the parameter $K = K_{ref}/8$, where with K_{ref} is indicated the value reported in the table, while all the other control parameters have been maintained constant, and the results are shown in Fig. 6.6 (b) and (e). Analogously, step responses of active and reactive power have been tested by setting $J = 10\, J_{ref}$, where the subscript "ref" has the same meaning as above, while maintaining the other parameters constant. The results are reported in Fig. 6.6 (c) and (f), showing an acceptable match between measurements and simulations in all the investigated cases. Finally, the performed experiments further confirm the aspect discussed in Section 4.2.2, related to the cross-coupling between active and reactive power loops.

Model validation - Two GFM converters

Further experiments have been performed in order to validate the developed analytical model for the case of two synchronverters operating in parallel, and the results are reported in Fig. 6.7. The control parameters of the two converters are identical and correspond to the values reported in Table 6.3. Again, the case of a strong grid is simulated, and the figure shows the dynamic behaviour of the measured active and reactive power of Converter

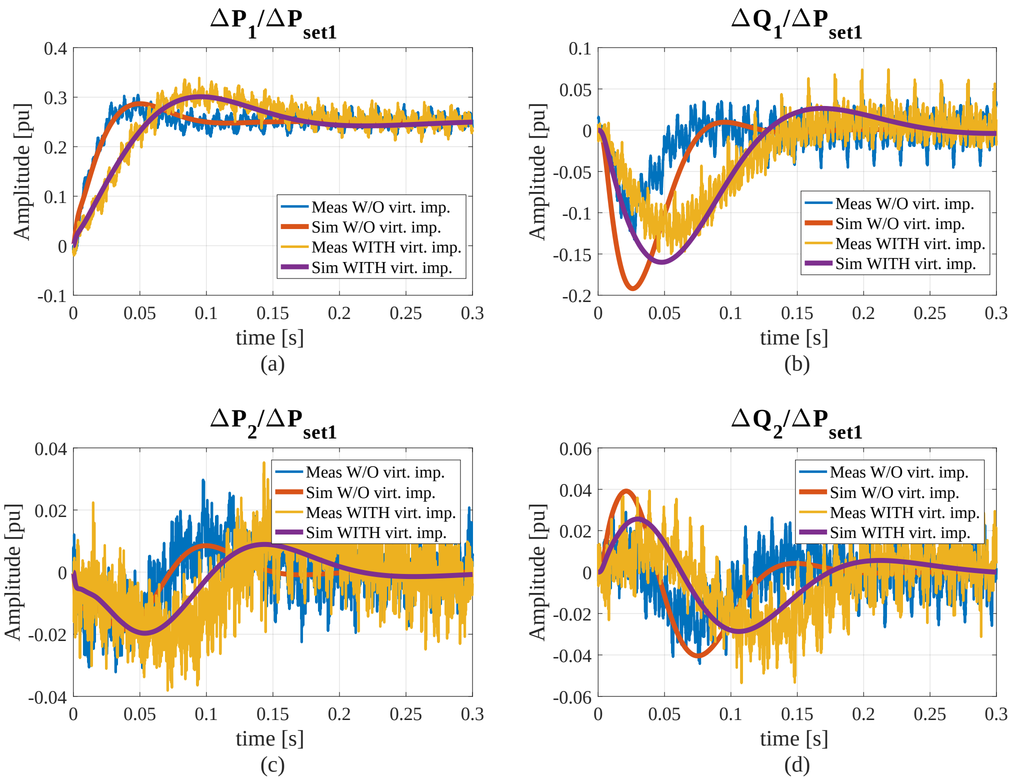

Figure 6.8: Comparison experimental results vs. EMT simulations. (blue) measurements without virtual impedance implementation, (red) simulations without virtual impedance implementation, (yellow) measurements with virtual impedance implementation, (violet) simulations with virtual impedance implementation. (a) $\frac{\Delta_{P1}}{\Delta_{Pset1}}$, (b) $\frac{\Delta_{Q1}}{\Delta_{Pset1}}$, (c) $\frac{\Delta_{P2}}{\Delta_{Pset1}}$, (d) $\frac{\Delta_{Q2}}{\Delta_{Pset1}}$.

1, respectively indicated as P_1 and Q_1, according to steps of active and reactive power set-points of the two converters, indicated with P_{set1}, Q_{set1}, P_{set2}, and Q_{set2}. Also in this case, an acceptable match between simulations and measurements can be appreciated, both for quantities within the same converter, namely: $\frac{\Delta_{P1}}{\Delta_{Pset1}}$, $\frac{\Delta_{Q1}}{\Delta_{Pset1}}$, $\frac{\Delta_{P1}}{\Delta_{Qset1}}$, and $\frac{\Delta_{Q1}}{\Delta_{Qset1}}$, as well as for the cross-coupling effects between the two converters: $\frac{\Delta_{P1}}{\Delta_{Pset2}}$, $\frac{\Delta_{Q1}}{\Delta_{Pset2}}$, $\frac{\Delta_{P1}}{\Delta_{Qset2}}$, $\frac{\Delta_{Q1}}{\Delta_{Qset2}}$.

Interactions between two GFM converters

In order to prove the results of the analysis performed in Chapter 4, related to the interactions between two GFM converters, experimental tests have been performed so as to show the effects of a virtual impedance implementation on the stability of two synchronverters operating in parallel. According to the purposes of the test, the virtual impedance implementation proposed in [99], has been adopted. Among the virtual impedance implementations discussed in Section 2.4.3, this represents the simplest solution for virtually modifying the output impedance of the converter without increasing control complexity. Nevertheless, since its operating principle has been already explained in Fig. 2.26, this is not repeated here.

Fig. 6.8 compares the dynamic behaviour of the two converters according to power steps of

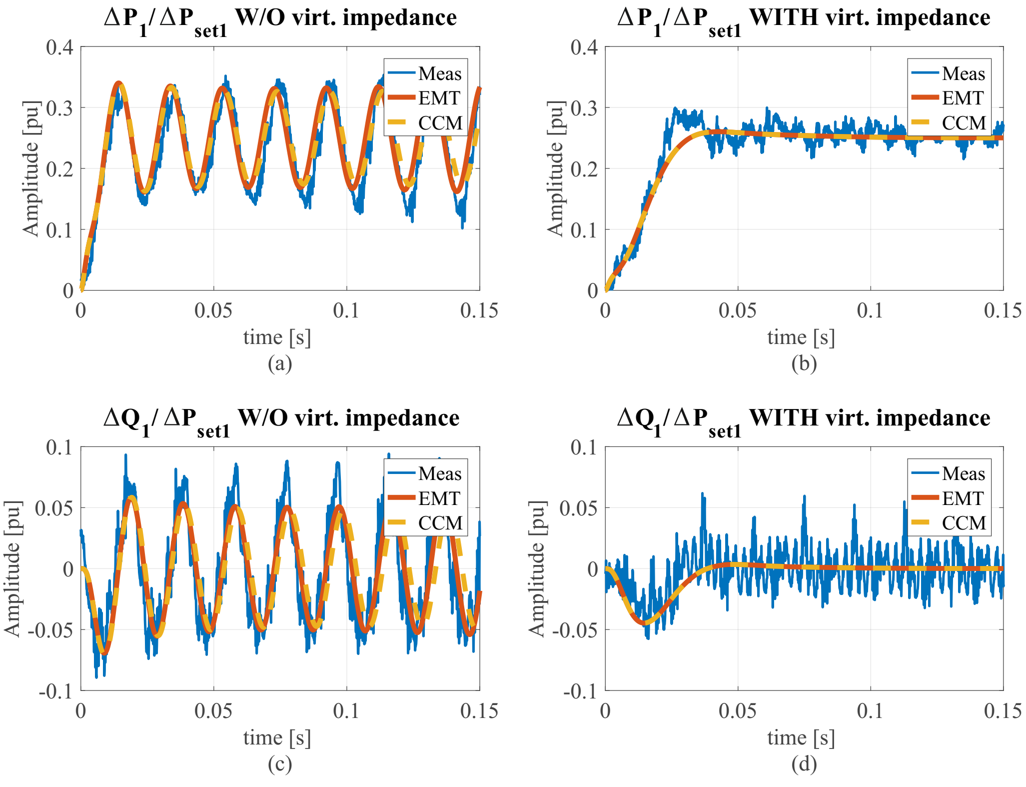

Figure 6.9: Comparison experimental results (blue), EMT simulations (red), linearized model (yellow). (a) $\frac{\Delta_{P1}}{\Delta_{Pset1}}$ without virtual impedance, (b) $\frac{\Delta_{Q1}}{\Delta_{Pset1}}$ with virtual impedance, (c) $\frac{\Delta_{Q1}}{\Delta_{Pset1}}$ without virtual impedance, (d) $\frac{\Delta_{Q1}}{\Delta_{Pset1}}$ with virtual impedance.

P_{set1}, with and without virtual impedance implementation in the control of Converter 1. Measurements are compared to simulation results obtained by doubling the output impedance of the converter filter. In order to reproduce this behaviour, the factor m of the virtual impedance in eq. (2.34) has been set to $m = 2$. In order to test the effects on the stability of the two converters operating in parallel, a similar procedure as the one adopted in Section 4.2.3, for proving the results of the eigenvalue analysis has been adopted. Hence, the parameters K of the two converters have been simultaneously reduced compared to the default value reported in Table 6.3, in order to bring the converters close to an unstable operating condition. When one synchronverter operates alone, the lowest value of K_1 causing instability is $K_{lim} \approx 50$. However, when the second converter is connected in parallel, this having the same parameters as Converter 1, the critical values of $K_1 = K_2$ causing instability becomes $K_{lim} \approx 60$. Fig. 6.9 (a) and (c) show the dynamic behaviour of Converter 1 without virtual impedance implementation for a step of $P_{set} = 0.25\ pu$, when operating in parallel to Converter 2, and when the K factors of the two converters are set to $K_1 = K_2 = 55$. Fig. 6.9 (b) and (d) show instead the behaviour of the converter under the same conditions, but when the virtual impedance is implemented in the control of Converter 1. These results confirm the benefits due to a virtual impedance implementation on the stability of the two GFM converters operating in parallel, and which would cause a further reduction of K_{lim} to a value of 20 when implemented in the control of both converters.

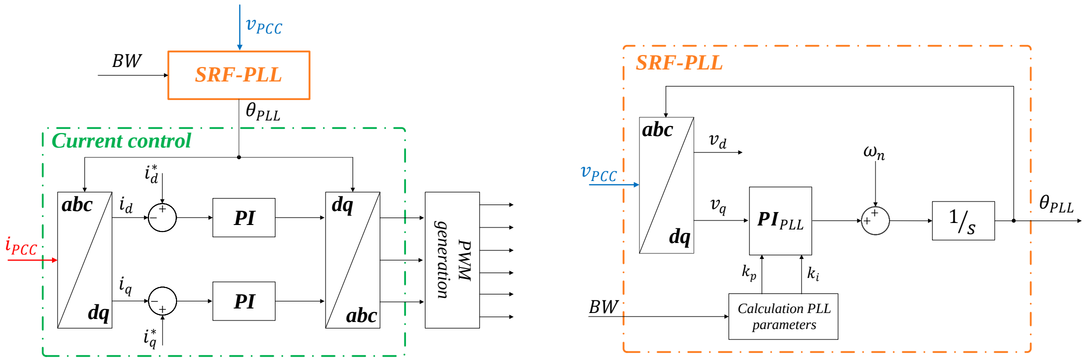

(a) (b)

Figure 6.10: Scheme of the GFL control structure adopted for the tests: (a) overview, (b) SRF-PLL implemented for the tests.

6.2.2 GFL converters

In order to study the effects caused by the PLL-bandwidth variation on the stability of a GFL converter, the control structure shown in Fig. 6.10 has been implemented in the dSPACE control Desk. A PI-based current control loop is employed, where the angle required for the transformations of voltages and currents from the *abc* to the *dq* reference frame is provided by a SRF-PLL, whose structure is reported in Fig. 6.10 (b). This represents the same structure shown in Fig. 2.10, where additionally the calculation of the proportional and of the integral gains k_p and k_i according to a given bandwidth setpoint BW, is introduced. Furthermore, in order to reproduce similar conditions as those investigated in Section 4.3.3, the capacitor filter C_f has been disconnected, so as to result in a L-filter configuration.

The parameters of the test are reported in Table 6.4, where the proportional and the integral gain of the current control, indicated respectively with k_{pi} and k_{ii}, have been selected according to the technical optimum technique [25]. First the case of a single GFL converter has been investigated. The bandwidth of the PLL has been maintained constant to a defined value, and the converter has been controlled so as to inject only d-component of the current. The current setpoint has been slowly ramped up from $i_{d1}^* = 0$ A to a value of $i_{d1}^* = 7$ A, corresponding to an injected power $P \approx 1.5$ kW according to the line-to-line voltage of Table 6.4, while the second converter has been switched off. According to the injected currents and the simulated grid conditions, the corresponding SCR is around 12, and the measured PLL-bandwidth causing instability is approximately $f_{c1} \approx 620$ Hz. In Fig. 6.11 (a) and (b), experimental tests are compared to simulation results performed in MATLAB/Simulink/-PLECS by means of converter average models.

Table 6.4: Parameters for the tests

Description	Symbol	Value	Description	Symbol	Value
Line-to-line Voltage	V_{LL}	$100\sqrt{3}$ V (rms)	Proportional gain current control	k_{pi}	16.7
Rated current	I_n	5.79 A (rms)	Integral gain current control	k_{ii}	1500
Simulated grid inductance	L_g	0.091 pu	Simulated grid resistance	R_g	0.017 pu

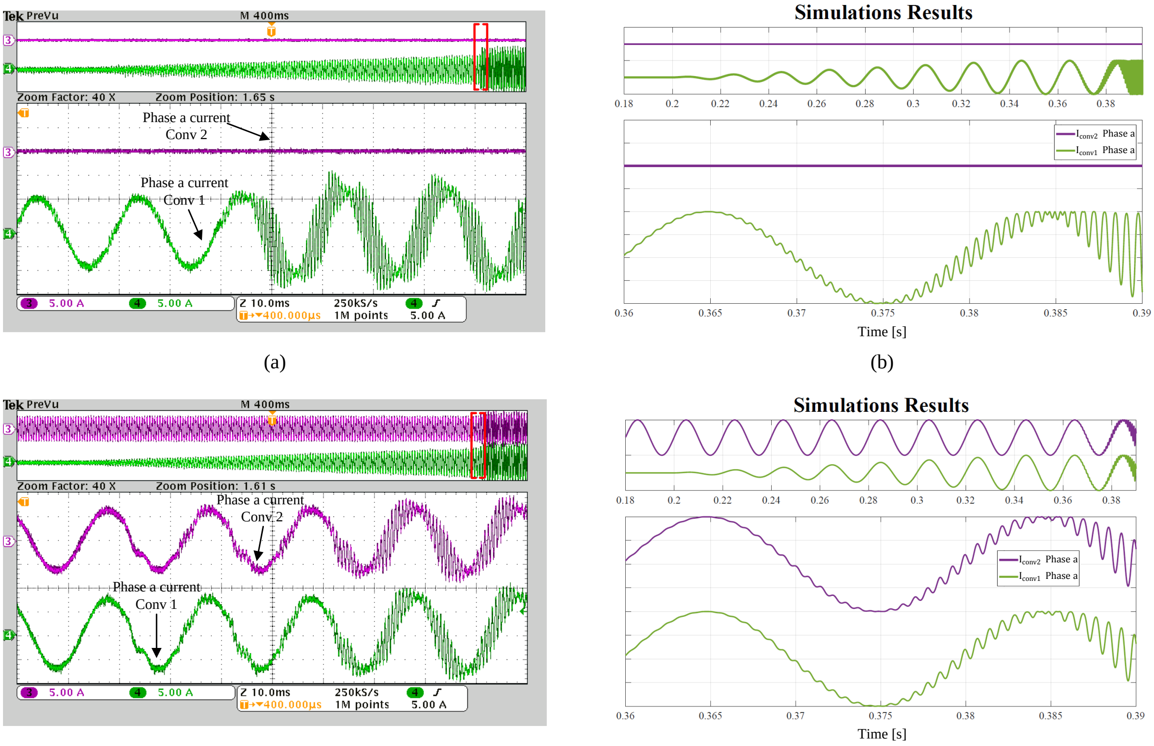

(a) (b)

(c) (d)

Figure 6.11: One GFL converter: (a) experimental results, (b) simulations. Two GFL in paralell: (c) experimental results, (d) simulations.

The test has been repeated connecting in parallel the second converter, whose control parameters are identical to those of the first converter, both for the current control as well as for the PLL, and which has been controlled so as to inject a constant current of $i_{d2} = 7$ A. When both converters reach a value of the injected current of $i^*_{d1} = i^*_{d2} = 7$ A, the corresponding SCR is approximately 6, and the PLL bandwidth causing instability becomes $f_{c1} = f_{c2} \approx 250$ Hz. Similar as in the previous case, experimental tests are compared to simulation results in Fig. 6.11 (c) and (d), showing a qualitatively good match between the measured and the simulated waveforms.

6.2.3 Interactions between GFL and GFM converters

In order to investigate the interactions between GFL and GFM converters, and the effects of the electrical distance on such phenomena, a similar approach as the one described above for the case of GFL converters operating in parallel has been adopted. The additional inductors indicated with L_{add1} and L_{add2} in Fig. 6.1 (a), have been either connected or disconnected by means of the switches $S3$ and $S4$. Converter 1 has been controlled in order to behave as a GFL converter, by implementing the control structure shown in Fig. 6.10, whereas Converter 2 has been either controlled as a GFL or a GFM converter, in the latter case by adopting the control scheme shown in Fig. 6.3. In order to reproduce similar conditions as those investigated in Section 4.3.3, the simulated grid impedance has been selected in order to be complementary to the additional inductance L_{add}, so that the total impedance seen by the

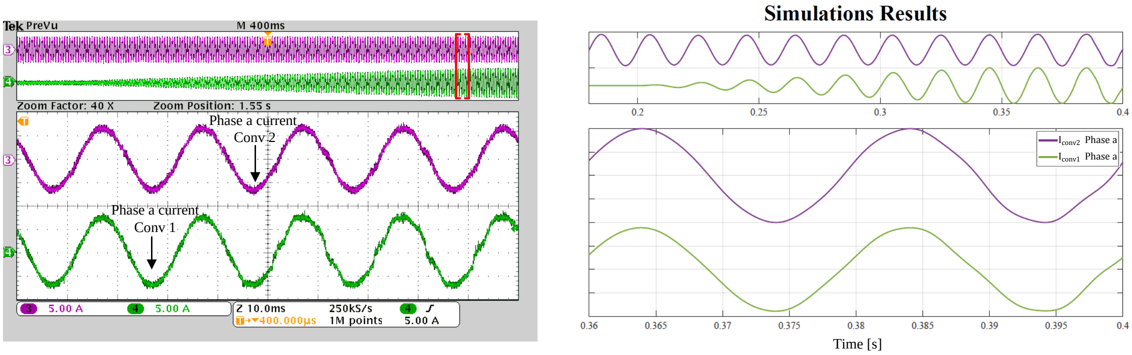

(a) (b)

Figure 6.12: Parallel operation between GFL and GFM converter: (a) experimental results, (b) simulations.

converter, and namely $L_{c1} = L_{add1} + L_g$ for Converter 1, and $L_{c2} = L_{add2} + L_g$ for Converter 2, is constant and equal to the value reported in Table 6.4.

The same procedure described above in order to investigate the interactions between GFL converters, has been repeated for the case of a GFL converter operating in parallel to a GFM one. The parameters of the GFM converter correspond to those reported in Table 6.3, while its power setpoint has been set to P_{set2} =1.5 kW, so as to result in the same magnitude of the injected currents by the GFL converter at the desired operating point. Then the current setpoint of Converter 1 has been slowly ramped up from $i^*_{d1} = 0$ A to $i^*_{d1} = 7$ A and, even though the total current injected into the grid by the two converters is the same as for the case examined above of two GFL converter operating in parallel, the critical PLL-bandwidth causing instability is instead noticeably increased, resulting in a value of $f_{c1} \approx 600$ Hz for the examined condition. In Fig. 6.12, the current waveforms of the two converters during one of the tests performed according to the described procedure are shown, corresponding to a case close to the stability borders, as it can be deduced by the slightly distorted currents, both in the measurements, as well as in the simulated waveforms.

Then the same procedure has been repeated for testing the effects of the electrical distance between converters, and the outcomes of the performed experiments are summarized in Table 6.5, where the critical PLL-bandwidths experimentally obtained for each of the investigated case are reported. These are compared to the values calculated analytically by means of the simplified model assuming the ideal current source behaviour of the converter adopted for the analysis of Section 4.3.3, confirming the expected trend.

Table 6.5: Critical PLL-bandwidths for the different test cases

Case	Operating mode Conv. 2	S1	S2	S3	S4	critical f_c (experimental)	critical f_c (simulated)
1	OFF	Closed	Open	Closed	Closed	$f_{c1} \approx 620$ Hz	$f_{c1} = 670$ Hz
2	PLL-based	Closed	Closed	Closed	Closed	$f_{c1} \approx 250$ Hz	$f_{c1} = 325$ Hz
3	PLL-based	Closed	Closed	Open	Open	$f_{c1} \approx 400$ Hz	$f_{c1} = 360$ Hz
4	Synchronverter	Closed	Closed	Closed	Closed	$f_{c1} \approx 600$ Hz	$f_{c1} = 645$ Hz
5	Synchronverter	Closed	Closed	Open	Open	$f_{c1} \approx 460$ Hz	$f_{c1} = 520$ Hz

6.3 FRT of GFM converters

In this section, the most significant results of a measurement campaign performed in order to validate the FRT capabilities of the GFM control strategy presented in Chapter 5 are presented. For the purpose of the investigation, the setup shown in Fig. 6.2 has been adopted, and the performed tests can be sorted into three main categories: symmetrical faults, asymmetrical faults, and bolted three-phase faults. The obtained results are discussed in the following.

6.3.1 Symmetrical faults

The first examined condition is represented by the case of a symmetrical fault. This scenario is commonly investigated in the literature, when LVRT strategies for grid-connected converters are addressed, and constitutes the simplest faulted condition to be handled by a converter. Nevertheless, symmetrical faults statistically represent only a limited percentage of real faults happening in the field. Indeed, these are caused by either a three-phase or a three-phase to ground short-circuit, and have been categorized as *type A* faults in the classification provided in [25]. A symmetrical fault is characterized by the reduction of all the three-phase voltage magnitudes of the same quantity, this depending on the distance between the measurement point and the fault location, however without producing a phase-angle jump between the pre-fault and the faulty voltages.

The results of two tested symmetrical fault conditions are reported in the following, and Fig. 6.13 shows the outcomes of the first examined case. In order to replicate similar conditions as those simulated in Section 5.3, in which the converter is able to inject fault currents up to 1.5 *pu* of its rated value, the converter has been controlled so as to inject two-thirds of its rated current previous fault occurrence, thus active and reactive power setpoints have been set to $P_{set} = 0.67$ *pu*, while $Q_{set} = 0$ *pu*. The power amplifier used as grid emulator has been programmed so as to suddenly reduce the magnitude of the three voltages to a value of 0.7 *pu* for 1 *sec*. Active and reactive power measured at the PCC are shown in Fig. 6.13 (a), while the measured converter currents, along with the setpoints i_a^{**}, i_b^{**}, and i_c^{**} generated by the control and forwarded to the FPGA board, are reported in Fig. 6.13 (b). Finally, Fig. 6.13 (c) shows the vector diagrams of voltages and currents, comparing magnitudes and phases of the respective quantities previous and during the fault. The phase displacement between voltages and currents, which are instead perfectly in phase during normal operation according to the given power setpoints, can be clearly observed in the figure. It is worth to emphasize that this reaction is automatically resulting from system conditions, hence it is purely caused by the voltage source behind impedance behaviour reproduced by the converter. As a consequence, the converter is able to promptly react to a voltage depression by injecting reactive power almost instantaneously, and without the need for an estimation of the magnitude and the phase of the grid voltages during the fault. Moreover, in order to assess compliance with the draft specifications reported in Section 5.1.4, the response within the first 5 *ms* after fault occurrence is highlighted in Fig. 6.13 (a).

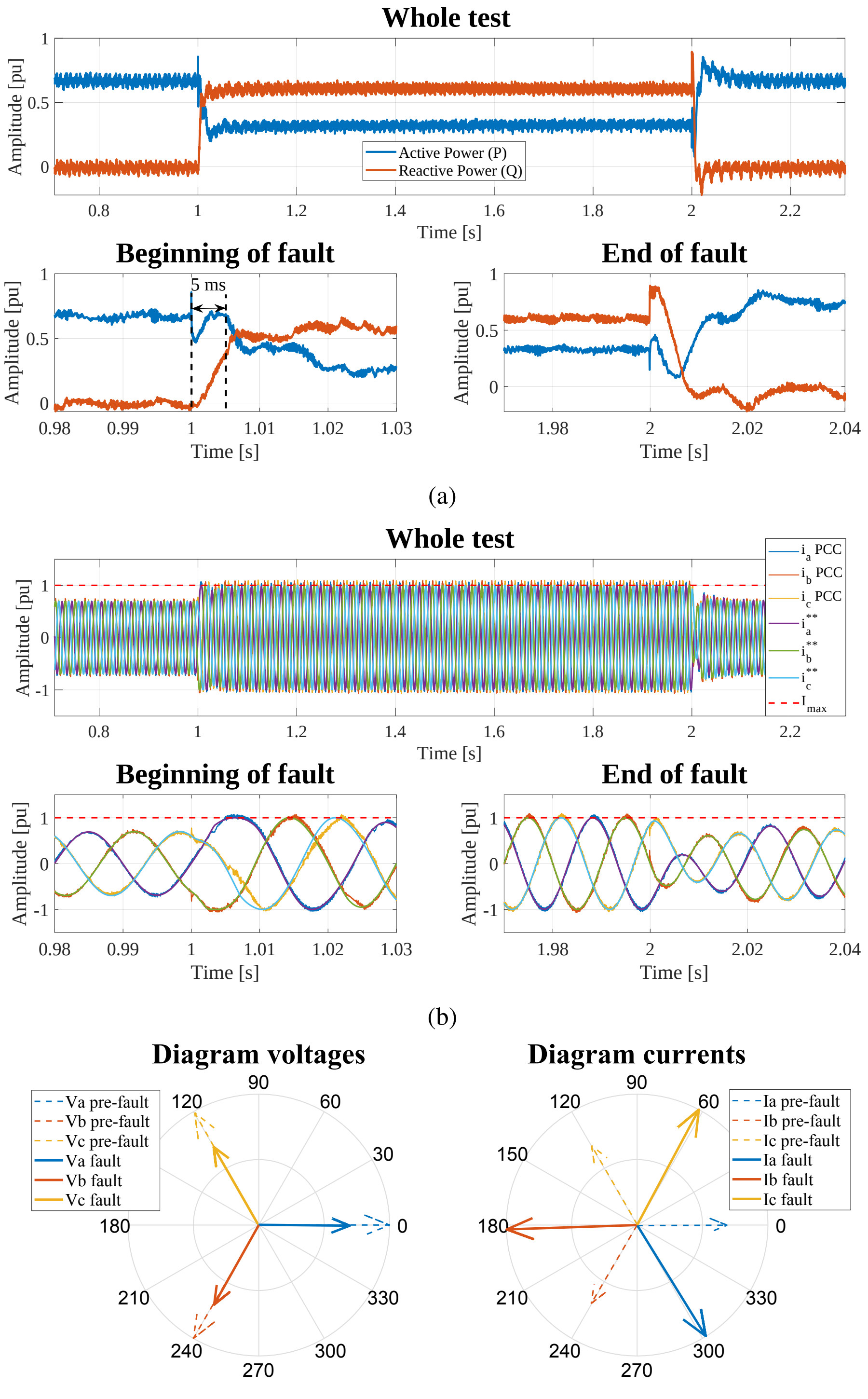

(a)

(b)

(c)

Figure 6.13: Experimental results: symmetrical fault Case 1. (a) Active and reactive power, (b) converter currents, (c) vector diagrams of voltages and currents before and during the fault.

In order to show the capabilities of properly limiting converter currents independently from pre-fault conditions, and from the magnitude of the voltage depression, the same experiment has been repeated by setting the power setpoint of the converter previous the emulated fault event to $P_{set} = 0.9\ pu$, and by reducing the magnitude of the grid voltages during the fault to $0.2\ pu$. The results are shown in Fig. 6.14, where again the prompt reaction of the converter

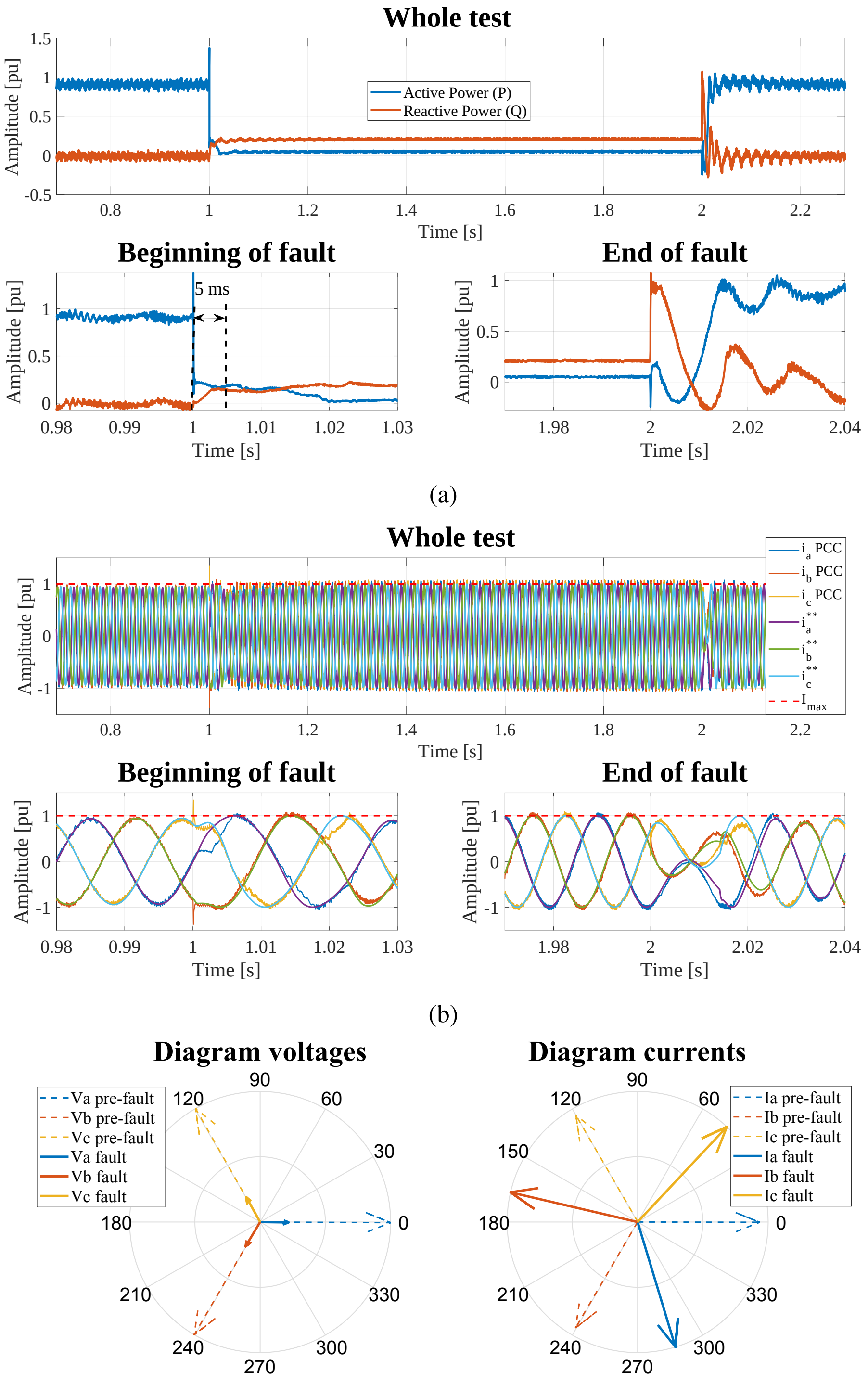

(a) (b) (c)

Figure 6.14: Experimental results: symmetrical fault Case 2. (a) Active and reactive power, (b) converter currents, (c) vector diagrams of voltages and currents before and during the fault.

in injecting reactive power within few millisecond after fault occurrence, yet respecting converter current limitations, are demonstrated. It is interesting to notice from the comparison between Fig. 6.14 (a) and Fig. 6.13 (a), that the ratio between the injected reactive power Q and active power P during the fault is higher in the second examined case. This becomes also evident by comparing the phase displacement of the currents during the faults in the vector diagrams of Fig. 6.13 (c) and Fig. 6.14 (c), and can be attributed to the fact that the voltage depression is higher in the second examined case.

6.3.2 Asymmetrical faults

Asymmetrical faults represent the most common condition in a real power system. These are generally caused by either single-phase to ground connections or by a short-circuit between two phases, resulting in a reduction of the voltage magnitude of one or two phases, and in certain cases also of a phase displacement between pre-fault and faulted voltages. Furthermore, due to the presence of transformers located between the PCC of a converter and the point in the system where the fault occurs, a modification of the fault characteristics has to be expected in practice, and, according to the magnitude of the voltage sag and the resulting phase displacement, a categorization of faults has been reported in [25].

In the following, experimental tests showing the converter behaviour in case of unbalanced fault conditions are shown. Among the different types of asymmetrical faults that can occur in practice, the case of an asymmetrical fault labeled as *type G* in the classification of [25], has been investigated. This is for example resulting from the propagation of a two-phase to ground fault through two series transformers with Δ/Y connections and, in addition to an unequal decrease of the voltage magnitude in all the three phases, it is characterized by an angle displacement in two phases compared to pre-fault conditions.

Fig. 6.15 shows the experimental tests for the first investigated asymmetrical fault condition. Analogously to the first examined case of symmetrical faults, active and reactive power setpoints are respectively set to $P_{set} = 0.67$ *pu* and $Q_{set} = 0$ *pu* before the occurrence of the event, so as to emulate a current injection capability of the converter up to 1.5 *pu*. At time $t = 1$ *sec*, a fault is reproduced by the grid emulator, and active and reactive power injected by the converter are shown in Fig. 6.15 (a), while the resulting converter currents are reported in Fig. 6.15 (b). The prompt reaction of the converter in terms of reactive power injection at the occurrence of the fault can be appreciated in Fig. 6.15 (a), where the reaction within the first 5 *ms* is highlighted. Vector diagrams of voltages and currents are reported in Fig. 6.16 (c), showing the displacement between the injected currents before and during the fault, automatically resulting from the reproduced symmetrical voltage source behaviour of the converter and the asymmetrical fault condition.

As for the second examined symmetrical fault case, the same experiment has been repeated by modifying the power setpoint previous fault to $P_{set} = 0.9$ *pu*, while further increasing the intensity of the voltage sag, so as to reproduce a more severe fault condition. The results of this experiment are reported in Fig. 6.16, where analogous conclusions as for the other examined cases regarding the reactive power injection, as well as the limitation of converter currents can be drawn. Finally, Fig. 6.16 (c) shows the vector diagrams of voltages and currents comparing magnitudes and phases previous and during the fault.

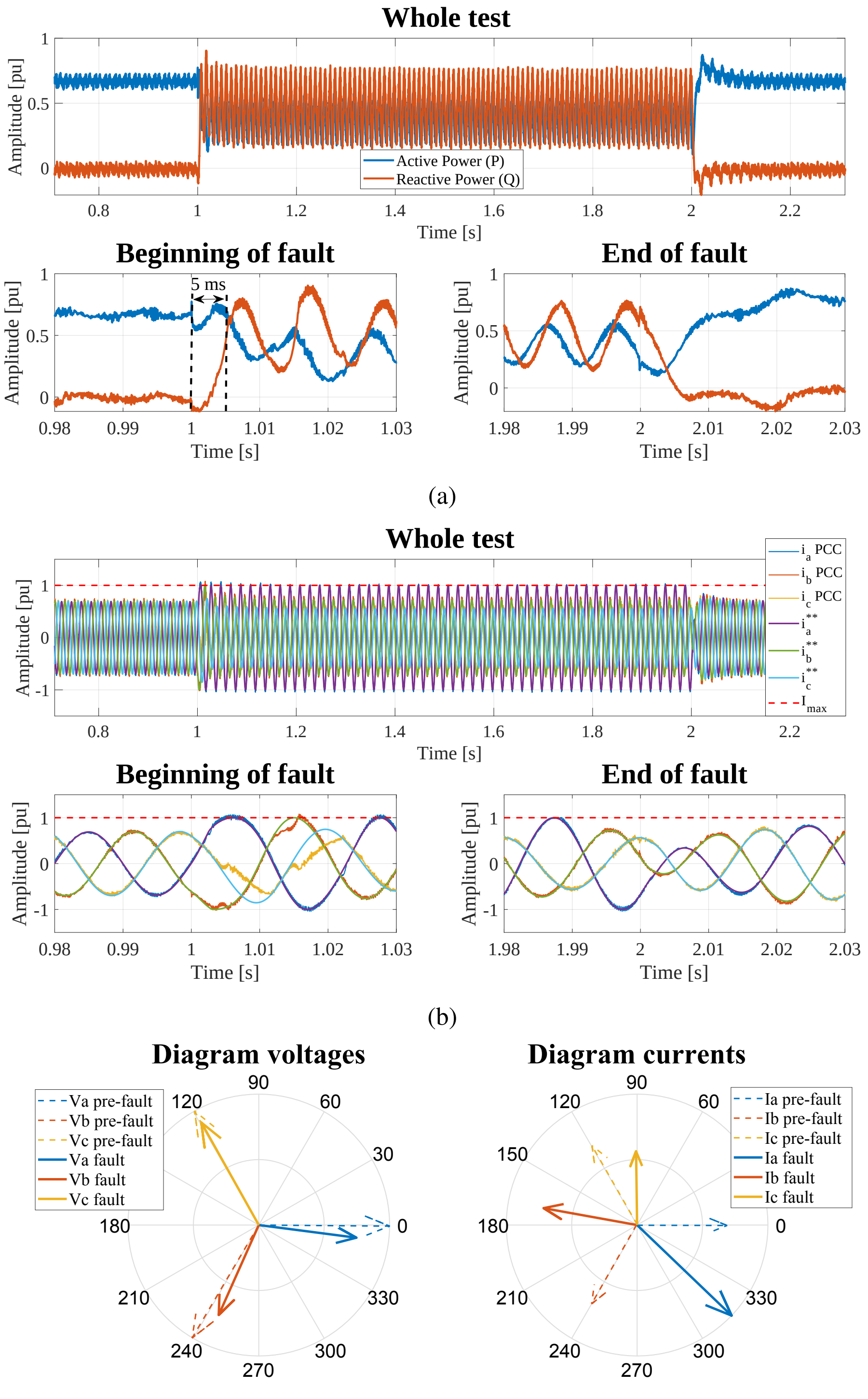

(a)

(b)

(c)

Figure 6.15: Experimental results: asymmetrical fault Case 1. (a) Active and reactive power, (b) converter currents, (c) vector diagrams of voltages and currents before and during the fault.

6.3.3 Bolted three-phase faults

The last examined set of tests is the case of three-phase bolted faults. For a GFM converter intrinsically behaving as a voltage source behind impedance, this represents surely the most challenging fault condition that could be faced, since it generally gives rise to the highest

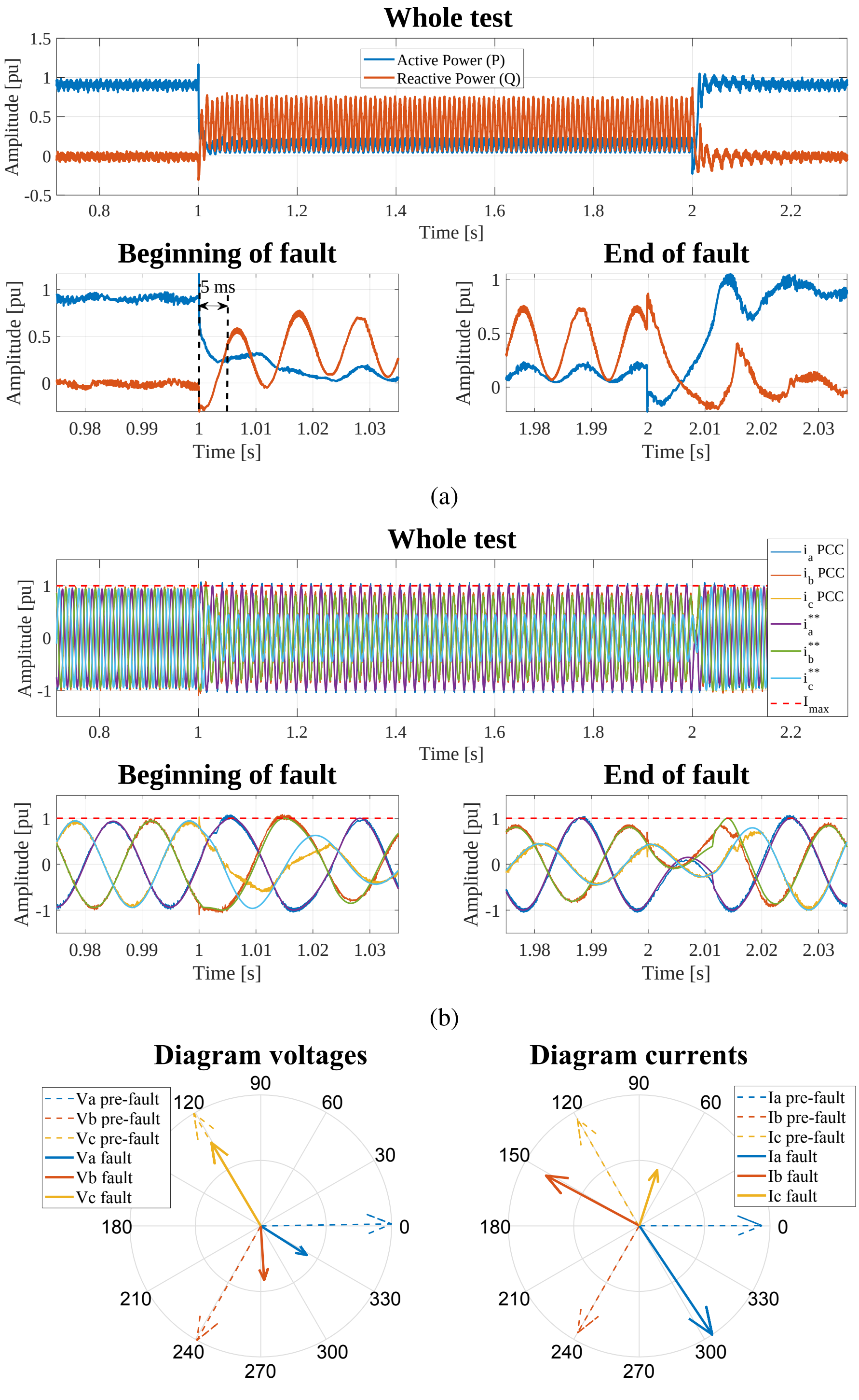

(a)

(b)

(c)

Figure 6.16: Experimental results: asymmetrical fault Case 2. (a) active and reactive power, (b) converter currents, (c) vector diagrams of voltages and currents before and during the fault.

possible fault currents, if the fault is not properly handled, and hence to the most dangerous situation for the converter hardware components. Fig. 6.17 shows the results of the first investigated case for this category of faults. The power stepoint of the converter has been set to $P_{set} = 0.9$ *pu*, and $Q_{set} = 0$ *pu*, while the three-phase voltages of the grid emulator are suddenly reduced to zero at $t = 1$ *sec*. Due to the fact that the impedance between the

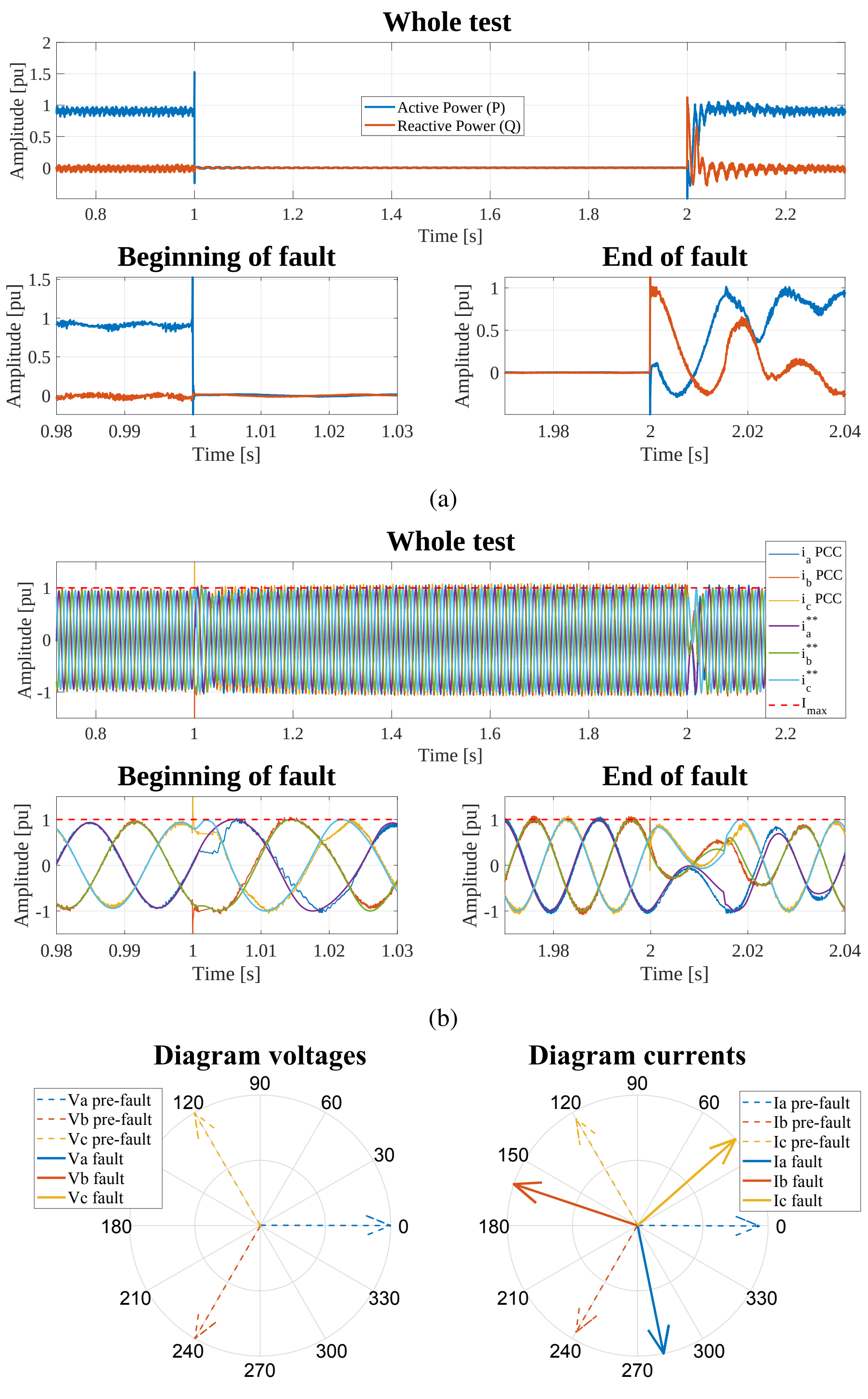

(a)

(b)

(c)

Figure 6.17: Experimental results: bolted three-phase fault Case 1. (a) Active and reactive power, (b) converter currents, (c) vector diagrams of voltages and currents before and during the fault.

fault and the converter is only represented by the converter filter and the transformer, active and reactive power measured at the converter terminals are almost nullified, as it becomes evident by looking at Fig. 6.17 (a). Nevertheless, the converter reacts by injecting a fault current up to its hardware limit of 1 *pu* almost instantaneously, as shown in Fig. 6.17 (b). Furthermore, the vector diagram of 6.17 (c) clearly shows the phase jump of the injected

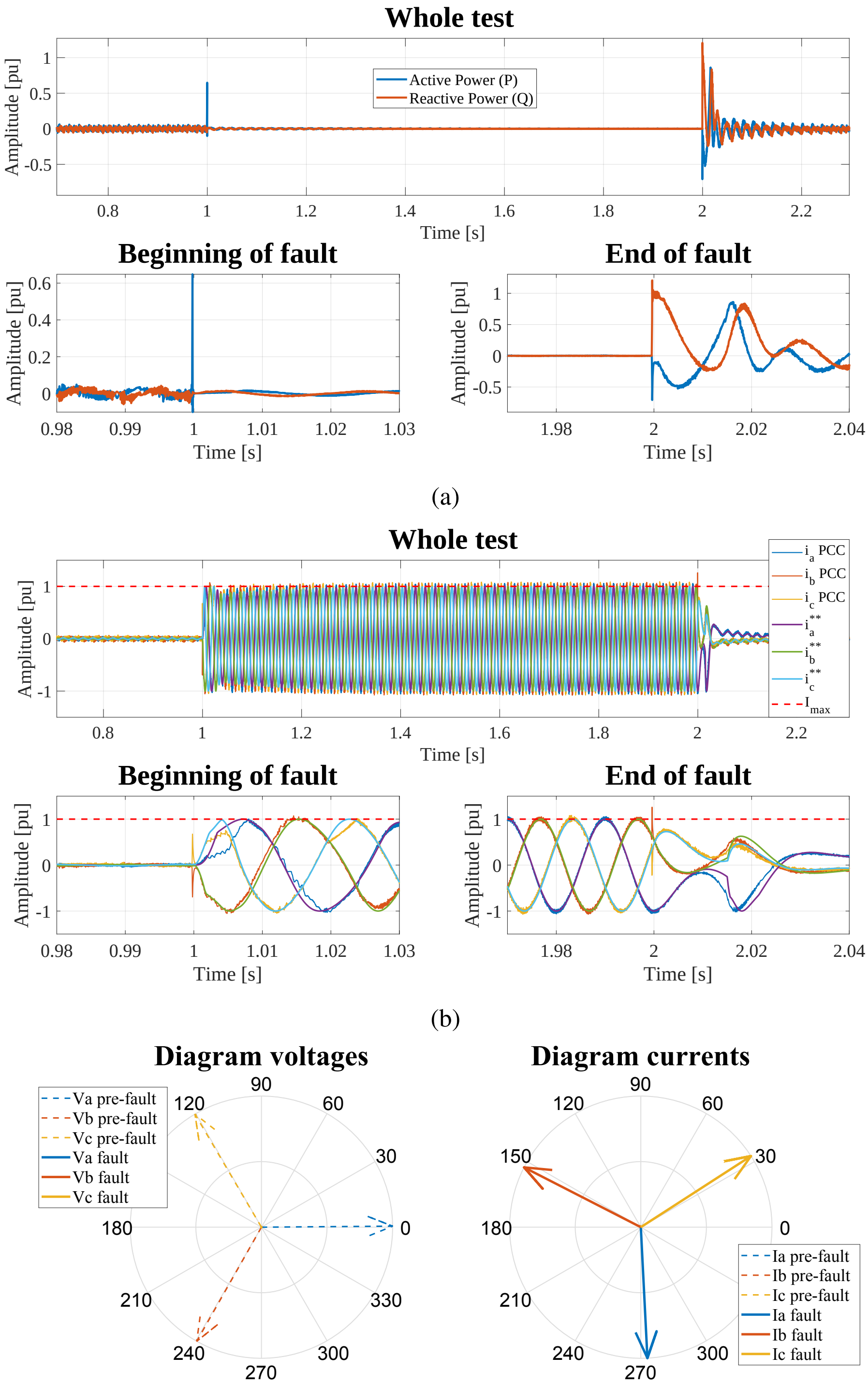

(a)

(b)

(c)

Figure 6.18: Experimental results: bolted three-phase fault Case 2. (a) Active and reactive power, (b) converter currents, (c) vector diagrams of voltages and currents before and during the fault.

fault currents, which due to the extreme drop of the grid voltages, is even higher than the one measured in Fig. 6.14, for the second examined case of a symmetrical fault.

In order to investigate the dynamic performances of the converter and its capability of injecting fault currents up to its hardware limitation within few milliseconds, a second bolted fault condition has been tested, and the results are reported in Fig. 6.18. In this case, active and reactive power setpoints have been both set to zero at pre-fault, then a bolted fault as for the case shown in Fig. 6.17, has been reproduced at the converter terminals. The fast fault current injection capability of the converter can be observed in Fig. 6.17 (b), where the increase of the converter currents from zero to their maximum value I_{max} within few milliseconds, yet by respecting the hardware limitations, can be appreciated. Additionally, Fig. 6.17 (c) highlights how under such operating condition the injected currents are almost purely reactive, resembling the behaviour of a synchronous condenser, which spins freely during normal operation without exchanging power with the grid, but can contribute to voltage stability by injecting short-circuit currents at the occurrence of a fault.

6.4 Summary of the chapter

In this chapter, the results of the experiments performed in order to validate the analysis reported in Chapter 4, related to the stability analysis of GFL and GFM converters and the interactions among them, along with the most significant results of an extensive measurement campaign performed in order assess the FRT capability of the GFM control structure proposed in Chapter 5, have been presented.

For the purposes of the tests, two different setups have been adopted, which are described in the first part of this chapter. The first setup has been used in order to validate the results of the stability analysis of GFL and GFM converters and the interactions among them, by addressing first the case of a single GFM converter implemented by means of the well-known synchronverter structure. To this extent, the synchronverter pre-synchronization procedure introduced in Chapter 2, has been first discussed, then a practical example has been reported in order to better clarify its working principle. Afterwards, the linearized synchronverter model developed in Chapter 4, and adopted for the stability analysis performed in Section 4.2.2, has been validated by means of PHIL tests. Similarly, the linearized model of two GFM converters operating in parallel developed in Section 4.2.3, has been first validated. Subsequently, the reduction of stability margin of a GFM converter caused by the presence of another converter of the same type operating in close electrical proximity has been demonstrated. Finally, in accordance to the results of the analysis performed in Section 4.3.1, it has been proven that the implementation of a virtual impedance in the control of the two GFM converters can enhance their stability when operating in parallel.

Afterwards, the case of GFL converters has been examined, so as to validate the results of the stability analysis performed in Section 4.1, and which focuses on the effects of the PLL-bandwidth variation on converter stability. First the case of a single GFL converter has been examined, searching for the critical PLL-bandwidth causing instability. Then the case of two converters operating in parallel has been addressed, demonstrating that the critical PLL-bandwidth is affected by the presence of the second converter operating nearby. Similar experiments have been performed in order to assess the effects of the interactions between

GFL and GFM converters, as well as the effects of the electrical distance between converters, confirming the trend observed by means of the analysis performed in Section 4.3.1.

The second part of this chapter addresses the FRT capabilities of the GFM control structure presented in Chapter 5, for which the setup at the Energy Systems laboratory of the WRD facilities in Aurich has been adopted. Three main categories of faults have been examined, and namely symmetrical faults, asymmetrical faults, and bolted three-phase faults. For each of the investigated categories, the current limitation capabilities, as well as the prompt reaction of the converter in terms of reactive power injection within few milliseconds after fault occurrence without the need for detecting first the faulted condition, have been proven even under extreme operating conditions.

7 Summary, conclusions, and future research

7.1 Summary and conclusions

Due to the evolution of the electric power system from centralized generation toward DERs, commonly coupled to the grid by means of power electronics-based converters, concerns have been expressed by SOs worldwide about the stability of the future power system, triggering discussions in different countries about the need for new converter control strategies ensuring stable operation in the new system configuration. In this context, the concept of GFM converters has increasingly gained attention during the last decade, and it has been proposed as a possible solution in order to ensure stable operation of a power system characterized by high-penetration of power electronics-based generation.

One of the main concerns related to the replacement of SGs by means of power electronics-based generating units, is represented by the reduction of total system inertia, which is essential for the survival of the power system in its actual configuration. To this extent, the concept of VSMs has been introduced in the last decade, and the terms GFM converter and VSM have been often used interchangeably in the literature, causing a certain degree of confusion around their real meanings. One of the objectives of this thesis is to clearly identify the characteristics of GFM converters independently from the considered application. In fact, this concept has been initially introduced in the context of microgrids, requiring therefore a revision in order to be extended to applications in wide interconnected systems. Hence, the definitions of converters adopted in the microgrid literature have been first introduced, then these have been critically reviewed, so that the general characteristics of the two main categories of grid-connected converters, identified as GFL and GFM units, are revealed. Finally, the conceptual differences in the behaviour of a GFM converter compared to state-of-the-art GFL units have been highlighted, and a general structure of a GFM converter has been outlined by identifying the main subsystems composing it, providing an overview on their possible implementations according to an extensive literature overview.

Once identified the characteristics of GFL and GFM converters, a comprehensive stability analysis of the aforementioned control strategies has been performed, in order to assess their influence on the stability of a power system characterized by high-penetration of power electronics-based generation. However, due to the articulated nature of a real power system, the concept of *stability* for such a study case is a rather multifaceted phenomenon. Therefore, the definition of stability of a dynamic system has been first introduced from a control theory perspective, then the definition of system stability adopted by the power system community has been discussed, along with the definition of system stability for microgrids recently elaborated within the power electronics community.

According to the characteristics of the targeted system, and the identified phenomena of interest, it has been decided to address the interactions between power electronics-based converters operating nearby, giving particular attention to the effects caused by the adopted synchronization technique, by means of a small-signal stability analysis. To this extent, various techniques could be employed. Among them, frequency-domain approaches, such as the impedance-based analysis well-established within the power electronics community, or time-domain approaches, e. g. the modal eigenvalue analysis widely adopted by the power system community, represent possible candidates. Nevertheless, due to the MIMO nature of the studied system, a robust stability analysis by means of SSVs has been proposed in this thesis. Though well-known in control theory, this approach is rather seldom utilized by the power system or by the power electronics communities. It allows assessing stability for a broad set of possible plants rather than addressing only a defined configuration, and results particularly useful for investigating the robustness of controllers in a power electronics-dominated system.

Practical examples of applications of the aforementioned approaches for studying small-signal stability of grid-connected converters have been reported, highlighting advantages and drawbacks of each method. Among the main outcomes of the performed analysis, it has been revealed that, if from one side is desired by SOs that grid-connected converters should react promptly to system contingencies, there exist physical limitations for the maximum bandwidth of the synchronization unit adopted by a GFL converter, which become more stringent when operating in proximity to converters of the same type, and under weak grid conditions. On the other side, it is demonstrated that a GFM converter, which intrinsically behaves as a voltage source behind impedance, and generally do not require a dedicated unit for synchronization, is instead suitable for weak grid operating conditions.

The performed analysis has also revealed that, as a consequence of its operating principle, the robust stability of a GFM converter is enhanced by increasing the electrical distance between the converter and any other GFM unit operating nearby, as also confirmed by the investigation of the parallel operation between two GFM converters. According to the obtained results, control design guidelines for a GFM converter have been proposed, which also take into account the implementation of a virtual impedance in the control structure, so as to artificially modify the output impedance of the converter according to the operating condition. Finally, the parallel operation between GFL and GFM converters has been addressed, as well as the effects of the electrical distance between operating units. The outcome of this study indicates that a GFM converter can enhance the robust stability of a GFL converter operating under weak grid conditions when located in electrical proximity to it, suggesting that a strategical distribution of GFM operating units in a power system could aid integration of power electronics-based generation in the actual power system, without the need for a radical replacement of all existing units.

Even though GFM converters might overcome some of the limitations of GFL converters, there exist several practical concerns regarding their implementation. In fact, since they can reproduce some of the characteristics of real SMs, e. g. their synchronization principle, instability phenomena of a classical power system, such as angle instability, might be inherited by such control structures. Furthermore, due to the reproduced behaviour of voltage source behind impedance, they are able to react to a grid fault almost instantaneously without the need for detecting first the fault condition. Though this characteristic is surely beneficial for system stability, a sudden increase of the converter currents might jeopardize the integrity of the converter hardware components.

These aspects have been issued in detail in Chapter 5, first from the theoretical point of view by reviewing electrical machines theory, then their practical implications on a GFM converter have been assessed, proposing possible countermeasures for overcoming potential instability problems. In the specific, the online calculation of a stability index is proposed, which allows identifying operation in a potential unstable region of the power-angle curve. On the other side, a particular implementation of a variable virtual admittance in the inner current control loop of a GFM converter has been discussed, which allows the converter reproducing the behaviour of a voltage source behind impedance before, during, and after the fault, yet by preventing from the risk of overcurrents. Finally, the results of the performed stability analysis, along with the efficacy of the proposed FRT strategy for GFM converters have been experimentally proven by means of suitable test benches.

7.2 Research contribution

Identification of the characteristics of a GFM converter

- The classification of grid-connected converters proposed for microgrid applications has been reviewed, identifying the characteristics of GFL and GFM converters independently from their application.
- Conceptual differences in the behaviour of GFL and GFM converters have been specified, along with the consequences deriving from them.
- The concept of VSMs has been introduced, highlighting that a VSM simply represents a particular implementation of a GFM converter.
- A general structure of a GFM converter has been presented, and possible implementations of the main subsystems composing it have been discussed, hence providing a comprehensive literature overview.

Review of approaches for stability analysis of grid-connected converters

- The concept of stability of a dynamic system has been first introduced from the control theory point of view. Then a review of the stability concept from the classical power system perspective, as well as from the perspective of microgrids have been given.
- Approaches for stability analysis of grid-connected converters currently adopted in the literature have been discussed, highlighting advantages and drawbacks of each method.
- The robust stability analysis by means of SSVs is proposed as an effective means for assessing robustness of grid-connected converters in a system with high-penetration of power electronics-based generation.

Stability analysis of GFL and GFM converters in power electronics-dominated power systems

- The effects of the dedicated synchronization unit of a GFL converter, commonly implemented by means of a PLL, have been investigated, demonstrating that there exist physical limitations for the maximum PLL-bandwidth of a GFL converter.
- It is proven that interactions between synchronization units of converters operating nearby might take place, which are accentuated by weak grid operating conditions, and further reduce the maximum achievable PLL-bandwidth.
- The robust stability analysis performed for a GFM converter emulating the power-synchronization principle of a SM reveals that, contrary to a PLL-based converter, a GFM is particularly suitable for weak grid operating conditions.
- It is demonstrated, that an increase of the emulated inertia constant of a VSM can reduce the robust stability of the converter in the low frequency range, if damping is not accordingly increased.
- A control tuning procedure for a GFM converter implemented by means of a synchronverter structure is proposed, including indications for the tuning of a virtual impedance, so as to enhance the robust stability of GFM converters operating in parallel.
- The parallel operation between GFL and GFM converters has been investigated, demonstrating that the presence of a GFM converter located in electrical proximity can enhance the robust stability of a GFL operating under weak grid conditions.

Enhancement of FRT capabilities of GFM converters

- The most relevant issues related to the implementation of GFM converters have been identified by reviewing electrical machines theory. Then practical examples of how these effects influence the behaviour of a GFM converter are reported.
- It is highlighted that a GFM converter reproducing the power-synchronization mechanism of a SM might face angle instability problems, and possible countermeasures are proposed.
- A particular implementation of the inner control loop of a GFM converter is presented, which allows the converter behaving as a voltage source behind impedance before, during, and after a grid fault, while preventing from the risk of overcurrents.

7.3 Future research

The topic investigated in this thesis is extremely broad, and for addressing it properly, a multi-disciplinary approach involving power system analysis, as well as power electronics and control expertise is required. In the following, some aspects extending the contribution of this thesis are listed:

- **Inclusion of DC-link control loop in the converter model**: for the stability analysis performed in Chapter 4, the synchronverter structure has been adopted as a general implementation of a GFM converter, and the reason for this choice has been properly motivated in the same chapter. Nevertheless, the DC-link dynamic has not been taken into account in the performed analysis and, even though this might represent a reasonable assumption for the case that the converter is coupled with a BESS, this is generally not valid for a converter associated with a wind or a PV plant. Therefore, it would be interesting to extend the analysis including the DC-link voltage control loop in the converter model.

- **Mechanical stress caused by grid-side events on the structural components of a wind turbine**: the challenges related to the implementation of a GFM control algorithm on a converter interfaced with different types of primary energy sources might be of diverse nature. In the specific case of a WT, the implementation of a GFM control algorithm might give rise to potential interactions between the structural components (blades, tower, etc...) and perturbations from the grid side. Therefore, assessing the influence of control parameters of the grid-side converter on the structural components of the turbine, taking into account the nature (capacitors, super-capacitors, batteries), as well as the size of the energy storage located in the DC-link of the back-to-back converter, is of high interest for practical applications.

- **Extend the analysis at system level by adopting suitable grid benchmarks**: the robust stability analysis performed in Chapter 4, has been motivated by the fact that, by properly choosing the uncertainty function for the construction of the generalized plant, control robustness can be assessed for a broad set of possible configurations, hence also taking into account the presence of other power electronics-based converters operating nearby. However, it would be interesting to extend the analysis to a system perspective, in order to investigate the beneficial effects due to the implementation of a GFM control algorithm on converters operating in a real power system. To this extent, suitable grid benchmarks should be adopted, and different grid scenarios should investigated.

- **Large-signal stability analysis**: the choice of performing a small-signal stability analysis for investigating the identified phenomena of interest for this thesis, has been comprehensively motivated in Chapter 3. These, in fact, concern control interactions between converters operating in a power electronics-dominated power system, by giving particular emphasis to the effects caused by the adopted synchronization mechanism. Nevertheless, as it has been pointed out in Chapter 5, the adopted approaches are not anymore suitable for investigating converter stability according to large transients that are generally caused by severe system contingencies, since the assumption of a linear system does not hold any longer. Thus, for assessing converter stability under such operating conditions, a systematic large-signal stability analysis becomes necessary.

- **Power reduction to avoid angle instability**: the solution proposed in Chapter 5, in order to prevent from an acceleration of the virtual rotor angle that might lead to an angle instability condition, consists on temporarily reducing the converter power setpoint as soon as the calculated stability index falls below a defined threshold, then ramping it again slowly up while waiting for fault clearance. In case of a sustained fault, alternative ways for properly limiting the power setpoint to the highest achievable value according to the actual operating conditions, could be investigated.

- **Active thermal monitoring for temporary boost of converter currents**: the measurement-less fast fault current injection capabilities of a GFM converter within few milliseconds after fault occurrence, have been thoroughly discussed throughout the thesis. However, a strict current limitation up to a pre-determined threshold has been considered, taking for granted that the converter needs to be accordingly designed in order to allow such current injection during the fault. Nevertheless, the implementation of an active thermal monitoring combined with a particular modulation strategy could be investigated, which, according to the actual converter operating conditions, could allow increasing the magnitude of the injected fault currents without the necessity for oversizing the converter hardware components.

8 References

[1] *High penetration of power electronic interfaced power sources and the potential contribution of grid forming converters.* Technical report, ENTSO-E, [Available online], 2020.

[2] *Ten-year network development plan 2016.* Technical report, ENTSO-E, [Available online], 2016.

[3] *The massive integration of power electronic devices (MIGRATE) project, https://www.h2020-migrate.eu/about.html.* Technical report, MIGRATE, 2019.

[4] Emanuel, H. *et al.*: *Requirements for control strategies of grd-connected converters in the future power system.* IET Renewable Power Generation, 14(8):1288–1295, June 2020, ISSN 1557-9948.

[5] *Fault current contribution from PPMS & HVDC.* Technical report, ENTSO-E, [Available online], 2017.

[6] Johnson, A.: *Fast fault current injection, fault-ride-through, and banding - terms of reference.* Technical report, NGESO, http://www.nationalgrideso.com.

[7] *Expert group - grid supporting fast fault current and associated control including virtual synchronous machine approaches.* Technical report, NGESO, https://www.nationalgrid.com/uk/electricity/codes/gridcode/meetings/vsm-expert-workshop.

[8] *System disturbance on 4 november 2006, final report.* Technical report, UCTE, [Available online], 2006.

[9] *Netzregelung 2.0: Verbundprojekt zur Regelung und Stabilität im stromrichterdominierten Verbundnetz.* Technical report, Fraunhofer IEE, [Available online], 2018.

[10] *Netz:Kraft - Netzwiederaufbau unter Berücksichtigungzukünftiger Kraftwerkstrukturen, Öffentlicher Abschlussbericht.* Technical report, Fraunhofer IEE, [Available online], 2019.

[11] Wetzler, F. U.: *Power/energy: Connecting renewable power sources into the system: Windmills, fuel cells, and photovoltaics may serve existing grids, but first many technical, legal, and economic issues must be addressed.* IEEE Spectrum, 19(11):42–45, Nov 1982, ISSN 1939-9340.

[12] Chen, Z., Guerrero, J. M., and Blaabjerg, F.: *A review of the state of the art of power electronics for wind turbines.* IEEE Transactions on Power Electronics, 24(8):1859–1875, Aug 2009, ISSN 1941-0107.

[13] Blaabjerg, F., Teodorescu, R., Liserre, M., and Timbus, A. V.: *Overview of control and grid synchronization for distributed power generation systems.* IEEE Transactions on Industrial Electronics, 53(5):1398–1409, Oct 2006, ISSN 1557-9948.

[14] Blaabjerg, F., Zhe Chen, and Kjaer, S. B.: *Power electronics as efficient interface in dispersed power generation systems*. IEEE Transactions on Power Electronics, 19(5):1184–1194, Sep. 2004, ISSN 1941-0107.

[15] Ackermann, T.: *Wind Power in Power Systems*. John Wiley and Sons, 2005.

[16] *IEEE Standard for interconnecting distributed resources with electric power systems*. IEEE Std 1547-2003, pages 1–28, July 2003.

[17] *IEEE Standard for interconnecting distributed resources with electric power systems - amendment 1*. IEEE Std 1547a-2014 (Amendment to IEEE Std 1547-2003), pages 1–16, May 2014.

[18] *IEEE Standard for interconnection and interoperability of distributed energy resources with associated electric power systems interfaces*. IEEE Std 1547-2018 (Revision of IEEE Std 1547-2003), pages 1–138, April 2018.

[19] Lasseter, R. H.: *Microgrids*. In *2002 IEEE Power Engineering Society Winter Meeting. Conference Proceedings (Cat. No.02CH37309)*, volume 1, pages 305–308 vol.1, Jan 2002.

[20] Lasseter, R. H. *et al.*: *CERTS microgrid laboratory test bed*. IEEE Transactions on Power Delivery, 26(1):325–332, Jan 2011, ISSN 1937-4208.

[21] Farrokhabadi, M. *et al.*: *Microgrid stability definitions, analysis, and examples*. IEEE Transactions on Power Systems, 35(1):13–29, Jan 2020, ISSN 1558-0679.

[22] Rocabert, J., Luna, A., Blaabjerg, F., and Rodriguez, P.: *Control of power converters in AC microgrids*. IEEE Transactions on Power Electronics, 27(11):4734–4749, Nov 2012, ISSN 1941-0107.

[23] Matevosyan, J. *et al.*: *Grid-forming inverters: Are they the key for high renewable penetration?* IEEE Power and Energy Magazine, 17(6):89–98, Nov 2019, ISSN 1558-4216.

[24] Paolone, M. *et al.*: *Fundamentals of power systems modelling in the presence of converter-interfaced generation*. In *21st Power Systems Computation Conference (PSCC), invited paper, Porto, Portugal*, June 2020.

[25] R. Teodorescu, M. Liserre, P. Rodriguez: *Grid converters for photovoltaic and wind power systems*. John Wiley and Sons, 2011.

[26] P. C. Krause, O. Wasynczuk, S. D. Sudhoff: *Analysis of electric machinery and drive systems, 2nd edition*. John Wiley and Sons, 2002.

[27] Zmood, D. N. and Holmes, D. G.: *Stationary frame current regulation of PWM inverters with zero steady-state error*. IEEE Transactions on Power Electronics, 18(3):814–822, May 2003, ISSN 1941-0107.

[28] Guerrero, J. M., Vasquez, J. C., Matas, J., Castilla, M., and Garcia de Vicuna, L.: *Control strategy for flexible microgrid based on parallel line-interactive UPS systems.* IEEE Transactions on Industrial Electronics, 56(3):726–736, March 2009, ISSN 1557-9948.

[29] Pogaku, N., Prodanovic, M., and Green, T. C.: *Modeling, analysis and testing of autonomous operation of an inverter-based microgrid.* IEEE Transactions on Power Electronics, 22(2):613–625, March 2007, ISSN 1941-0107.

[30] D'Arco, S. and Suul, J. A.: *Virtual synchronous machines - classification of implementations and analysis of equivalence to droop controllers for microgrids.* In *2013 IEEE Grenoble Conference*, pages 1–7, June 2013.

[31] Kundur, P., Balu, N. J., and Lauby, M. G.: *Power system stability and control.* McGraw-Hill New York, 1994.

[32] Prodanovic, M. and Green, T. C.: *High-quality power generation through distributed control of a power park microgrid.* IEEE Transactions on Industrial Electronics, 53(5):1471–1482, Oct 2006, ISSN 1557-9948.

[33] Zhong, Q.: *Power-electronics-enabled autonomous power systems: Architecture and technical routes.* IEEE Transactions on Industrial Electronics, 64(7):5907–5918, July 2017, ISSN 1557-9948.

[34] Liserre, M., Buticchi, G., Andresen, M., De Carne, G., Costa, L. F., and Zou, Z.: *The smart transformer: Impact on the electric grid and technology challenges.* IEEE Industrial Electronics Magazine, 10(2):46–58, June 2016, ISSN 1941-0115.

[35] Zou, Z., De Carne, G., Buticchi, G., and Liserre, M.: *Smart transformer-fed variable frequency distribution grid.* IEEE Transactions on Industrial Electronics, 65(1):749–759, Jan 2018, ISSN 1557-9948.

[36] Pattabiraman, D., Lasseter., R. H., and Jahns, T. M.: *Comparison of grid following and grid forming control for a high inverter penetration power system.* In *2018 IEEE Power Energy Society General Meeting (PESGM)*, pages 1–5, Aug 2018.

[37] Lasseter, R. H., Chen, Z., and Pattabiraman, D.: *Grid-forming inverters: A critical asset for the power grid.* IEEE Journal of Emerging and Selected Topics in Power Electronics, 8(2):925–935, June 2020, ISSN 2168-6785.

[38] Beck, H. and Hesse, R.: *Virtual synchronous machine.* In *2007 9th International Conference on Electrical Power Quality and Utilisation*, pages 1–6, Oct 2007.

[39] Driesen, J. and Visscher, K.: *Virtual synchronous generators.* In *2008 IEEE Power and Energy Society General Meeting - Conversion and Delivery of Electrical Energy in the 21st Century*, pages 1–3, July 2008.

[40] Zhong, Q. and Weiss, G.: *Synchronverters: Inverters that mimic synchronous generators*. IEEE Transactions on Industrial Electronics, 58(4):1259–1267, April 2011, ISSN 1557-9948.

[41] Zhong, Q., Nguyen, P., Ma, Z., and Sheng, W.: *Self-synchronized synchronverters: Inverters without a dedicated synchronization unit*. IEEE Transactions on Power Electronics, 29(2):617–630, Feb 2014, ISSN 1941-0107.

[42] P. Rodriguez, I. Candela, J. Rocabert and Teodorescu, R.: *Virtual controller of electromechanical characteristics for static power converters*, WO2012117132A1, 2012.

[43] Remon, D., Cantarellas, A. M., Rakhshani, E., Candela, I., and Rodriguez, P.: *An active power synchronization control loop for grid-connected converters*. In *2014 IEEE PES General Meeting | Conference Exposition*, pages 1–5, July 2014.

[44] Rodriguez, P., Citro, C., Candela, J. I., Rocabert, J., and Luna, A.: *Flexible grid connection and islanding of SPC-based PV power converters*. IEEE Transactions on Industry Applications, 54(3):2690–2702, May 2018, ISSN 1939-9367.

[45] Ierna, Richard, Zhu, Jiebei, Roscoe, Andrew J., Yu, Mengran, Dysko, Adam, Booth, Campbell D., and Urdal, Helge: *Effects of VSM convertor control on penetration limits of non-synchronous generation in the GB power system*. In *15th Wind Integration Workshop*, November 2016.

[46] Roscoe, Andrew J, Yu, Mengran, Ierna, Richard, Zhu, Jiebei, Dyśko, Adam, Urdal, Helge, and Booth, Campbell: *A VSM (virtual synchronous machine) convertor control model suitable for RMS studies for resolving system operator/owner challenges*. In *15th Wind Integration Workshop*, November 2016.

[47] Tielens, P., De Rijcke, S., Srivastava, K., Reza, M., Marinopoulos, A., and Driesen, J.: *Frequency support by wind power plants in isolated grids with varying generation mix*. In *2012 IEEE Power and Energy Society General Meeting*, pages 1–8, July 2012.

[48] Gevorgian, V., Zhang, Y., and Ela, E.: *Investigating the impacts of wind generation participation in interconnection frequency response*. IEEE Transactions on Sustainable Energy, 6(3):1004–1012, July 2015, ISSN 1949-3037.

[49] Zhu, J., Guerrero, J. M., Hung, W., Booth, C. D., and Adam, G. P.: *Generic inertia emulation controller for multi-terminal voltage-source-converter high voltage direct current systems*. IET Renewable Power Generation, 8(7):740–748, Sep. 2014, ISSN 1752-1424.

[50] Yu, M., Roscoe, A. J., Booth, C. D., Dysko, A., Ierna, R., Zhu, J., Grid, N., and Urdal, H.: *Use of an inertia-less virtual synchronous machine within future power networks with high penetrations of converters*. In *2016 Power Systems Computation Conference (PSCC)*, pages 1–7, June 2016.

[51] Yu, M.: *Framework for assessing stability challenges in future converter-dominated power networks*. PhD thesis, Dept. of Electronic and Electrical Eng., Univ. of Strathclyde, UK, 2018.

[52] Zhang, L., Harnefors, L., and Nee, H.: *Power-synchronization control of grid-connected voltage-source converters*. IEEE Transactions on Power Systems, 25(2):809–820, May 2010, ISSN 1558-0679.

[53] Ersoy, O. K.: *A comparative review of real and complex fourier-related transforms*. Proceedings of the IEEE, 82(3):429–447, March 1994, ISSN 1558-2256.

[54] Hostetter, G.: *Recursive discrete fourier transformation*. IEEE Transactions on Acoustics, Speech, and Signal Processing, 28(2):184–190, April 1980, ISSN 0096-3518.

[55] Best, P. C. R. E.: *Phase-locked loops. Design, simulation and applications, 4th ed.* Harlow, New York: McGraw-Hill, 1999.

[56] Krause, P. C., Waysynczuk, O., and Sudhoff, S. D.: *Analysis of electric machinery and drive systems, 2nd Edition*. John Wiley and Sons, 2002.

[57] Santos Filho, R. M., Seixas, P. F., Cortizo, P. C., Torres, L. A. B., and Souza, A. F.: *Comparison of three single-phase PLL algorithms for UPS applications*. IEEE Transactions on Industrial Electronics, 55(8):2923–2932, Aug 2008, ISSN 1557-9948.

[58] Freijedo, F. D., Yepes, A. G., Lopez, O., Fernandez-Comesana, P., and Doval-Gandoy, J.: *An optimized implementation of phase locked loops for grid applications*. IEEE Transactions on Instrumentation and Measurement, 60(9):3110–3119, Sep. 2011, ISSN 1557-9662.

[59] Kaura, V. and Blasko, V.: *Operation of a phase locked loop system under distorted utility conditions*. IEEE Transactions on Industry Applications, 33(1):58–63, Jan 1997, ISSN 1939-9367.

[60] Se-Kyo Chung: *A phase tracking system for three phase utility interface inverters*. IEEE Transactions on Power Electronics, 15(3):431–438, May 2000, ISSN 1941-0107.

[61] Freijedo, F. D., Doval-Gandoy, J., Lopez, O., and Acha, E.: *Tuning of phase-locked loops for power converters under distorted utility conditions*. IEEE Transactions on Industry Applications, 45(6):2039–2047, Nov 2009, ISSN 1939-9367.

[62] Golestan, S., Monfared, M., Freijedo, F. D., and Guerrero, J. M.: *Design and tuning of a modified power-based PLL for single-phase grid-connected power conditioning systems*. IEEE Transactions on Power Electronics, 27(8):3639–3650, Aug 2012, ISSN 1941-0107.

[63] Golestan, S., Ramezani, M., Guerrero, J. M., and Monfared, M.: *dq-frame cascaded delayed signal cancellation-based PLL: Analysis, design, and comparison with moving average filter-based PLL*. IEEE Transactions on Power Electronics, 30(3):1618–1632, March 2015, ISSN 1941-0107.

[64] Rodriguez, P., Pou, J., Bergas, J., Candela, J. I., Burgos, R. P., and Boroyevich, D.: *Decoupled double synchronous reference frame PLL for power converters control*. IEEE Transactions on Power Electronics, 22(2):584–592, March 2007, ISSN 1941-0107.

[65] Awad, H., Svensson, J., and Bollen, M. J.: *Tuning software phase-locked loop for series-connected converters*. IEEE Transactions on Power Delivery, 20(1):300–308, Jan 2005, ISSN 1937-4208.

[66] Wen, B., Boroyevich, D., Burgos, R., Mattavelli, P., and Shen, Z.: *Analysis of D-Q small-signal impedance of grid-tied inverters*. IEEE Transactions on Power Electronics, 31(1):675–687, Jan 2016, ISSN 1941-0107.

[67] Schroeder, D.: *Elektrische Antriebe - Regelung von Antriebssystemen, 2nd ed.* Springer-Verlag, Germany, 2001.

[68] Harnefors, L., Bongiorno, M., and Lundberg, S.: *Input-admittance calculation and shaping for controlled voltage-source converters*. IEEE Transactions on Industrial Electronics, 54(6):3323–3334, Dec 2007, ISSN 1557-9948.

[69] Cespedes, M. and Sun, J.: *Impedance modeling and analysis of grid-connected voltage-source converters*. IEEE Transactions on Power Electronics, 29(3):1254–1261, March 2014, ISSN 1941-0107.

[70] Kimbark, E. Wilson: *Power system stability, Volume I: elements of stability calculations*. Wiley-IEEE Press, 1995.

[71] Chandorkar, M. C., Divan, D. M., and Adapa, R.: *Control of parallel connected inverters in standalone AC supply systems*. IEEE Transactions on Industry Applications, 29(1):136–143, Jan 1993, ISSN 1939-9367.

[72] D'Arco, S. and Suul, J. A.: *Equivalence of virtual synchronous machines and frequency-droops for converter-based microgrids*. IEEE Transactions on Smart Grid, 5(1):394–395, Jan 2014, ISSN 1949-3061.

[73] Ndreko, Mario, Rueberg, Sven, and Winter, Wilhelm: *Grid forming control for stable power systems with up to 100 % inverter based generation: A paradigm scenario using the IEEE 118-bus system*. In *17th international workshop on large-scale integration of wind power into power system (LSI), Sweden*, October 2018.

[74] Ndreko, M., Rueberg, S., and Winter, W.: *Grid forming control scheme for power systems with up to 100% power electronic interfaced generation: a case study on Great Britain test system*. IET Renewable Power Generation, 14(8):1268–1281, 2020, ISSN 1752-1424.

[75] Noguchi, T., Tomiki, H., Kondo, S., and Takahashi, I.: *Direct power control of PWM converter without power-source voltage sensors*. IEEE Transactions on Industry Applications, 34(3):473–479, May 1998, ISSN 1939-9367.

[76] Zhi, D., Xu, L., and Williams, B. W.: *Improved direct power control of grid-connected DC/AC converters*. IEEE Transactions on Power Electronics, 24(5):1280–1292, May 2009, ISSN 1941-0107.

[77] A. E. Fitzgerald, C. Kingsley Jr., S. D. Umans: *Electric machinery, sixth edition*. McGraw-Hill, 2003.

[78] Dong, S. and Chen, Y. C.: *A method to directly compute synchronverter parameters for desired dynamic response*. IEEE Transactions on Energy Conversion, 33(2):814–825, June 2018, ISSN 1558-0059.

[79] Roldan-Perez, J., Rodriguez-Cabero, A., and Prodanovic, M.: *Design and analysis of virtual synchronous machines in inductive and resistive weak grids*. IEEE Transactions on Energy Conversion, 34(4):1818–1828, Dec 2019, ISSN 1558-0059.

[80] Dong, S. and Chen, Y. C.: *Adjusting synchronverter dynamic response speed via damping correction loop*. IEEE Transactions on Energy Conversion, 32(2):608–619, June 2017, ISSN 1558-0059.

[81] Zhang, W., Cantarellas, A. M., Rocabert, J., Luna, A., and Rodriguez, P.: *Synchronous power controller with flexible droop characteristics for renewable power generation systems*. IEEE Transactions on Sustainable Energy, 7(4):1572–1582, Oct 2016, ISSN 1949-3037.

[82] Li, C., Burgos, R., Cvetkovic, I., Boroyevich, D., Mili, L., and Rodriguez, P.: *Analysis and design of virtual synchronous machine based STATCOM controller*. In *2014 IEEE 15th Workshop on Control and Modeling for Power Electronics (COMPEL)*, pages 1–6, June 2014.

[83] Ooi, B. T. and Wang, X.: *Voltage angle lock loop control of the boost type PWM converter for HVDC application*. IEEE Transactions on Power Electronics, 5(2):229–235, April 1990, ISSN 1941-0107.

[84] Li, Z., Li, Y., Wang, P., Zhu, H., Liu, C., and Gao, F.: *Single-loop digital control of high-power 400-Hz ground power unit for airplanes*. IEEE Transactions on Industrial Electronics, 57(2):532–543, Feb 2010, ISSN 1557-9948.

[85] Wang, X., Loh, P. C., and Blaabjerg, F.: *Stability analysis and controller synthesis for single-loop voltage-controlled VSIs*. IEEE Transactions on Power Electronics, 32(9):7394–7404, Sep. 2017, ISSN 1941-0107.

[86] Liao, Y. and Wang, X.: *Evaluation of voltage regulators for dual-loop control of voltage-controlled VSCs*. In *2019 IEEE Energy Conversion Congress and Exposition (ECCE)*, pages 5036–5042, Sep. 2019.

[87] Liao, Y., Wang, X., and Blaabjerg, F.: *Passivity-based analysis and design of linear voltage controllers for voltage-source converters*. IEEE Open Journal of the Industrial Electronics Society, 1:114–126, 2020, ISSN 2644-1284.

[88] Poh Chiang Loh and Holmes, D. G.: *Analysis of multiloop control strategies for LC/CL/LCL-filtered voltage-source and current-source inverters*. IEEE Transactions on Industry Applications, 41(2):644–654, March 2005, ISSN 1939-9367.

[89] Geng, Y., Yun, Y., Chen, R., Wang, K., Bai, H., and Wu, X.: *Parameters design and optimization for LC-type off-grid inverters with inductor-current feedback active damping*. IEEE Transactions on Power Electronics, 33(1):703–715, Jan 2018, ISSN 1941-0107.

[90] He, J. and Li, Y. W.: *Analysis, design, and implementation of virtual impedance for power electronics interfaced distributed generation*. IEEE Transactions on Industry Applications, 47(6):2525–2538, Nov 2011, ISSN 1939-9367.

[91] He, J., Li, Y. W., and Munir, M. S.: *A flexible harmonic control approach through voltage-controlled DG - grid interfacing converters*. IEEE Transactions on Industrial Electronics, 59(1):444–455, Jan 2012, ISSN 1557-9948.

[92] Guerrero, J. M., Luis Garcia de Vicuna, Matas, J., Castilla, M., and Miret, J.: *Output impedance design of parallel-connected UPS inverters with wireless load-sharing control*. IEEE Transactions on Industrial Electronics, 52(4):1126–1135, Aug 2005, ISSN 1557-9948.

[93] Paquette, A. D. and Divan, D. M.: *Virtual impedance current limiting for inverters in microgrids with synchronous generators*. IEEE Transactions on Industry Applications, 51(2):1630–1638, March 2015, ISSN 1939-9367.

[94] Wang, X., Li, Y. W., Blaabjerg, F., and Loh, P. C.: *Virtual-impedance-based control for voltage-source and current-source converters*. IEEE Transactions on Power Electronics, 30(12):7019–7037, Dec 2015, ISSN 1941-0107.

[95] Harnefors, L., Zhang, L., and Bongiorno, M.: *Frequency-domain passivity-based current controller design*. IET Power Electronics, 1(4):455–465, December 2008, ISSN 1755-4535.

[96] Harnefors, L., Wang, X., Yepes, A. G., and Blaabjerg, F.: *Passivity-based stability assessment of grid-connected VSCs - an overview*. IEEE Journal of Emerging and Selected Topics in Power Electronics, 4(1):116–125, March 2016, ISSN 2168-6785.

[97] Tarraso, A., Candela, J. I., Rocabert, J., and Rodriguez, P.: *Grid voltage harmonic damping method for SPC based power converters with multiple virtual admittance control*. In *2017 IEEE Energy Conversion Congress and Exposition (ECCE)*, pages 64–68, Oct 2017.

[98] Wu, H., Ruan, X., Yang, D., Chen, X., Zhao, W., Lv, Z., and Zhong, Q.: *Small-signal modeling and parameters design for virtual synchronous generators*. IEEE Transactions on Industrial Electronics, 63(7):4292–4303, July 2016, ISSN 1557-9948.

[99] Natarajan, V. and Weiss, G.: *Synchronverters with better stability due to virtual inductors, virtual capacitors, and anti-windup*. IEEE Transactions on Industrial Electronics, 64(7):5994–6004, July 2017, ISSN 1557-9948.

[100] Morales, S. Pérez: *Optimal model reference control design for grid connected voltage source converters*. PhD thesis, University of Alcalá, Spain, 2017.

[101] Pérez, J., Cóbreces, S., Pizarro, D., Rodríguez Sánchez, F. J., and Griñó, R.: *Resonance damping of LCL filters via input admittance frequency shaping*. In *2016 IEEE 25th International Symposium on Industrial Electronics (ISIE)*, pages 516–521, June 2016.

[102] Pérez, J., Cóbreces, S., Griñó, R., and Rodríguez Sánchez, F. J.: *$\mathcal{H}_\infty$ current controller for input admittance shaping of VSC-based grid applications*. IEEE Transactions on Power Electronics, 32(4):3180–3191, April 2017, ISSN 1941-0107.

[103] Skogasted, S. and Postlethwaite, I.: *Multivariable feedback control, analysis and design*. John Wiley and Sons, 2001.

[104] Johnson, B. B., Sinha, M., Ainsworth, N. G., Dörfler, F., and Dhople, V.: *Synthesizing virtual oscillators to control islanded inverters*. IEEE Transactions on Power Electronics, 31(8):6002–6015, Aug 2016.

[105] Sinha, M., Dörfler, F., Johnson, B. B., and Dhople, V.: *Uncovering droop control laws embedded within the nonlinear dynamics of van der pol oscillators*. IEEE Transactions on Control of Network Systems, 4(2):347–358, Jun 2017.

[106] Shi, Z., Li, J., Nurdin, H. I., and Fletscher, J. E.: *Comparison of virtual oscillator and droop controlled islanded three-phase microgrids*. IEEE Transactions on Energy Conversion, 34(4):1769–1780, Dec 2019.

[107] Colombino, M., Groβ, D., Brouillon, J., and Dörfler, F.: *Global phase and magnitude synchronization of coupled oscillators with application to the control of grid-forming power inverters*. IEEE Transactions on Automatic Control, 64(11):4496–4511, Nov 2019.

[108] Seo, G., Colombino, M., Subotic, I., Johnson, B., Groβ, D., and Dörfler, F.: *Dispatchable virtual oscillator control for decentralized inverter-dominated power systems: analysis and experiments*. In *2019 IEEE Applied Power Electronics Conference and Exposition (APEC)*, pages 561–566, 2019.

[109] Raisz, D., Thai, T. T., and Monti, A.: *Power control of virtual oscillator controlled inverters in grid-connected mode*. IEEE Transactions on Power Electronics, 34(6):5916–5926, Jun 2019.

[110] Lu, M., Dutta, S., Purba, V., , Dhople, S., and Johnson, B. B.: *A grid-compatible virtual oscillator controller: Analysis and design*. In *2019 IEEE Energy Conversion Congress and Exposition (ECCE)*, pages 2643–2649, 2019.

[111] Kundur, P. *et al.*: *Definition and classification of power system stability IEEE/CIGRE joint task force on stability terms and definitions*. IEEE Transactions on Power Systems, 19(3):1387–1401, Aug 2004, ISSN 1558-0679.

[112] J-J. E. Slotine, W. Li: *Applied nonlinear control*. Prentice Hall, Inc., 1991.

[113] Crary, S. B., Herlitz, I., and Favez, B.: *System stability and voltage, power and frequency control*. Technical report, CIGRE SC32 Report, Appendix 1, Rep. 347, 1948.

[114] *Proposed terms definitions for power system stability*. IEEE Transactions on Power Apparatus and Systems, PAS-101(7):1894–1898, July 1982, ISSN 0018-9510.

[115] Wang, X. and Blaabjerg, F.: *Harmonic stability in power electronic-based power systems: concept, modeling, and analysis*. IEEE Transactions on Smart Grid, 10(3):2858–2870, May 2019, ISSN 1949-3061.

[116] Wang, X., Blaabjerg, F., Chen, Z., and Wu, W.: *Modeling and analysis of harmonic resonance in a power electronics based AC power system*. In *2013 IEEE Energy Conversion Congress and Exposition*, pages 5229–5236, Sep. 2013.

[117] Wang, X., Blaabjerg, F., and Wu, W.: *Modeling and analysis of harmonic stability in an AC power-electronics-based power system*. IEEE Transactions on Power Electronics, 29(12):6421–6432, Dec 2014, ISSN 1941-0107.

[118] Wen, B., Boroyevich, D., Mattavelli, P., Shen, Z., and Burgos, R.: *Influence of phase-locked loop on input admittance of three-phase voltage-source converters*. In *2013 Twenty-Eighth Annual IEEE Applied Power Electronics Conference and Exposition (APEC)*, pages 897–904, March 2013.

[119] Zou, Z., Buticchi, G., Liserre, M., Kettner, A. M., and Paolone, M.: *Voltage stability analysis using a complete model of grid-connected voltage-source converters*. In *2016 IEEE Energy Conversion Congress and Exposition (ECCE)*, pages 1–8, Sep. 2016.

[120] Khalil, H. K.: *Nonlinear systems*. 2nd edition, Prentice Hall, Inc., 1996.

[121] Middlebrook, R. D.: *Input filter consideration in design and application of switching regulators*. In *IEEE Industry Application Society Annual Meeting*, pages 336–382, 1976.

[122] Sun, J.: *Impedance-based stability criterion for grid-connected inverters*. IEEE Transactions on Power Electronics, 26(11):3075–3078, Nov 2011, ISSN 1941-0107.

[123] Wen, B., Boroyevich, D., Burgos, R., Mattavelli, P., and Shen, Z.: *Small-signal stability analysis of three-phase AC systems in the presence of constant power loads based on measured d-q frame impedances*. IEEE Transactions on Power Electronics, 30(10):5952–5963, Oct 2015, ISSN 1941-0107.

[124] Lyu, J., Cai, X., and Molinas, M.: *Frequency domain stability analysis of MMC-based HVDC for wind farm integration*. IEEE Journal of Emerging and Selected Topics in Power Electronics, 4(1):141–151, March 2016, ISSN 2168-6785.

[125] Wang, X., Harnefors, L., Blaabjerg, F., and Loh, P. C.: *A unified impedance model of voltage-source converters with phase-locked loop effect*. In *2016 IEEE Energy Conversion Congress and Exposition (ECCE)*, pages 1–8, Sep. 2016.

[126] Wang, X., Harnefors, L., and Blaabjerg, F.: *Unified impedance model of grid-connected voltage-source converters*. IEEE Transactions on Power Electronics, 33(2):1775–1787, Feb 2018, ISSN 1941-0107.

[127] Harnefors, L.: *Modeling of three-phase dynamic systems using complex transfer functions and transfer matrices*. IEEE Transactions on Industrial Electronics, 54(4):2239–2248, Aug 2007, ISSN 1557-9948.

[128] MacFarlane, A. G. J.: *Complex variable methods for linear multivariable feedback systems*. Taylor and Francis Ltd, 1980.

[129] Maciejowski, J. M.: *Multivariable feedback design*. Addison-Wesley, 1989.

[130] Belkhayat, M.: *Stability criteria for AC power systems with regulated loads*. PhD thesis, Electrical Engineering, Purdue University, West Lafayette, 1997.

[131] Jessen, L., Zou, Z., Benkendorff, B., Liserre, M., and Fuchs, F. W.: *Resonance identification and damping in AC-grids by means of multi MW grid converters*. In *IECON 2016 - 42nd Annual Conference of the IEEE Industrial Electronics Society*, pages 3762–3768, Oct 2016.

[132] Luhtala, R., Roinila, T., and Messo, T.: *Implementation of real-time impedance-based stability assessment of grid-connected systems using MIMO-identification techniques*. IEEE Transactions on Industry Applications, 54(5):5054–5063, Sep. 2018, ISSN 1939-9367.

[133] Gustavsen, B. and Semlyen, A.: *Rational approximation of frequency domain responses by vector fitting*. IEEE Transactions on Power Delivery, 14(3):1052–1061, July 1999, ISSN 1937-4208.

[134] Zou, Z., Buticchi, G., and Liserre, M.: *Grid identification and adaptive voltage control in a smart transformer-fed grid*. IEEE Transactions on Power Electronics, 34(3):2327–2338, March 2019, ISSN 1941-0107.

[135] Alghassi, A., Perinpanayagam, S., Samie, M., and Sreenuch, T.: *Computationally efficient, real-time, and embeddable prognostic techniques for power electronics*. IEEE Transactions on Power Electronics, 30(5):2623–2634, May 2015, ISSN 1941-0107.

[136] Kim, K. A., Shenoy, P. S., and Krein, P. T.: *Converter rating analysis for photovoltaic differential power processing systems*. IEEE Transactions on Power Electronics, 30(4):1987–1997, April 2015, ISSN 1941-0107.

[137] Jedtberg, H., Pigazo, A., Liserre, M., and Buticchi, G.: *Analysis of the robustness of transformerless PV inverter topologies to the choice of power devices*. IEEE Transactions on Power Electronics, 32(7):5248–5257, July 2017, ISSN 1941-0107.

[138] Reigosa, P. D., Wang, H., Yang, Y., and Blaabjerg, F.: *Prediction of bond wire fatigue of IGBTs in a PV inverter under a long-term operation*. IEEE Transactions on Power Electronics, 31(10):7171–7182, Oct 2016, ISSN 1941-0107.

[139] Li, W.: *Risk assessment of power systems: models, methods, and applications*. Piscatawey, Wiley-IEEE Press, 2005.

[140] Zhou, K. and Doyle, J. C.: *Essentials of robust control*. Prentice Hall, Inc., 1999.

[141] Zhou, K., Doyle, J. C., and Glover, K.: *Robust and optimal control*. Prentice Hall, Inc., 1996.

[142] Perez-Arriaga, I. J., Verghese, G. C., and Schweppe, F. C.: *Selective modal analysis with applications to electric power systems, part I: heuristic introduction*. IEEE Transactions on Power Apparatus and Systems, PAS-101(9):3117–3125, Sep. 1982, ISSN 0018-9510.

[143] Pal, B. and Chaunduri, B.: *Robust control in power systems*. Springer, 2005.

[144] Feliachi, A.: *Identification of critical modes in power systems*. IEEE Transactions on Power Systems, 5(3):783–788, Aug 1990, ISSN 1558-0679.

[145] Pagola, F. L., Perez-Arriaga, I. J., and Verghese, G. C.: *On sensitivities, residues and participations: applications to oscillatory stability analysis and control*. IEEE Transactions on Power Systems, 4(1):278–285, Feb 1989, ISSN 1558-0679.

[146] Larsen, E. V., Sanchez-Gasca, J. J., and Chow, J. H.: *Concepts for design of FACTS controllers to damp power swings*. IEEE Transactions on Power Systems, 10(2):948–956, May 1995, ISSN 1558-0679.

[147] Rouco, L. and Pagola, F. L.: *An eigenvalue sensitivity approach to location and controller design of controllable series capacitors for damping power system oscillations*. IEEE Transactions on Power Systems, 12(4):1660–1666, Nov 1997, ISSN 1558-0679.

[148] Sun, Ji guang: *Multiple eigenvalue sensitivity analysis*. Linear Algebra and its Applications, 137-138:183 – 211, 1990, ISSN 0024-3795. http://www.sciencedirect.com/science/article/pii/002437959090129Z.

[149] Lefebvre, S.: *Decentralized control of multiterminal HVDC systems embedded in AC networks*. PhD thesis, Electrical Engineering, Purdue University, West Lafayette, 1980.

[150] Gaba, G., Lefebvre, S., and Mukhedkar, D.: *Comparative analysis and study of the dynamic stability of AC/DC systems*. IEEE Transactions on Power Systems, 3(3):978–985, Aug 1988, ISSN 1558-0679.

[151] Wang, Y., Wang, X., Chen, Z., and Blaabjerg, F.: *Small-signal stability analysis of inverter-fed power systems using component connection method*. IEEE Transactions on Smart Grid, 9(5):5301–5310, Sep. 2018, ISSN 1949-3061.

[152] Bakhshizadeh, M. K., Yoon, C., Hjerrild, J., Bak, C. L., Kocewiak, Ł. H., Blaabjerg, F., and Hesselbaek, B.: *The application of vector fitting to eigenvalue-based harmonic stability analysis*. IEEE Journal of Emerging and Selected Topics in Power Electronics, 5(4):1487–1498, Dec. 2017, ISSN 2168-6785.

[153] Bequette, B. W.: *Process control: modeling, design and simulation*. Prentice Hall, Inc., 2002.

[154] Doyle, J. C., Wall, J. E., and Stein, G.: *Performance and robustness analysis for structured uncertainty*. In *1982 21st IEEE Conference on Decision and Control*, pages 629–636, Dec 1982.

[155] Sumsurooah, S., Odavic, M., and Bozhko, S.: *μ approach to robust stability domains in the space of parametric uncertainties for a power system with ideal CPL*. IEEE Transactions on Power Electronics, 33(1):833–844, Jan 2018, ISSN 1941-0107.

[156] Sumsurooah, S., Odavic, M., Bozhko, S., and Boroyevic, D.: *Toward robust stability of aircraft electrical power systems: Using a μ-based structural singular value to analyze and ensure network stability*. IEEE Electrification Magazine, 5(4):62–71, Dec 2017, ISSN 2325-5889.

[157] Balas, G. J., Doyle, J. C., Glover, K., Packard, A., and Smith, R.: *μ-analysis synthesis toolbox, version 3, User Manual*. MathWorks, 1998.

[158] Kwon, J. B., Wang, X., Blaabjerg, F., Bak, C. L., Wood, A. R., and Watson, N. R.: *Harmonic instability analysis of a single-phase grid-connected converter using a harmonic state-space modeling method*. IEEE Transactions on Industry Applications, 52(5):4188–4200, Sep. 2016, ISSN 1939-9367.

[159] De Carne, G., Langwasser, M., Ndreko, M., Bachmann, R., De Doncker, R. W., Dimitrovski, R., Mortimer, B. J., Neufeld, A., Rojas, F., and Liserre, M.: *Which deepness class is suited for modeling power electronics?: A guide for choosing the right model for grid-integration studies*. IEEE Industrial Electronics Magazine, 13(2):41–55, June 2019, ISSN 1941-0115.

[160] Wen, B., Dong, D., Boroyevich, D., Burgos, R., Mattavelli, P., and Shen, Z.: *Impedance-based analysis of grid-synchronization stability for three-phase paralleled converters*. IEEE Transactions on Power Electronics, 31(1):26–38, Jan 2016, ISSN 1941-0107.

[161] Wu, W., Zhou, L., Chen, Y., Luo, A., Dong, Y., Zhou, X., Xu, Q., Yang, L., and Guerrero, J. M.: *Sequence-impedance-based stability comparison between VSGs and traditional grid-connected inverters*. IEEE Transactions on Power Electronics, 34(1):46–52, Jan 2019, ISSN 1941-0107.

[162] Zhou, J. Z., Ding, H., Fan, S., Zhang, Y., and Gole, A. M.: *Impact of short-circuit ratio and phase-locked-loop parameters on the small-signal behavior of a VSC-HVDC converter*. IEEE Transactions on Power Delivery, 29(5):2287–2296, Oct 2014, ISSN 1937-4208.

[163] Buticchi, G., De Carne, G., Barater, D., Zou, Z., and Liserre, M.: *Analysis of the frequency-based control of a master/slave micro-grid*. IET Renewable Power Generation, 10(10):1570–1576, 2016, ISSN 1752-1424.

[164] Wu, H. and Wang, X.: *Design-oriented transient stability analysis of PLL-synchronized voltage-source converters*. IEEE Transactions on Power Electronics, 35(4):3573–3589, April 2020, ISSN 1941-0107.

[165] Trevisan, A. S., El-Deib, A. A., Gagnon, R., Mahseredjian, J., and Fecteau, M.: *Field validated generic EMT-type model of a full converter wind turbine based on a gearless externally excited synchronous generator*. IEEE Transactions on Power Delivery, 33(5):2284–2293, Oct 2018, ISSN 1937-4208.

[166] Wang, X., Blaabjerg, F., Liserre, M., Chen, Z., He, J., and Li, Y.: *An active damper for stabilizing power-electronics-based AC systems*. IEEE Transactions on Power Electronics, 29(7):3318–3329, July 2014, ISSN 1941-0107.

[167] Hiti, S., Vlatkovic, V., Borojevic, D., and Lee, F. C. Y.: *A new control algorithm for three-phase PWM buck rectifier with input displacement factor compensation*. IEEE Transactions on Power Electronics, 9(2):173–180, March 1994, ISSN 1941-0107.

[168] Hengchun Mao, Boroyevich, D., and Lee, F. C. Y.: *Novel reduced-order small-signal model of a three-phase PWM rectifier and its application in control design and system analysis*. IEEE Transactions on Power Electronics, 13(3):511–521, May 1998, ISSN 1941-0107.

[169] Liu, Z., Liu, J., Bao, W., and Zhao, Y.: *Infinity-norm of impedance-based stability criterion for three-phase AC distributed power systems with constant power loads*. IEEE Transactions on Power Electronics, 30(6):3030–3043, June 2015, ISSN 1941-0107.

[170] Bowes, S. R., Grewal, S., and Holliday, D.: *Novel adaptive hysteresis band modulation strategy for three-phase inverters*. IEE Proceedings - Electric Power Applications, 148(1):51–61, Jan 2001, ISSN 1350-2352.

[171] Young, K. D., Utkin, V. I., and Ozguner, U.: *A control engineer's guide to sliding mode control.* IEEE Transactions on Control Systems Technology, 7(3):328–342, May 1999, ISSN 1558-0865.

[172] Rodriguez, J.: *Predictive control of power converters and electric drives.* Piscatawey, Wiley-IEEE Press, 2012.

[173] Geyer, T.: *Model predictive control of high power converters and industrial drives.* John Wiley and Sons, 2017.

[174] V. Yaramasu, B. Wu: *Model predictive control of wind energy conversion systems.* John Wiley and Sons, 2017.

[175] Zhou Wei, Chen Jie, and Gong Chunying: *Small signal modeling and analysis of synchronverters.* In *2015 IEEE 2nd International Future Energy Electronics Conference (IFEEC)*, pages 1–5, Nov 2015.

[176] Amin, M., Rygg, A., and Molinas, M.: *Self-synchronization of wind farm in an MMC-based HVDC system: a stability investigation.* IEEE Transactions on Energy Conversion, 32(2):458–470, June 2017, ISSN 1558-0059.

[177] Aouini, R., Marinescu, B., Ben Kilani, K., and Elleuch, M.: *Synchronverter-based emulation and control of HVDC transmission.* IEEE Transactions on Power Systems, 31(1):278–286, Jan 2016, ISSN 1558-0679.

[178] Unamuno, E., Rygg, A., Amin, M., Molinas, M., and Barrena, J. A.: *Impedance-based stability evaluation of virtual synchronous machine implementations in converter controllers.* In *2018 International Power Electronics Conference (IPEC-Niigata 2018 -ECCE Asia)*, pages 759–766, May 2018.

[179] Liserre, M., Blaabjerg, F., and Hansen, S.: *Design and control of an LCL-filter-based three-phase active rectifier.* IEEE Transactions on Industry Applications, 41(5):1281–1291, Sep. 2005, ISSN 1939-9367.

[180] Shuai, Z., Hu, Y., Peng, Y., Tu, C., and Shen, Z. J.: *Dynamic stability analysis of synchronverter-dominated microgrid based on bifurcation theory.* IEEE Transactions on Industrial Electronics, 64(9):7467–7477, Sep. 2017, ISSN 1557-9948.

[181] Hou, P., Ebrahimzadeh, E., Wang, X., Blaabjerg, F., Fang, J., and Wang, Y.: *Harmonic stability analysis of offshore wind farm with component connection method.* In *IECON 2017 - 43rd Annual Conference of the IEEE Industrial Electronics Society*, pages 4926–4932, Oct 2017.

[182] Crow, Mariesa L.: *Computational methods for electric power systems, 2nd ed.* CRC Press, 2010.

[183] Hashlamoun, W. A., Hassouneh, M. A., and Abed, E. H.: *New results on modal participation factors: revealing a previously unknown dichotomy.* IEEE Transactions on Automatic Control, 54(7):1439–1449, July 2009, ISSN 1558-2523.

[184] Ganjian-Aboukheili, M., Shahabi, M., Shafiee, Q., and Guerrero, J. M.: *Seamless transition of microgrids operation from grid-connected to islanded mode*. IEEE Transactions on Smart Grid, 11(3):2106–2114, May 2020, ISSN 1949-3061.

[185] Du, Y., Lu, X., Wang, J., and Lukic, S.: *Distributed secondary control strategy for microgrid operation with dynamic boundaries*. IEEE Transactions on Smart Grid, 10(5):5269–5282, Sep. 2019, ISSN 1949-3061.

[186] Vandoorn, T. L., Meersman, B., De Kooning, J. D. M., and Vandevelde, L.: *Transition from islanded to grid-connected mode of microgrids with voltage-based droop control*. IEEE Transactions on Power Systems, 28(3):2545–2553, Aug 2013, ISSN 1558-0679.

[187] Lissandron, S. and Mattavelli, P.: *A controller for the smooth transition from grid-connected to autonomous operation mode*. In *2014 IEEE Energy Conversion Congress and Exposition (ECCE)*, pages 4298–4305, Sep. 2014.

[188] Guerrero, J. M., Vasquez, J. C., Matas, J., de Vicuna, L. G., and Castilla, M.: *Hierarchical control of droop-controlled AC and DC microgrids - a general approach toward standardization*. IEEE Transactions on Industrial Electronics, 58(1):158–172, Jan 2011, ISSN 1557-9948.

[189] Sharma, S., Pushpak, S., Chinde, V., and Dobson, I.: *Sensitivity of transient stability critical clearing time*. IEEE Transactions on Power Systems, 33(6):6476–6486, Nov 2018, ISSN 1558-0679.

[190] ENTSO-E: *Determining generator fault clearing time for the synchronous zone of continental europee*. Technical report, ENTSO-E, 2017.

[191] *VDE-Technische Regeln für den Anschluss von Kundenanlagen an das Hochspannungsnetz und deren Betrieb (TAR Hochspannung), VDE-AR-N4120*. Standard, VDE, 2018.

[192] Kimbark, E. Wilson: *Power system stability, Volume III: synchronous machines*. Wiley-IEEE Press, 1995.

[193] Valdes, M. E. and Dougherty, J. J.: *Advances in protective device interlocking for improved protection and selectivity*. IEEE Transactions on Industry Applications, 50(3):1639–1648, May 2014, ISSN 1939-9367.

[194] Lin, H., Jia, C., Guerrero, J. M., and Vasquez, J. C.: *Angle stability analysis for voltage-controlled converters*. IEEE Transactions on Industrial Electronics, 64(8):6265–6275, Aug 2017, ISSN 1557-9948.

[195] Wu, H. and Wang, X.: *Transient angle stability analysis of grid-connected converters with the first-order active power loop*. In *2018 IEEE Applied Power Electronics Conference and Exposition (APEC)*, pages 3011–3016, March 2018.

[196] Wu, H. and Wang, X.: *Design-oriented transient stability analysis of grid-connected converters with power synchronization control*. IEEE Transactions on Industrial Electronics, 66(8):6473–6482, Aug 2019, ISSN 1557-9948.

[197] Shuai, Z., Shen, C., Liu, X., Li, Z., and Shen, Z. J.: *Transient angle stability of virtual synchronous generators using Lyapunov's direct method*. IEEE Transactions on Smart Grid, 10(4):4648–4661, July 2019, ISSN 1949-3061.

[198] Qi, C., Wang, K., and Li, G.: *Parameter space and rotor angle stability control of virtual synchronous machine*. In *2018 IEEE Power Energy Society General Meeting (PESGM)*, pages 1–5, Aug 2018.

[199] Qoria, T., Gruson, F., Colas, F., Denis, G., Prevost, T., and Guillaud, X.: *Critical clearing time determination and enhancement of grid-forming converters embedding virtual impedance as current limitation algorithm*. IEEE Journal of Emerging and Selected Topics in Power Electronics, 8(2):1050–1061, June 2020, ISSN 2168-6785.

[200] Xin, H., Huang, L., Zhang, L., Wang, Z., and Hu, J.: *Synchronous instability mechanism of P-f droop-controlled voltage source converter caused by current saturation*. IEEE Transactions on Power Systems, 31(6):5206–5207, Nov 2016, ISSN 1558-0679.

[201] Huang, L., Xin, H., Wang, Z., Zhang, L., Wu, K., and Hu, J.: *Transient stability analysis and control design of droop-controlled voltage source converters considering current limitation*. IEEE Transactions on Smart Grid, 10(1):578–591, Jan 2019, ISSN 1949-3061.

[202] Taul, M. G., Wang, X., Davari, P., and Blaabjerg, F.: *Current limiting control with enhanced dynamics of grid-forming converters during fault conditions*. IEEE Journal of Emerging and Selected Topics in Power Electronics, 8(2):1062–1073, June 2020, ISSN 2168-6785.

[203] Zamani, M. A., Yazdani, A., and Sidhu, T. S.: *A control strategy for enhanced operation of inverter-based microgrids under transient disturbances and network faults*. IEEE Transactions on Power Delivery, 27(4):1737–1747, Oct 2012, ISSN 1937-4208.

[204] Bottrell, N. and Green, T. C.: *Comparison of current-limiting strategies during fault ride-through of inverters to prevent latch-up and wind-up*. IEEE Transactions on Power Electronics, 29(7):3786–3797, July 2014, ISSN 1941-0107.

[205] Du, W., Lasseter, R. H., and Khalsa, A. S.: *Survivability of autonomous microgrid during overload events*. IEEE Transactions on Smart Grid, 10(4):3515–3524, July 2019, ISSN 1949-3061.

[206] He, J. and Li, Y. W.: *Analysis, design, and implementation of virtual impedance for power electronics interfaced distributed generation*. IEEE Transactions on Industry Applications, 47(6):2525–2538, Nov 2011, ISSN 1939-9367.

[207] Wang, X., Li, Y. W., Blaabjerg, F., and Loh, P. C.: *Virtual-impedance-based control for voltage-source and current-source converters*. IEEE Transactions on Power Electronics, 30(12):7019–7037, Dec 2015, ISSN 1941-0107.

[208] Alipoor, J., Miura, Y., and Ise, T.: *Voltage sag ride-through performance of virtual synchronous generator*. In *2014 International Power Electronics Conference (IPEC-Hiroshima 2014 - ECCE ASIA)*, pages 3298–3305, May 2014.

[209] Zhong, Q., Konstantopoulos, G. C., Ren, B., and Krstic, M.: *Improved synchronverters with bounded frequency and voltage for smart grid integration*. IEEE Transactions on Smart Grid, 9(2):786–796, March 2018, ISSN 1949-3061.

[210] Shuai, Z., Huang, W., Shen, C., Ge, J., and Shen, Z. J.: *Characteristics and restraining method of fast transient inrush fault currents in synchronverters*. IEEE Transactions on Industrial Electronics, 64(9):7487–7497, Sep. 2017, ISSN 1557-9948.

[211] He, L., Shuai, Z., Zhang, X., Liu, X., Li, Z., and Shen, Z. J.: *Transient characteristics of synchronverters subjected to asymmetric faults*. IEEE Transactions on Power Delivery, 34(3):1171–1183, June 2019, ISSN 1937-4208.

[212] Piya, P., Ebrahimi, M., Karimi-Ghartemani, M., and Khajehoddin, S. A.: *Fault ride-through capability of voltage-controlled inverters*. IEEE Transactions on Industrial Electronics, 65(10):7933–7943, Oct 2018, ISSN 1557-9948.

[213] Zheng, T., Chen, L., Guo, Y., and Mei, S.: *Comprehensive control strategy of virtual synchronous generator under unbalanced voltage conditions*. IET Generation, Transmission Distribution, 12(7):1621–1630, 2018, ISSN 1751-8695.

[214] Zarei, S. F., Mokhtari, H., Ghasemi, M. A., and Blaabjerg, F.: *Reinforcing fault ride through capability of grid forming voltage source converters using an enhanced voltage control scheme*. IEEE Transactions on Power Delivery, 34(5):1827–1842, Oct 2019, ISSN 1937-4208.

[215] Ierna, R., Pholboon, S., Sumner, M., and Li, C.: *VSM (virtual synchronous machine) control system design, implementation, performance, models and possible implications for grid codes*. In *18th international workshop on large-scale integration of wind power into power system (LSI), Dublin*, October 2019.

[216] *IEEE guide for identification, testing, and evaluation of the dynamic performance of excitation control systems*. IEEE Std 421.2-1990, pages 1–44, Aug 1990.

[217] Wang, H., Davari, P., Kumar, D., Zare, F., and Blaabjerg, F.: *The impact of grid unbalances on the reliability of DC-link capacitors in a motor drive*. In *2017 IEEE Energy Conversion Congress and Exposition (ECCE)*, pages 4345–4350, Oct 2017.

[218] Wang, H., Davari, P., Wang, H., Kumar, D., Zare, F., and Blaabjerg, F.: *Lifetime estimation of DC-link capacitors in adjustable speed drives under grid voltage unbalances*. IEEE Transactions on Power Electronics, 34(5):4064–4078, May 2019, ISSN 1941-0107.

[219] Brown, R. Groven: *An introduction to random signal analysis and Kalman filtering*. John Wiley and Sons, 1983.

[220] Rodriguez, P., Luna, A., Ciobotaru, M., Teodorescu, R., and Blaabjerg, F.: *Advanced grid synchronization system for power converters under unbalanced and distorted operating conditions*. In *IECON 2006 - 32nd Annual Conference on IEEE Industrial Electronics*, pages 5173–5178, Nov 2006.

[221] Sharifabadi, K., Harnefors, L., Nee, H., Norrga, S., and Teodorescu, R.: *Design, control, and application of modular multilevel converters for HVDC transmission systems*. John Wiley and Sons, 2016.

[222] Camacho, A., Castilla, M., Miret, J., Borrell, A., and de Vicuna, L. G.: *Active and reactive power strategies with peak current limitation for distributed generation inverters during unbalanced grid faults*. IEEE Transactions on Industrial Electronics, 62(3):1515–1525, March 2015, ISSN 1557-9948.

[223] Yin, Z., Gao, F., Zhang, Y., Du, C., Li, G., and Sun, X.: *A review of nonlinear Kalman filter appling to sensorless control for AC motor drives*. CES Transactions on Electrical Machines and Systems, 3(4):351–362, Dec 2019, ISSN 2096-3564.

[224] Bolognani, S., Tubiana, L., and Zigliotto, M.: *EKF-based sensorless IPM synchronous motor drive for flux-weakening applications*. IEEE Transactions on Industry Applications, 39(3):768–775, May 2003, ISSN 1939-9367.

[225] Quang, N. K., Hieu, N. T., and Ha, Q. P.: *FPGA-based sensorless PMSM speed control using reduced-order extended Kalman filters*. IEEE Transactions on Industrial Electronics, 61(12):6574–6582, Dec 2014, ISSN 1557-9948.

[226] Wang, Z., Zheng, Y., Zou, Z., and Cheng, M.: *Position sensorless control of interleaved CSI fed PMSM drive with extended Kalman filter*. IEEE Transactions on Magnetics, 48(11):3688–3691, Nov 2012, ISSN 1941-0069.

[227] Hoffmann, N. and Fuchs, F. W.: *Minimal invasive equivalent grid impedance estimation in inductive-resistive power networks using extended Kalman filter*. IEEE Transactions on Power Electronics, 29(2):631–641, Feb 2014, ISSN 1941-0107.

[228] Macias, J.A.R. and Exposito, A.G.: *Kalman filter tuning for digital protection applications*. In *2003 IEEE Bologna Power Tech Conference Proceedings,*, volume 4, pages 1–5, 2003.

[229] Buso, S., Fasolo, S., Malesani, L., and Mattavelli, P.: *A dead-beat adaptive hysteresis current control*. IEEE Transactions on Industry Applications, 36(4):1174–1180, July 2000, ISSN 1939-9367.

[230] Karimi-Ghartemani, M., Khajehoddin, S. A., Jain, P. K., Bakhshai, A., and Mojiri, M.: *Addressing DC component in PLL and notch filter algorithms*. IEEE Transactions on Power Electronics, 27(1):78–86, Jan 2012, ISSN 1941-0107.

[231] Golestan, S., Guerrero, J. M., and Gharehpetian, G. B.: *Five approaches to deal with problem of DC offset in phase-locked loop algorithms: Design considerations and performance evaluations*. IEEE Transactions on Power Electronics, 31(1):648–661, Jan 2016, ISSN 1941-0107.

[232] Lauss, G. F., Faruque, M. O., Schoder, K., Dufour, C., Viehweider, A., and Langston, J.: *Characteristics and design of power hardware-in-the-loop simulations for electrical power systems*. IEEE Transactions on Industrial Electronics, 63(1):406–417, Jan 2016, ISSN 1557-9948.

9 Attachment

9.1 Interconnection matrices two GFM in parallel

The interconnection matrices $\mathbf{L}_{11}$, $\mathbf{L}_{12}$, $\mathbf{L}_{21}$, and $\mathbf{L}_{22}$ of the system composed of two GFM converters operating in parallel and indicated in eq. (4.54), are reported below:

$$\mathbf{L}_{21} = \begin{bmatrix} 0&0&0&0&0&0&0&0&1&0&0&0&0 \\ 0&0&0&0&0&0&0&0&0&1&0&0&0 \\ 0&0&0&0&0&0&0&0&0&0&0&0&1 \end{bmatrix}; \qquad \mathbf{L}_{22} = \begin{bmatrix} 0^{3\times 2} \end{bmatrix};$$

$$\mathbf{L}_{11}^{T} = \begin{bmatrix} 0&0&0&0&0&0&0&0&0&1&0&0&0&0&0&0&0&0&0&0&0&0 \\ 0&0&0&0&0&0&0&0&0&0&1&0&0&0&0&0&0&0&0&0&0&0 \\ 0&0&0&0&0&0&0&0&0&0&0&0&0&1&0&0&0&0&1&0&0&0 \\ 0&0&0&0&0&0&0&0&0&0&0&0&0&0&1&0&0&0&0&1&0&0 \\ 0&0&0&0&0&0&0&0&0&0&0&0&0&1&0&0&0&0&0&0&1&0 \\ 0&0&0&0&0&0&0&0&0&0&0&0&0&0&1&0&0&0&0&0&0&1 \\ 0&0&0&0&0&0&0&1&0&0&0&1&0&0&0&0&1&0&0&0&0&0 \\ 0&0&0&0&0&0&0&0&1&0&0&0&1&0&0&0&0&1&0&0&0&0 \\ 0&0&0&0&0&0&0&0&0&0&0&0&0&0&0&0&0&0&0&0&0&0 \\ 0&0&0&0&0&0&0&0&0&0&0&0&0&0&0&0&0&0&0&0&0&0 \\ 0&1&0&0&0&0&0&0&0&0&0&0&0&0&0&0&0&0&0&0&0&0 \\ 0&0&0&1&0&0&0&0&0&0&0&0&0&0&0&0&0&0&0&0&0&0 \\ 0&0&0&0&1&0&0&0&0&0&0&0&0&0&0&0&0&0&0&0&0&0 \end{bmatrix};$$

$$\mathbf{L}_{12}^{T} = \begin{bmatrix} 0&0&0&0&0&1&0&0&0&0&0&0&0&0&0&0&0&0&0&0&0&0 \\ 0&0&0&0&0&0&1&0&0&0&0&0&0&0&0&0&0&0&0&0&0&0 \end{bmatrix}. \tag{9.1}$$

9.2 Publications related to this thesis

9.2.1 Journal publications

J1 R. Rosso, J. Cassoli, G. Buticchi, S. Engelken, and M. Liserre, "Robust stability analysis of LCL filter based synchronverter under different grid conditions", in IEEE Transactions on Power Electronics, vol. 34, no. 6, pp. 5842-5853, June 2019.

J2 R. Rosso, S. Engelken and M. Liserre, "Robust stability analysis of synchronverters operating in parallel," IEEE Transactions on Power Electronics, vol. 34, no. 11, pp. 11309-11319, Nov. 2019.

J3 R. Rosso, M. Andresen, S. Engelken, and M. Liserre, "Analysis of the interaction among power converters through their synchronization mechanism," IEEE Transactions on Power Electronics, vol. 34, no. 12, pp. 12321- 12332, Dec. 2019.

J4 R. Rosso, S. Engelken and M. Liserre, "Robust stability investigation of the interactions among grid-forming and grid-following converters," IEEE Journal of Emerging and Selected Topics in Power Electronics (JESTPE), vol. 8, no. 2, pp. 991-1003, June 2020. (*Recipient of the second paper prize award of IEEE JESTPE 2020.*)

J5 Z. Zou, R. Rosso and M. Liserre, "Modeling of the phase detector of a synchronous-reference-frame phase-locked loop based on second-order approximation," in IEEE Journal of Emerging and Selected Topics in Power Electronics (JESTPE), vol. 8, no. 3, pp. 2534-2545, Sept. 2020.

J6 R. Rosso, X. Wang, M. Liserre, X. Lu and S. Engelken, "Grid-Forming converters: control approaches, grid-synchronization, and future trends - a review," in IEEE Open Journal of Industry Applications, vol. 2, pp. 93-109, 2021.

J7 Z. Zou, B. D. Besheli, R. Rosso, M. Liserre and X. Wang, "Interactions between two phase-locked loop synchronized grid converters," in IEEE Transactions on Industry Applications, vol. 57, no. 4, pp. 3935-3947, July-Aug. 2021.

J8 R. Rosso, S. Engelken and M. Liserre, "On the implementation of a FRT strategy for grid-forming (GFM) converters under symmetrical and asymmetrical grid faults," in IEEE Transactions on Industry Applications, vol. 57, no. 5, pp. 4385-4397, Sept.-Oct. 2021.

9.2.2 Conference publications

C1 R. Rosso, J. Cassoli, S. Engelken, G. Buticchi, and M. Liserre, "Analysis and design of LCL filter based synchronverter", 2017 IEEE Energy Conversion Congress and Exposition (ECCE), Cincinnati, OH, 2017, pp. 5587-5594.

C2 R. Rosso, G. Buticchi, M. Liserre, Z. Zou, and S. Engelken, "Stability analysis of synchronization of parallel power converters", IECON 2017 - 43rd Annual Conference of the Industrial Electronics Society, Beijing, 2017, pp. 440-445.

C3 R. Rosso, S. Engelken, M. Liserre, "Analysis of the behavior of synchronverters operating in parallel by means of component connection method (CCM)", 2018 IEEE Energy Conversion Congress and Exposition (ECCE), Portland, OR, 2018, pp. 2228-2235.

C4 R. Rosso, S. Engelken, and M. Liserre, "A generalized formulation of active power synchronization based control algorithms for grid connected converters," IECON 2018 - 44th Annual Conference of the IEEE Industrial Electronics Society, Washington, DC, 2018, pp. 883-888.

C5 R. Rosso, S. Engelken, Z. Zou, V. Willich, and M. Liserre, "Parameter sensitivity analysis of SPC-based control under different grid conditions," IECON 2018 - 44th Annual Conference of the IEEE Industrial Electronics Society, Washington, DC, 2018, pp. 2404-2409.

C6 R. Rosso, S. Engelken, and M. Liserre, "Analysis of the parallel operation between synchronverters and PLL-based converters," 2019 IEEE Energy conversion Congress and Exposition (ECCE), Baltimore, MD, USA, 2019, pp. 2583-2590.

C7 Z. Zou, B. D. Besheli, R. Rosso and M. Liserre, "Interactions between phase-locked loop synchronized grid converters with different bandwidths and power ratings," 2019 IEEE Energy Conversion Congress and Exposition (ECCE), Baltimore, MD, 2019, pp. 5430-5437.

C8 R. Rosso, S. Engelken, and M. Liserre, "Current limitation strategy for grid-forming converters under symmetrical and asymmetrical grid faults," 2020 IEEE Energy Conversion Congress and Exposition (ECCE), Detroit, MI, 2020, pp. 3746-3753.

C9 R. Rosso, X. Wang, M. Liserre, X. Lu, and S. Engelken, "Grid-forming converters: an overview of control approaches and future trends," 2020 IEEE Energy Conversion Congress and Exposition (ECCE), Detroit, MI, 2020, pp. 4292-4299.

9.2.3 Patent applications

P1 R. Rosso, S. Engelken, and M. Liserre, *"Wind farm comprising a power flow unit, and such a power flow unit"*, PCT/EP2019/072482, 2020.

P2 R. Rosso, S. Engelken, and M. Liserre, *"Wind farm comprising a stabilization unit, and such a stabilization unit"*, PCT/EP2019/072490, 2020.

P3 R. Rosso, S. Engelken, and M. Liserre, *"Device and method for angle stabilization of a virtual synchronous machine"*, US Patent Appl. No. 17/108,846. 2021.

P4 R. Rosso, S. Engelken, and M. Liserre, *"Methods for current limitation of a virtual synchronous machine"*, US Patent Appl. No. 17/118,049. 2021.